



**HAL**  
open science

## Nouvelles méthodes pseudo-MOSFET pour la caractérisation des substrats SOI avancés

Amer El Hajj El Hajj Diab Diab

► **To cite this version:**

Amer El Hajj El Hajj Diab Diab. Nouvelles méthodes pseudo-MOSFET pour la caractérisation des substrats SOI avancés. Autre. Université de Grenoble, 2012. Français. NNT : 2012GRENT060 . tel-00796613

**HAL Id: tel-00796613**

**<https://theses.hal.science/tel-00796613>**

Submitted on 4 Mar 2013

**HAL** is a multi-disciplinary open access archive for the deposit and dissemination of scientific research documents, whether they are published or not. The documents may come from teaching and research institutions in France or abroad, or from public or private research centers.

L'archive ouverte pluridisciplinaire **HAL**, est destinée au dépôt et à la diffusion de documents scientifiques de niveau recherche, publiés ou non, émanant des établissements d'enseignement et de recherche français ou étrangers, des laboratoires publics ou privés.

## THÈSE

Pour obtenir le grade de

## DOCTEUR DE L'UNIVERSITÉ DE GRENOBLE

Spécialité : **NANO ELECTRONIQUE ET NANO TECHNOLOGIES  
(NENT)**

Arrêté ministériel : 7 août 2006

Présentée par

**Amer EL HAJJ DIAB**

Thèse dirigée par **Sorin CRISTOLOVEANU**  
et codirigée par **Irina IONICA**

préparée au sein du **Laboratoire IMEP-LAHC**  
dans l'**École Doctorale EEATS**

# Nouvelles méthodes pseudo- MOSFET pour la caractérisation des substrats SOI avancés

(**Novel pseudo-MOSFET methods for the characterization of  
advanced SOI substrates**)

Thèse soutenue publiquement le **10 Décembre 2012**,  
devant le jury composé de :

**M. Olivier BONNAUD**

Professeur, Université de Rennes (Président, Rapporteur)

**Mme. Daniela MUNTEANU**

Directrice de Recherche CNRS, IM2NP Marseille (Rapporteur)

**M. Francisco GÁMIZ PÉREZ**

Professeur, Université de Granada (Membre)

**M. Daniel DELPRAT**

Manager advanced R&D, Soitec (Membre)

**M. Sorin CRISTOLOVEANU**

Directeur de Recherche CNRS, IMEP-LAHC (Directeur de thèse)

**Mme. Irina IONICA**

Maître de conférences, IMEP-LAHC/INPG (Co-encadrante de thèse)



*To my parents, brother, sister  
and my secret love*

# TABLE OF CONTENTS

<b>ACKNOWLEDGEMENTS</b>	<b>5</b>
<b>LIST OF ACRONYMS</b>	<b>7</b>
<b>LIST OF SYMBOLS</b>	<b>8</b>
<b>LIST OF CONSTANTS</b>	<b>10</b>
<b>GENERAL INTRODUCTION</b>	<b>11</b>
<b>CHAPTER I: INTRODUCTION TO SOI MATERIALS AND DEVICES</b>	<b>13</b>
INTRODUCTION	14
1. SOI DEVICES	15
1.1 SOI technology: an answer to scaling and diversity in Moore's law	15
1.2 Advantages of the SOI technology	16
1.3 SOI MOSFETs	19
1.3.1 Partially depleted transistors: PD MOSFETs	20
1.3.2 Fully depleted transistors: FD MOSFETs	22
1.4 Innovative SOI transistors	23
1.4.1 Multi-gate transistors	23
1.4.1.1 Double-gate (DG) transistors	24
1.4.1.2 Triple-gate transistors	24
1.4.1.3 Four-gate (G <sup>4</sup> -FET) transistors	25
1.4.2 Gate-All-Around (GAA) transistors	26
1.4.3 Tri-dimensional nanowires (3D NWs)	26
2. SOI MATERIALS	27
2.1 State-of-the-art	27
2.2 Fabrication methods	28
2.2.1 SIMOX technology	28
2.2.2 SOI by wafer bonding	30
2.2.2.1 BESOI	32
2.2.2.2 ELTRAN	32
2.2.2.3 Unibond (Smart-Cut™ process)	33
2.2.3 Silicon-On-Nothing (SON)	36
2.2.4 Other SOI technologies	36
2.2.4.1 Silicon-On-Sapphire	36
2.2.4.2 Insulation by Porous Oxidized Silicon	37
2.2.4.3 Zone Melting Recrystallization and Epitaxial Layer Overgrowth	37
2.3 Novel semiconductor on insulator structures	38
2.3.1 Strained SOI materials	38
2.3.2 Hybrid orientation technologies	39
2.3.3 Germanium-On-Insulator	40
2.3.4 Other semiconductor, BOX and substrate materials	41
2.3.4.1 Conductive film materials	41
2.3.4.2 BOX and substrate materials	41
2.4 Defects of SOI material	42
CONCLUSION	43
REFERENCES CHAPTER I	44

<b>CHAPTER II: ELECTRICAL CHARACTERIZATION OF SOI SUBSTRATES</b>	<b>47</b>
INTRODUCTION	48
1. PSEUDO-MOSFET PRINCIPLE AND OPERATION	49
1.1 Overview	49
1.2 Point-contact $\Psi$ -MOSFET technique	51
1.2.1 Sample preparation	52
1.2.2 Typical $I_D$ - $V_G$ in $\Psi$ -MOSFET configuration	53
1.2.3 Substrate effect	55
1.2.4 Influence of probe pressure	56
1.3 Extraction methods of the electrical parameters	57
1.3.1 Threshold voltage and flat-band voltage	59
1.3.2 Carrier mobility	60
1.3.3 Mobility reduction factor and series resistance	62
1.3.4 Subthreshold swing and interface traps density	62
1.4 Impact of the top interface in thin SOI films	63
1.5 Revisited $\Psi$ -MOSFET models	67
2. CHARACTERIZATION OF ULTRA AND EXTRA THIN SOI WAFERS	69
2.1 Experimental conditions	69
2.1.1 Sample preparation	70
2.1.2 Measurement system	70
2.2 Results obtained on UT/ET SOI	71
3. LOW-TEMPERATURE $\Psi$ -MOSFET MEASUREMENTS	74
3.1 Interest of low-temperature measurements	74
3.2 Experimental set-up	74
3.3 Drain current variation with temperature	75
3.4 Extracted parameters	77
3.4.1 Carrier mobility	78
3.4.2 Subthreshold swing and threshold voltage	82
CONCLUSION	86
REFERENCES CHAPTER II	87
<b>CHAPTER III: NOVEL DEVELOPMENTS OF <math>\Psi</math>-MOSFET METHOD</b>	<b>89</b>
INTRODUCTION	90
1. LOW-FREQUENCY NOISE MEASUREMENTS ON BARE SOI WAFERS	91
1.1 Why noise measurements?	91
1.2 Overview of the electronic noise	91
1.2.1 Fundamentals of noise	92
1.2.2 Different sources of noise in MOS transistor	93
1.2.2.1 White noise	93
1.2.2.2 Excess noise	94
1.3 LFN on SOI wafers	99
1.3.1 LFN in $\Psi$ -MOSFET: experimental set-up	99
1.3.2 Experimental results	101
1.3.2.1 $1/f$ noise behavior	101
1.3.2.2 Noise model: CNF or HMF?	102
1.3.2.3 Probe pressure impact on LFN	103
1.3.2.4 $D_{it}$ extraction	104
1.3.2.5 Impact of the surface preparation on LFN	105

1.3.2.6 Feasibility of LFN on extra-thin SOI structures	107
1.4 Conclusion of section 1	107
2. SPLIT $C$ - $V$ MEASUREMENT IN $\Psi$ -MOSFET CONFIGURATION	109
2.1 Split $C$ - $V$ technique and principle	109
2.2 Interest of split $C$ - $V$ for SOI wafer characterization	110
2.3 Extension of $\Psi$ -MOSFET for split $C$ - $V$ measurements	111
2.3.1 Method and experiment	111
2.3.2 Experimental $C$ - $V$ curves	112
2.4 Impact of experimental conditions on $C$ - $V$ measurements	113
2.4.1 Probe pressure impact on $C$ - $V$ curves	113
2.4.2 Frequency effects	114
2.5 Extraction of $\mu_{\text{eff}}$ by split $C$ - $V$ technique	118
2.5.1 Adapted methodology to extract $\mu_{\text{eff}}$	118
2.5.2 Applications of $\mu_{\text{eff}}$ extraction for advanced SOI structures	120
2.6 Conclusion of section 2	123
CONCLUSION	124
REFERENCES CHAPTER III	125
<b>CHAPTER IV: INNOVATIVE APPLICATIONS OF PSEUDO-MOSFET</b>	<b>127</b>
INTRODUCTION	128
1. CHARACTERIZATION OF HEAVILY DOPED SOI WAFERS	129
1.1 From undoped to doped SOI	129
1.2 $\Psi$ -MOSFET characterizations	129
1.2.1 Y-function	131
1.3 Revised model for parameter extraction in HD SOI	131
1.3.1 Volume conduction	132
1.3.2 Surface accumulation	133
1.3.3 Extracted parameters	134
1.3.3.1 Van der Pauw and Hall effect	135
1.3.3.2 Comparison of $\Psi$ -MOSFET, Van der Pauw and Hall effect results	137
1.4 Conclusion of section 1	138
2. SOI-BASED SENSOR FOR GOLD NANOPARTICLES DETECTION	140
2.1 SOI as a detection platform	140
2.2 Gold nanoparticles detection by $\Psi$ -MOSFET	141
2.2.1 Fabrication steps of SOI sensors	142
2.2.2 Sensor response	143
2.2.2.1 Reproducibility	144
2.2.2.2 Impact of particle size and density	145
2.2.2.3 Sensitivity improvement	146
2.3 Conclusion of section 2	148
3. $\Psi$ -MOSFET CHARACTERIZATION OF 3D VERTICALLY STACKED SiGe AND SiGeC NANOWIRES	149
3.1 Overview	149
3.2 Fabrication process	151
3.3 Electrical transport properties of SiGe NWs	154
3.3.1 Basic characteristics	154
3.3.2 Carrier transport and impact of series resistance	156
3.3.2.1 Hole carrier transport and mobility	157
3.3.2.2 Impact of series resistance	159
3.3.3 Low-temperature measurements	160

3.3.4 Multiple parallel NWs at 300 K _____	162
3.4 Conclusion of section 3 _____	163
CONCLUSION _____	164
REFERENCES CHAPTER IV _____	165
<b>GENERAL CONCLUSION _____</b>	<b>168</b>
<b>LIST OF SCIENTIFIC PUBLICATIONS _____</b>	<b>172</b>
<b>ABSTRACT/RÉSUMÉ _____</b>	<b>174</b>
<b>FRENCH THESIS SUMMARY _____</b>	<b>175</b>
INTRODUCTION GENERALE _____	176
PARTIE I: LE MATERIAU SOI FABRICATION ET CARACTERISATION _____	177
A. Le procédé Unibond (Smart-Cut™) _____	178
B. La technique pseudo-MOSFET _____	179
C. Extraction des paramètres électriques _____	180
D. Caractérisation des plaques SOI très minces _____	182
PARTIE II: NOUVELLES TECHNIQUES DE CARACTERISATION DES PLAQUES SOI _____	184
A. Mesures $\Psi$ -MOSFET à basse température _____	184
B. Mesures de bruit à basse fréquence _____	188
C. Mesures split C-V _____	192
CONCLUSION GENERALE _____	196
RÉFÉRENCES _____	198

# ***Acknowledgements***

A major research project like this is never the work of a single person. The contributions of many different people, in their different ways, have made this possible. I would like to express my appreciation especially to the following.

First, I would like to particularly express my gratitude and my thanks to my supervisors. Sorin Cristoloveanu and Irina Ionica, my dear thesis supervisors, who had allowed me to develop positively towards independent thinking and led me to adopt my subject, something essential in the world of research. Thank you for having always supported me, encouraged me and corrected my papers/my presentations several times... Sorin, my professor in the “three things”, I learned a lot from you not only in SOI but also in project management, conference organization, scientific human relations and many other things.

Irina, I will be always your “jeune padawan”, I am deeply grateful for your help in the research, presentation, paper/thesis writing, moral and teaching levels during these three years. You were always near me for any help I needed. I appreciate a lot your personality, kindness, your humor and your ability to listen and understand people, your way of thinking and dealing with things. Sorin and Irina, no words can express my thanks for you both!

For Gérard Ghibaudo, my third non official supervisor, what I can say! Thanks are not enough. It has always been very simple and motivating to work with you, your kindness, your humanity and your loyalty make you one of the persons that I respect most. Of course, I will not forget your great and deep knowledge in the semiconductor area and thank you for sharing a part of it with me.

I would like to express my gratitude to the committee of this thesis: Prof. Olivier Bonnaud, Prof. Francisco Gámiz Pérez, Dr. Daniela Munteanu and Manager advanced R&D Daniel Delprat. I am honored by their participation to my Ph.D. defense and their expert judgment of my work.

My collaboration with Soitec™ engineers and scientists was much appreciated: Carlos Mazuré, Frédéric Allibert, Daniel Delprat and William Van Den Daele (“I will always remember Bonjour Madame every morning”).



Next, I'd like to thank the French Ministry of National Education and the doctoral school EEATS (University of Grenoble and Grenoble Institute of Technology), for offering me a chance to conduct this Ph.D. thesis research and for their financial support (Allocation de Recherche) during the three years. I would also like to thank our collaborators, Akiko Ohata, Young-Ho Bae, Crisitina Fernández “pseudo-MOSFET girl”, my friend Noel Rodriguez, Emeline Saracco and Jean-François Damlencourt for providing me many insightful discussions as well as the help in paper's preparing and other technical problems. Additionally, I'd like to acknowledge people at IMEP-LAHC laboratory for giving me help and support during experiments: Jan Chroboczek, Xavier Mescot, Martine Gri. Thanks to Fanyu Liu, Luca Pirro, Mehdi Daanoune and Sofiane Sirajeddine for the good work that we did and we will continue to do together.

I would like also thank all my friends “Ph.D. students” at IMEP-LAHC laboratory, my present and my ex office colleagues (A286), all the members of the laboratory IMEP-LAHC council, IMEP technical and administration staff and my foreign, French and Lebanese friends in Grenoble/France.

Special thanks to my professor Bilal Beydoun in the Lebanese University for introducing me to the world of nanotechnology.

Finally, loving thanks to my parents Abla & Ahmad, brother Assem and sister Katia. Without their support and motivation, my achievements would have been incomplete. I love you all.

# List of acronyms

---

<b>Acronym</b>	<b>Nomination</b>
MOS	Metal oxide semiconductor
MOSFET	Metal oxide semiconductor field effect transistor
$\Psi$ -MOSFET	Pseudo-MOSFET
BOX	Buried oxide
CMOS	Complementary metal oxide semiconductor
SOI	Silicon-On-Insulator
HD SOI	Heavily-doped Silicon-On-Insulator
VDP	Van der Pauw
NWs	Nanowires
GAA	Gate-All-Around
Low-T	Low-temperature
1D, 2D and 3D	One, two and tri-Dimensional
NP	Nanoparticles
APTES	Amino-Propyl-Tri-Ethoxy-Silane
AFM	Atomic force microscopy
PD	Partially depleted
FD	Fully depleted
SIMOX	Separation by IMplantation of OXYgen
BESOI	Bond-and-Etch-back Silicon-On-Insulator
ELTRAN	Epitaxial Layer TRANsfer
ITOX	Internal Thermal OXidation
MLD	Modified Low Dose
UT	Ultra-thin
ET	Extra-thin
$h^+$	Hole
$e^-$	Electron
LFN	Low-frequency noise
RTS	Random Telegraph Signal
G-R	Generation-recombination
CNF	Carrier number fluctuation
HMF	Hooge mobility fluctuation

---

# List of symbols

Symbol	Unit	Description
$I_D$	A	Drain current
$I_{D,corr}$	A	Corrected drain current from series resistance
$I_S$	A	Source current
$I_G$	A	Gate current
$I_{acc}$	A	Accumulation current
$I_{vol}$	A	Volume current
$V_D$	V	Drain voltage
$V_S$	V	Source voltage
$V_G$	V	Back-gate voltage
$V_T$	V	Threshold voltage
$V_{FB}$	V	Flat-band voltage
$S$	V.dec <sup>-1</sup>	Subthreshold swing
$S_n$	V.dec <sup>-1</sup>	Subthreshold swing for electrons
$S_p$	V.dec <sup>-1</sup>	Subthreshold swing for holes
PSD, $S(f)$	W.Hz <sup>-1</sup>	Power spectral density
$S_{I_d}$	A <sup>2</sup> .Hz <sup>-1</sup>	Drain current power spectral density
$S_{V_g}$	V <sup>2</sup> .Hz <sup>-1</sup>	Gate voltage power spectral density
$S_{V_{fb}}$	V <sup>2</sup> .Hz <sup>-1</sup>	Flat-band voltage power spectral density
$S_{I_d}/I_D^2$	Hz <sup>-1</sup>	Normalized power spectral density
$S_{eff}$	mm <sup>2</sup>	Effective surface
$D_{it}$	cm <sup>-2</sup> /eV	Interface trap density
$D_{it1}$	cm <sup>-2</sup> /eV	Interface trap density at film-BOX (back) interface
$D_{it2}$	cm <sup>-2</sup> /eV	Interface traps density at top interface
$\mu_o$	cm <sup>2</sup> /V.s	Low-field mobility
$\mu_{eff}$	cm <sup>2</sup> /V.s	Effective mobility
$\mu_n$	cm <sup>2</sup> /V.s	Low-field electrons mobility
$\mu_p$	cm <sup>2</sup> /V.s	Low-field holes mobility
$\mu_{vol}$	cm <sup>2</sup> /V.s	Volume mobility
$\mu_s$	cm <sup>2</sup> /V.s	Accumulation mobility
$\mu_H$	cm <sup>2</sup> /V.s	Hall mobility
$\mu_{Ph}$	cm <sup>2</sup> /V.s	Low-field mobility limited by phonon scattering
$\mu_{sr}$	cm <sup>2</sup> /V.s	Low-field mobility limited by surface roughness
$\mu_C$	cm <sup>2</sup> /V.s	Low-field mobility limited by phonon scattering
$R_{SD}$	$\Omega$	Series resistance between source and drain
$R_{\square}$	$\Omega$	Sheet resistance
$G$	$\Omega^{-1}$	Electrical conductance
$g_m$	S	Transconductance
$f$	Hz	Frequency
$f_g$	unitless	Geometrical factor in pseudo-MOSFET
$T$	K	Temperature

Symbol	Unit	Description
$C_{Si}, C_{film}$	F.cm <sup>-2</sup>	Surface silicon film capacitance
$C_{it1}$	F.cm <sup>-2</sup>	Surface traps density capacitance at film-BOX interface
$C_{it2}$	F.cm <sup>-2</sup>	Surface traps density capacitance at top interface
$C_{ox}$	F.cm <sup>-2</sup>	Surface oxide capacitance/BOX capacitance per unit area
$C_{dep}$	F.cm <sup>-2</sup>	Dynamic depletion capacitance
$C_{gc}$	F.cm <sup>-2</sup>	Gate-to-channel capacitance
$C_{gb}$	F.cm <sup>-2</sup>	Gate-to-bulk capacitance
$C_{max}$	F	Maximum value of the gate-oxide capacitance
$C_{sub}$	F.cm <sup>-2</sup>	Depleted substrate capacitance
$\rho$	cm. $\Omega$	Electrical resistivity
$\theta_1$	V <sup>-1</sup>	First order mobility attenuation factor
$\theta_2$	V <sup>-1</sup>	Second order mobility attenuation factor
$\phi_F$	V	Fermi level potential
$\phi_{fb}$	V	Work function difference between Si film and substrate
$Q_{ox}$	C	The fixed charge in the buried oxide
$Q_{dep}$	C	Depletion charge
$Q_{inv}$	C	Inversion charge
$Q_{acc}$	C	Accumulation charge
$E_G$	eV	Band gap
$E_{eff}$	V/cm	Effective transversal electric field
$N_t$	cm <sup>-3</sup> /eV	Volume trap density
$N_{it}$	cm <sup>-2</sup> /eV	Surface trap density in the oxide
$N_{inv}$	cm <sup>-2</sup>	The concentration of carriers in the inversion layer
$N_A$	cm <sup>-3</sup>	Acceptor impurities concentration
$N_D$	cm <sup>-3</sup>	Donor impurities concentration
$N_{film}$	cm <sup>-3</sup>	Doping level in the silicon film
$N_{sub}$	cm <sup>-3</sup>	Doping level in the substrate
$n_i, n_i(T)$	cm <sup>-3</sup>	Intrinsic carrier density
$t_{Si}$	nm	Silicon film thickness
$t_{BOX}$	nm	Buried oxide thickness
$W_D$	nm	Width of the depletion layer
$p$	g	Pseudo-MOSFET probe pressure

# List of constants

---

Symbol	Value/Unit	Description
k	$1.38 \times 10^{-23}$ J/K	Boltzmann constant
q	$1.602 \times 10^{-19}$ C	Elementary charge
$\epsilon_0$	$8.85 \times 10^{-12}$ F/m	Vacuum permittivity
$\epsilon_{Si}$	$11.8 \times \epsilon_0$ F/m	Silicon permittivity
$\epsilon_{SiO_2}$	$3.9 \times \epsilon_0$ F/m	Silicon dioxide permittivity

---

# ***General introduction***

Since the era of portable multimedia, Smartphones and other state-of-the-art applications, the demand for smaller, smarter and deeper processors was accelerated, pulling behind it all the microelectronics industry and intensifying the rhythm of the technological research. In this challenging context of evolution of microelectronics, the use of Silicon-On-Insulator (SOI) substrates instead of bulk silicon opens new avenues for innovation, delivering performance, power and miniaturization. Indeed, SOI technology can overcome some of the major issues of bulk silicon technology (*e.g.* device isolation is less complex thanks to the presence of the buried oxide). Moreover, SOI devices offer a much better electrostatic control of the channel thanks to advanced architectures (*e.g.* multi-gate transistors).

In order to take full advantage of all SOI benefits, the SOI wafers must be of an excellent electrical quality. In this highly competitive field, the aim of this thesis is to contribute to the analysis and to the optimization of advanced SOI substrates by the development of innovative methods of electrical characterization and new physical models, starting from the classical, well-known pseudo-MOSFET ( $\Psi$ -MOSFET) configuration.

This manuscript is composed of four chapters: one on the review of SOI technology, the second about  $\Psi$ -MOSFET characterization technique and its developments, the third on innovative electrical methods and the last on the use of  $\Psi$ -MOSFET configuration for more exotic applications in nanoelectronics.

The first chapter will cover Semiconductor-On-Insulator (SOI) materials and devices as well as their characteristics. In the first section, we will introduce SOI technology and transistor structures fabricated on SOI substrate. We will concentrate on partially depleted (PD) and fully depleted (FD) SOI MOSFETs by presenting their principles and challenging issues. Finally, we will show some innovative SOI-based technology architectures. In the second section, the state-of-the art of SOI material technology and the fabrication methods are discussed. We also introduce novel semiconductor on insulator structures emerged from SOI technologies. Finally, we will present the defects of SOI materials.

In the second chapter, we start from the classical well known  $\Psi$ -MOSFET characterization method for SOI materials. Firstly, we describe the principles, standard operation and classical parameters extraction for  $\Psi$ -MOSFET. In second section we wanted to know whether it is possible to extend the  $\Psi$ -MOSFET to advanced SOI substrates with ultra-thin film and/or BOX. Furthermore, the main question of the third section is: can we also extend  $\Psi$ -MOSFET at low temperature?

In the third chapter, we investigate the possibility to expand the range of  $\Psi$ -MOSFET from classical I-V measurements to other types of characterizations. The first track followed concerns the low frequency noise measurements. Is it possible to measure low-frequency noise in  $\Psi$ -MOSFET configuration? Furthermore, is it reasonable to apply MOS-like models to these measurements and extract material parameters? The second road taken drove us to C-V measurements in  $\Psi$ -MOSFET. Would a split C-V technique be possible for SOI in  $\Psi$ -MOSFET? Is the effective mobility extraction possible here, as it is in MOSFETs?

In the last chapter, we let our imagination run towards exotic uses of  $\Psi$ -MOSFET. Would it be possible to apply  $\Psi$ -MOSFET to heavily doped SOI films and could we obtain parameters such as the doping level? The SOI in  $\Psi$ -MOSFET is sensitive to the environment, but could it be used as a reliable sensor? We will present the answer to this question for gold nanoparticle detection. Finally the paradigm of  $\Psi$ -MOSFET is based on the use of back gate. Can this configuration be suitable for 3D vertically-stacked nanowires? Would the conduction through these nanowires be controlled by a back-gate as it is in  $\Psi$ -MOSFET? Could one obtain electrical parameters concerning the NWs from this kind of measurements?

The main answers to these questions will be developed chapter after chapter and synthesized in the general conclusion. During this Ph.D., some doors were opened albeit further investigations are needed; they will be presented as perspectives.

# **Chapter I:**

## ***Introduction to SOI materials and devices***



## ***Introduction***

This chapter introduces Semiconductor-On-Insulator (SOI) materials and devices as well as their characteristics.

In the first section, the motivations and the advantages of SOI structure for building transistors are shown. Then we discuss SOI devices by presenting successively the partially depleted (PD) and fully depleted (FD) transistors; finally, some innovative architectures based on SOI technology are described.

In the second section, we give an overview of the state of art of SOI technology and fabrication methods, followed by an introduction to new SOI-like materials. The defects of SOI material are also discussed.

## **1. SOI devices**

### **1.1 SOI technology: an answer to scaling and diversity in Moore's law**

The use of Silicon-On-Insulator (SOI) components is technically imperative in diverse domains of the electronics. Here are some examples: very low consumption circuits, in particular for laptops, telephones, tablets, game consoles, computers, watches; very fast microprocessors intended for PCs and servers; Radio Frequency circuits for wireless communication; average and high-voltage circuits for the lighting or engines command control; high temperature circuits for the oil, automobile and the aeronautics industries; hardened circuits for the space and the defense.

Silicon-On-Insulator is gaining momentum as bulk complementary metal oxide semiconductor (CMOS) technology is confronted with scaling, power and performance challenges. The miniaturization driven by Moore's Law requires doubling the density of transistors per unit area every two years. This law has very strong economic implications and makes the market very beneficial for the most powerful microelectronic integrated circuit manufacturers. The topic is hot, being situated at the crossing of two Moore avenues: continuing the scaling and diversity.

The milestones of the scaling are measurable in nanometers for the transistor feature size and in billions for the number of transistors in a System-On-Chip (SOC). SOI is certainly able to take us far beyond the current status. SOI circuits are denser, smaller, and faster. This is why the device miniaturization is more efficient and comfortable if transistors are fabricated "On Insulator". In addition, an effort to gain a stronger foothold in the coming fully depleted (FD) CMOS era: the world leader for SOI manufacturing (Soitec) is already providing SOI wafers to both planar two-Dimensional FD (FD-2D) and tri-Dimensional FD (FD-3D FinFET) customers for the next technological nodes (Figure I-1).

The diversity side of the Moore's law departs from the traditional forms of scaling. This route is imposed by the need for enriched circuit functionality. SOI is flexible for the co-integration of heterogeneous technologies and multi-functional devices. Skilled circuit design can take advantage of multiple gates, independently

biased, to reduce the transistor count for a given logic function or to elaborate new schemes of operation. Some innovative SOI devices will be illustrated later.

On the other hand, SOI circuits naturally offer low-power consumption without fundamentally disrupting the current CMOS process and design infrastructure [1]. A comparison of state-of-the-art bulk and SOI circuits provides unquestionable evidence. The main advantages of SOI technology will be discussed in the next sub-sections.



Figure I-1: SOI wafer roadmap from Soitec for next technological nodes [2].

The superior performances of SOI devices justify additional cost, which moreover is decreasing under the influence of the increase of the volume of markets. Finally, there is wide space for further improvements enabling a massive increase of the SOI segment in the global market for integrated circuits.

## 1.2 Advantages of the SOI technology

The main originality of the SOI transistor compared with the silicon bulk transistor comes from the presence of the buried oxide (BOX) under the Si film. By isolating the thin silicon film from the substrate, we limit the parasitic effects associated with it that may damage the good function of devices. Indeed, in a MOSFET there is only the superficial layer of silicon, with a thickness of 0.006-0.1  $\mu\text{m}$  (that is to say less than 0.01 % of the total thickness of the silicon wafer), which is really useful for the transport of carriers [3]. The rest of the Si wafer (99.99 %) is

responsible for the undesirable parasitic effects, which can be avoided by calling a solution such as SOI.

A schematic configuration cross section of a metal oxide semiconductor (MOS) transistor built in SOI is shown in Figure I-2a. An interesting specificity of SOI transistor is the possibility of applying simultaneously front-gate voltage ( $V_{G1}$ ) and back-gate voltage ( $V_{G2}$ ) to the gates G1 (front-gate) and G2 (back-gate). According to the bias applied to the gates G1 and G2, the body of the transistor can accommodate two conduction channels: the front-channel at the film/gate oxide interface and the back-channel at the film/BOX interface (Figure I-2b).

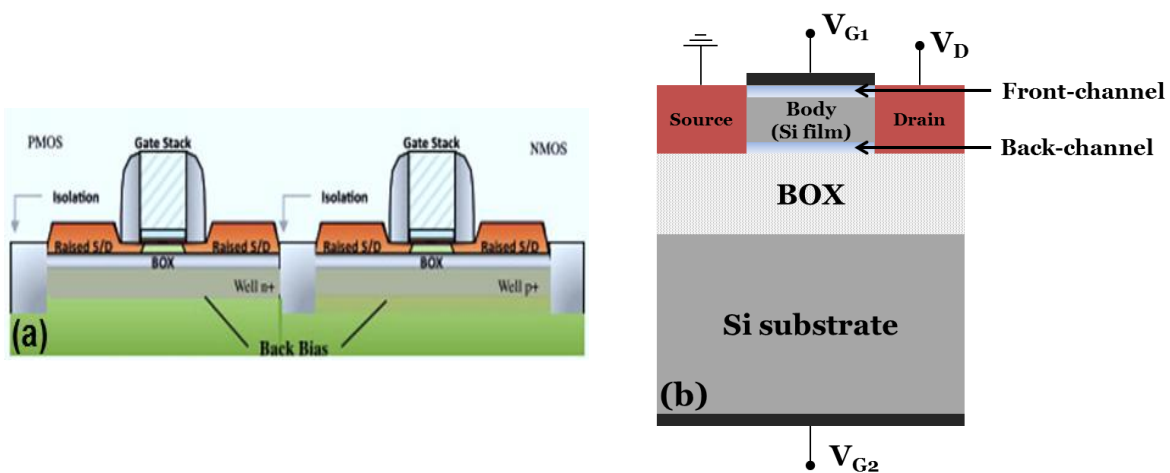


Figure I-2: SOI MOS transistor cross section (a) of schematic architecture [4], (b) of the transistor.

The SOI transistors, thanks to their structure, present advantages with respect to bulk MOSFETs. Below we expose some of these advantages.

**Immunity against radiations:** historically, there have been three reasons for developing and using SOI. In the 1970's and 1980's, radiation hardness of integrated circuits was the main motivation for choosing these new substrates. Transistors with thin SOI film are exceptionally tolerant to the transient effects of the ionizing irradiations. The majority of charges generated in the Si substrate would be stopped by the buried oxide, thus reducing the current surge in the active film. Besides, compared with silicon bulk, SOI possesses superior immunity for the induced degradation by hot carriers.

**Device and structure isolation:** SOI chips consist of millions of single-transistor islands dielectrically isolated from each other and from the underlying silicon substrate. The entire transistor body (the source, the drain, and the channel in

between) is isolated from the Si substrate and from every other transistor by means of the buried oxide below, and by a combination of thermally grown and deposited oxide above and on the sides of the transistor.

The lateral isolation makes inter-device separation in SOI free of complicated schemes of trench or well formation. The overall technology and circuit design are, in this respect, highly simplified and result in more compact Very-Large-Scale Integration chips compared to Si bulk circuit concept and design. On the other hand, the vertical isolation protects the thin active silicon layer (Si film) from most parasitic effects induced by the Si bulk substrate: leakage currents, radiation-induced photocurrents, *latch-up* effects between contiguous devices, *etc.*

**Reduction of parasitic capacitances:** the source and drain regions spread out down to the buried oxide so that the junctions between source/drain and the Si body do not present more than a lateral side and minimized surface [3]. It results a strong reduction of the current leakage and the junction capacitances. This offers the opportunity to fabricate CMOS circuits with lower power dissipation in standby and operating modes, improved speed, and wider temperature range.

**Reduction of short-channel effects (SCEs):** the limited extension of drain and source regions makes SOI MOS transistors less sensitive to the short-channel effects, induced by the charge sharing between gate and junctions. Indeed, the surfaces of the source/drain junctions depend only on the film thickness, the depleted zones are less spread and the SCEs decrease. Furthermore, the possibility of bias by the back-gate offers an additional way for controlling the short-channels effects.

**Low voltage and low power (LV/LP) circuits:** it is especially in this very competitive domain that SOI expresses its full potential. A low voltage applied to the gate is desirable to switch the transistor from the off state to the on state, leading to the need for a low subthreshold swing ( $S$ ). Only the SOI offers almost ideal slope in weak inversion ( $S \approx 60$  mV/decade at room temperature), and thus the possibility of lowering the threshold voltage ( $V_T$ ) around 0.2 to 0.3 V. The low leakage currents minimize the dissipated power in static mode, while the dynamic power is saved by the decrease of parasitic capacitances and of power supply voltage.

A gain in performance of about 20-30 % as compared to bulk-silicon circuits is systematically observed during operation with similar voltage power, whereas

operation at similar low power dissipation yields higher the gain by more than two times. In other words, SOI circuits of  $n$  generation and bulk-Si circuits from the next generation ( $n + 1$ ) perform comparably [5]. This argument is strong enough for major companies to include SOI technology in their strategy. IBM, Sony, AMD, Sharp, STMicroelectronics, *etc.*, are currently fabricating commercial SOI-enhanced PC processors and mobile communication devices.

The main disadvantage which the SOI had to undergo is the fact that the enumeration of this impressive list of advantages was not enough for perturbing the fast and continuous progress of the silicon technology. Moreover, the presence of the BOX asks to take into account other phenomena (*e.g.*, floating body, self-heating, BOX and Si-SiO<sub>2</sub> interface quality) which can affect the operating of SOI devices.

In the following sub-sections of this chapter we will describe the traditional technologies (PD and FD) of SOI MOSFETs and give examples of innovative SOI device architectures. The aim of these examples is to show how the SOI can improve performance.

### 1.3 SOI MOSFETs

The two technologies, which we denote now FD for fully depleted and PD for partially depleted are specific for “film On Insulator” structures, such as SOI or GeOI. PD technology is closer to the Si bulk technology in terms of electrical behavior, but does not have as many advantages as the FD technology in terms of reduced short-channel effects.

For a MOS transistor, there are different operating regimes (weak and strong inversion, depletion and accumulation). When we bias the gate in inversion mode, the majority carriers are pushed away from the oxide/semiconductor interface to create a depletion zone and then an inversion layer. Once the inversion regime appears, the depletion zone freezes and possesses a maximal width ( $W_{Dmax}$ ). It is expressed by the following relationship [6]:

$$W_{Dmax} = \sqrt{\frac{4\epsilon_{Si}\Phi_F}{qN_{A,D}}} = \sqrt{\frac{4\epsilon_{Si}kT}{q^2N_{A,D}} \ln\left(\frac{N_{A,D}}{n_i(T)}\right)} \quad (I-1)$$

where  $\epsilon_{Si}$  is the silicon permittivity,  $q$  is the elementary charge,  $k$  is the Boltzmann constant,  $T$  is the temperature,  $\phi_F$  is the Fermi level potential,  $n_i(T)$  is the intrinsic carrier density and  $N_{A,D}$  is the impurities concentration for acceptors ( $N_A$ ) or donors ( $N_D$ ).

In the case of SOI MOSFET, there are two MOS stacks, the first one corresponding to metal gate/gate oxide/Si film and the second to Si film/BOX/Si substrate. In that case, it is possible according to  $W_{Dmax}$  and to the film thickness ( $t_{Si}$ ) to distinguish the two modes (PD and FD) for SOI transistors:

- The PD mode, or **partially depleted**, corresponds to a film thickness  $t_{Si}$  superior two times to the maximal depletion width  $W_{Dmax}$ . In that case, there is a part of the film which will be ‘neutral’ (no space charge region can cover this part). Thus, the condition of PD mode can be written as  $t_{Si} > 2W_{Dmax}$ .
- The FD mode, or **fully depleted**, is obtained in case of  $t_{Si} < 2W_{Dmax}$ . The depletion zones overlap and the potential of both interfaces interacts by coupling.

The FD and PD modes depend only on the intrinsic carrier density, on the impurities concentration and on the temperature. Therefore, they are really specific to the semiconductor material used. To give an example,  $W_{Dmax}$  for a Si film with a doping concentration level ( $N_A = 10^{17} \text{ cm}^{-3}$ ), at room temperature ( $T = 300 \text{ K}$ ), is almost equal to 100 nm. The future generations of SOI transistors for the advanced nodes must be made on FD SOI to keep all the advantages of short-channel effects control ([7], [8]).

Notice that the previous analysis corresponds to long channels. In short channel transistors, the depletions of the source/drain are added to the depletion of the gate modifying the actual doping and leading to two-dimensional (2D) effects [9].

### 1.3.1 Partially depleted transistors: PD MOSFETs

As previously mentioned, in this case the depletion zones do not overlap and the electric potentials of the two interfaces (gate oxide/Si film and Si film/BOX) remain independent. This situation is very similar for the electrical operating to the architecture of bulk silicon transistors. The Si film must be inevitably doped to reduce

the depletion width so to decrease the short-channel effects. Nevertheless, in PD films there are additional effects named “floating-body effects”. In Si-bulk architecture, if majority carriers are created during the operating of the transistor, they can be evacuated by the substrate because it is directly connected to ground. On the other hand, in the case of a PD SOI transistor, the film potential is not fixed; it is then floating. The film potential is determined by the capacitances related to source and drain, by the front and back gate and also by the current which circulates in the channel. In most of the cases, the parasitic effects appear because of created majority carriers excess which cannot be evacuated from the Si film. Below are the most frequently encountered “floating-body effects”:

- The **kink effect** occurs in strong longitudinal field due to high drain voltage ( $V_D$ ). Majority carriers are then produced by impact ionization and increase the body potential. The potential increase has the impact of decreasing the threshold voltage ( $V_T$ ) and increasing the drain current ( $I_D$ ) [10].
- The **parasitic bipolar transistor effect** appears at strong  $V_D$  when a strong majority carrier density is accumulated, the body potential becomes high enough so that the PN (body-Source) junction turns on. The NPN (Source/film/Drain) bipolar transistor is activated. The drain current increases, it is the second kink effect.
- The **transient effects** (variations of body potential, threshold voltage, and current) occur during the switching of transistors [11]. When the gate is switched on, majority carriers are expelled from the depletion region (instantly formed by capacitive coupling) and collected in the neutral body, giving rise to a drain current ‘overshoot’. The drain current decreases gradually with time during electron-hole recombination. A reciprocal ‘undershoot’ occurs when the gate is switched from strong to weak inversion: the drain current increases with time as the majority carriers are generated and allow the depletion depth to shrink. The amplitude of current overshoot or undershoot is proportional to the difference between the final and initial body charges, and the transient duration depends on the generation-recombination rate in the film volume, at interfaces and on the edges.



- The **Gate-Induced Floating Body Effect** (GIFBE) effect [12] occurs for very thin gate oxides and at strong gate voltage; the leakage currents by tunnel effect can be important, leading to body charging, a variation of the film potential (even for low drain current) and an increase of the drain current.

In order to face all these floating-body effects and to ameliorate the transistor performances, FD technology presented in the next sub-section was found suitable to replace the PD technology.

### 1.3.2 Fully depleted transistors: FD MOSFETs

Unlike PD technology, full depletion appears when the depletion regions cover the whole transistor body (*i.e.*; the film thickness). The depletion charge is constant and cannot extend further when the gate bias increases. There is no neutral zone.

In SOI MOSFETs, two inversion channels can be activated, one at the front Si-gate oxide interface and the other at the back Si-BOX interface. A better coupling is then obtained between the gate bias and the inversion charge, leading in particular to an increase of the drain current. Besides, the front and back surface potentials become inter-related [3]. The interface coupling means that the electrical characteristics of one channel vary with the bias applied to the opposite gate. In practice, the front gate measurements may include contributions from the BOX and from the BOX/bulk Si interface, and highly depend on the back gate bias.

This FD technology presents numerous advantages:

- The possibility to non-dope the conduction channel enables increasing the mobility compared with a PD SOI transistor.
- Short-channel effects are largely reduced if  $t_{Si}$  is very small ([7], [8]).
- Lower threshold voltage compared to Si bulk technologies allows low power consumption applications.
- The subthreshold slope (S) is reduced due to the replacement of the dynamic depletion capacitance ( $C_{dep}$ ) by a fixed Si film capacitance ( $C_{Si} = \epsilon_{Si}/t_{Si}$ ).

Nevertheless FD SOI transistors have several issues especially in the case of ultra-thin films:

- Very sensitive threshold voltages to the ultra-thin Si film uniformity (especially for  $t_{\text{Si}} < 10$  nm).
- Defect coupling in FD MOSFETs means that carriers flowing at one interface are influenced by the presence of defects at the opposite interface.
- A mobility variation with the film thickness [13].
- Self-heating conveyed by the low thermal conductivity of the BOX.
- Drain-induced virtual substrate biasing (DIVSB) effect is due to the lateral penetration of the electric field into the BOX and underlying substrate. The fringing field causes an increase in the potential at the film-BOX interface; by consequence the front-channel threshold voltage and subthreshold slope are lowered [14].

To ameliorate the electrical behavior (lower  $V_T$ , steeper S, higher mobility, *etc.*) of SOI transistors, several innovative structures based on this technology were proposed.

## **1.4 Innovative SOI transistors**

The SOI structure and the advanced development of the film layer transfer technology allow the conception of transistors with innovative architectures and with improved performances. In this sub-section, we show various SOI-based architectures.

### **1.4.1 Multi-gate transistors**

Transistors with multi-gate are innovative architectures but with more complicated technological steps compared to SOI single-gate transistors (Figure I-3a). Their basic structure is the same as that of FD SOI: an extremely thin silicon film and a relatively thick buried oxide on a silicon substrate are always part of the structure.

The number, shape and the location of the gates improve the gate control over the channel and isolate it from parasitic effects which can appear in single-gate architectures. Components with multi-gates will lead microelectronics industry into the near future. These components present several advantages when the gate length becomes shorter than 25 nm.

#### 1.4.1.1 Double-gate (DG) transistors

The conception of double-gate transistors appeared as a solution for the penetration of the electric field in the BOX for ultra-thin SOI transistors. The addition of the second gate under the silicon blocks the penetration of the electric field and offers a better control of the channel (Figure I-3b). The presence of the back-gate increases the channel surface conduction and favors the volume inversion, thus, the drain current is increased compared with the single-gate SOI transistor (Figure I-3a). The subthreshold slope and the short-channel effects are also improved [15].

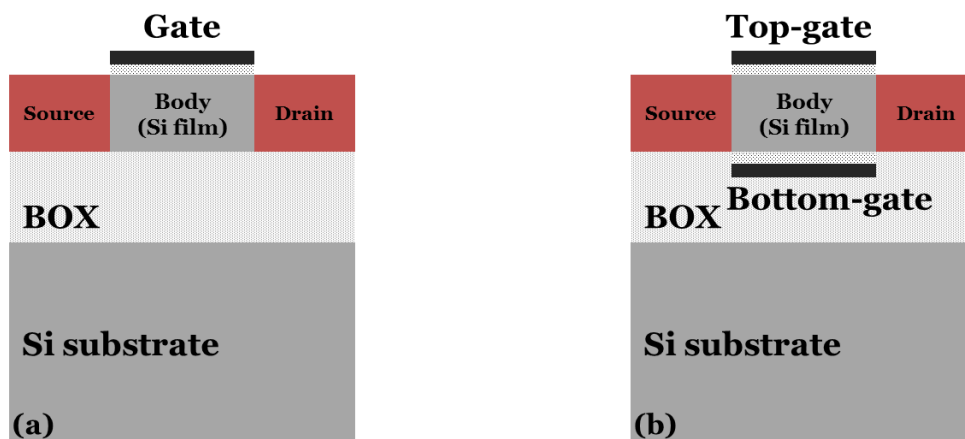


Figure I-3: (a) Conventional thin film SOI MOSFET, (b) SOI MOSFET with top and bottom gate (DG MOSFET).

#### 1.4.1.2 Triple-gate transistors

In triple-gate (Figure I-4a) or FinFET (Figure I-4b) transistors, the gate recovers the three faces of the Si 'fin', forming then three channels. The upper channel could be deactivated by using a thicker oxide, forming a semi-vertical double-gate transistor. The current is horizontal, but controlled by two vertical gates, which can be possibly biased independently. Because of the FinFET configuration, the coupling effects are tri-dimensional (3D): 'lateral' coupling between the opposite

gates, the ‘vertical’ coupling between channels and the substrate voltage and the ‘longitudinal’ coupling between the drain and the channel. Nevertheless, the performances are excellent thanks to the strengthening of the gate role. In general, FinFET transistors are made on bulk Si, but their structure and operation, in fully depleted regime, are similar to their cousins on SOI (Figure I-4b).

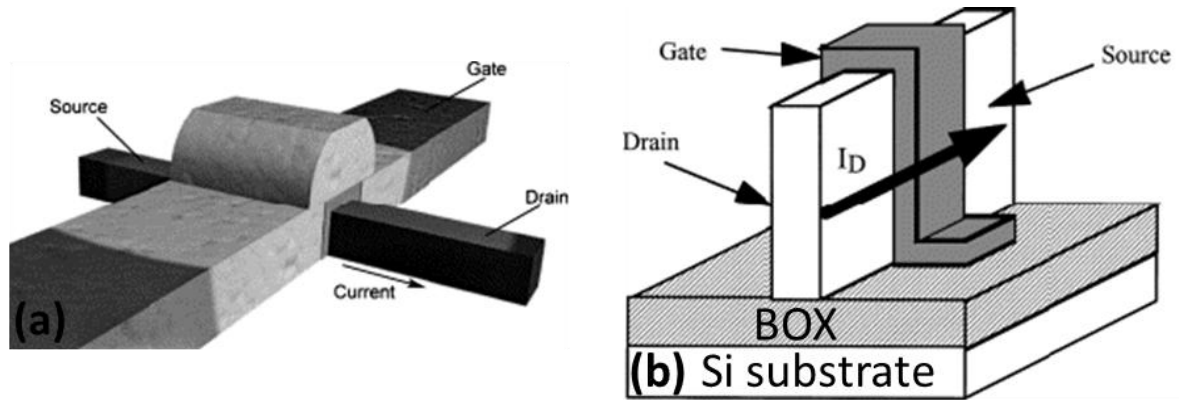


Figure I-4: (a) triple-gate SOI MOSFET, (b) SOI FinFET structure [16].

#### 1.4.1.3 Four-gate (G<sup>4</sup>-FET) transistors

The four-gate (G<sup>4</sup>-FET) transistor (Figure I-5) has four independently biased gates [17]. The source and the drain are doped N<sup>+</sup> and the body is N type, as in a transistor in accumulation mode. We form on sides two P<sup>+</sup> junctions which play the role of lateral gates. These gates allow modulating the effective width of the transistor while the usual MOS gates, situated in front and back face, govern the accumulation or the depletion of the carriers. G<sup>4</sup>-FET combines MOSFET and JFET (junction field-effect transistor) operating types where every gate can cut the current. The published results [17] show that G<sup>4</sup>-FET turns out to be a useful and new transistor, with a high flexibility in the modulation of the subthreshold slope, threshold voltage and noise.

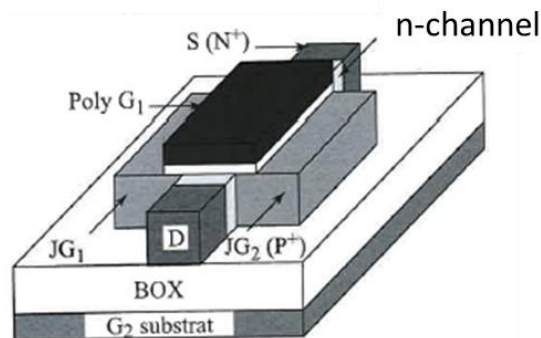


Figure I-5: Configuration of the n-channel G<sup>4</sup>-FET [17].

### 1.4.2 Gate-All-Around (GAA) transistors

The Gate-All-Around (GAA) transistor (Figure I-6) possesses a unique gate which surrounds the body, rectangular or circular. The electrostatic control being ideal, this transistor, called also ‘nanowire MOSFET’, turns out to be the most scalable. A recent variant is the transistor without junction (‘junctionless’ FET) where the source, the drain and the body have all a very high doping [18]. It is in fact a resistance the center part of which is surrounded by a gate able to cut the current by full depletion. This implies a technological compromise between strong doping ( $>> 10^{19} \text{ cm}^{-3}$ ) and low diameter ( $< 5 \text{ nm}$ ).

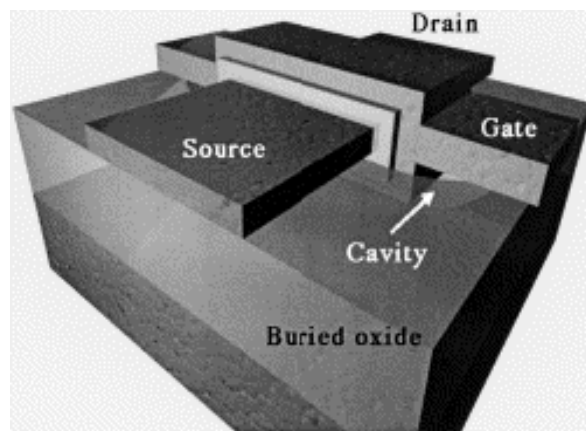


Figure I-6: Gate-All-Around (GAA) MOSFET [16].

### 1.4.3 Tri-dimensional nanowires (3D NWs)

Another alternative to increase the on-current at the end of roadmap is the fabrication of multi-gate and multi-channel superposed structures working in parallel (Figure I-7). Components are made by iterations using the Silicon-On-Nothing (SON) technology, which can give rise to very good performances [19].

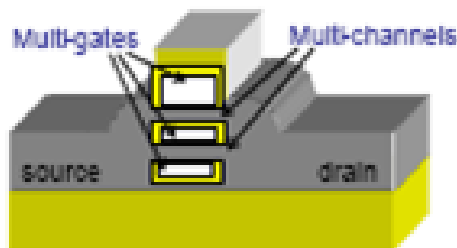


Figure I-7: Schematic representation of multi-gate and multi-channel MOSFET.

## 2. SOI materials

The zoology of architectures of SOI devices previously shown represents different answers to efficient scaling. Obviously, the condition for efficient scaling is the use of high quality SOI wafers. In this section we will show different SOI materials and the technologies of fabrication. We will resume the best technological choices in order to obtain high quality SOI materials.

### 2.1 State-of-the-art

The Semiconductor-On-Insulator is a new generation of materials for an alternative technology to traditional “bulk” substrates used in the microelectronics industry. The SOI substrates are composed of a buried oxide (BOX) inserted between the active silicon layer (Si film) on which electronic components are made, and the silicon substrate which serves for mechanical support (Figure I-8) [3].

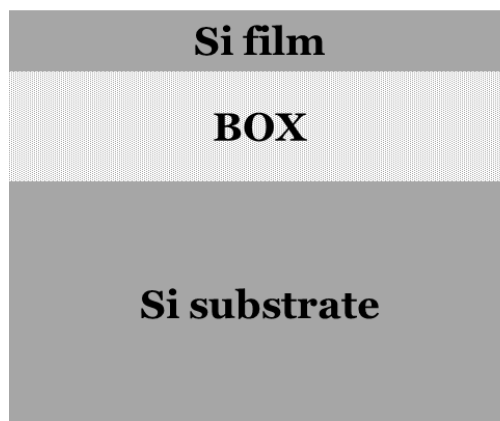


Figure I-8: Schematic representation of SOI structure.

SOI technology has been developed in the 1960-1970s. The first SOI substrate was the Silicon-On-Sapphire (SOS) which used the sapphire ( $\text{Al}_2\text{O}_3$ ) as an insulator [20]. This technology has been used for long time in niche applications such as spacecraft and military electronics, because it improves the resistance of the integrated circuits against ionizing radiation. The use of SOS was limited due to their high cost and material issues.

Thanks to the advance in the technology and especially the patent of the Smart-Cut™ process [21], the SOI material was able to prove itself and to enter the

world of microelectronics industry. Below we discuss the different fabrication methods of SOI wafers.

## 2.2 Fabrication methods

The main problem to fabricate an SOI wafer comes up when a crystalline silicon layer must be deposited on top of an insulator, usually an oxide sitting on top of a silicon wafer. Ideally both the silicon layer and the oxide layer should be defect-free, stress-free and uniform in thickness, and should display excellent interface properties.

There are numerous methods for manufacturing SOI wafers ([3], [5]). In this section, we briefly describe the most relevant techniques that have been developed and we focus on the technological approaches that gained commercial significance. It is possible to separate them into two main groups: the formation of buried oxide layer by implantation through the substrate (SIMOX: Separation by IMplantation of OXYgen) and wafer bonding (BESOI: Bond-and-Etch-back SOI, ELTRAN: Epitaxial Layer TRANSfer and Smart Cut™).

### 2.2.1 SIMOX technology

In 1966 the first publications reported the attempt to form silicon dioxide ( $\text{SiO}_2$ ) by oxygen (O) implantation into silicon [22]. However, it was not until the late 1970's that the SIMOX process was actually developed and demonstrated for the fabrication of MOS devices with SOI structure [23].

The principle of SIMOX material formation is quite simple, and consists of the synthesis of a buried layer of  $\text{SiO}_2$  by oxygen ions implantation beneath the surface of a silicon wafer. The silicon oxide is made by internal oxidation during the deep implantation of oxygen ions at high doses (in the order of  $2 \times 10^{18}$  ions. $\text{cm}^{-2}$ ), at high energies (200 KeV) and at temperatures close to  $600^\circ\text{C}$  [5]. After implantation, very high temperature annealing ( $\sim 1300^\circ\text{C}$ ) is required (Figure I-9) to restore film crystallinity.

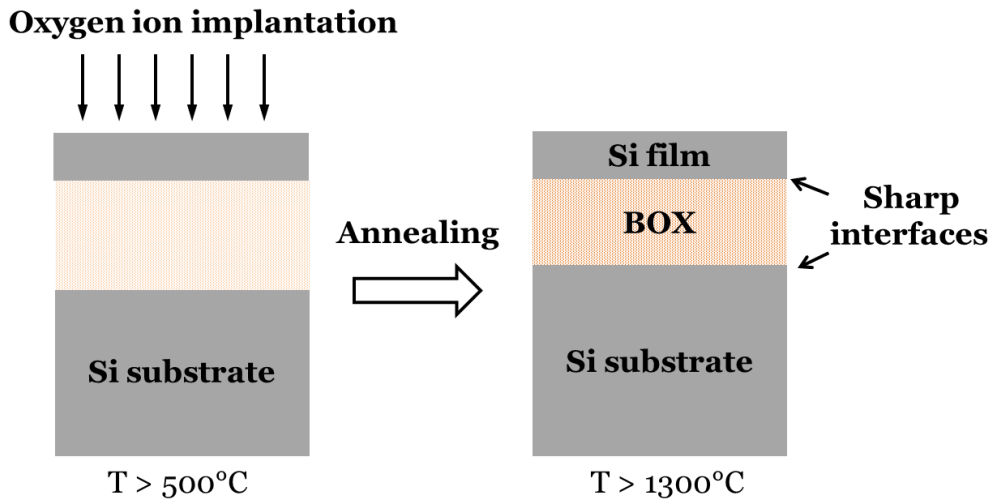


Figure I-9: The principle of SIMOX: a heavy-dose oxygen implantation into silicon followed by a very high temperature annealing step produces a buried layer of silicon dioxide, below a thin single-crystal Si film [24].

Figure I-10 shows the annealing impact by changing the time and by increasing the temperature (from  $11150^{\circ}\text{C}$  to  $1250^{\circ}\text{C}$  and then to  $1405^{\circ}\text{C}$ ). The aim of this annealing is to induce the reaction between oxygen ions and silicon in order to form  $\text{SiO}_2$ , to eliminate the high density of precipitates and residual defects and finally to obtain atomically sharp and planar interfaces between the near-surface regions of Si and the buried oxide (Figure I-10). A single-crystal but highly defective silicon overlayer (Si film) above the oxide is obtained.

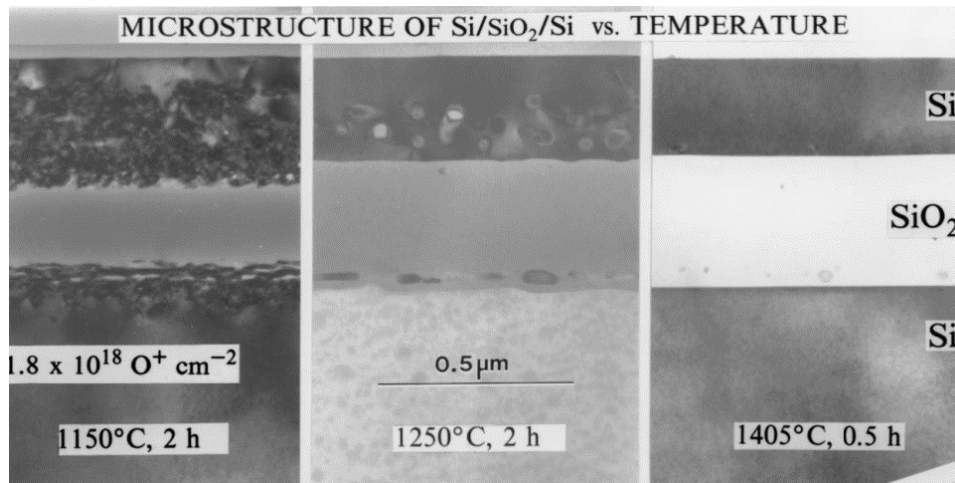


Figure I-10: Evolution of SIMOX microstructure with annealing temperature and time [25].

The first wafers obtained by SIMOX technology with high implanted dose presented numerous crystalline defects in the active Si layer as well as numerous roads of BOX leakage, harmful defects for the good electric properties of the SOI.



Several advances consisted in modifying the implanters to improve the crystalline quality of SIMOX substrate. Due to these advances and to the fact that the wafer cost is a strong function of the implant dose, the SIMOX “low dose” was achieved. The implant parameters, mainly the energy (120 KeV), dose ( $1-4 \times 10^{17}$  ions.cm<sup>-2</sup>) and temperature (600°C), were used to improve and also to engineer the SIMOX structure and interface properties [5]. The lower oxygen dose needed implies a considerable gain in processing time and wafer cost. In addition, it enabled the drastic limitation of the dislocation density (reduced to  $10^6$  cm<sup>-2</sup>) in the Si layer (with thickness between 170 and 215 nm) [26]. A continuous planar buried oxide (between 80 and 200 nm thickness) was obtained. Low dose implantation has the benefit of reduced implantation damage and as a direct consequence fewer defects are present in the final annealed wafers [27].

In addition, it is possible to obtain thinner films and buried oxides [28] by variation of the oxygen implanted dose, energy and the annealing temperature. One concern with the thinner BOX is a higher probability of Si pipes that electrically short the Si film to the substrate. Another SIMOX process called ITOX (Internal Thermal OXidation) is effective in reducing the density of dislocations and Si pipes in the BOX [29]. By oxidizing an SOI wafer at 1350°C, a small fraction of the oxygen spreads through the Si film and re-acts at the film/BOX interface (instead of oxidizing the Si film). This internal oxidation ameliorates the quality of the SiO<sub>2</sub> with electrical properties comparable to those obtained from a thermal oxide.

SIMOX technology presents several disadvantages such as cost and processing time, crystalline defects, BOX quality and thickness scaling limitation of BOX and Si film, *etc.*

### **2.2.2 SOI by wafer bonding**

Wafer bonding (WB) is another mature SOI technology. It was first proposed in the 1980’s at Bell laboratories and IBM ([30], [31]). Wafer bonding method consists in putting in contact two substrates having an excellent surface state [32]. It is then possible to bond Si-Si, SiO<sub>2</sub>-Si and SiO<sub>2</sub>-SiO<sub>2</sub>. In the case of the SOI (Figure I-11aA), we have one substrate with oxidized surface (which will represent later the insulator) and another substrate (with or without surface oxidation). Both substrates are cleaned in an RCA solution [33] followed by a water rinse in order to eliminate

any possible contamination: particles, organic, or metallic (Figure I-11aB). The surface cleaning makes the non-oxidized substrate “hydrophilic” and water ( $H_2O$ ) molecules are able to fix on the surface during the rinsing. After putting in contact both substrates (Figure I-11aC), OH molecules related to the hanging connections of Si form a very thin film of water ( $\sim 2$  nm) by making hydrogen connections (Figure I-11b). A high-temperature stabilization annealing (for example,  $1100^\circ\text{C}$  for the standard Unibond), allows then to break the connections of Si-OH for the benefit of Si-O-Si connections ( $\text{Si-O-H} + \text{H-O-Si} \rightarrow \text{Si-O-Si} + \text{H-O-H}$ ). After further heating of the samples a complete closure of the interface (Figure I-11b) occurs by coupling the remaining interface hydroxyl species and diffusion of the hydrogen into the Si (Figure I-11aD).

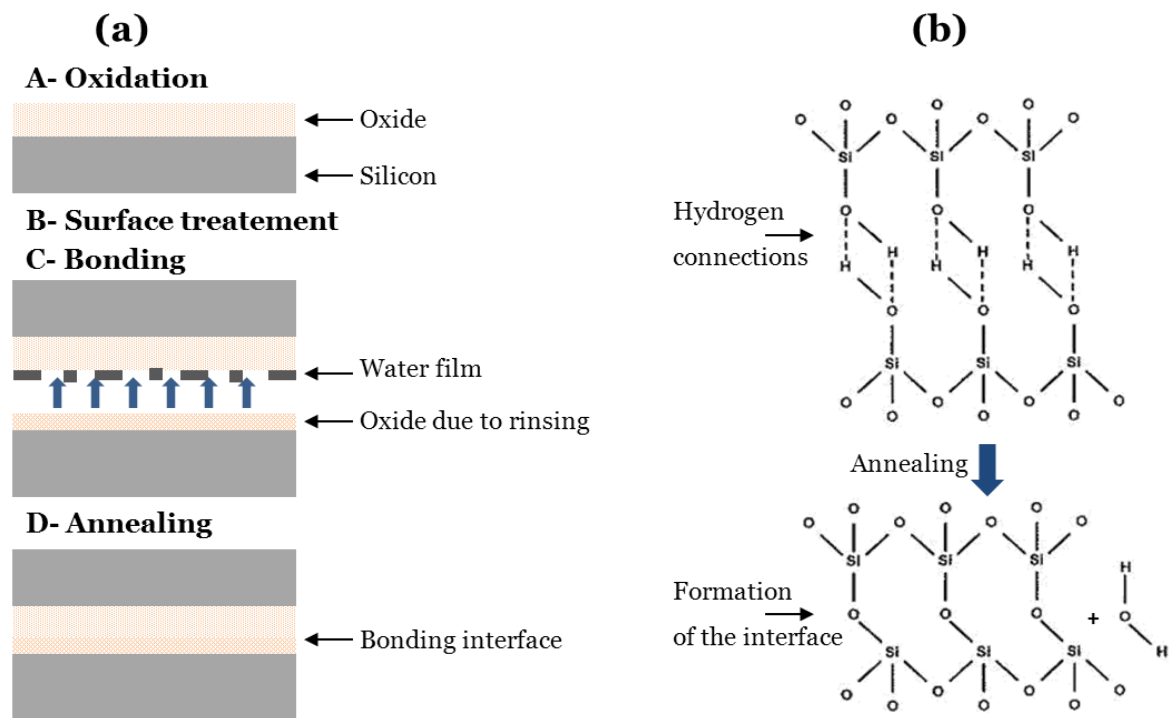


Figure I-11: Principle of the (a) hydrophilic bonding, (b) formation of interface bonding.

Generally, the bonding interface is placed below the BOX, far from the silicon film (where the components will be made).

The essential advantage of wafer bonding is to supply almost unlimited combinations of film and BOX thicknesses, which are attractive for the manufacturing of sensors and power circuits. On the other hand, its limitation is the practical difficulty to produce ultrathin films ( $< 100$  nm), with uniform thickness, low stress, and excellent crystallinity. By using this principle of bonding, three techniques

were developed (described in the following sub-sections) as variants for the thinning down of the Si film.

### 2.2.2.1 BESOI

The Bond-and-Etch-back SOI (BESOI) technique relies on the hydrophilic bonding described previously. The specificity of this technique is the thinning down of the upper wafer, by mechanical polishing followed by mechanico-chemical polishing and/or by sacrificial oxidations (Figure I-12). Etch-stop layers can be introduced before bonding as for example a selective doping (junction P<sup>+</sup>/P<sup>-</sup> or P/N) or a different structure (SiGe, *etc.*) [32]. However, we to note that this technique presents disadvantages, in particular mechanical constraints and poor uniformity of the film thickness [3]. Thus, it is mainly used for the applications which require thick Si film (several micrometers thickness). Further, this method is relatively expensive because of the use of two wafers for the manufacturing of one SOI wafer.

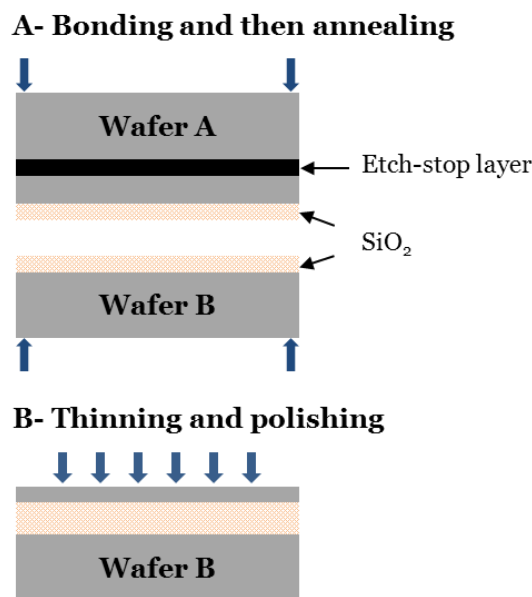


Figure I-12: Schematic representation of BESOI process. Bonding and annealing (A) of wafer A and wafer B are carried out, then the upper wafer A is thinned and polished (B) [5].

### 2.2.2.2 ELTRAN

The Epitaxial Layer TRANSfer (ELTRAN) technique is another approach that combines the formation of a porous layer and wafer bonding to produce a material with good film thickness uniformity. This technique was developed by Canon in 1990 for the industrial production of SOI wafers [34].

A donor Si substrate ‘Wafer A’ undergoes an electrolytic attack making the Si surface porous (Figure I-13). Two successive epitaxial steps, first of porous silicon followed by single-crystal silicon allow forming a layer of non-porous silicon with high crystalline quality. The porous silicon wafer with the epitaxial layer film is then oxidized and bonded to another wafer ‘Handle Wafer’. The fracture is made by means of a high-power water jet along the planar porous layers which are mechanically more fragile, leading to a more uniform cleavage. After wafers splitting, the residual porous Si on the SOI wafer is etched away, and the newly exposed SOI wafer surface is smoothed by a second application of hydrogen annealing at about 1100°C.

The wafer ‘A’ that donated the epitaxial film can be reclaimed, polished if necessary, and then reutilized. The crystal quality of the SOI material obtained by wafer bonding and etch-back is, in principle, as good as that of the starting silicon wafer. The control of film thickness is challenging.

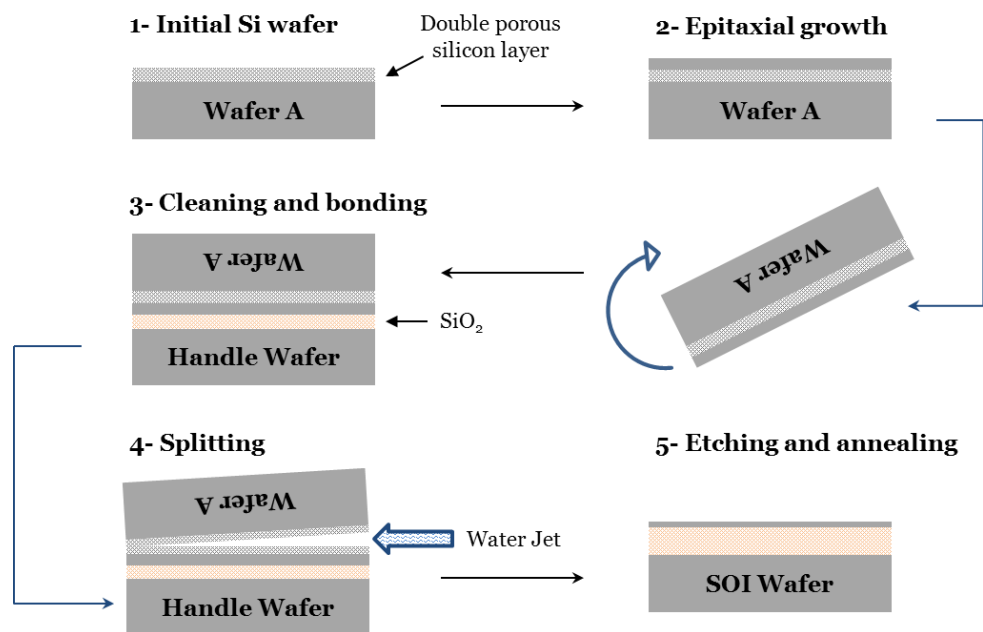


Figure I-13: Schematic representation of ELTRAN process for SOI wafer manufacturing [34].

### 2.2.2.3 Unibond (Smart-Cut™ process)

In the 1990s, a revolutionary process of wafer separation, named Smart-Cut™, was invented by Michel Bruel from CEA-Leti (France-Grenoble) [35] and constitutes the technological exclusivity of the company Soitec (France-Bernin). The key step of the Smart-Cut™ process is the implantation of hydrogen for splitting the wafers (Figure I-14).

First the ‘donor wafer’ A undergoes a thermal oxidation to form an oxide which will serve as a BOX. Its thickness is easily adjustable by the control of oxidation. Then, a dose of hydrogen between  $3 \times 10^{16}$  and  $1 \times 10^{17} \text{ cm}^{-2}$  is implanted through this oxide. The hydrogen engenders micro-cavities (zone in dashed lines on Figure I-14). These are going to allow defining a plan of the fracture. The ‘donor wafer’ and ‘Handle wafer’ B are then cleaned to eliminate particles and contaminations on surface. This stage also allows returning both surfaces hydrophilic. The two wafers are aligned and putted in contact so that the bonding is made on the entire surface. During the bonding of wafers A and B (Figure I-14) and of the annealing that follows, the pressure of hydrogen molecules ( $\text{H}_2$ ) in micro-cavities increases.  $\text{H}_2$  propagates then in micro-cavities and provokes a horizontal fracture which leads to a natural separation of wafers. This separation takes place, not at the bonding interface, but in the region defined by the localization of hydrogen micro-cavities.

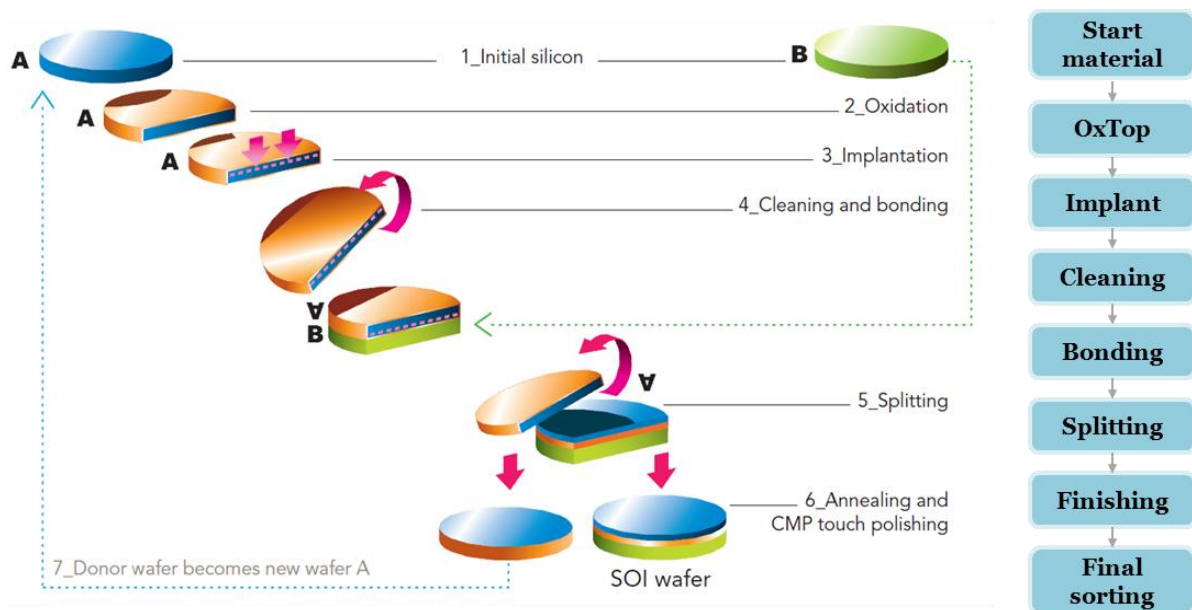


Figure I-14: Schematic illustration of the fabrication steps for a standard Unibond SOI wafer with Smart-Cut™ process described by Soitec [36].

After this step, the surface roughness is of the order of some nanometers. It is important to underline that one of the advantages of this technique is to be able to reuse wafer A: the process is called “refresh”.

To improve the crystalline quality of the transferred layer, some fracture processes use at present the co-implantation of hydrogen-helium. The implanted dose varies between  $2.5 \times 10^{16}$  and  $5 \times 10^{16} \text{ cm}^{-2}$ . Helium implanted after the hydrogen

fills the voids and provides most of the pressure that causes separation of a Si film from the bulk substrate. In addition, the helium improves the quality of the fracture. A better quality of the film and a reduction in the production cost are obtained.

The extraordinary potential of the Smart-Cut™ approach is evidenced by several essential key benefits [5]:

- i. The thinning step can be achieved without any limitations.
- ii. The donor wafer (A) undergoes only the removal of a thin Si surface layer and can be recycled several times. The quality of this mother wafer must be excellent, while that of the wafer B, used primarily for mechanical support, is not critical. Therefore, the Smart-Cut™ is almost mono-wafer, with a low cost for the wafer B. This translates into competitive production costs.
- iii. Conventional implantation and annealing equipments are used, even for the manufacturing of 12 inch wafers, which is not the case of SIMOX where only maximum 8 inch wafers can be obtained.
- iv. The silicon film and the BOX thicknesses are adjustable (*via* the implantation energy of hydrogen and oxidation time) in a wide range ( $t_{\text{Si}} = 0.01$  to 1.5 microns and  $t_{\text{BOX}} = 0.01$  to 5 microns) in order to adapt to most architectures of integrated components: ultra-thin CMOS, power transistors or sensors with thick films.
- v. The crystal quality, defect density and characteristics of the Si film are excellent, while the buried oxide keeps the usual properties of the thermal oxide. The fact that the bonding interface is below the BOX improves the Si film quality.

The Smart-Cut™ wafer manufacturing technology gives Soitec the flexibility to tailor SOI substrates to meet most demanding design specifications and to cover the full range of applications for microelectronics markets (Figure I-15). Note that the Smart-Cut™ is universal in the sense of adaptability to a variety of materials. These new products (showed in the next section) allow Soitec to answer the expectation of the microelectronics market subjected to the technological nodes defined by the ITRS (International Technology Roadmap for Semiconductors) and to invest new market shares still dominated by the Si bulk technology.

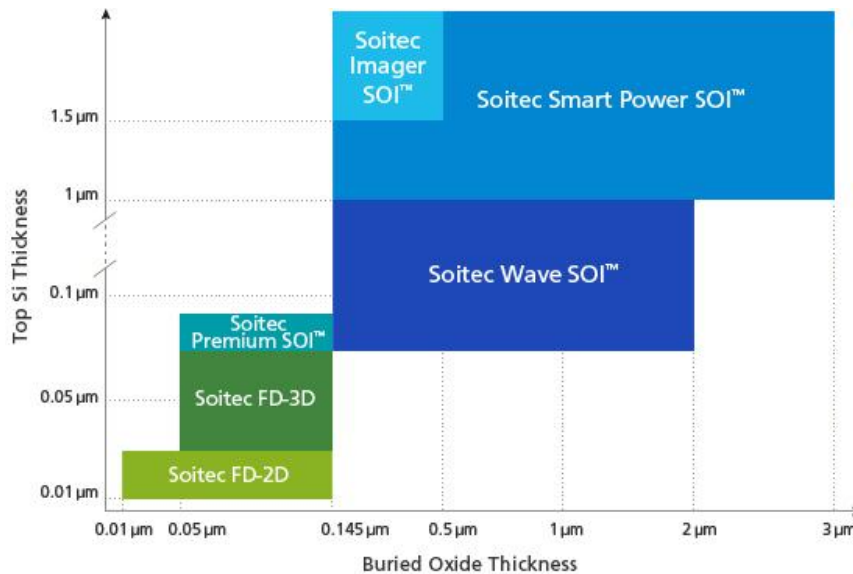


Figure I-15: Soitec's Unibond SOI wafers with wide flexibility in top Si and buried oxide thicknesses to meet the industry's most rigorous requirements [37].

### 2.2.3 Silicon-On-Nothing (SON)

The Silicon-On-Nothing (SON) technology was invented in 2000 to realize localized SOI regions favoring the cohabitation of SOI and bulk Si circuits [38]. On a isolated bulk wafer, is epitaxied in predefined regions, a stack of sacrificial SiGe and Si layers. The selective etching of the SiGe leaves a vacuum ('Nothing') under the Si film. This space is filled by a dielectric to form "integrated" SOI in silicon. The thin layer of Si can also be used for the fabrication of Gate-All-Around transistors. The SON process allows the buried dielectric (which may be an oxide but also an air gap) to be fabricated locally in dedicated parts of the chip, which may present advantages in terms of cost and facility of System-On-Chip integration.

The innovative SON process enables fabrication of SOI-like structures on bulk substrates with well-controlled and extremely thin buried oxide (10 to 30 nm) and silicon films (5 to 20 nm). The very thin layers in the SON transistor allow good control of the short-channel effects (SCEs) and excellent electrical performances [38].

### 2.2.4 Other SOI technologies

#### 2.2.4.1 Silicon-On-Sapphire

The Silicon-On-Sapphire (SOS) is the godfather of the SOI family. The epitaxial growth of a silicon film on a bulk sapphire ( $\text{Al}_2\text{O}_3$ ) substrate gives rise to

small Si islands that finally coalesce. The interface transition region contains numerous crystallographic defects, mainly stacking faults, due to the lattice mismatch and aluminum contamination from the sapphire substrate. The electrical properties are affected by the lateral stress, difference in thermal expansion, in depth inhomogeneity of SOS films, and interface traps [20].

However, the quasi-infinite thickness of the insulator makes SOS look very attractive for RF applications. SOS has recently been improved for larger wafers (150-200 mm diameter) with thinner films (0.1  $\mu\text{m}$ ) and better crystal quality, by a SPER step. Solid Phase Epitaxial Regrowth (SPER) consists in implanting silicon ions to amorphize the film and erases the memory of the damaged lattice and interface. An annealing allows the epitaxial re-growth of the film, starting from “seeding” surface towards the Si/Al<sub>2</sub>O<sub>3</sub> interface. Another solution is to remove most of the SOS film by sacrificial oxidation and to adjust the thickness by a second epitaxial growth [39]. The increase of the carrier mobility and life time reflects the efficiency of the process. The SOS can be also fabricated by Smart-Cut™ process.

#### 2.2.4.2 Insulation by Porous Oxidized Silicon

The Porous Oxidized Silicon (FIPOS) technique is established on the high selectivity of the porous silicon oxidation by comparison to the bulk silicon [3]. Indeed, the porous silicon presents a very strong surface/volume ratio ( $10^3 \text{ cm}^2/\text{cm}^3$ ), which makes it particularly oxidable. The key step is the conversion of selected *p*-type regions of the silicon wafer into porous silicon, by controlling their thickness and porosity *via* anodic reaction. FIPOS has been proposed for combining photo and electro-luminescent porous silicon devices with fast SOI-CMOS circuits on a single chip.

#### 2.2.4.3 Zone Melting Recrystallization and Epitaxial Layer Overgrowth

Zone Melting Recrystallization (ZMR) material is formed by depositing a poly-silicon layer on an oxidized wafer. ZMR is achieved with high-energy sources (lamps, laser, electron beam, or graphite strip heater) scanned across the wafer [5]. The ZMR process can be seeded or un-seeded, but is basically limited by the small lateral extension of single-crystal regions, free from grain sub-boundaries and associated defects. In the Epitaxial Lateral Overgrowth (ELO) method, the single-



crystal silicon film is grown on a seeded oxide. Since the epitaxial growth proceeds in both vertical and lateral directions (with a ratio of 1 to 10-100), the ELO process requires a post epitaxy thinning of the silicon film.

The ELO and ZMR process are fundamentally limited by the reduced size of the silicon single-crystal regions, exempt from joints of grains, dislocations and other defects. However, these two techniques allow the fabrication of tri-Dimensional (3D) integrated circuits. Indeed, after the integration of the first layer of the active circuits on SOI, the growth steps can be repeated several times.

## **2.3 Novel semiconductor on insulator structures**

With the aim of improving the performances of electronic components made on SOI substrate and to meet the requirements of new generations of transistors, the introduction of new materials is attractive. In general, Smart-Cut™ allows to introduce in the kingdom of the silicon other semiconductors and insulators with their range of specific properties. For that reason, SOI acronym has evolved, corresponding at the moment to *Semiconductor On Insulator*. All these advantages and potentialities make the Unibond/Smart-Cut™ couple to fully dominate the market of SOI wafers.

Three axes of development are possible: vary the material in the active zone, change the buried dielectric or even replace the substrate serving as support.

### **2.3.1 Strained SOI materials**

Recent studies have successfully demonstrated that carrier transport properties can be enhanced by applying an adapted strain to the conduction channel. This has led to an increasing interest in strained SOI substrates, used to improve the drive current and transconductance in SOI MOSFETs ([40], [41]).

It was demonstrated, by using pseudo-MOSFET ( $\Psi$ -MOSFET) measurements, that the electrons and holes mobilities show higher values for strained SOI compared to standard SOI wafers [42].

The techniques used to create strain in SOI substrates can be classified within two families, depending on whether the final SOI substrate contains a Silicon-Germanium (SiGe) layer:

- i. *SGOI strained Silicon-On-Insulator via intermediate relaxed SiGe layer on insulator.* The production of strained Si substrates requires several Si and SiGe epitaxial steps to obtain the thin layer of strained silicon at the wafer surface. By transferring a thin layer of relaxed  $\text{Si}_{1-x}\text{Ge}_x$  from the starting epitaxial substrate to an oxidized handle wafer, an SOI-like structure is obtained (Figure I-16a). The strained Si film is epitaxially grown on relaxed  $\text{Si}_{1-x}\text{Ge}_x$ ; the degree of strain achieved is a function of the germanium percentage (Ge %) [43].
- ii. *sSOI strained Silicon-On-Insulator without any intermediate SiGe layer.* The strained Si sits directly on the insulator without the SiGe template (Figure I-16b). sSOI has the same basic structure as conventional SOI, with a strained Si layer replacing the conventional relaxed Si film. The film thicknesses vary from 15 to 80 nm which follows the similar guidelines for film thickness to those provided by the industry roadmap for SOI.

While sSOI is more likely to be used in circuit manufacturing due to many advantages, sSOI is more complex to fabricate than SGOI [43].

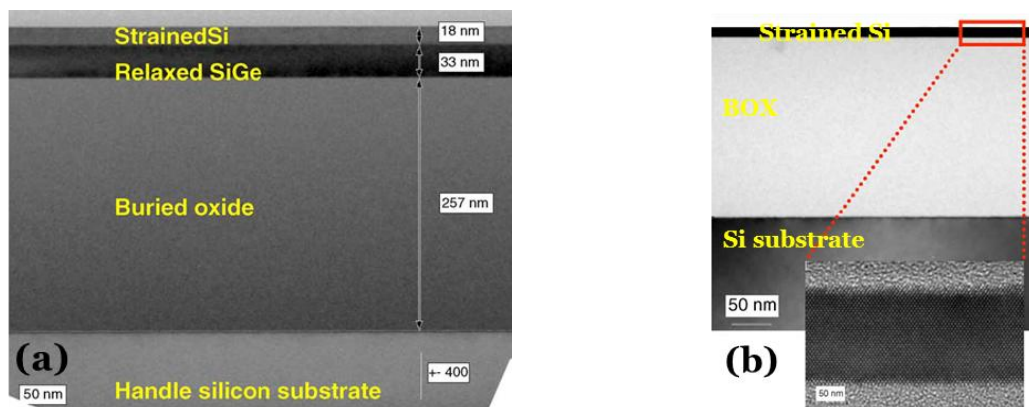


Figure I-16: Transversal cross-section transmission electron microscopy (TEM) image showing (a) 18 nm thick strained Si grown onto a 33 nm thick SGOI and (b) strained SOI wafer with good crystalline quality [43].

### 2.3.2 Hybrid orientation technologies

Hybrid orientation technologies (HOT) have received a renewal of interest during the past decades to overcome the problem of the mobility degradation in the conduction channel. A simple approach consists in taking benefits from Si surface orientation: on a (100) oriented Si surface, the hole mobility is low for a channel

along the (110) direction, whereas it is maximal for a (110) surface orientation. On the contrary, the electron mobility is maximal on a (100) oriented surface, and significantly decreases on a (110) oriented surface [44]. It is thus desirable to enclose hybrid (110) and (100) Si oriented areas on a same “hybrid” layer to maximize both carriers mobility.

The co-integration of silicon layers with strong mobility of electrons (100) and of holes (110) begins with a bi-layer stacking (110)/(100). The lower layer (100) is locally amorphized by Si implantation and the Solid Phase Epitaxial Regrowth recrystallization process converts it to (110) orientation. After elimination of the superior layer (110) we obtain neighboring regions (110 and 100) on same SOI wafer [45].

### **2.3.3 Germanium-On-Insulator**

It was demonstrated these last 10 years that it is possible to realize functional and successful Ge *p*MOSFETs (MOS transistors with *p*-type channel) with two to three times superior mobility values in comparison with an equivalent *p*MOSFET with silicon channel [46]. On the other hand, Ge *n*MOSFETs (MOS transistors with *n*-type channel) suffer from poor electrons mobility values which make them unusable at the moment.

Germanium was abandoned since his first use on transistor in 1974 by J. Barden, W. Brattain and W. Shockley. The main cause was the insufficient chemical stability of the oxide (GeO<sub>2</sub>). The germanium made its comeback in the world of the microelectronics thanks to the introduction of new metal gate dielectric (with high permittivity), the improvement of deposition techniques and its high hole mobility, superior to that in silicon.

GeOI substrates are fabricated by using Ge condensation technique [47], which exploits the selective oxidation of a SiGe layer grown on SOI. During oxidation, only Si atoms are consumed whereas the diffusion of Ge atoms is blocked by the BOX barrier. This process results in a thinner Ge-enriched film; the initial SOI layer can be totally converted into thin GeOI film. The layer thickness can be completed *via* a Ge epitaxial step.

An attractive solution is the co-integration of *n*-channel SOI and *p*-channel GeOI transistors within the same chip. Local Ge condensation in selected islands enables the fabrication of SOI-GeOI hybrid substrates and related devices. On the other hand, Ge possesses an excellent lattice agreement with Gallium Arsenide (GaAs). It could be so used as a buffer material for the growth of GaAs, in particular for *n*MOSFET applications with high mobility or in photonic or photovoltaic fields. GeOI can also be fabricated by Smart-Cut™.

### **2.3.4 Other semiconductor, BOX and substrate materials**

#### **2.3.4.1 Conductive film materials**

Current research is directed towards the achievement of mixed structures with novel properties by replacing the film material with composed semiconductor and wide band gap films: GaAs, GaN (Gallium Nitride) or SiC (Silicon Carbide).

The wafer bonding and the layers transfer by Smart-Cut™ technology opened new perspectives of structures with III-V materials, intended for optoelectronic applications. The first GaAs layer transfer on silicon substrate was published by Jalaguier *et al* [48] and the optimization of the implantation conditions allowed improving the quality of the transferred GaAs layer. SiCOI (Silicon Carbide-On-Insulator) substrates were also obtained [49]. The engineered substrates are attractive for the development of high-temperature, high-power, high-frequency and GaN-based optoelectronic devices.

#### **2.3.4.2 BOX and substrate materials**

In a device fabricated on SOI substrate, the heating is widely higher than on bulk substrate due to the presence of the buried oxide. SiO<sub>2</sub> is characterized by a low thermal conductivity ( $\approx 1.4 \text{ W}\cdot\text{m}^{-1}\cdot\text{K}^{-1}$ ), hundred times less than for silicon. SiO<sub>2</sub> plays the role of thermal barrier preventing the evacuation of the thermal power from the Si layer towards the substrate. This effect is called “self-heating” and can be an obstacle in the integration of advanced SOI circuits.

To improve the thermal dissipation in devices, it is possible to replace the SiO<sub>2</sub> by more thermal conductive dielectrics. Four dielectrics, which are already well studied and used in the microelectronics industry, are considered as potential

candidates: sapphire ( $\text{Al}_2\text{O}_3$ ), Silicon Carbide (SiC), Aluminum Nitride (AlN) and Diamond [50]. Silicon-On-Diamond (SOD) wafers were recently demonstrated, and SOD MOSFETs exhibit excellent characteristics [51]. Also, a buried Oxide-Nitride-Oxide (ONO) stack is useful as a reservoir of non-volatile charges, enabling a new paradigm of a “unified” SOI memory.

The Smart-Cut™ technology allows also the use of High Resistivity SOI substrate (HR SOI for Radio Frequency (RF) circuits) [52] and silicon film on transparent substrates (Silicon-On-Quartz (SOQ) for optoelectronics and high-frequency telecom applications). SOQ offers a single crystal silicon layer on a fused silica substrate, a development that is extendable to Silicon-On-Glass (SOG).

## 2.4 Defects of SOI material

Despite the concern to limit the number of defects introduced by the manufacturing process of SOI wafers, some defects remain and can be harmful for the good operating of devices: mobility decrease, degradation of oxide break down voltage, increase of the junction current leakage, modifications of threshold voltages, *etc.* Various defects can be observed in SOI structures (see Figure I-17). Some defects are of conventional nature, the same as encountered in bulk Si and in epitaxial Si films, *e.g.*, dislocations and stacking faults. In SOI, the majority of dislocations are threading through the thickness of the film, terminating at the BOX and the surface. Other defects are unique to the method of SOI wafers fabrication. The evaluation of SOI structures requires different characterization techniques. These techniques must be able to overcome difficulties that are intrinsic to SOI structures: very thin Si films and BOX, BOX isolation, multiple Si/SiO<sub>2</sub> interfaces, and defects unique to SOI, in-depth inhomogeneities, stress effects, *etc.* The traditional techniques detailed in [5] and other novel characterization methods are discussed in chapters II and III.

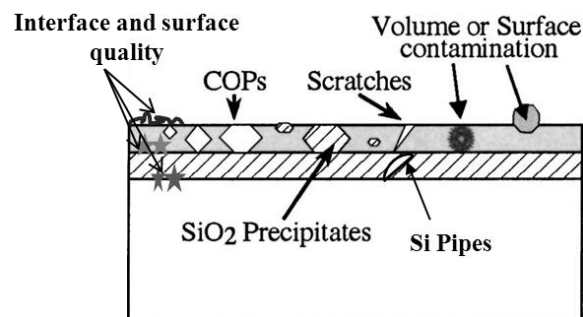


Figure I-17: Typical defects in SOI wafers [5].

## ***Conclusion***

In this chapter, the main characteristics of the SOI technologies were presented at both device level and substrate level. The performances and the weaknesses of SOI devices were addressed with a brief outline of innovative transistor architectures made possible by the SOI structure.

We exposed the SOI technology history, the main fabrication methods of SOI substrates, as well as the innovative technologies which allow the improvement of device performances. The issues and the new challenges of SOI substrates were also explained.

Nowadays, as the SOI substrates are more and more used for device/circuit manufacturing, high quality wafers are required. It is difficult to monitor and optimize the electric properties of ultra-thin SOI materials with nanometer size thicknesses using traditional characterization techniques. New methods to evaluate advanced SOI wafers will be proposed in details in the following chapters.

## References chapter I

- [1] R. Pottier, J. Tong, C. Hawkins, R. Kundu and J. L. Pelloie, "ARM 1176 implementation in SOI 45nm technology and silicon measurement," in *SOI Conference, 2009 IEEE International*, pp. 1-4, 2009.
- [2] Semiconductor Manufacturing & Design Community: <http://semimd.com/blog/tag/fd-soi/>
- [3] S. Cristoloveanu and S. S. Li, *Electrical Characterization of Silicon-On-Insulator Materials and Devices*, Kluwer, Boston, 1995.
- [4] Advanced Substrate News: <http://www.advancedsubstratenews.com/2011/05/fd-soi-a-quick-background/>
- [5] G. K. Celler and Sorin Cristoloveanu, "Frontiers of silicon-on-insulator," *Journal of Applied Physics*, vol. 93, pp. 4955-4978, 2003.
- [6] S. M. Sze, *Physics of Semiconductor Devices (Second Edition)*, Wiley press, New York, 1981.
- [7] T. Tsuchiya, Y. Sato and M. Tomizawa, "Three mechanisms determining short-channel effects in fully-depleted SOI MOSFETs," *Electron Devices, IEEE Transactions on*, vol. 45, pp. 1116-1121, 1998.
- [8] V. P. Trivedi and J. G. Fossum, "Scaling fully depleted SOI CMOS," *Electron Devices, IEEE Transactions on*, vol. 50, pp. 2095-2103, 2003.
- [9] D. J. Frank, Y. Taur and H. S. P. Wong, "Generalized scale length for two-dimensional effects in MOSFETs," *Electron Device Letters, IEEE*, vol. 19, pp. 385-387, 1998.
- [10] K. Kato, T. Wada and K. Taniguchi, "Analysis of kink characteristics in Silicon-on-insulator MOSFET's using two-carrier modeling," *Electron Devices, IEEE Transactions on*, vol. 32, pp. 458-462, 1985.
- [11] Daniela Munteanu, "*Modélisation et caractérisation des transistors SOI: du pseudo-mosfet au mosfet submicronique ultra-mince*", Grenoble, France, 1999.
- [12] J. Pretet, T. Matsumoto, T. Poiroux, S. Cristoloveanu, R. Gwoziecki, C. E. Raynaud, A. Roveda and H. Brut, "New Mechanism of Body Charging in Partially Depleted SOI-MOSFETs with Ultra-thin Gate Oxides," in *Solid-State Device Research Conference, 2002. Proceeding of the 32nd European*, pp. 515-518, 2002.
- [13] K. Uchida, H. Watanabe, A. Kinoshita, J. Koga, T. Numata and S. Takagi, "Experimental study on carrier transport mechanism in ultrathin-body SOI nand p-MOSFETs with SOI thickness less than 5 nm," in *Electron Devices Meeting, 2002. IEDM '02. International*, pp. 47-50, 2002.
- [14] T. Ernst, R. Ritzenthaler, O. Faynot and S. Cristoloveanu, "A Model of Fringing Fields in Short-Channel Planar and Triple-Gate SOI MOSFETs," *Electron Devices, IEEE Transactions on*, vol. 54, pp. 1366-1375, 2007.
- [15] F. Balestra, S. Cristoloveanu, M. Benachir, J. Brini and T. Elewa, "Double-gate silicon-on-insulator transistor with volume inversion: A new device with greatly enhanced performance," *Electron Device Letters, IEEE*, vol. 8, pp. 410-412, 1987.
- [16] V. Jaju, "Silicon-On-Insulator Technology," in *Advances in MOSFETs EE 530*, pp. 1-12, 2004.
- [17] B. Dufrene, K. Akarvardar, S. Cristoloveanu, B. J. Blalock, R. Gentil, E. Kolawa and M. M. Mojarradi, "Investigation of the four-gate action in G<sup>4</sup>-FETs," *Electron Devices, IEEE Transactions on*, vol. 51, pp. 1931-1935, 2004.
- [18] Jean-Pierre Colinge, Chi-Woo Lee, Aryan Afzalian, Nima Dehdashti Akhavan, Ran Yan, Isabelle Ferain, Pedram Razavi, Brendan O'Neill, Alan Blake, Mary White, Anne-Marie Kelleher, Brendan Mccarthy and Richard Murphy, "Nanowire transistors without junctions," *Nat Nano*, vol. 5, pp. 225-229, 2010.
- [19] T. Ernst, L. Duraffourg, C. Dupre, E. Bernard, P. Andreucci, S. Becu, E. Ollier, A. Hubert, C. Halte, J. Buckley, O. Thomas, G. Delapierre, S. Deleonibus, B. De Salvo, P. Robert and O.

- Faynot, "Novel Si-based nanowire devices: Will they serve ultimate MOSFETs scaling or ultimate hybrid integration?," in *Electron Devices Meeting, 2008. IEDM 2008. IEEE International*, pp. 1-4, 2008.
- [20] Sorin Cristoloveanu, "Silicon films on sapphire," *Reports on Progress in Physics*, vol. 50, pp. 327-371, 1987.
- [21] Michel Bruel, "Process for the production of thin semiconductor materials films," U.S. Patent n°5,374,564, 1994.
- [22] M. Watanabe and A. Tooi, "Formation of the SiO<sub>2</sub> films by oxygen-ion bombardment," *Japanese Journal of Applied Physics*, vol. 5, pp. 737-745, 1966.
- [23] Katsutoshi Izumi, "Historical overview of SIMOX," *Vacuum*, vol. 42, pp. 333-340, 1991.
- [24] P. L. F. Hemment, K. J. Reeson, J. A. Kilner, R. J. Chater, C. Marsh, G. R. Booker, J. R. Davis and G. K. Celler, "Novel dielectric/silicon planar structures formed by ion beam synthesis," *Nuclear Instruments and Methods in Physics Research Section B: Beam Interactions with Materials and Atoms*, vol. 21, pp. 129-133, 1987.
- [25] D. Marsh, G. R. Booker, K. J. Reeson, P. L. F. Hemment, R. J. Chater, J. A. Kilner, J. A. Alderman and G. K. Celler, "The influence of high temperature anneals on the microstructure of SOI structures formed by high-dose oxygen implantation into silicon," in *Proceedings of the European MRS Conference, Materials Research Society*, Pittsburgh, p. 137, 1986.
- [26] S. Nakashima and K. Izumi, "Analysis of buried oxide layer formation and mechanism of threading dislocation generation in the substoichiometric oxygen dose region," *Journal of Materials Research*, vol. 8, pp. 523-534 1993.
- [27] B. Aspar, C. Guilhalmenc, C. Pudda, A. Garcia, A. M. Papon, A. J. Auberton-Hervé and J. M. Lamure, "Buried oxide layer formed by low dose SIMOX processes," *Microelectronic Engineering*, vol. 28, pp. 411-414, 1995.
- [28] M. J. Anc, R. P. Dolan, J. Jiao and T. Nakai, "Thin-layer SIMOX for future applications," in *Proceedings of IEEE International SOI Conference*, pp. 106-107, 1999.
- [29] A. Matsumura, I. Hamaguchi, K. Kawamura, T. Sasaki, S. Takayama and Y. Nagatake, "Technological innovation in low-dose SIMOX wafers fabricated by an internal thermal oxidation (ITOX) process," *Microelectronic Engineering*, vol. 66, pp. 400-414, 2003.
- [30] R. C. Frye, J. E. Griffith and Y. H. Wong, "Dielectrically isolated semiconductor devices," U.S. Patent n°4,501,060, 1985.
- [31] J. B. Lasky, "Wafer bonding for silicon-on-insulator technologies," *Applied Physics Letters*, vol. 48, pp. 78-80, 1986.
- [32] Kiyoshi Mitani and Ulrich Gösele, "Wafer bonding technology for silicon-on-insulator applications: A review," *Journal of Electronic Materials*, vol. 21, pp. 669-676, 1992.
- [33] Werner Kern, "The Evolution of Silicon Wafer Cleaning Technology," *Journal of the Electrochemical Society*, vol. 137, pp. 1887-1892, 1990.
- [34] Takao Yonehara, Kiyofumi Sakaguchi and Nobuhiko Sato, "Epitaxial layer transfer by bond and etch back of porous Si," *Applied Physics Letters*, vol. 64, pp. 2108-2110, 1994.
- [35] M. Bruel, "Silicon on insulator material technology," *Electronics Letters*, vol. 31, pp. 1201-1202, 1995.
- [36] Soitec (Smart Cut): [http://www.soitec.com/pdf/Soitec\\_SmartCut\\_EN.pdf](http://www.soitec.com/pdf/Soitec_SmartCut_EN.pdf)
- [37] Soitec: <http://www.soitec.com/en/products-and-services/microelectronics/>
- [38] M. Jurczak, T. Skotnicki, M. Paoli, B. Tormen, J. Martins, J. L. Regolini, D. Dutartre, P. Ribot, D. Lenoble, R. Pantel and S. Monfray, "Silicon-on-Nothing (SON)-an innovative process for advanced CMOS," *Electron Devices, IEEE Transactions on*, vol. 47, pp. 2179-2187, 2000.
- [39] Y. Moriyasu, T. Morishita, M. Matsui and A. Yasujima, "Preparation of high quality silicon on sapphire," In: *Hemment PLF et al. Silicon-on-insulator technology and devices. Electrochemical Society Proceedings*, vol. 99, pp. 137-142, 1999.



- [40] K. Rim, J. L. Hoyt and J. F. Gibbons, "Fabrication and analysis of deep submicron strained-Si n-MOSFET's," *Electron Devices, IEEE Transactions on*, vol. 47, pp. 1406-1415, 2000.
- [41] Xiang Qi, Goo Jung-Suk, J. Pan, Yu Bin, S. Ahmed, Zhang John and Lin Ming-Ren, "Strained silicon NMOS with nickel-silicide metal gate," in *VLSI Technology, 2003. Digest of Technical Papers. 2003 Symposium on*, pp. 101-102, 2003.
- [42] C. Dupre, T. Ernst, J. M. Hartmann, F. Andrieu, J. P. Barnes, P. Rivallin, O. Faynot, S. Deleonibus, P. F. Fazzini, A. Claverie, S. Cristoloveanu, G. Ghibaudo and F. Cristiano, "Carrier mobility degradation due to high dose implantation in ultrathin unstrained and strained silicon-on-insulator films," *Journal of Applied Physics*, vol. 102, pp. 104505-104508, 2007.
- [43] Bruno Ghyselen, "Strain engineering in SOI-type materials for future technologies," *Materials Science and Engineering: B*, vol. 124-125, pp. 16-23, 2005.
- [44] Yang Min, V. W. C. Chan, K. K. Chan, L. Shi, D. M. Fried, J. H. Stathis, A. I. Chou, E. Gusev, J. A. Ott, L. E. Burns, M. V. Fischetti and Jeong Meikei, "Hybrid-orientation technology (HOT): opportunities and challenges," *Electron Devices, IEEE Transactions on*, vol. 53, pp. 965-978, 2006.
- [45] T. Signamarcheix, F. Andrieu, B. Biasse, M. Cassé, A. M. Papon, E. Nolot, B. Ghyselen, O. Faynot and L. Clavelier, "Fully depleted silicon on insulator MOSFETs on (1 1 0) surface for hybrid orientation technologies," *Solid-State Electronics*, vol. 59, pp. 8-12, 2011.
- [46] P. Zimmerman, G. Nicholas, B. De Jaeger, B. Kaczer, A. Stesmans, L. A. Ragnarsson, D. P. Brunco, F. E. Leys, M. Caymax, G. Winderickx, K. Opsomer, M. Meuris and M. M. Heyns, "High performance Ge pMOS devices using a Si-compatible process flow," in *Electron Devices Meeting, 2006. IEDM '06. International*, pp. 1-4, 2006.
- [47] T. Tezuka, S. Nakaharai, Y. Moriyama, N. Sugiyama and Takagi Shin-Ichi, "Selectively-formed high mobility SiGe-on-Insulator pMOSFETs with Ge-rich strained surface channels using local condensation technique," in *VLSI Technology, 2004. Digest of Technical Papers. 2004 Symposium on*, pp. 198-199, 2004.
- [48] E. Jalaguier, B. Aspar, S. Pocas, J. F. Michaud, M. Zussy, A. M. Papon and M. Bruel, "Transfer of 3 in GaAs film on silicon substrate by proton implantation process," *Electronics Letters*, vol. 34, pp. 408-409, 1998.
- [49] L. Di Cioccio, Y. Le Tiec, F. Letertre, C. Jaussaud and M. Bruel, "Silicon carbide on insulator formation using the Smart Cut process," *Electronics Letters*, vol. 32, pp. 1144-1145, 1996.
- [50] N. Bresson, S. Cristoloveanu, C. Mazuré, F. Letertre and H. Iwai, "Integration of buried insulators with high thermal conductivity in SOI MOSFETs: Thermal properties and short channel effects," *Solid-State Electronics*, vol. 49, pp. 1522-1528, 2005.
- [51] J. P. Mazellier, J. Widiez, F. Andrieu, M. Lions, S. Saada, M. Hasegawa, K. Tsugawa, L. Brevard, J. Dechamp, M. Rabarot, V. Delaye, S. Cristoloveanu, L. Clavelier, S. Deleonibus, P. Bergonzo and O. Faynot, "First demonstration of heat dissipation improvement in CMOS technology using Silicon-On-Diamond (SOD) substrates," in *SOI Conference, 2009 IEEE International*, pp. 1-2, 2009.
- [52] D. Lederer, C. Desrumeaux, F. Brunier and J. P. Raskin, "High resistivity SOI substrates: how high should we go?," in *SOI Conference, 2003. IEEE International*, pp. 50-51, 2003.

## **Chapter II:**

### ***Electrical characterization of SOI substrates***

## ***Introduction***

We saw in chapter I that the Smart-Cut™ technology presents several advantages and is dominant at present in the manufacturing industry of SOI substrate. The characterization of SOI wafers for the quality control accompanies the manufacturing process and allows optimization of the products. The aim of this chapter is to present the electrical study of SOI structures by pseudo-MOSFET ( $\Psi$ -MOSFET) technique.

The first part proposes an overview of the  $\Psi$ -MOSFET method through the preparation of samples, its principle of operation and the extraction of the electrical parameters for different SOI structures.

The second part presents the  $\Psi$ -MOSFET results of electrical characterization of advanced SOI substrates with thin films down to 12 nm and thin BOX down to 10 nm.

The third part is dedicated to the study of the electrical properties of SOI wafers at low-temperature with  $\Psi$ -MOSFET concept. Our aim is to reveal the electrical behavior and parameters variation with temperature.

## **1. Pseudo-MOSFET principle and operation**

### **1.1 Overview**

As shown in chapter I, the evolution of SOI materials and their more and more frequent employment in integrated circuit fabrication make an effective and fast quality control necessary. The SOI electrical characterization aims revealing the wafer parameters that will have a direct impact on the components realized on that substrate. The characterization of SOI materials and devices requires techniques able to adapt to difficulties induced by very thin film layers, presence of thin BOX, strong coupling between interfaces (Si/BOX, BOX/substrate and Si/air) and typical defects (stress effects, in-depth in-homogeneities, dislocations, precipitates, *etc.*). Some conventional methods show their limits for thin films and BOX, whereas novel techniques were implemented and will be discussed in chapter III.

The electrical characterization of SOI wafers involves mainly measuring the conductivity of the silicon top layer. Moreover, the natural MOS-like structure of SOI allows using the bulk substrate as a gate to control the conductivity in the top silicon film. Based on current flowing into the film *versus* gate voltage, one can extract numerous electrical parameters of the film. This is basically the philosophy of a pseudo-MOS transistor, called the  $\Psi$ -MOSFET.

The  $\Psi$ -MOSFET technique has been developed to characterize the quality of the silicon layer and the BOX in as-fabricated SOI wafers before any device processing ([1], [2], [3]). It is largely used for evaluation of material parameters such as mobility of carriers and interface quality. Contrary to the characterization performed for a conventional MOS transistor, it is here the lower interface of the silicon film (in touch with the BOX) that is estimated. While the information extracted from a MOSFET concerns normally the gate oxide, in  $\Psi$ -MOSFET the data is related to the buried oxide.

The important advantage of  $\Psi$ -MOSFET is to allow the extraction of the electrical characteristics intrinsic to the SOI material, avoiding the subsequent modifications which arise during a complete CMOS process manufacturing in clean room.

There are two ways to measure the current flowing into the film: four-probe configuration and two-probe configuration.

The four-point (4-point) probe is used to measure the semiconductor resistivity when the volume of the material is not accessible and only the surface may be probed (Figure II-1a). It was originally proposed in 1916 to measure the earth's resistivity and then adopted for semiconductor wafer resistivity ( $\rho$ ) measurements in 1954 [4]. Most commonly it measures the sheet resistance ( $R_{\square}$ ) of thin conducting layers and wafers.

As shown in Figure II-1a, the 4 probes are generally collinear, *i.e.*, arranged in-line, with equal probe spacing (1 mm). The outer probes (1 and 4) are carrying the current whereas the voltage is sensed between the inner probes (2 and 3). The current is probed *via* drain and source contacts. While the probe 1 is grounded, a current source is connected to probe 4 ( $I_{41}$ ) and the differential potential,  $V_{32}$ , is recorded with high impedance voltmeters ([2], [5]). The sheet resistance ( $R_{\square}$ ) and the average resistivity ( $\rho$ ) are given by:

$$R_{\square} = \frac{\rho}{t_{\text{Si}}} = 4.53 \frac{V_{32}}{I_{41}} \quad (\text{II-1})$$

The advantage of the 4-point probe  $\Psi$ -MOSFET method, compared to two-point probes  $\Psi$ -MOSFET, lies in the way the current and voltage are measured. Due to the high input impedance voltmeter, very low current is drawn so, the contact resistances of probes 2 and 3 usually play a negligible role in the measurements. Thus, the 4-point probe characteristics are not influenced by parasitic effects (contact resistances) [2]. Unfortunately, extracting MOS parameters from the configuration is tedious because one needs to readjust the  $I_{14} = I_D$  current in order to keep  $V_{32}$  constant ( $V_o$ ) during measurements.

A simpler two-probe configuration was proposed. Two contacts on the top silicon film (body of the transistor) serve as source and drain, while the bulk silicon substrate can be biased as a gate. The buried oxide (BOX) is used as a gate dielectric. Direct  $I_D$ - $V_G$  curves are thus obtained.

In FD SOI layers, the substrate is biased as a gate and inversion or accumulation layers are induced at the Si/BOX interface.

Two main versions of the pseudo-MOSFET technique exist; they differ in the way the source and drain contacts are formed. The first one, the point-contact  $\Psi$ -MOSFET (see Figure II-1b), which uses two metal tips (pressure probe technique), has been developed by Cristoloveanu *et al* in 1992 at IMEP [1]. The second one, the Hg-FET (see Figure II-1c), uses mercury probes and has been developed by Hovel in 1997 at IBM [6]. The Hg-FET is based on S/D contacts formed by two concentric circles of mercury creating ohmic contacts and allowing to obtain a perfectly defined geometry for SOI characterization [6]. Note that some groups are working with deposited metal contacts (see Figure II-1d) on the top Si film [7]. The modeling of this configuration is more complicated since the source/drain contacts to film are Schottky diodes.

Let us also cite here a more exotic method called SHG (Second-Harmonic-Generation). This method frees itself from probes or from physical contact. It is based on the reflections of a laser beam at various interfaces of the SOI film and gives information on the carrier charge density by the analysis of the second harmonic of the signals [8].

The simplest and most efficient of all these techniques is the point-contact  $\Psi$ -MOSFET (Figure II-1b) with pressure probes to form source and drain contacts as detailed below.

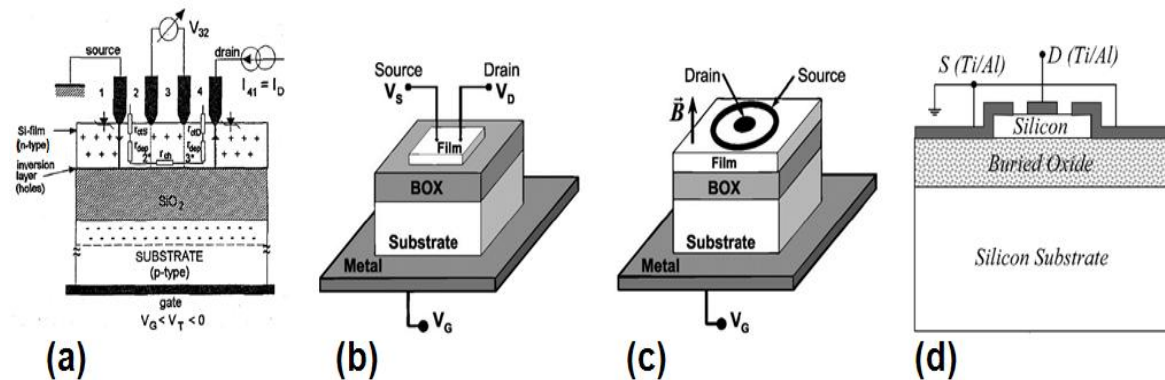


Figure II-1: (a) Principle of the 4-point probe measurement [5].  $\Psi$ -MOSFET configuration with: (b) metallic pressure probes [9], (c) mercury probes [9] and (d) deposited metal contacts [7].

## 1.2 Point-contact $\Psi$ -MOSFET technique

The point-contact  $\Psi$ -MOSFET equipment is a standard JANDEL universal probe station for electrical testing.

It consists of a chuck which must be a brass conductive table that can be biased as a gate. It is composed of 4 tungsten carbide probes with a tunable pressure and with  $\sim 40 \mu\text{m}$  tip radius. The distance between two successive probes is 1 mm. Needles load is controllable (between 0 and 100 g) by adjustable individual tension gauges. The chuck and the 4 needles (Figure II-2a) are covered by a dark box enabling the test in dark conditions. The external electrical connection with  $\Psi$ -MOSFET equipment is done using 6 independent electrical outputs: 5 BNC (female) corresponding to the 4 probes and the chuck, and one simple output for dark box ground (typically banana plug).

Note that different electrical measurements could be made using  $\Psi$ -MOSFET: the 2-point probes measurements (standard  $I_D$ - $V_G$ ,  $g_m$ - $V_G$ ,  $I_G$ - $V_G$  and  $I_D$ - $V_D$ ) and the four-point (4-point) probes measurement discussed previously.

The  $\Psi$ -MOSFET technique conquered the world of SOI substrates characterization by its simplicity and its speed of implementation. As specified in the previous sub-section, the point-contact  $\Psi$ -MOSFET can be presented as an upside-down MOS configuration. The contacts (source and drain) are insured by two probes (Figure II-3a). The substrate acts as a gate where we can apply a back-gate voltage ( $V_G$ ) through the metallic holder (chuck).

### 1.2.1 Sample preparation

The capability to characterize full SOI wafers was demonstrated [2], but is very sensitive to the edge effects and to the defects that may be present in the BOX (leakage). Therefore, using a wafer with isolated silicon islands is preferable in order to reduce leakage current on the edges (Figure II-2b) and also for wafer mapping.

The size of these islands must be sufficient to be able to place the needles without any difficulty, without being too large in order to reduce the probability of a BOX defect. However, the defects that cause leakage through the buried oxide became rare; thanks to the improvement of the SOI materials fabrication, the islands surface can go to a few  $\text{cm}^2$ . It is important that the etching of the film around the Si islands reaches the BOX to isolate well each island. Indeed, if a thin layer of semiconductor material remained, the current could spread from one island to another. We must also take into account possible variations of the film thickness.

Similarly, if the islands are too close to each other, the conductive particles can connect them together. In practice, typical islands have  $5 \times 5 \text{ nm}^2$  size, separated by 2 nm wide trenches.

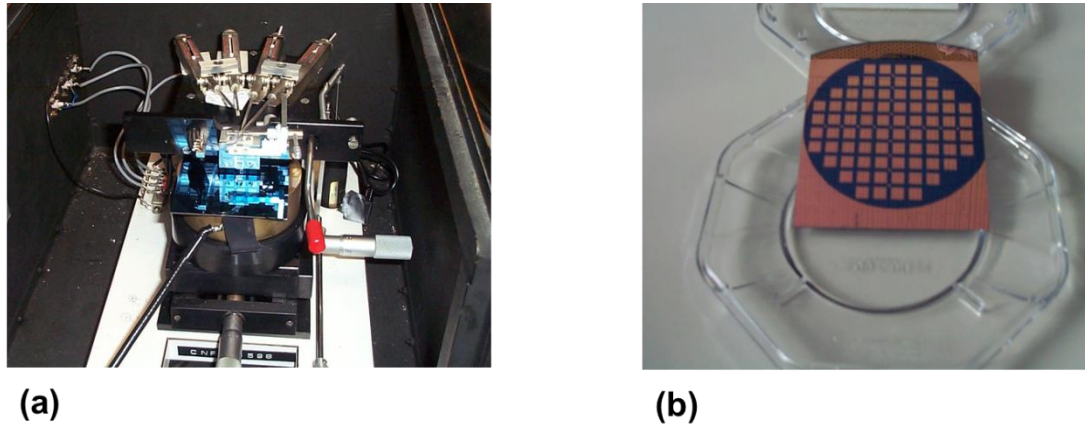


Figure II-2: (a) Pseudo-MOSFET equipment and (b) SOI wafer after islands fabrication.

### 1.2.2 Typical $I_D$ - $V_G$ in $\Psi$ -MOSFET configuration

The back-gate bias has the effect of creating a conduction channel at the film/BOX interface (Figure II-3b). There are three main regimes of a MOS structure: accumulation, depletion and inversion, presented in Figure II-4 [3].

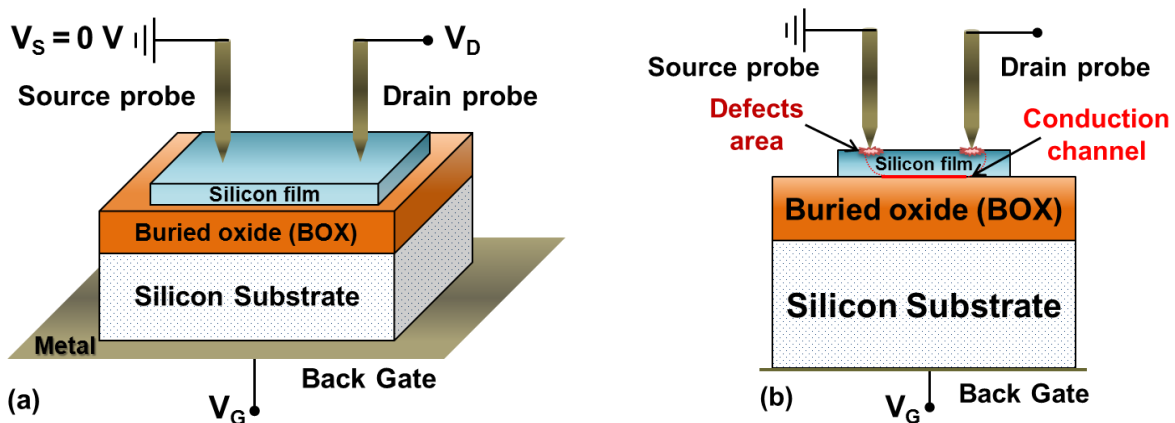


Figure II-3: Experimental schematics of  $\Psi$ -MOSFET measurement: (a) two metallic pressure probes are used as source and drain, (b) a conduction channel is created at the film/BOX interface through the bias of the substrate ( $V_G$ ) and defects areas were generated due to the probes penetration in the Si film.

The probes for current measurement being metallic and the source and drain areas being undoped, it is possible to study the conduction of both holes ( $h^+$ ) and electrons ( $e^-$ ) in a single  $I_D$ - $V_G$  measure (Figure II-4c), contrary to a classical MOSFET working with only a single type of carriers.



If we apply a positive gate voltage ( $V_G$  from 0 to +10 V in Figure II-4a), there is generation of a hole accumulation layer at the BOX/substrate interface (zone 1) and the electrons are rejected towards the gate which leads to a positive gate current ( $I_G$ ) in Figure II-6. At the Si film level, the holes are evacuated (zone 2) and an inversion layer forms resulting in a drain current ( $I_D$ ) visible on the  $I_D$ - $V_G$  curves in logarithmic scale (Figure II-4c).

If we apply a negative gate voltage ( $V_G$  from 0 to -10 V in Figure II-4b), there is a depletion area before the creation of an inversion zone at the BOX/substrate interface (zone 1). The holes are collected by the gate which leads to a negative gate current (Figure II-6). In the Si film, a hole conduction channel is formed (zone 2) and a positive drain current flows (Figure II-4c). The current is zero when the film is totally depleted ( $-1 \text{ V} < V_G < +1 \text{ V}$ ).

In Figure II-4c, we show standard 2-point probes measurement: drain current ( $I_D$ ) and transconductance ( $g_m = \partial I_D / \partial V_G$ ) versus  $V_G$  curves. Note that  $I_D$ - $V_G$  and  $g_m$ - $V_G$  characteristics are very pure, similar to those of a conventional MOS transistor. The two conduction mechanisms just explained (accumulation and inversion) depend on the voltage range applied on the Si substrate.

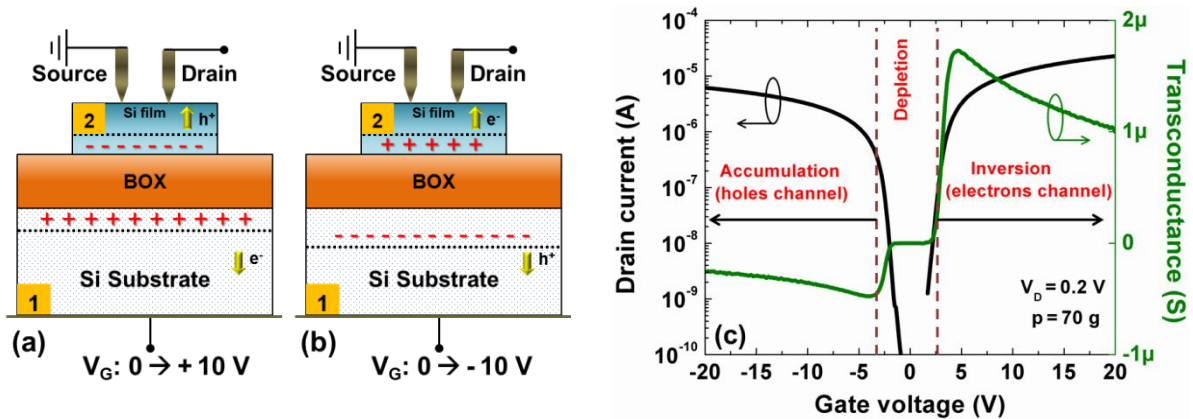


Figure II-4: Carriers movement induced by a voltage sweep of a  $\Psi$ -MOSFET structure for (a)  $V_G$  from 0 to +10 V and (b)  $V_G$  from 0 to -10 V. (c) Illustration of ambipolarity conduction  $I_D$ - $V_G$  (logarithmic scale) and transconductance  $g_m$ - $V_G$  on p-type ( $N_A \approx 10^{15} \text{ cm}^{-3}$ ) SOI film with  $t_{Si} = 88 \text{ nm}$  and  $t_{BOX} = 145 \text{ nm}$ .

Note that the  $I_D$ - $V_G$  curves in Figure II-4c were obtained in linear regime (low  $V_D$  value). Figure II-5 shows linear drain current versus drain voltage curves for various back-gate voltages. The curves exhibit a clear ohmic conduction for negative  $V_G$  (see Figure II-5a) and for positive  $V_G$  (see Figure II-5b). Moreover, the drain current is modulated by the voltage applied on the substrate, which confirms the

MOSFET-like characterization. Without substrate biasing ( $V_G = 0$  V), the current is zero because the Si film is fully depleted.

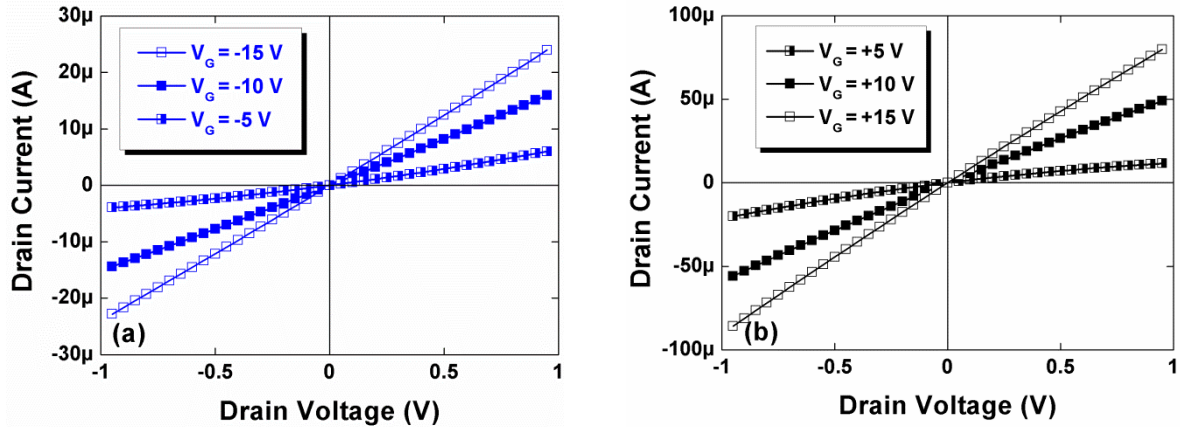


Figure II-5:  $I_D$  versus  $V_G$  curves for various back-gate voltages: negative in (a) and positive in (b). SOI film with  $t_{Si} = 88$  nm and  $t_{BOX} = 145$  nm ( $p = 70$  g).

In the following sub-sections, we will discuss the impact of two main aspects which should be taken into account during the measurements: the substrate effect and the probe pressure contact influence.

### 1.2.3 Substrate effect

To better understand the  $\Psi$ -MOSFET operation mechanisms, the effects due to the substrate below the BOX can be studied [3]. Indeed, the substrate acts as a gate, and contrary to conventional MOSFETs, the gate here is not metallic or heavily doped; it is thick (total thickness of the substrate exceeds 500  $\mu\text{m}$ ) and lightly doped ( $p$ -type,  $N_A \approx 10^{15} \text{ cm}^{-3}$ ).

This leads to the appearance of large depletion areas (about 1  $\mu\text{m}$  depth) under the BOX with possible formation of an inversion layer for negative  $V_G$ . An accumulation layer forms for positive  $V_G$ . The access to the substrate current is easy; a study of the gate current ( $I_G$ ) as a function of  $V_G$  (Figure II-6), collected at the back-gate contact of the SOI wafer is enough. Note that the values of the gate current must be less than 100 nA during each  $I_D$ - $V_G$  measurement in order to avoid polluting the drain current measurement by leakage through the BOX. The gate voltage is limited by oxide breakdown. The two picks of the gate current for  $V_G > 0$  and  $V_G < 0$  respectively correspond to the threshold ( $V_T$ ) and flat-band voltage ( $V_{FB}$ ) at the BOX-substrate interface.

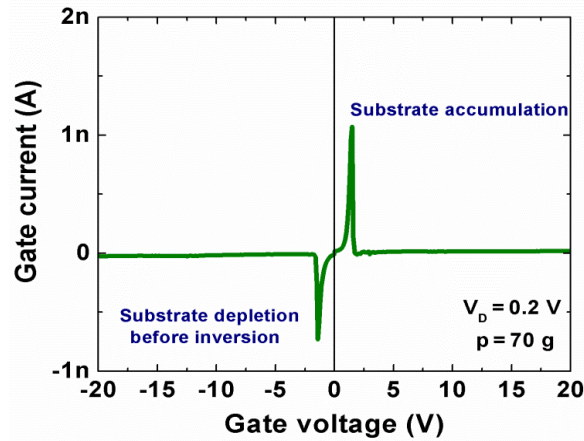


Figure II-6: Gate current versus gate voltage in SOI wafer with  $t_{Si} = 88$  nm and  $t_{BOX} = 145$  nm.

### 1.2.4 Influence of probe pressure

As the source and drain contacts are metallic, while the undoped silicon film is semiconductor, for low drain voltages one would expect to have Schottky barriers dominating the source and drain access. This is definitely the case for deposited metal contacts (*i.e.* Ti/Al) [7].

As shown by linear symmetrical  $I_D$ - $V_D$  curves in Figure II-5, the situation is different for pressure probes  $\Psi$ -MOSFET: the pressure applied on the probes allows recovering the ohmic contact for source and drain as it was previously demonstrated in [10]. Figure II-7 shows drain current and transconductance characteristics obtained for a 200 nm film thickness and a 400 nm BOX thickness [10]. The measurements performed with higher pressures are clearly evidencing an increase in the current level and in the transconductance peak. This effect is due to the variation of the series resistances with the probe pressure.

In addition, it was proven in [10] that the pressure applied on the probes results in a localized damage of the Si layer, with formation of craters (Figure II-7b and Figure II-7c). Figure II-7b and Figure II-7c show atomic force microscopy topographies of two craters obtained with the same probe, for different pressures. The shape of the craters is the same, but their sizes are increasing with pressure. The diameter and the height of these craters were both increasing with pressure. The height obtained was quasi-linear dependent on the pressure, with a slope of 1-2 nm/g [10]. This confirms also the earlier estimation of 10 nm probe penetration for 10 g pressure [3]. Increasing pressure induces deeper penetration of probes into the film and higher crystal local damage, which allows decreasing the Schottky barrier and

obtaining an ohmic probe-to-film contact. Since the probe inter-distance (1 mm) is much larger than the probe size ( $\sim 40 \mu\text{m}$  diameter), the generated local defects, which may arise over a few micrometers near the contacts, can be neglected and do not affect the interface properties and the parameters extraction.

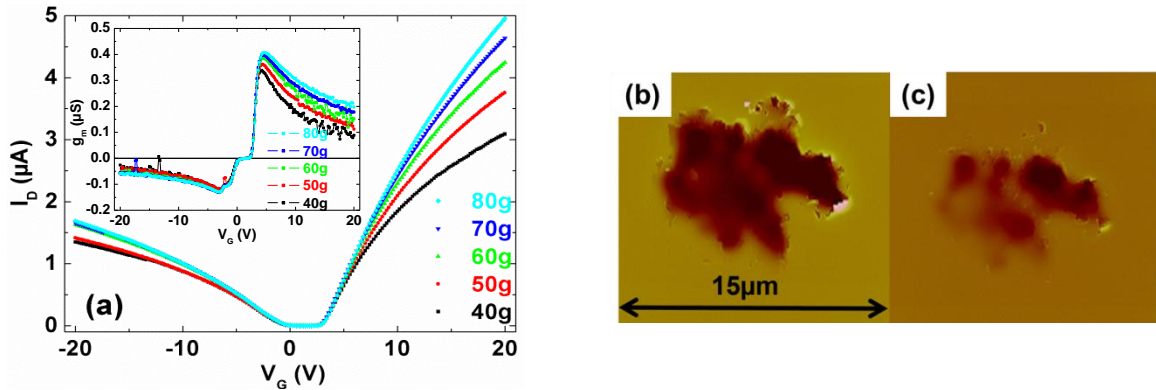


Figure II-7: (a) Drain current (linear scale) and transconductance (inset) versus back-gate voltage for various pressures applied on the  $\Psi$ -MOSFET probes [10]. There is no visible variation of  $V_T$  and  $V_{FB}$ . Atomic Force Microscope topographies of two craters obtained with the same probe at two different pressures: (b)  $p = 70 \text{ g}$  and (c)  $p = 50 \text{ g}$  [11]. The shape of each crater is not regular and it represents the “fingerprint” of the probe, the size of which is pressure-related.

A good control of series resistances is essential to obtain realistic material parameters and the optimal control is obtained by the pressure applied on the probes. For thick films, the degradation induced by the probes is made far from the conduction zone. On the other hand, the applied probe pressure becomes very critical for the measurements of thin and extra-thin films where the needles can penetrate into the BOX and result in a current leakage. In these cases, it is necessary to decrease the probe pressure but to keep it at a value sufficient to ensure ohmic contacts between probes and thin Si film.

### 1.3 Extraction methods of the electrical parameters

As in the case of an ordinary MOSFET, two operation modes exist for the  $\Psi$ -MOSFET: linear (or ohmic) regime and saturated regime. For all our measurements and parameters extraction we place ourselves at low  $V_D$  (ohmic region). Note that  $I_D$ - $V_G$  curves previously showed in Figure II-4c were obtained in this regime. The transistor behaves like a quasi-two-dimensional conductance controlled by the back-gate. If we consider the case of fully depleted films, where the volume current is negligible, we can detail the expressions of the current in inversion and accumulation. In such configuration, the theoretical relationships of the MOS transistor can be

directly applied [12]. The drain current ( $I_D$ ) in ohmic regime for a MOSFET is given by the relation:

$$I_D(V_G) = f_g C_{ox} \frac{\mu_0}{[1 + \theta_1(V_G - V_{T,FB}) + \theta_2(V_G - V_{T,FB})^2]} (V_G - V_{T,FB}) V_D \quad (\text{II-2})$$

where:

- $f_g$  is the geometrical factor taking into account the size of the devices (similar to the ratio  $W/L$  in classical MOSFETs;  $f_g = W/L = 0.75$  in the case of  $\Psi$ -MOSFET [1], [2], [13]).
- $C_{ox}$  represents the buried oxide capacitance per unit area.
- $\mu_0$  is the low-field mobility ( $\mu_n$  accounts for electrons and  $\mu_p$  for holes).
- $V_T$  is the threshold voltage for electrons channel and  $V_{FB}$  is the threshold voltage for holes channel (or the flat-band voltage).
- $\theta_1$  is the first-order mobility attenuation factor related to the series resistances ( $R_{SD}$ ) and to the interaction between the carriers and the phonons of the crystal lattice.
- $\theta_2$  is the second-order mobility attenuation factor which takes into account the surface roughness of the Si/SiO<sub>2</sub> interface and becomes important for transistors with thin gate oxide at high vertical field.

In the case of the  $\Psi$ -MOSFET where the BOX is thick enough, the second mobility attenuation factor ( $\theta_2$ ) is negligible because it only occurs at very high gate voltage (very strong inversion). Therefore, we re-write the simplified expressions for the drain current ( $I_D$ ) and transconductance ( $g_m$ ):

$$I_D(V_G) = f_g C_{ox} \frac{\mu_0}{[1 + \theta_1(V_G - V_{T,FB})]} (V_G - V_{T,FB}) V_D \quad (\text{II-3})$$

$$g_m = \frac{\partial I_D}{\partial V_G} = f_g C_{ox} V_D \frac{\mu_0}{[1 + \theta_1(V_G - V_{T,FB})]^2} \quad (\text{II-4})$$

$\theta_1$  coefficient measures the reduction of the “pure” mobility  $\mu_0$  with vertical field and is a function of series resistance ( $R_{SD}$ ); and of carrier confinement at the interface ( $\theta_{1,0}$ ):

$$\theta_1 = \theta_{1,0} + f_g C_{ox} \mu_0 R_{SD} \quad (\text{II-5})$$

Important material parameters appear in these equations (*e.g.* mobilities,  $V_{FB}$ ,  $V_T$ ,  $R_{SD}$  *etc.*). Their extraction methods will be described in the next sections.

### 1.3.1 Threshold voltage and flat-band voltage

There are various methods to extract the threshold voltage [14]:

- The gate voltage corresponding to a drain current equal to  $10^{-7}$  A/ $\mu\text{m}$  (difficult to use in our case as  $W$  is unknown in  $\Psi$ -MOSFET).
- The maximum of the transconductance  $g_m$  (inaccurate approximation) [15].
- The Y-function [16].
- The maximum of  $\partial g_m / \partial V_G$  ( $\partial^2(I_D) / \partial(V_G^2)$ ) [17].

For accuracy reason, the last two methods will be used. We prefer to proceed with the Y-function method developed by Ghibaudo [16]. The main advantage of this method comes from its independence from  $\theta_1$  factor enabling to avoid the impact of  $R_{SD}$  which is critical in our measurements. If we consider the drain current given by equation (II-3), the Y-function is linear for  $|V_G| \geq |V_{T,FB}|$  and is given by:

$$Y(V_G) = \frac{I_D}{\sqrt{g_m}} = \sqrt{f_g C_{ox} \mu_0 V_D} (V_G - V_{T,FB}) \quad (\text{II-6})$$

Due to the ambipolarity of the  $\Psi$ -MOSFET measurements, the Y-function can be plotted at the same time in accumulation and in inversion, in order to extract the thresholds voltages of the corresponding channels. The extraction of the  $V_T$  and  $V_{FB}$  voltages requires extrapolating the tangent of the linear part of the  $Y-V_G$  curve in inversion or accumulation. The intersection of the tangent with the  $V_G$  axis gives the searched values (Figure II-8a).

$V_{T,FB}$  can be extracted by the voltages corresponding to the peaks of  $\partial^2(I_D) / \partial(V_G^2)$  or to the inflexion points of the  $g_m(V_G)$  curve [17]. This last method is illustrated by Figure II-8b. By comparing the two methods, Y-function and peak of  $\partial^2 I_D / \partial V_G^2$ , we notice that the extracted values are extremely close. But we prefer to use in our extraction the Y-function technique because the double derivative is more tedious and results in noise.

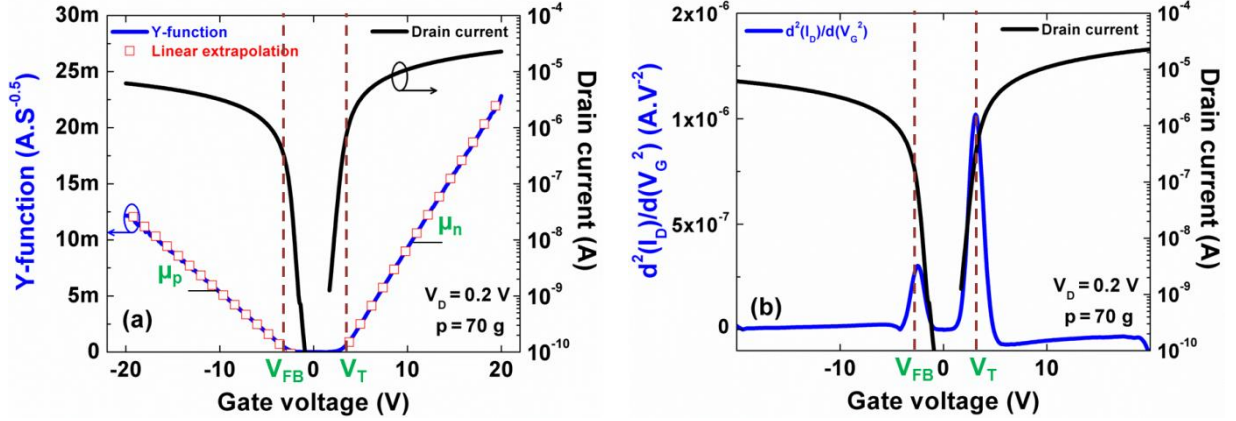


Figure II-8: Extraction of  $V_T$  and  $V_{FB}$ : (a) by Y-function method [16], (b) by the maximum of the second derivative of the drain current [17]. The film thickness is 88 nm while the BOX thickness is 145 nm.

### 1.3.2 Carrier mobility

Again, the mobility of holes and electrons is extracted from a single measurement. Two notions of mobility are to be differentiated: the low-field mobility ( $\mu_0$ ) and the effective mobility ( $\mu_{eff}$ ). The first one corresponds to a maximum value of mobility that carriers could reach if there was no mobility degradation factor. The effective mobility is variable, depending on the effective electric field (*i.e.* on  $V_G$ ), and reflects the real mobility of carriers in the channel at a certain gate bias.

To determine the low-field mobility, we use the slope of the linear part of the “Y-function” (Figure II-9). The value of this slope is given by:

$$\beta_n = \sqrt{f_g C_{ox} \mu_n V_D} \quad \text{and} \quad \beta_p = \sqrt{f_g C_{ox} \mu_p V_D} \quad (\text{II-7})$$

The values of low-field mobility for electrons ( $\mu_n$ ) and for holes ( $\mu_p$ ) can be then extracted by:

$$\mu_n = \frac{\beta_n^2}{f_g C_{ox} V_D} \quad \text{and} \quad \mu_p = \frac{\beta_p^2}{f_g C_{ox} V_D} \quad (\text{II-8})$$

Note that another method of mobility extraction is based on the transconductance ( $g_m$ ). Indeed, according to the equation (II-4) the transconductance reaches a maximum ( $g_{mmax}$ ) for  $V_G \approx V_T$ . We can then determine the mobility  $\mu_0$  by:

$$\mu_0 = \frac{g_{mmax}}{f_g C_{ox} V_D} \quad (\text{II-9})$$

Nevertheless the use of the transconductance tends to underestimate the value of the low-field mobility as the peak of  $g_m$  does not exactly correspond to  $V_G = V_T$ . The peak actually appears at a voltage slightly superior to  $V_T$ . Equation (II-4) is valid in strong inversion and neglects the proximity of weak inversion. That is why  $\mu_0$  will be extracted by the Y-function in our measurements, the  $g_{mmax}$  method being only used for comparisons.

The effective mobility is defined in the simplified case of  $\Psi$ -MOSFET as:

$$\mu_{eff} = \frac{\mu_0}{1 + \theta_1(V_G - V_{T,FB})} \quad (II-10)$$

It is also possible to draw the effective mobility curves as a function of gate voltage for electrons and holes, without making use of the mobility reduction factor ( $\theta_i$ ) thanks to:

$$\mu_{eff} = \sqrt{\mu_{FE}\mu_0} \text{ where } \mu_{FE} = \frac{g_m}{f_g C_{ox} V_D} = \frac{\mu_0}{[1 + \theta_1(V_G - V_{T,FB})]^2} \quad (II-11)$$

The notation  $\mu_{FE}$  means “field-effect mobility”. It characterizes the dependence of the transconductance on the effective electric field. This mobility overestimates the impact of the vertical field on the current. A new method to evaluate the effective mobility by capacitance measurements will be proposed in section 2 of chapter III.

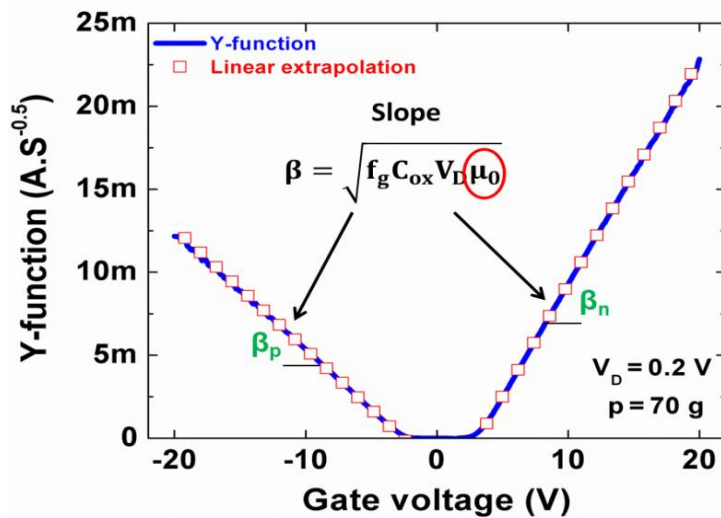


Figure II-9: Extraction of  $\beta_n$  and  $\beta_p$  factors by Y-function method [16] in the case of a SOI substrate with 88 nm film and 145 nm BOX thicknesses.



### 1.3.3 Mobility reduction factor and series resistance

The mobility degradation factor for electrons and holes,  $\theta_1$ , is obtained by combining equations (II-3) and (II-4), for gate voltage much higher than  $V_{T,FB}$ :

$$\theta_1 = \frac{I_D}{g_m(V_G - V_{T,FB})^2} - \frac{1}{(V_G - V_{T,FB})} \quad (\text{II-12})$$

The series resistance for electrons and holes can be simply deduced from  $\theta_1$ , using equation (II-5):

$$R_{SD} \cong \frac{\theta_1}{f_g C_{ox} \mu_0} \quad (\text{II-13})$$

Note that the coefficient  $\theta_{1,0}$  in equation (II-5) is proportional to  $C_{ox}$  and can be neglected in the standard case of thick buried oxides.

### 1.3.4 Subthreshold swing and interface traps density

If we focus on the semi-*log* scale  $I_D$ - $V_G$  curves another parameter can be extracted: the subthreshold swing (S). The density of interface states is calculated from S. For this purpose we need to use the current in weak inversion regime. In practice, to extract the subthreshold swing is given by the inverse of the slope of the logarithmic drain current with respect to the gate voltage, *i.e.*:

$$S = \left( \frac{\partial \log(I_D)}{\partial V_G} \right)_{V_D=\text{cte}}^{-1} \quad (\text{II-14})$$

The subthreshold swing depends on the interface trap density ( $D_{it}$ ) and the Si film capacitance ( $C_{Si}$ ) [12]:

$$S = 2.3 \frac{kT}{q} \left( 1 + \frac{C_{Si} + qD_{it}}{C_{ox}} \right) \quad (\text{II-15})$$

As we can see in Figure II-10, it is more convenient to measure the slope of the linear  $\log(I_D)$ - $V_G$  curve. The subthreshold swing S is the reciprocal of the slope. The subthreshold swings  $S_n$  for electrons and  $S_p$  for holes may be different because they are directly affected by the effective density of interface traps which can be different in accumulation and inversion.

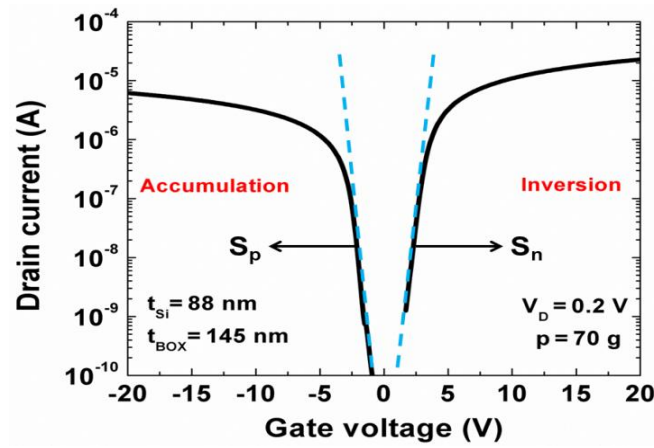


Figure II-10: Extraction of the subthreshold swing  $S_n$  and  $S_p$  of a  $\Psi$ -MOSFET for electron and hole channels.

Once the subthreshold swing was determined, the trap density at Si-BOX interface can be calculated, for both conduction modes, by:

$$D_{it(n,p)} = \frac{C_{ox}}{q} \left[ \frac{S_{n,p}}{2.3 \frac{kT}{q}} - \left( 1 + \frac{C_{Si}}{C_{ox}} \right) \right] \quad (\text{II-16})$$

Obviously,  $D_{it(n,p)}$  are only average values of the defect density in the band gap. They correspond more to “mid-gap” defects situated at the middle of the band gap. Furthermore, this extracted value has sense only if the opposite interface (in general the free wafer surface) is rather far from the BOX. We will discuss this aspect in sub-section 1.4 and in section 3 of chapter III will propose a new method for the evaluation of  $D_{it}$  by noise measurements in  $\Psi$ -MOSFET configuration.

#### 1.4 Impact of the top interface in thin SOI films

As seen in chapter I, thin SOI films have considerable technological interest in the race for device scaling. The film thickness has been drastically reduced in order to achieve very small gate lengths. Consequently, the characterization of ultra-thin (UT) films has become a cornerstone for manufacturers of SOI substrates. The characterization of thick SOI films is reliable and the parameters extraction can be easily extracted.

The extraction of electrical parameters on thin films remains rather challenging, for two main reasons:

- $I_D$ - $V_G$  and  $g_m$ - $V_G$  curves strongly depend on the film thickness (see for example Figure II-11).
- The top interface can dramatically affect the current flow in thin films because of strong electrostatic coupling.

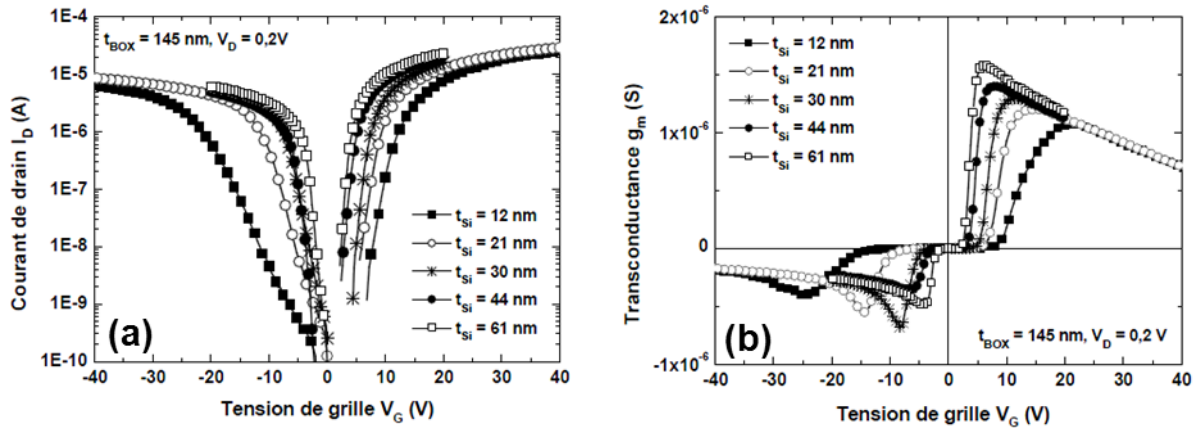


Figure II-11: (a) Drain current and (b) transconductance curves versus gate voltage for various film thicknesses. We observe for ultra-thin films a shift of the threshold and flat band voltages and a reduction in the peak of transconductance [18].

Previous studies have indicated that  $\Psi$ -MOSFET characteristics are affected by silicon thickness ([19], [20]). As the film gets thinner, the current level decreases leading to a decrease of the transconductance; the subthreshold swing and the absolute values of both threshold and flat-band voltages increase. This effect leads to underestimated values of electron and hole mobilities as well as overestimated interface state density [20]. This evolution is marked on wafers thinner than 50 nm and is linked to the particular configuration of the  $\Psi$ -MOSFET technique, not to a degradation of the SOI material quality.

The top surface of the SOI wafer is normally covered by a native oxide (or chemical oxide). This top interface contains a very high density of dangling bonds and, thus, a high density of interface states and charges. The conduction channel formed during the  $\Psi$ -MOSFET measurement is located at the silicon film/BOX interface. As the Si film thickness is reduced, the top free surface gets very close to the channel. Therefore, the thinner the silicon film, the more sensitive to the free surface states the channel is and the more the transistor parameters are affected.

Hamaide *et al* discussed and investigated in detail the impact of the surface quality on the electrical results [21]. Systematic  $\Psi$ -MOSFET measurements of SOI wafers, with and without surface passivation, for different film thicknesses and for

the same BOX thickness of 145 nm, were performed. One group of wafers were considered as a reference (Figure II-12a), the other group underwent a dry oxidation at 900°C in order to passivate the surface with a 10 nm thermal oxide (Figure II-12b). The surface oxide was removed for some wafers in 5 % HF to collect the “post-HF” data.

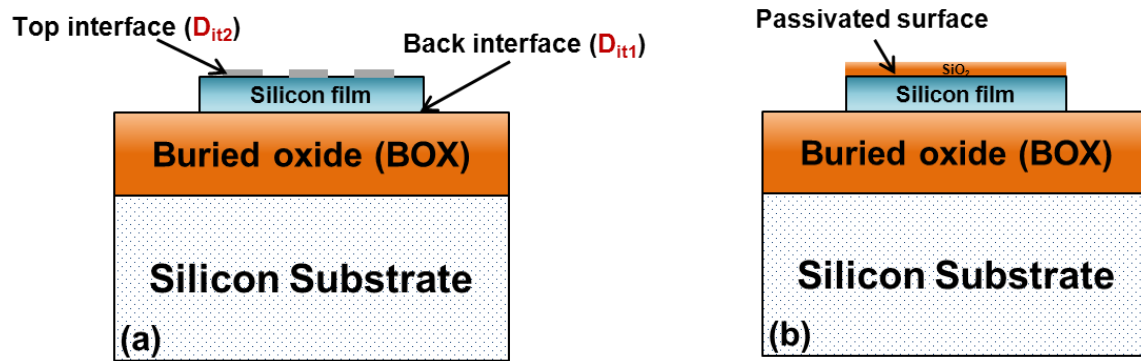


Figure II-12: SOI structure for (a) non-passivated sample where  $D_{it1}$  and  $D_{it2}$  represent the state densities at the back and top interface respectively, and for (b) passivated sample with 10 nm surface oxide.

The evolution of carrier mobility (low-field mobility) *versus* film thickness for samples with and without surface oxide is reproduced in Figure II-13. It is clear that the electron mobility values (Figure II-13a) are increased by about 25 % after surface passivation for the whole range of film thickness. Post-HF mobility values drop back to preoxidation level (reference samples).

This result demonstrates that the increase of mobility with surface oxide is not due to thermal curing during oxidation. Hamaide *et al* mentioned that the mobility values right after the HF treatment and before the native oxide formation are the same as with the oxide, due to the HF passivating effect where the impurities at the top Si film are cleaned [21]. As the films became thinner, part of the electron mobility degradation is only “apparent”, being induced by the electrostatic coupling effect between the top surface states and the conduction channel which gains importance.

A more significant improvement of mobility values for holes than for electrons with surface passivation was observed (Figure II-13b). This stronger influence of surface quality is explained by the fact that in an accumulation channel, the conduction of majority carriers extends further in the volume of the film than do

the minority carriers of the inversion layer. The majority carriers are more influenced by the top surface and thus benefit more from the  $D_{it2}$  (top interface) reduction.

The results in Figure II-13 show that the thickness film dependence is much reduced for electron mobility and nearly suppressed for hole mobility.

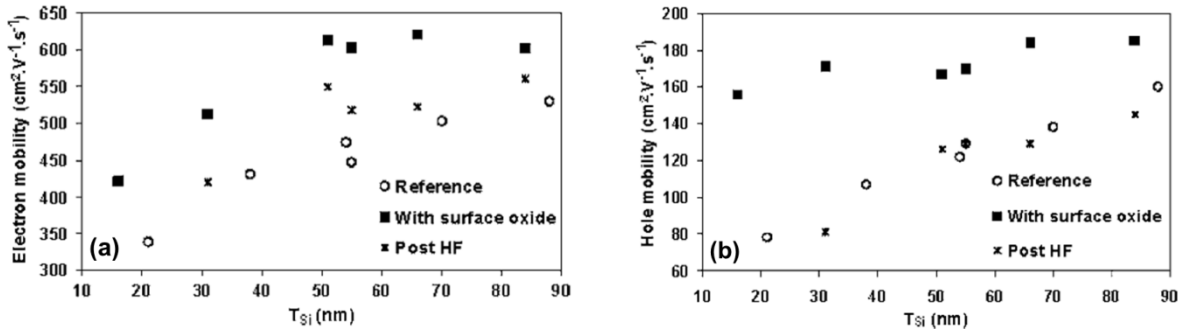


Figure II-13: Comparison of (a) electron mobility and (b) hole mobility measured on samples without surface oxide (reference), with surface oxide, and long after oxide removal (post-HF) [21].

After surface passivation the results in Figure II-14a show a decrease of both the absolute values of  $V_T$  and  $V_{\text{FB}}$  and of their thickness dependence. As for the inversion and accumulation threshold voltages, the interface state density at the top surface is expected to have a strong influence on the subthreshold swing. In particular, the knowledge of the top surface state density  $D_{it2}$  is necessary to extract a realistic density  $D_{it1}$  at the Si/BOX interface. As anticipated, the swing is strongly surface-quality dependent (Figure II-14b), especially at small film thicknesses ( $< 20$  nm). Once again, passivating the top surface significantly reduces both S and its dependence on film thickness.

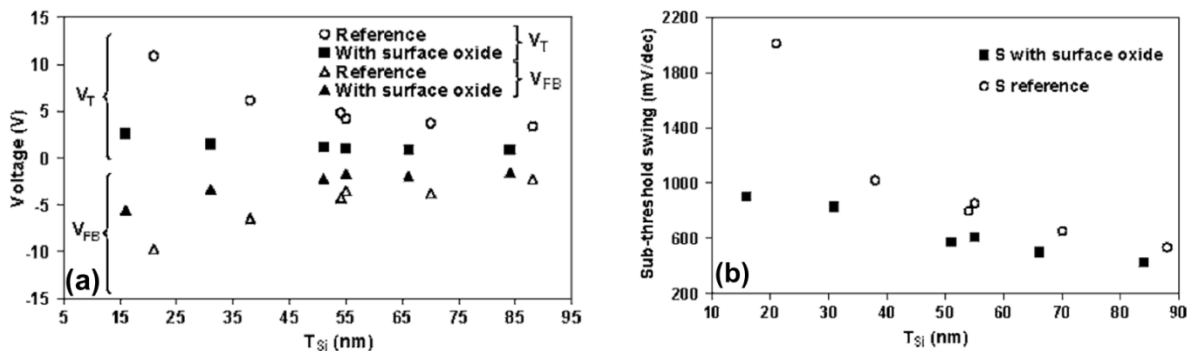


Figure II-14: Comparison of (a) threshold and flat-band voltages and (b) subthreshold swing variations with film thickness obtained on samples without surface oxide (reference, open symbols) and with surface oxide (solid symbols) [21].

These results in Figure II-13 and in Figure II-14 clearly reveal the role of the top interface states which is reinforced by the interface coupling effect ([2], [22]). In addition, the results showed in Figure II-14 are in good agreement with the

mathematical model presented by Hovel where the coupling effect between the two interfaces of the Si film is taken into account [23].

## 1.5 Revisited $\Psi$ -MOSFET models

In the case of  $\Psi$ -MOSFET on partially depleted (PD) Si films, where the back interface maximum depletion width ( $W_{Dmax}$ ) does not reach the top interface, it is possible to use the conventional  $\Psi$ -MOSFET equations below [2]:

$$V_{FB} \cong \frac{kT}{q} \ln \left( \frac{N_{film}}{N_{sub}} \right) - \frac{Q_{ox}}{C_{ox}} \quad (II-17)$$

$$V_T \cong V_{FB} + \frac{qN_{film}t_{Si}}{C_{ox}} + 2\phi_F \left( 1 + \frac{qD_{it1}}{C_{ox}} \right) \quad (II-18)$$

where  $N_{film}$  and  $N_{sub}$  are the doping levels in the silicon film and substrate (in Unibond SOI wafers  $N_{film} \approx N_{sub}$ ).  $Q_{ox}$  is the fixed charge in the buried oxide and  $D_{it1}$  is the trap density at the film-BOX interface. These equations show no dependence of  $V_{FB}$  with the silicon film thickness ( $t_{Si}$ ), and suggest a decrease of  $V_T$  for thinner films. In the frequent case of fully depleted (FD) Si films, the potential of the back interface (Si/BOX) can be influenced by the top interface state (charges present at Si/air interface). The experimental data (reproduced in Figure II-14a) suggests that a corrected model is needed to account for the coupling between the top and bottom interfaces of UT films ( $< 100$  nm).

Recently, Rodriguez *et al* [24] have revisited the associated  $\Psi$ -MOSFET models to fit the case of ultra-thin film SOI. In this new model, the analytical expressions are determined from the 1-D numerical solution of Poisson equation (adapted for the case of a low doped semiconductor) by taking into account the charges resulting from the bands bending at film/BOX interface. In the case of non-passivated SOI films, a new boundary condition appears at the film interface/surface level. The top-surface field is no longer negligible, being defined by the Gauss law and implying a new definition of the threshold voltage [24]:

$$V_T = \phi_{fb} + 2\phi_F \left( 1 + \frac{C_{it1}}{C_{ox}} + \frac{C_{Si}C_{it2}}{C_{ox}(C_{Si} + C_{it2})} \right) \quad (II-19)$$

where  $\phi_{fb}$  is the work function difference between Si film and substrate (here  $\phi_{fb} \approx 0$ ) and the surface trap density capacitances associated to the top and back interfaces are

calculated by:  $C_{it1,2} = qD_{it1,2}$ . In addition, the model could be extended to calculate the subthreshold swing S:

$$S = 2.3 \frac{kT}{q} \left( 1 + \frac{C_{it1}}{C_{ox}} + \frac{C_{Si}C_{it2}}{C_{ox}(C_{Si} + C_{it2})} \right) \quad (\text{II-20})$$

In our work we will focus on these two equations (II-19) & (II-20). Other equations for passivated SOI films and an empirical model for  $V_T$  in  $\Psi$ -MOSFET configuration for very thin films can be found in Rodriguez *et al* [24].

## **2. Characterization of ultra and extra thin SOI wafers**

In the previous section, we showed that the  $\Psi$ -MOSFET technique has constantly been used for studying the electrical properties of as-fabricated fully depleted SOI wafers. While the film and the BOX of SOI structures are getting thinner we are facing problems with the characterization and the extraction methods. Nowadays, two recent challenges drive the research for advanced SOI wafers:

- (i) Application of  $\Psi$ -MOSFET to ultra-thin and extra-thin SOI structures;
- (ii) Extension to other types of electrical measurements.

In the section 3 of this chapter and in chapter III, we will address the second challenge by proving the possibility of low-temperature, low-frequency noise and split  $C$ - $V$  measurements with  $\Psi$ -MOSFET configuration.

In this sub-section, we will prove that the  $\Psi$ -MOSFET is still a very successful characterization technique for bare SOI even when the film and BOX thickness are dramatically reduced [25]. We demonstrate for the first time the ability to characterize advanced SOI structures with ultra-thin films (down to 12 nm) and extra-thin BOX (down to 10 nm) using the  $\Psi$ -MOSFET. In addition, the impact of surface passivation on some samples is also showed and discussed.

The UT/ET SOI wafers are produced by Soitec with Smart-Cut™ process but with different technologies compared to thick SOI samples. Notice that these characterizations are recent and no paper was published by other groups on this subject. Due to the confidential and the continuing progress of UT/ET SOI wafers, we will show only the  $I_D$ - $V_G$  and  $g_m$ - $V_G$  characteristics without mentioning the technology details or the extracted values of mobility and  $D_{it}$ .

### **2.1 Experimental conditions**

In our work, square mesas with 7 cm  $\times$  7 cm size of bonded Unibond/Smart-Cut™ SOI wafers were used with low-doped ( $N_A \approx 10^{15}$  cm<sup>-3</sup>)  $p$ -type silicon layers. Different couples of Si layers and BOX were characterized: between 12 and 200 nm for film thickness and between 10 and 400 nm for BOX thickness. Some of the wafers



underwent a clean dry oxidation at 900°C in order to passivate the surface with a 4-10 nm surface oxide (SiO<sub>2</sub>).

### **2.1.1 Sample preparation**

As mentioned previously, the  $\Psi$ -MOSFET technique requires very few technological steps to be implemented. The wafer is etched in silicon islands isolated from the edges where a leakage current between the gate and the electrodes may occur, which would degrade the measured electrical characteristics.

We engraved several islands per sample in the clean room by dry etching. The wafer is covered with a photosensitive resist using a spin coater with a speed previously set in order to obtain uniform spread on the wafer surface. The sample is then irradiated with UV light passing through a mask which degrades the structure of the exposed resist. A development step allows removing exposed resist. The wafer undergoes a Reactive Ion Etching (RIE), which frees silicon islands with a slight over-etching. The remaining resist is removed by an organic solution called “Remover”. Samples are cleaned and dried and ready to be characterized.

### **2.1.2 Measurement system**

The measuring system consists of a JANDEL probing station (normally used for 4-point probes measurements) and a semiconductor parameter analyzer Agilent HP-4156B (or HP-4155A). This station has undergone some changes, by linking the chuck to a triaxial connector in order to bias the back-gate substrate. The advantage of this station is that the pressure applied on the probes (spaced out by 1 mm) is manually adjustable and from 0 to 100 g. The measurements are performed in the darkness. All measurements were performed at low drain voltage ( $V_D$ ) so as to ensure linear mode operation. In addition, two important parameters in the configuration of the semiconductor parameter analyzer should be well defined especially for advanced electrical measurements of extra-thin film and ultra-thin BOX: the hold time (standby time before each measurement) and the delay time (standby time between two successive gate biases).

In our work, the measurements were done by applying a single sweep gate voltage (forward) from zero to positive value then from zero to a negative value. Some

measurements can be done also by using dual sweep, forward and backward (from positive value to zero and then from negative value to zero) to reveal hysteresis effects.

## 2.2 Results obtained on UT/ET SOI

By adjusting the configuration settings such as the probe pressure, hold and delay time and the gate bias we succeeded to characterize these very thin structures. First, we measured the drain current (in Figure II-15a) and the transconductance (in Figure II-15b) curves *versus* gate voltage for passivated and non-passivated SOI with 88 nm thick Si film and 25 nm BOX thickness.

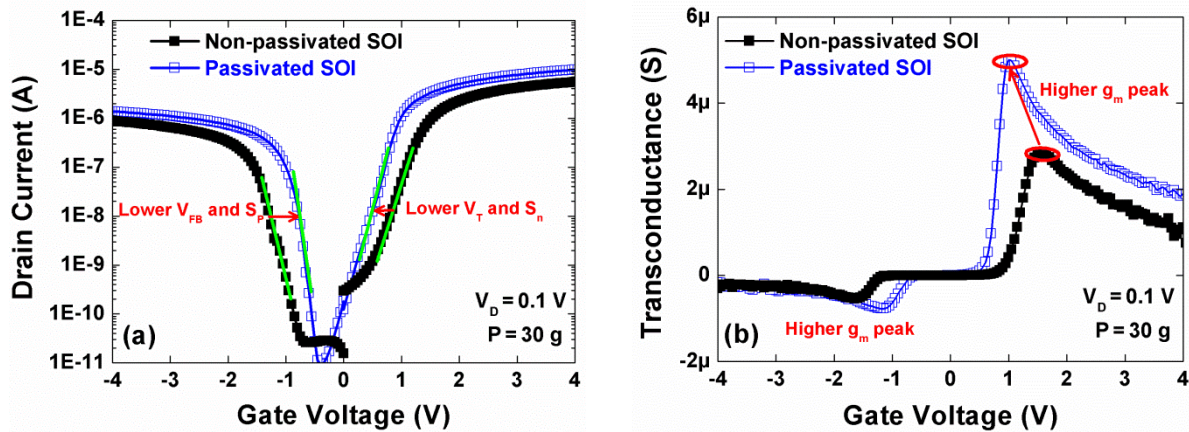


Figure II-15: (a) Drain current and (b) transconductance versus gate voltage for 88 nm Si film (passivated and non-passivated) and 25 nm BOX.

The probability to damage the BOX by the probes and to have current leakage is high. In our measurements we monitored the gate current which in general is below 100 nA for all the range of  $V_G$ . This means that no BOX damage (and consequently no current leakage) is visible. The feasibility to characterize an SOI structure with 25 nm BOX is clearly demonstrated in Figure II-15.

As we discussed above, in ultrathin films ( $< 100$  nm) the coupling of the buried channel with the free surface defects is very strong [21]. We studied the impact of this coupling by measuring both passivated (with 4 nm oxide layer on the film surface) and non-passivated samples in Figure II-15. The drain current curve for passivated samples (Figure II-15a) exhibits lower threshold/flat-band voltages ( $V_{T,FB}$ ) and lower subthreshold swings ( $S_{n,p}$ ) than non-passivated ones. This is a direct consequence of a reduction in the density of surface states by passivation ([21], [24]). The  $g_m$ - $V_G$  curve (Figure II-15b) for passivated sample shows a large increase of the

apparent mobility compared to non-passivated sample (if we extract the mobility by  $g_m$  peak method, a higher  $g_m$  peak implies a higher mobility).

After we proved the  $\Psi$ -MOSFET characteristics for 25 nm BOX with 88 nm film, we characterized for the first time extra-thin (12 nm) layer of silicon with same BOX thickness (25 nm). Here, the probability to damage the buried oxide by the probes and to have current leakage is even higher. Successful  $I_D$ - $V_G$  curves are showed in Figure II-16a and  $g_m$ - $V_G$  curves in Figure II-16b. No leakage current is visible and clean curves were obtained.

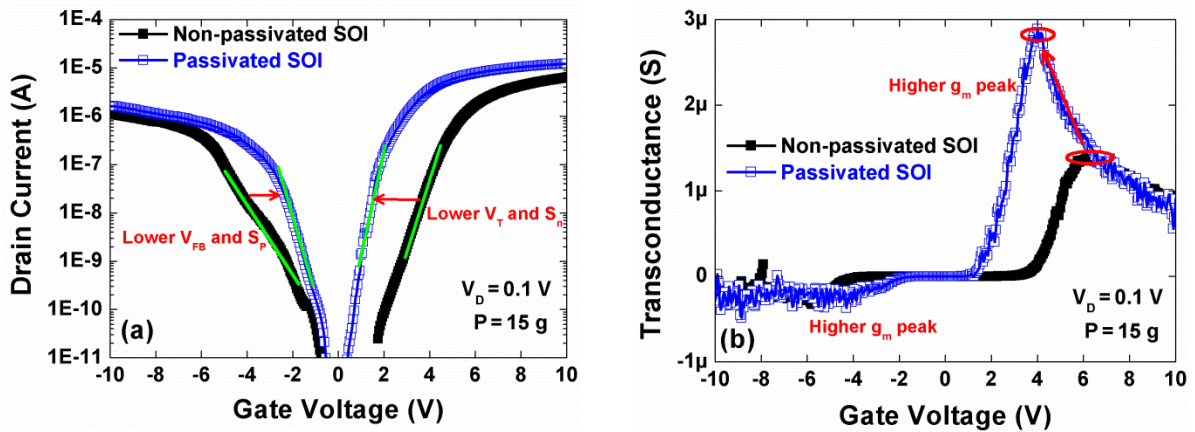


Figure II-16: (a) Drain current and (b) transconductance versus gate voltage for 12 nm Si film (passivated and non-passivated) and 25 nm BOX.

The passivation issue was also studied on 12 nm thin films (Figure II-16), where the channel-surface coupling is stronger. A similar behavior is observed compared to Figure II-15, albeit the benefit of surface passivation is accentuated. The curve shape differs for electrons and holes in 12 nm Si film. This is due to the high impact of series resistance ( $R_{SD}$ ) which is 10 times higher for holes compared to electrons [10] and more evident in thinner films. It is worth reminding that the apparent degradation of the subthreshold swing for thinner films is connected to the stronger surface-channel coupling and does not imply a degradation of the film-BOX interface.

The results in Figure II-15 and in Figure II-16 of surface passivation for thin BOX (25 nm) confirm those obtained for thick BOX (145 nm) [21]. Their merit is to have been obtained on such thin film/BOX couple.

We further studied two SOI wafers with extra-thin (10 nm) BOX and thick (180 nm) or ultra-thin (20 nm) Si film. The  $I_D$ - $V_G$  (Figure II-17a) and  $g_m$ - $V_G$  (Figure II-17b) curves confirm the adaptability of  $\Psi$ -MOSFET technique to extra-thin BOX

(no leakage current or BOX damage are visible). The comparison of these two wafers (Figure II-17) confirms the role of the Si film thickness on the electrical parameters: higher  $V_{T,FB}$  and lower  $\mu_{n,p}$  for thinner film (20 nm).

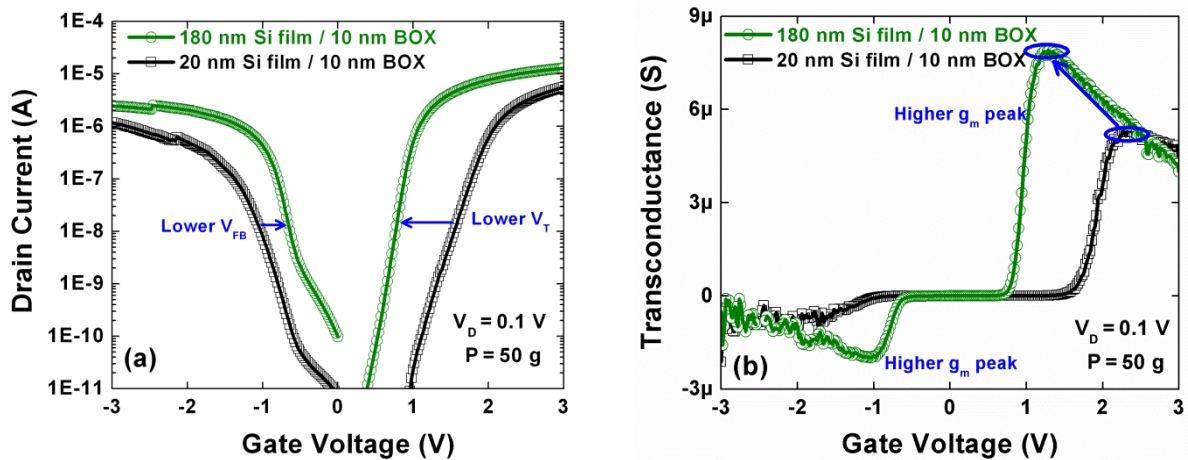


Figure II-17: (a) Drain current and (b) transconductance versus gate voltage.

It is worth mentioning that in ultrathin films and thin BOX SOI wafers, the channel-to-surface and channel-to-substrate coupling are important effects. The equations used before for the extraction of the electrical parameters did not account for the substrate underneath the BOX. Rodriguez *et al* proposed new three-interface (free surface, channel/BOX and BOX/substrate) models for the threshold voltage and the subthreshold swing extractions, which are more appropriate for addressing the case of SOI wafers with ultrathin film and BOX [26].

In conclusion, we demonstrated for the first time the capability of exploring very thin as-grown SOI films, down to 12 nm and BOX layers down to 10 nm, using the  $\Psi$ -MOSFET. More systematic investigations would be interesting in order to evaluate the electrical behavior of these advanced and recent structures. Other innovative measurements were also made on some of these wafers (see chapter III).

### **3. Low-temperature $\Psi$ -MOSFET measurements**

We demonstrated the extension of the  $\Psi$ -MOSFET technique to the low-temperature (low-T) range in order to investigate the transport properties of as-fabricated SOI wafers [27]. The temperature is a most valuable experimental parameter able to provide additional information on the mechanism governing the carrier mobility, threshold voltage and swing. We will first see the interest of such measurements and how to setup the experimental conditions. Then, the evolution of the drain current characteristics with temperature (T) will be presented in order to prove the feasibility of our new extension of  $\Psi$ -MOSFET. From these experimental results, we show and explain the temperature dependence of the extracted electrical parameters (hole and electron mobility, subthreshold slope and threshold voltage). Finally, the impact of the coupling between channel and free surface on the extracted parameters in ultra-thin SOI films will be discussed.

#### **3.1 Interest of low-temperature measurements**

The semiconductors, generally, are extremely sensitive to the temperature. Crucial parameters are dependent on T, such as the carrier mobility, the band gap ( $E_G$ ), the effective density of states in the valence band  $N_V$  or in the conduction band  $N_C$ , and consequently the intrinsic carrier density of the semiconductor ( $n_i$ ), *etc.*

The low-temperature measurements give detailed information on the transport parameters (dominant scattering mechanisms, interfaces quality), which is not available from room temperature experiments. Identifying the main scattering mechanism in bare SOI wafers reveals the quality of the film and the Si-SiO<sub>2</sub> interface which is very important for the SOI manufacturing process.

#### **3.2 Experimental set-up**

The aim of our measurements is to expand the  $\Psi$ -MOSFET technique at low-temperature to characterize SOI wafers. Using a 200 mm wafer cryogenic probe station (Suss Microtec), we performed measurements in a temperature range from liquid nitrogen (T = 77 K) to ambient (T = 300 K) with a temperature control better than  $\pm 0.1$  K. Two metallic probes have been used to form source and drain contacts

on the SOI wafer surface and a voltage ( $V_G$ ) was applied to the metallic plate holder (chuck) to ensure back-gate biasing of the Si substrate, as in normal  $\Psi$ -MOSFET configuration.

The distance between source and drain was maintained fixed ( $\sim 1$  mm). Drain current versus drain voltage  $I_D$ - $V_D$  curves and drain current versus gate voltage  $I_D$ - $V_G$  curves were recorded using a HP-4156 semiconductor parameter analyzer connected to the cryogenic station. The main difference comes from the probes used. In standard  $\Psi$ -MOSFET set-up at room temperature, the JANDEL station with **pressure-adjustable probes** is used. The contacts between pressure probes and Si film are converted from Schottky contacts into ohmic contacts by increasing the pressure as it was shown in sub-section 1.2.4 [10]. In the cryogenic station, the electrical set-up is similar but the pressure on the probes is not controllable which may cause contact problems in our measurements.

The FD-SOI wafers under test had 145 nm thick BOX and 88 or 40 nm thick silicon films. Silicon islands of  $5 \times 5$  mm<sup>2</sup> size were etched on the wafer in order to avoid edge effects. No surface treatment was performed. Therefore, Si film was covered by native oxide which contains a high density of defects and forms a rather poor top interface. We will discuss the impact of the top interface on the extracted parameters in the following.

### 3.3 Drain current variation with temperature

A preliminary experiment was conducted to verify the possibility to obtain ohmic contacts in the cryo-station.  $I_D$ - $V_D$  curves were measured with positive and negative  $V_G$  (Figure II-18a) at different temperatures for 40 nm Si film. The linear shape of the curves confirms that the contacts between probes and Si film have ohmic behavior even though there is no adjustable pressure control on the probes. This result was obtained by proper adjustment of the probe penetration in the Si film during the measurements. Ohmic behavior is obtained for both electrons ( $V_G > 0$ ) and holes ( $V_G < 0$ ). The  $I_D$ - $V_G$  curves for 40 nm thick Si film at several temperatures are presented in Figure II-18b, where electron and hole channels are gradually activated, confirming that the  $\Psi$ -MOSFET is still operating at low temperature. In the positive  $V_G$  region, drain current decreases with the temperature rise, being dominated by the mobility evolution with temperature. For negative  $V_G$  region, which corresponds to

holes channel,  $I_D$  curves have a more complex behavior resulting from competing variations of mobility,  $V_{FB}$  and series resistance  $R_{SD}$  (about one order of magnitude higher than for the electron channel) [10].

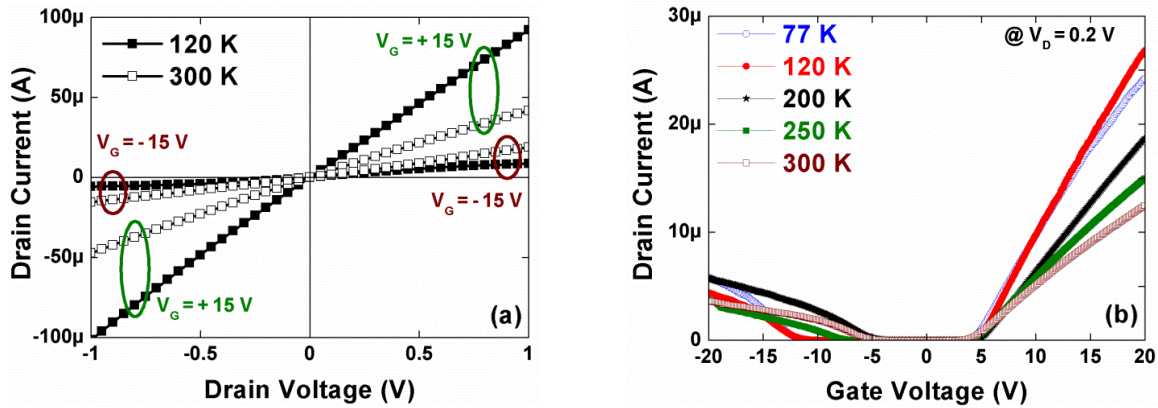


Figure II-18: (a) Drain current vs. drain voltage with  $V_G = \pm 15 V$  for two different temperatures (120 K and 300 K) and (b) drain current vs. gate voltage for various temperatures (77 K, 120 K, 200 K, 250 K and 300 K). BOX thickness is of 145 nm and  $t_{Si} = 40$  nm.

The behavior of the  $I_D$ - $V_G$  curves was reproduced on samples with 88 nm film thickness (Figure II-19) for several temperatures. The *semi-log* scale of the drain current curves (Figure II-19a) shows an increase of the slope in weak inversion regime with the decrease of T. This result is theoretically predictable and will be detailed later. The transconductance  $g_m$  vs.  $V_G$  curves (Figure II-19b) show that as the temperature decreases,  $g_m$  peak increases (for  $V_G > 0$ ) due to improved mobility at low temperature. Since the pressure cannot be increased to optimize the contact quality, small fluctuations in current cause significant noise in the derivative (*i.e.*, transconductance). Overall, the curves illustrated in Figure II-18 and in Figure II-19 prove qualitatively the feasibility of these measurements.

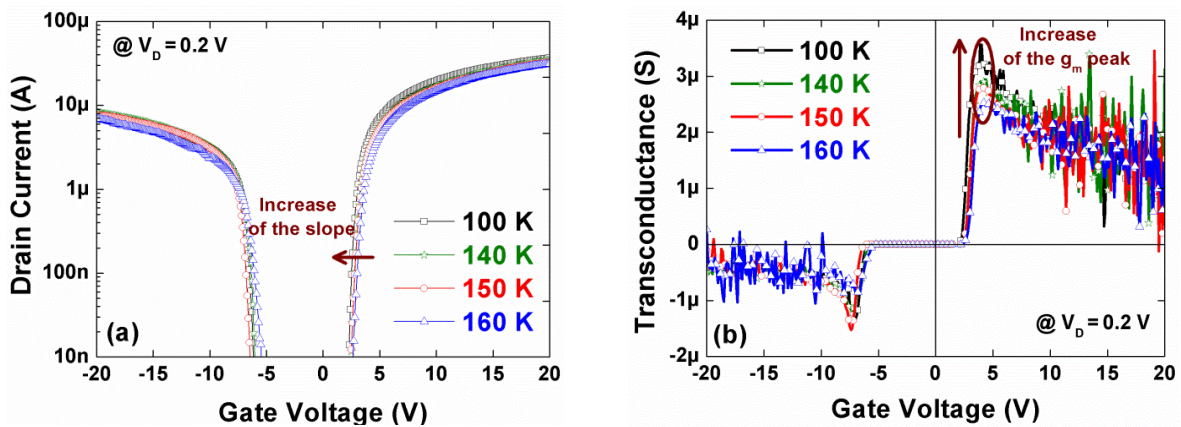


Figure II-19: (a) Drain current vs. back-gate voltage in semi-log scale for various temperatures (100 K, 140 K, 150 K and 160 K) and (b) transconductance vs. gate voltage for same temperatures. BOX thickness is of 145 nm and  $t_{Si} = 88$  nm.

### 3.4 Extracted parameters

The  $\Psi$ -MOSFET measurements are promising because the evolution of the curves with the temperature is qualitatively correct. In order to fully validate the  $\Psi$ -MOSFET capability at low-T, we need to extract the transistor parameters and compare their temperature dependence with theoretical expectations. For quantitative analysis, we use classical MOS models for low drain voltage and strong inversion or accumulation regime described in sub-section 1.3.

In order to avoid the impact of  $R_{SD}$ , which is critical in our measurements because the pressure on the probes is not tunable when using the cryogenic equipment, the parameters ( $\mu_0$ ,  $V_T$  and  $S$ ) extraction is performed with the Y-function method previously detailed see sub-section 1.3.1.

In absence of control of pressure on the probes, reproducibility could be an issue so we need to test it. We placed the probes again and re-tested same dies at one day interval. The superposition of the curves is quite good (Figure II-20). These experiments allowed calculating the variability between the parameter extracted values: 20 % error was obtained for  $\mu_p$  and  $\mu_n$  values, 10 % for  $V_T$  and 18 % for  $S$ . These values are slightly higher than the ones obtained with the JANDEL system (5 – 10 %). Error bars in our next curves indicate these percentages.

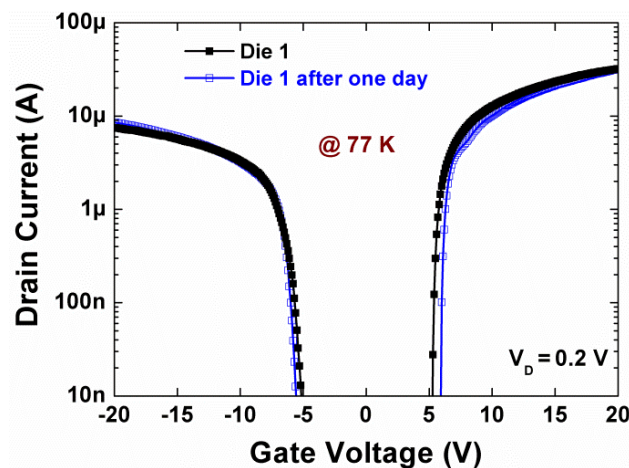


Figure II-20: Drain current versus gate voltage for two curves where the empty squares curve represents the same characterization of die 1 at one day interval compared to full squares curve. 88 nm Si film and 145 nm BOX.



### 3.4.1 Carrier mobility

The carrier mobility reflects the capability of carriers to move in the inversion layer under the influence of an electric field. A technology giving a good mobility allows obtaining a high level of current which is crucial for MOS transistors.

The mobility depends on numerous parameters: electric field, orientation of the crystal, substrate doping level, defects, temperature *etc.* The electron (or the hole) does not move freely in the crystal lattice but undergoes interactions (“scattering”) with its surroundings. The type and number of collisions the carriers experience define the mobility magnitude and its dependence on temperature.

The carrier mobility in a semiconductor is defined by the following equation:

$$\mu = \frac{q\langle\tau\rangle}{m^*} \quad (\text{II-21})$$

where  $m^*$  is the effective mass and  $\langle\tau\rangle$  is the average relaxation time of the carriers between two collisions. In an inversion layer, the frequency of interactions depends on electric field and temperature. When the interactions are independent from each other, the average relaxation time can be written, using Matthiessen’s law [12]:

$$\frac{1}{\langle\tau\rangle} = \sum_n \frac{1}{\tau_n} \quad (\text{II-22})$$

where  $n$  is the number of scattering mechanisms. The resulting inverse of the mobility can be written as:

$$\frac{1}{\mu} = \sum_n \frac{1}{\mu_n} \quad (\text{II-23})$$

Therefore, the scattering mechanism with the lowest relaxation time dominates the mobility.

We review the main effects that alter the mobility and in particular, the various collision mechanisms in the inversion layer. Then we will extract the mobility values with the aim of identifying the dominant scattering mechanism which brings important information on the quality of the film and Si-SiO<sub>2</sub> interface.

In an inversion layer, there are several types of interactions. We focus on three main mechanisms:

- (i) Interaction carrier/phonon,
- (ii) Coulomb interaction between carriers and charged defects
- (iii) Interaction carrier/surface roughness.

Each scattering mechanisms has a specific signature on the mobility *versus* T variation ([28], [29]) as illustrated below.

**Phonon scattering:**

This interaction resulting from vibrations of the crystal lattice is, in bulk Si and SOI, dominant in moderate electric field (0.1-1 MV/cm) at room temperature. There are two types of mechanisms following the energy of the carriers: the interactions with phonons intra-valley and inter-valley. The models are complex because they differentiate the interactions with optical and acoustic phonons which also depend on the occupied energy valleys [30]. A review of these mechanisms as well as their implication on the mobility of electrons in bulk Si can be found in [31].

The analytical expressions of the mobility limited by acoustic phonons in the inversion layer are as follows:

- 1) At low temperatures  $T < 100$  K, the sub-bands are not involved in the transport because the inversion layer electrons are in the lowest sub-band. Therefore, the interactions with intra-valley phonons are dominant and can be modeled by [29]:

$$\mu_{Ph} \propto N_{inv}^{-1/3} T^{-1} \quad (II-24)$$

where  $N_{inv}$  is the concentration of carriers in the inversion layer.

- 2) At higher temperature ( $100 < T < 370$  K), where the carriers can undergo inter-valley and inter-sub-band phonon scattering, the mobility is expressed by [29]:

$$\mu_{Ph} \propto N_{inv}^{-1/\tau} T^{-n} \quad (II-25)$$

where  $\tau = 3 - 6$  and  $n = 1 - 2$  are constants depending on the crystallographic orientation of the surface.

Note that our measurements being conducted at low  $V_D$ , optical phonon scattering can be discarded.

**Coulomb scattering:**

These interactions occur between carriers and charged centers: ionized dopants, interface traps  $D_{it}$  or oxide charges. They are called Coulomb scattering and are mainly responsible for the degradation of the mobility in low inversion regime. When  $N_{inv}$  increases the electrical potential created by the charged defects is gradually screened by the increasing number of the mobile charges in the channel [32]. The carrier mobility limited by charged defects (Coulomb scattering) is:

$$\mu_C \propto \frac{T^n}{N_{it}} \quad (\text{II-26})$$

where  $N_{it}$  is the interface charge density at the Si-SiO<sub>2</sub> interface and  $n = 1 - 2$  is a constant. Since  $\mu_C$  increases with temperature, this interaction is more visible below 100 K.

**Surface roughness:**

The surface-roughness scattering mobility is rather independent of temperature. Surface asperities at the Si-SiO<sub>2</sub> constitute a major cause of scattering at high electron concentrations. This mechanism, relevant only at high electric field (in very strong inversion/accumulation regime where carriers are more confined near the interface), is not likely to affect the low-field mobility. The resultant mobility can be modeled according to Jeon *et al* [29] by:

$$\mu_{sr} \propto E_{eff}^{-2} \quad (\text{II-27})$$

where  $E_{eff}$  is the effective transversal electric field.

The relative contribution of these three scattering mechanisms depends on the temperature and on the concentration of the carriers in the channel. At room temperature and in weak inversion, the mobility is controlled by the collisions on phonons and marginally by Coulomb scattering, while in strong inversion the surface roughness is dominating. At low temperature, only the latter two mechanisms are significant, the collisions on phonons being “masked” by the temperature decrease.

Figure II-21 summarizes this discussion in a simplistic way.

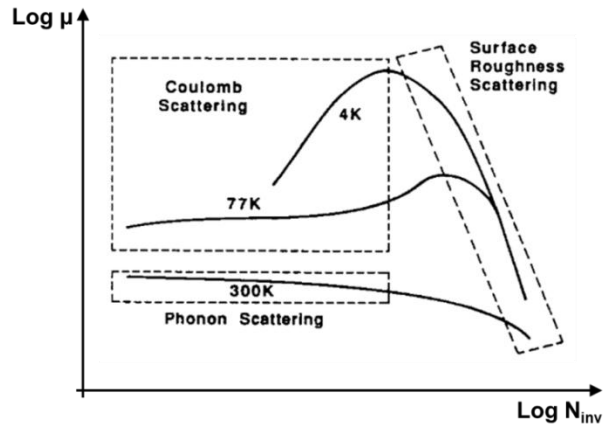


Figure II-21: Schematic of the channel mobility dependence on the inversion layer carrier density for various temperatures. The regions where a specific scattering mechanism is dominant are indicated in the boxes [29].

We have extracted the parameters (mobility, threshold voltage and subthreshold swing) with the Y-function method. The results in Figure II-22a and in Figure II-22b show the T-dependence of the low-field electron and hole mobility, respectively, in wafers with 88 and 40 nm film thickness. As theoretically predicted, carrier mobility increases as the temperature is lowered down to 100 K and then it decreases for  $T < 100$  K.

In order to reveal the contribution of the scattering effects on low-field mobility, we fit the experimental curves in Figure II-22a and in Figure II-22b with the theoretical  $\mu_0(T)$  curves deduced from the Matthiessen's rule for electrons and holes:

$$\frac{1}{\mu_0(T)} = \frac{1}{\mu_{Ph}(T)} + \frac{1}{\mu_C(T)} \quad (\text{II-28})$$

with:

$$\mu_{Ph}(T) = \mu_{0@300} \left( \frac{300}{T} \right)^{1.5} \quad \text{and} \quad \mu_C(T) = \alpha \mu_{0@77} \left( \frac{T}{77} \right)^{1.5} \quad (\text{II-29})$$

where  $\mu_{0@300}$  and  $\mu_{0@77}$  represent the extracted values of low-field mobility at 300 K and 77 K. For Coulomb mobility, we added 20 % for electrons ( $\alpha = 1.2$ ) and 50 % for holes ( $\alpha = 1.5$ ) to  $\mu_0$  values extracted at 77 K, in order to account for residual phonon scattering and to improve the fit. No other adjustable parameter was used for curves fitting.

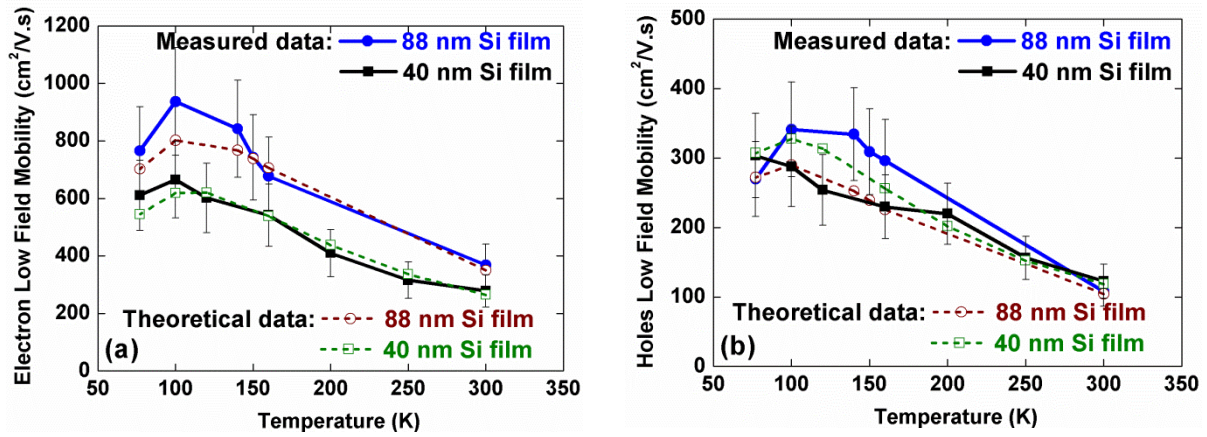


Figure II-22: Measured and theoretical low-field mobility for electrons (a) and holes (b) vs. temperature  $T$  for 88 nm and 40 nm Si film thickness. Experimental error bars are about 20 % (calculated from reproducibility measurements).

The theoretical curves deduced from equations ((II-28) & (II-29)) and the experimental curves in Figure II-22a merge together especially for high  $T$ . The slight difference, which subsists at very low temperature, stands within the limit of error bars for multiple tested samples. Similar behavior is obtained for the holes mobility (Figure II-22b). The actual fitting seems less precise due to less stable  $I_D$ - $V_G$  curves and higher series resistance  $R_{SD}$  for  $V_G < 0$ .

In order to further confirm more our results for  $T > 100$  K, we note that the mobility curves vary with  $T^{-n}$  where the value of  $n$  extracted from  $\mu(T)$  curves in *log-log* scale is between 1 and 2 for both 88 and 40 nm film thicknesses. That is in agreement with equation (II-25), meaning that phonon scattering mechanism dominates at high  $T$ . Let us remind that Coulomb scattering arises from interface traps ( $D_{it}$ ) at Si-SiO<sub>2</sub> interface or at the top surface because the film doping is very low. Therefore, the decrease of the mobility with increasing temperature shows that phonon scattering (and not Coulomb scattering) is responsible for mobility reduction in SOI wafer. This indirectly reflects the good quality of Si film and Si-SiO<sub>2</sub> interface.

### 3.4.2 Subthreshold swing and threshold voltage

The threshold voltage and subthreshold slope variations with temperature provide valuable informations about the density of defects at the top (film/native oxide) interface and film/BOX interface. We studied these variations and we concentrated on the electrons side, in order to avoid the higher  $R_{SD}$  impact that was visible on the holes side (see Figure II-18b).

The evolution of subthreshold swing ( $S$ ) with  $T$  is presented in Figure II-23 and compared with the theoretical values calculated using equation below:

$$S = 2.3 \frac{kT}{q} \left( 1 + \frac{C_{it1}}{C_{ox}} + \frac{C_{Si}C_{it2}}{C_{ox}(C_{Si} + C_{it2})} \right) \quad (\text{II-30})$$

where  $C_{Si}$  is the Si film capacitance and  $C_{it1,2} = qD_{it1,2}$  with  $D_{it1,2}$  the interface trap density at the top and film/BOX interfaces. The fitting values were  $D_{it1} = 6 \times 10^{11} \text{ cm}^{-2}\text{eV}^{-1}$  (good Si film/BOX interface) and  $D_{it2} = 2 \times 10^{13} \text{ cm}^{-2}\text{eV}^{-1}$  (typical value for a poor interface between Si film and native oxide), in agreement with the values used in [21] and [24]. The subthreshold swing is linearly dependent on temperature. The behavior of the measured curves is similar to the theoretical ones:  $S$  increases with  $T$  (Figure II-23). For confirmation, we have linearly interpolated the *log-log* curves and obtained variations of  $S \sim T^1$  in 88 nm and  $S \sim T^{0.6}$  in 40 nm Si film. This means that the predicted dependency with temperature is well followed for 88 nm and is less accurate for 40 nm film.

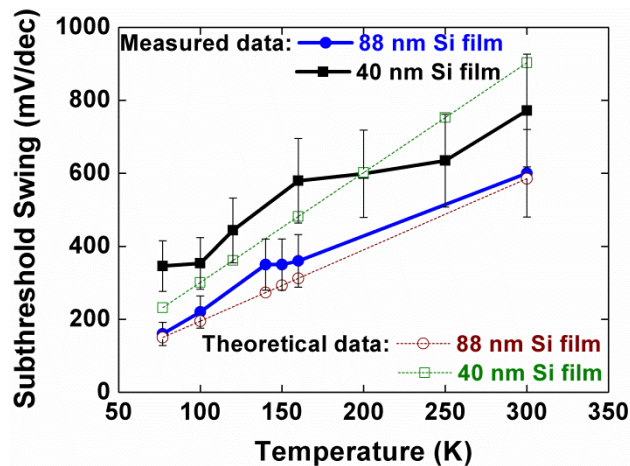


Figure II-23: Theoretical and measured subthreshold slope curves ( $S$ ) as a function of temperature  $T$  for 88 nm and 40 nm thick Si film. Experimental error bars are about 18 %.

The discrepancy is explained by electrostatic coupling effect. As documented earlier in sub-section 1.4, thinner films are more sensitive to the impact of top-surface defects due to a stronger coupling between the channel and the surface. If the Si film capacitance  $C_{Si}$  is small (*i.e.* thick film:  $C_{Si} \ll C_{it2}$ ), the influence of top surface defects is negligible in equation (II-30). On the contrary, in thinner films,  $C_{Si}$  and  $C_{it2}$ , are comparable so that  $D_{it2}$  becomes relevant. The sublinear dependence of swing on temperature is due to the increase in interface state density as the temperature is reduced and the Fermi level approaches the band edge where  $D_{it2}$  is higher [33].

Figure II-24 shows the threshold voltage ( $V_T$ ) variation with temperature. The theoretical curves were calculated using:

$$V_T = \phi_{fb} + 2\phi_F(T) \left( 1 + \frac{C_{it1}}{C_{ox}} + \frac{C_{Si}C_{it2}}{C_{ox}(C_{Si} + C_{it2})} \right) \quad (\text{II-31})$$

with:

$$\phi_F(T) = kT \left[ \log \left( \frac{N_A}{n_i(T)} \right) \right], n_i(T) = \sqrt{N_C(T)N_V(T)} e^{\left( \frac{-E_G(T)}{2kT} \right)}$$

$$\text{and} \begin{cases} E_G(T) = E_{G0} - \left( \frac{\alpha T^2}{\beta + T} \right) \\ N_C(T) = N_{C0} \left( \frac{T}{300} \right)^{3/2} \\ N_V(T) = N_{V0} \left( \frac{T}{300} \right)^{3/2} \end{cases} \quad (\text{II-32})$$

where  $E_{G0}$  is the energy gap at  $T = 0$  K ( $E_{G0} = 1.17$  eV),  $N_{C0}$  and  $N_{V0}$  are the effective density of states in the conduction band ( $N_{C0} = 1.133 \times 10^{19}$  cm $^{-3}$ ) or in the valence band ( $N_{V0} = 2.728 \times 10^{19}$  cm $^{-3}$ ) at  $T = 0$  K.  $\alpha$  and  $\beta$  are two constants ( $\alpha = 4.73 \times 10^{-4}$  eV/K $^3$  and  $\beta = 636$  K) [12]. The same values of  $D_{it1,2}$  were used for computing both  $V_T$  (T) (in Figure II-24) and  $S$  (T) (in Figure II-23) curves.

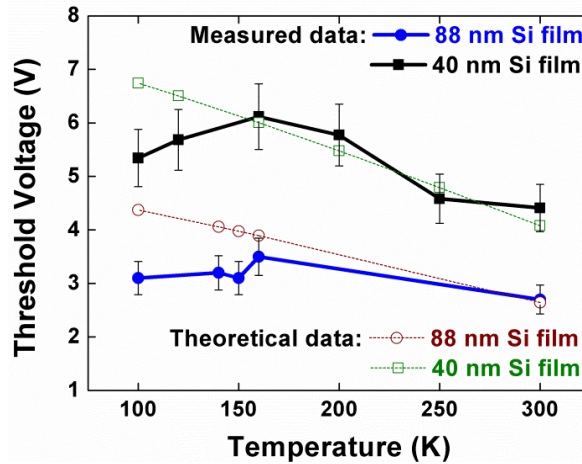


Figure II-24: Theoretical and measured threshold voltage curves ( $V_T$ ) as a function of temperature  $T$  for 88 nm and 40 nm thick Si film. Experimental error bars are about 10 %.

The experimental  $V_T$  (T) variation stands close to the theoretical prediction for  $T > 150$  K. The difference in behavior for the 40 nm and the 88 nm films, coming from the surface coupling, is well reproduced, which allows concluding that the  $\Psi$ -MOSFET measurements at low  $T$  are valid for reliable extractions of  $V_T$  and  $S$ .

We proved the extension of  $\Psi$ -MOSFET method to low temperature for SOI wafers. As theoretically expected, the drain current, transconductance peak and carrier mobility increase with decreasing temperature, whereas the subthreshold slope becomes more abrupt. The measured temperature dependence of holes and electrons mobility fits with the theoretical curves indicating a good Si-BOX interface quality.



## **Conclusion**

In this chapter II, we presented the  $\Psi$ -MOSFET technique, the characterization results of ultra and extra thin SOI wafers and the first extension to low-temperature measurements.

In section 1, the  $\Psi$ -MOSFET configuration was explained by a detailed methodology for the characterization of SOI wafers. The results shown are from measurements carried out on standard SOI substrates with 88 nm Si film and 145 nm BOX. The preparation of the samples and the set-up of the equipment were presented. Then, the extraction method of the electrical parameters was explained. Finally, the influence of the top interface and a revisited  $\Psi$ -MOSFET model for parameters extraction from the state of the art literature were discussed.

In section 2, we demonstrated for the first time the capability of exploring ultra and extra thin SOI wafers using the  $\Psi$ -MOSFET with pressure probes. The impact of the passivation of the top interface on the electrical behavior of SOI wafer was showed.

In section 3, we extended the characterization of SOI wafers to low-temperature measurements using  $\Psi$ -MOSFET principle. The feasibility of the measurements using cryogenic station was verified by achieving ohmic contacts. The drain current variation with temperature was examined by extracting the key parameters. The measured temperature dependence of holes and electrons mobility fits with the theoretical curves. For  $T > 100$  K, phonon scattering mechanism dominates and indicates a good quality of Si-BOX interface. The impact of the top interface defects on the swing and the threshold voltage is more prominent in thinner films and at lower temperature.

## References chapter II

- [1] S. Cristoloveanu and S. Williams, "Point-contact pseudo-MOSFET for in-situ characterization of as-grown silicon-on-insulator wafers," *Electron Device Letters, IEEE*, vol. 13, pp. 102-104, 1992.
- [2] S. Cristoloveanu and S. S. Li, *Electrical Characterization of Silicon-On-Insulator Materials and Devices*, Kluwer, Boston, 1995.
- [3] S. Cristoloveanu, D. Munteanu and M. S. T. Liu, "A review of the pseudo-MOS transistor in SOI wafers: operation, parameter extraction, and applications," *Electron Devices, IEEE Transactions on*, vol. 47, pp. 1018-1027, 2000.
- [4] Dieter K. Schroder, *Semiconductor material and device characterization (Third Edition)*, Wiley-Interscience, USA, 2006.
- [5] A. M. Ionescu, D. Munteanu, A. Chovet, A. Rusu and D. Steriu, "The intrinsic pseudo-MOSFET technique," in *Semiconductor Conference, 1997. CAS '97 Proceedings., 1997 International*, pp. 217-220 vol.211, 1997.
- [6] H. J. Hovel, "The HgFET: a new characterization tool for SOI silicon film properties," in *SOI Conference, 1997. Proceedings., 1997 IEEE International*, pp. 180-181, 1997.
- [7] Vadim Kushner, Jinman Yang, Joon Choi, Trevor Thornton and Dieter Schroder, "SOI Low Frequency Noise and Interface Trap Density Measurements with the Pseudo MOSFET," *ECS Transactions*, vol. 2, pp. pp. 491-502, 2006.
- [8] B. Jun, Y. V. White, R. D. Schrimpf, D. M. Fleetwood, F. Brunier, N. Bresson, S. Cristoloveanu and N. H. Tolc, "Characterization of multiple Si/SiO<sub>2</sub> interfaces in silicon-on-insulator materials via second-harmonic generation," *Applied Physics Letters*, vol. 85, pp. 3095-3097, 2004.
- [9] S. Cristoloveanu, T. V. C. Rao, Nguyen Quang Tuan, J. Antoszewski, H. Hovel, P. Gentil and L. Faraone, "The Corbino Pseudo-MOSFET on SOI: Measurements, Model, and Applications," *Electron Devices, IEEE Transactions on*, vol. 56, pp. 474-482, 2009.
- [10] I. Ionica, I. Savin, W. Van Den Daele, T. Nguyen, X. Mescot and S. Cristoloveanu, "Characterization of silicon-on-insulator films with pseudo-metal-oxide-semiconductor field-effect transistor: Correlation between contact pressure, crater morphology, and series resistance," *Applied Physics Letters*, vol. 94, pp. 012111-012113, 2009.
- [11] I. Ionica, A. El Hajj Diab, Y. H. Bae, X. Mescot, A. Ohata, F. Allibert and S. Cristoloveanu, "Advances in the pseudo-MOSFET characterization method," in *Semiconductor Conference (CAS), 2010 International*, pp. 45-51, 2010.
- [12] S. M. Sze, *Physics of Semiconductor Devices (Second Edition)*, Wiley press, New York, 1981.
- [13] K. Komiya, N. Bresson, Sato Shingo, S. Cristoloveanu and Y. Omura, "Detailed investigation of geometrical factor for pseudo-MOS transistor technique," *Electron Devices, IEEE Transactions on*, vol. 52, pp. 406-412, 2005.
- [14] Kazuo Terada, Katsuhiko Nishiyama and Kei-Ichi Hatanaka, "Comparison of MOSFET-threshold-voltage extraction methods," *Solid-State Electronics*, vol. 45, pp. 35-40, 2001.
- [15] Hao Chu, B. Cabon-Till, S. Cristoloveanu and G. Ghibaudo, "Experimental determination of short-channel MOSFET parameters," *Solid-State Electronics*, vol. 28, pp. 1025-1030, 1985.
- [16] G. Ghibaudo, "New method for the extraction of MOSFET parameters," *Electronics Letters*, vol. 24, pp. 543-545, 1988.
- [17] Hon-Sum Wong, Marvin H. White, Thomas J. Krutsick and Richard V. Booth, "Modeling of transconductance degradation and extraction of threshold voltage in thin oxide MOSFET's," *Solid-State Electronics*, vol. 30, pp. 953-968, 1987.
- [18] Q. Nguyen, "*Caractérisation et modélisation électrique de substrats SOI innovants*", Ph.D. dissertation, INPG, Grenoble, 2009.

- [19] N. Bresson and S. Cristoloveanu, "Innovating SOI films: impact of thickness and temperature," *Microelectronic Engineering*, vol. 72, pp. 357-361, 2004.
- [20] F. Allibert, N. Bresson, K. Bellatreche, C. Maunand-Tussot and S. Cristoloveanu, "Electrical characterization of ultra-thin SOI films: comparison of the pseudo-MOSFET and Hg-FET techniques," in *SOI Conference, 2005. Proceedings. 2005 IEEE International*, pp. 59-60, 2005.
- [21] G. Hamaide, F. Allibert, H. Hovel and S. Cristoloveanu, "Impact of free-surface passivation on silicon on insulator buried interface properties by pseudotransistor characterization," *Journal of Applied Physics*, vol. 101, pp. 114513-114516, 2007.
- [22] Lim Hyung-Kyu and J. G. Fossum, "Threshold voltage of thin-film Silicon-on-insulator (SOI) MOSFETs," *Electron Devices, IEEE Transactions on*, vol. 30, pp. 1244-1251, 1983.
- [23] H.J. Hovel, "Si film characterization in SOI substrates by the HgFET technique," *Solid State Electronics*, vol. 47, pp. 1311-1333, 2003.
- [24] N. Rodriguez, S. Cristoloveanu and F. Gamiz, "Revisited Pseudo-MOSFET Models for the Characterization of Ultrathin SOI Wafers," *Electron Devices, IEEE Transactions on*, vol. 56, pp. 1507-1515, 2009.
- [25] A. Diab, I. Ionica, S. Cristoloveanu, F. Allibert, Y. H. Bae, J. A. Chroboczek and G. Ghibaudo, "Static and low-frequency noise characterization of ultrathin SOI with very thin BOX in pseudo-MOSFET configuration," in *Semiconductor Device Research Symposium (ISDRS), 2011 International*, pp. 1-2, 2011.
- [26] Noel Rodriguez, Sorin Cristoloveanu, Mariazel Maqueda, Francisco Gámiz and Frederic Allibert, "Three-interface pseudo-MOSFET models for the characterization of SOI wafers with ultrathin film and BOX," *Microelectronic Engineering*, vol. 88, pp. 1236-1239, 2011.
- [27] A. Diab, L. Pirro, I. Ionica, X. Mescot, G. Ghibaudo and S. Cristoloveanu, "Low-temperature pseudo-metal-oxide-semiconductor field-effect transistor measurements on bare silicon-on-insulator wafers," *Applied Physics Letters*, vol. 101, pp. 092110-092114, 2012.
- [28] C. T. Sah, T. H. Ning and L. L. Tschoopp, "The scattering of electrons by surface oxide charges and by lattice vibrations at the silicon-silicon dioxide interface," *Surface Science*, vol. 32, pp. 561-575, 1972.
- [29] D. S. Jeon and D. E. Burk, "MOSFET electron inversion layer mobilities-a physically based semi-empirical model for a wide temperature range," *Electron Devices, IEEE Transactions on*, vol. 36, pp. 1456-1463, 1989.
- [30] Mark Lundstrom, *Fundamentals of carrier transport, second edition*, Cambridge University Press, UK, 2002.
- [31] Shin-Ichi Takagi, Judy L. Hoyt, Jeffrey J. Welser and James F. Gibbons, "Comparative study of phonon-limited mobility of two-dimensional electrons in strained and unstrained Si metal--oxide--semiconductor field-effect transistors," *Journal of Applied Physics*, vol. 80, pp. 1567-1577, 1996.
- [32] Frank Stern and W. E. Howard, "Properties of Semiconductor Surface Inversion Layers in the Electric Quantum Limit," *Physical Review*, vol. 163, pp. 816-835, 1967.
- [33] T. Elewa, F. Balestra, S. Cristoloveanu, I. M. Hafez, J. P. Colinge, A. J. Auberton-Herve and J. R. Davis, "Performance and physical mechanisms in SIMOX MOS transistors operated at very low temperature," *Electron Devices, IEEE Transactions on*, vol. 37, pp. 1007-1019, 1990.

## **Chapter III:**

### ***Novel developments of $\Psi$ -MOSFET method***

## **Introduction**

In chapter II, we explained the  $\Psi$ -MOSFET method and we extended it to ultra-thin films/buried oxides and to low-temperature measurements. The extraction of the electrical parameters using  $I_D$ - $V_G$  measurements is not always enough for advanced SOI structures, so the interest to implement advanced variants is very strong.

In this chapter, we will present two novel enrichments of the  $\Psi$ -MOSFET. In section 1, we prove for the first time that  $\Psi$ -MOSFET with pressure probes can be used for low-frequency noise measurements of as-fabricated SOI wafers. The experimental results will be presented and the interface states density extraction will be addressed. The impact of surface preparation on the noise level will be discussed.

In section 2, we present the proof of concept and systematic data documenting the applicability of split  $C$ - $V$  method in  $\Psi$ -MOSFET configuration. The experimental results of the  $C$ - $V$  measurements combined with the drain current curves allow obtaining the effective mobility as a function of the inversion/accumulation charge or effective field. The feasibility of this technique and extraction of the effective mobility are demonstrated on advanced SOI structures.

## **1. Low-frequency noise measurements on bare SOI wafers**

### **1.1 Why noise measurements?**

In the world of electronic devices, the noise indicates random fluctuations of current or voltage around an average value. If these fluctuations are not engendered by external disturbances then we talk about the “background noise” of devices. This means that the fluctuations in current are generated by sources of noise internal to the device. Noise has a huge impact on the electronics and analog circuits ([1], [2]) in particular in the nano-scale area.

By consequence, it is necessary to know the low-frequency noise (LFN) and its origin to be able to reduce it. Besides, with the transistor size shrinking, LFN impact increases dramatically which makes the study of the noise mandatory. The noise is sensitive to the technology, architecture, gate stacking, deposit and oxidation processes, channel type (N or P), materials, *etc.*

Moreover, the noise constitutes a powerful characterization tool. LFN measurements reveal the fluctuations of carrier mobility and concentration in the MOSFET channel as well as the oxide quality in terms of trap density. The physical models used to describe the fluctuation in current allow characterizing a certain technology in terms of low-frequency noise.

LFN technique has been widely applied to FD-SOI transistors [3], offering an insight into the trap density at the front and back interfaces, which is nowadays an important issue in ultra-thin FD devices. In our work, we studied for the first time the LFN on bare SOI wafers before any CMOS process in order to determine the dominant noise source and to qualify the Si/BOX and Si/air interfaces [4].

### **1.2 Overview of the electronic noise**

Before moving to LFN measurements in SOI wafers, let us remind the basic theory of the electronic noise, the different sources of noises and their analysis methods.

### 1.2.1 Fundamentals of noise

The electrical noise in electronic devices originates from the random behavior of free carriers as a function of time. Consequently, the usual parameters (*e.g.* current flowing in the device) which depend on carriers present fluctuations around their average values. The noise can have internal or external sources. For example, the “cross talk” between the adjacent circuits, the electrostatic or electromagnetic coupling between the DC or AC power supply lines, the vibrations and the light are external sources of noise. The disturbances resulting from these sources can be eliminated by filtering. On the other hand, the internal sources of noise are related to particular physical mechanisms. The internal noise cannot be eliminated, but it can be reduced by the improvement of manufacturing steps and architectures. We consider here only the internal sources of noise in devices.

The various sources of noise govern the electrical conductance ( $G$ ) fluctuations of devices and are thus accessible by the study of the current or the voltage. A nominal static electronic signal (voltage or current) is not microscopically stable but rather fluctuates around a fixed value. This fixed value is the mean value measured by a voltmeter or ampermeter and the small fluctuation for the same time period is the variance. In noise studies, it is the fluctuation or the variance of the parameters that is measured. These microscopic fluctuations cause the electronic noise.

The noise is always supposed to be a stationary random signal, *i.e.* it is independent with time. It is also supposed to be an ergodic signal, in other words any average of a group is equal to the temporal average. The temporal analysis of the fluctuations does not allow separating the various sources of noise because the amplitude of the current or the voltage fluctuations have generally a Gaussian distribution around the average value of the signal.

Noise analysis is commonly done using the Fourier transform which allows passing from the time domain into the frequency domain. In turn, the frequency analysis enables to identify the source of noise and to determine the physical characteristics relative to the noise signal. This analysis is possible through the measurement of the power spectral density (PSD or  $S(f)$ ) of the fluctuations, defined as the frequency distribution of the power of the noise signal.  $S(f)$  is just the Fourier transform of its autocorrelation function  $R(\tau)$  given by:

$$S(f) = \int_{-\infty}^{+\infty} R(\tau) e^{-i2\pi f\tau} d\tau \quad (\text{III-1})$$

PSD represents the signal power or energy per Hz, hence it indicates the signal power distribution with respect to frequency. The signal power equals to the dissipated energy on a  $1 \Omega$  resistive load, thus its unit is W/Hz. In real applications, the power is often denoted by the square of the real signal value either in voltage or in current, corresponding to the two forms of PSD:  $S_I$  and  $S_V$ . If the PSD is measured from a signal of drain current, the accordingly PSD is  $S_{I_d}$  with the unit of  $A^2/\text{Hz}$ . If the PSD is measured from a signal of gate voltage, the accordingly PSD is  $S_{V_g}$  with the unit of  $V^2/\text{Hz}$ . It should be noted that PSD is a function in frequency domain not in time domain.

In the next sub-section we describe the main types of electrical noise present in a MOS transistor and the associated models.

### 1.2.2 Different sources of noise in MOS transistor

As already said, we focus on the internal noise sources only. Any semiconductor-based device possesses a background noise. There are two different families of noise sources:

- **The fundamental noise called white noise:** intrinsic to semiconductor material and frequency independent (the sources are thermal and shot noise).
- **The excess noise:** this type of noise varies with the frequency and appears especially in the low frequency range ( $1/f$  noise, Lorentzian noise: Generation-Recombination and Random Telegraph Signal).

In the following, we present in a synthetic way these various sources of noise.

#### 1.2.2.1 White noise

**The thermal noise**, or Nyquist noise, results from the random thermal movement of the charge carriers in a material. It is independent of applied voltage and frequency, thus thermal noise is a white noise (*i.e.*, its PSD is constant over a large range of frequency, typically from few Hz to MHz). If the load is a resistance



with value of R and the noise is the current or the voltage drop measured on R, the thermal noise PSD reads:

$$S_I = \frac{4kT}{R} \text{ or } S_V = 4kTR \quad (\text{III-2})$$

**Shot noise:** this type of noise originates from the fact that the current flowing across a junction is not smooth and, as a result, the electrons pass through the junction independently and at random times. Such a non-uniform or quasi-discrete flow leads to broadband white noise, which becomes worse when increasing the current density. The associated PSD is:

$$S_I = 2qI \quad (\text{III-3})$$

#### 1.2.2.2 Excess noise

**Generation-recombination (G-R) noise:** in semiconductors, this noise results from the random trapping-release of carriers which causes fluctuations in the number of free carriers [5]. This trapping can provoke fluctuations in the mobility, in the height of the band gap, in the thickness of the space charge region, *etc.* The G-R takes place essentially in depleted regions, and is generally caused by traps located in the band gap of the semiconductor. The noise associated with a single trap presents a Lorentzian spectrum [6]:

$$S_N(f) = \frac{4\overline{\Delta N}^2 \tau}{1 + (2\pi f)^2 \tau^2} \quad (\text{III-4})$$

where  $\tau$  is the time constant characteristic (capture or emission) of the trap and  $\Delta N$  is the average fluctuation of carrier number. For low frequencies,  $f \ll 1/(2\pi\tau)$ , the noise spectrum presents a flat part, whereas for  $f \gg 1/(2\pi\tau)$  the noise spectrum decreases according to  $1/f^2$ .

A special case of G-R noise is the Random Telegraph noise Signal (RTS). It is generally related to the individual trapping of a single carrier at the Si/SiO<sub>2</sub> interface in MOS transistors. The traps can then capture or release carriers from or towards the channel. The RTS noise is characterized by random rectangular signals in the temporal domain. In the frequency domain, the S(f) spectrum is constituted by one or several Lorentzians (*i.e.*, a plateau followed by a slope of -2 in *log-log* scale), each of

them being characteristic of an individual active trap under the bias conditions of the structure.

Three parameters allow the description of the temporal signal: average time of capture  $\tau_c$  and of emission  $\tau_e$  (for acceptor-type) trap and the amplitude averages of the signal  $\Delta I$ . The PSD for each trap is then written [7] as:

$$S_1(f) = \frac{4A\tau\Delta I^2}{1 + \left(\frac{f}{f_c}\right)^2} \quad \text{with } A = \frac{\tau}{\tau_c + \tau_e} \quad \text{and } \tau = \frac{\tau_c\tau_e}{\tau_c + \tau_e} \quad (\text{III-5})$$

where  $f_c$  is the cutoff frequency and equals to  $1/2\pi\tau$ .

**Flicker or  $1/f$  noise:**  $1/f$  noise (Figure III-1) generally dominates the overall noise spectrum for the drain current at low frequencies; it is often called flicker noise since it was observed from a flat current. The name  $1/f$  results from the fact that its spectrum varies with frequency as  $1/f^\alpha$ , where the exponent  $\alpha$  is very close to unity ( $\alpha = 1 \pm 0.2$ ). This type of noise is associated with conductivity fluctuations in the channel [8]. The conductance fluctuations of  $1/f$  type were observed, such as in all semiconductors, in electronic devices and almost in all conductive materials.

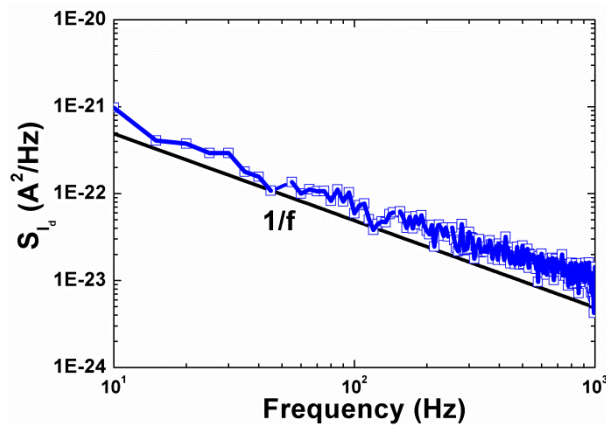


Figure III-1: Example of  $1/f$  spectrum in the frequency domain. Sample: bare SOI.

The definition of the electric conductance of a material is given by [9]:

$$G = \frac{qn\mu S}{L} \quad (\text{III-6})$$

where  $\mu$ ,  $n$ ,  $S$  and  $L$  are respectively the mobility, the density of free carriers, the surface and the length of the material under consideration.

Up to now, there is no universal explanation for the origin of  $1/f$  noise. Two theories have been developed for  $1/f$  noise in microelectronic devices. According to

equation (III-6), G fluctuation can either be due to the carrier number fluctuation  $\Delta n$  (model proposed by McWhorter [10]) or to the mobility fluctuation  $\Delta\mu$  (model proposed by Hooge [11]). These two sources can be simultaneously present, even if one will be dominant [8]. Let us give some details about the two models.

**Carrier number fluctuation (CNF) model:**

McWhorter proposed that the drain current fluctuation is due to the fluctuation of the mobile charge number in the channel near the semiconductor/oxide interface [10].  $\Delta n$  results from the dynamic charge capture/release by the slow traps distributed in the oxide. It is possible to characterize every trap by a time constant dependent on its energy and on its position in the oxide.

The capture of the free carriers in the traps located in the oxide causes a change of the oxide charge ( $Q_{ox}$ ). This modification of the trapped charge in the oxide ( $\delta Q_{ox}$ ) is associated with a change of  $V_{FB}$  [12]. Furthermore, the fluctuation in the inversion charge ( $\delta Q_{inv}$ ) and the oxide charge ( $\delta Q_{ox}$ ) (or the flat-band fluctuations  $\delta V_{FB}$ ) are related by the equation of the gate charge conservation [12].

The fluctuation in the inversion charge, *i.e.* of the number of free carriers ( $\Delta n$ ), entails that of the drain current. In addition, a variation of  $Q_{ox}$  due to the trapping/de-trapping of a free carrier may also lead to a variation in the effective mobility ( $\delta\mu_{eff}$ ), resulting again in drain current fluctuation. According to Ghibaudo *et al*, both possible fluctuations can be combined as [8]:

$$\delta I_D = \delta V_{FB} \left. \frac{\partial I_D}{\partial V_{FB}} \right|_{\mu_{eff}=\text{const}} + \delta\mu_{eff} \left. \frac{\partial I_D}{\partial \mu_{eff}} \right|_{V_{FB}=\text{const}} = -g_m \frac{\delta Q_{ox}}{C_{ox}} \pm \alpha \mu_{eff} I_D \delta Q_{ox} \quad (\text{III-7})$$

where  $\alpha$  is the Coulomb diffusion coefficient ( $\approx 10^4$  Vs/C) [13]. The  $\pm$  sign of the mobility is chosen either negative for acceptor-like traps or positive for donor-like traps.  $\delta V_{FB}$  is the fluctuation of the flat-band voltage:  $\delta V_{FB} = -\delta Q_{ox}/C_{ox}$ . Therefore, the normalized PSD is written as ([8], [12]):

$$\frac{S_{I_d}(f)}{I_D^2} = \frac{g_m^2}{I_D^2} S_{V_g} \quad \text{with} \quad S_{V_g} = \left( 1 \pm \alpha \mu_{eff} C_{ox} \frac{I_D}{g_m} \right)^2 S_{V_{fb}} \quad (\text{III-8})$$

where  $S_{V_g}$  and  $S_{V_{fb}}$  are respectively the gate voltage and flat-band voltage power spectral densities. Here  $S_{V_{fb}} = S_{Q_{ox}}/(C_{ox})^2$  and  $S_{Q_{ox}}$  is the spectral density of the

fluctuation of the oxide charge. From the second part of equation (III-8), it is clear that if  $\alpha \approx 0$ , *i.e.*, mobility is not sensitive to the trapped charges, thus  $S_{V_g} \approx S_{V_{fb}}$ . By consequence, only the  $(g_m/I_D)^2 S_{V_{fb}}$  subsists in equation (III-8) and the normalized power spectral density  $(S_{I_d}/I_D^2)$  essentially varies as  $(g_m/I_D)^2$ . Note that the formulas in equation (III-8) are valid at low and high  $I_D$ .

In general,  $S_{Q_{ox}}$  depends on the physical mechanism of charge trapping by the slow traps in the oxide. In the case of a *tunneling* process, the trapping probability decreases exponentially with the depth of traps in the oxide, so  $S_{V_{fb}}$  is [14]:

$$S_{V_{fb}} = \frac{q^2 k T \lambda N_t}{W L C_{ox}^2 f^\gamma} \quad (III-9)$$

where  $f$  is the frequency,  $\gamma$  is the characteristic exponent which is close to the unity,  $\lambda$  is the tunnel attenuation distance ( $\approx 0.1$  nm for a Si/SiO<sub>2</sub> interface) and  $N_t$  is the volume density of slow traps (or border traps) in the oxide near the Fermi level.

In the case of *trapping* process, the trapping probability decreases exponentially with the cross section activation energy  $E_a$ , and  $S_{V_{fb}}$  reads [15]:

$$S_{V_{fb}} = \frac{q^2 k^2 T^2 N_{it}}{W L C_{ox}^2 f^\gamma \Delta E_a} \quad (III-10)$$

where  $\Delta E_a$  is the amplitude of the activation energy dispersion,  $N_{it}$  is the surface trap density in the oxide.

Note that in the case of thermally activated mechanism,  $S_{V_{fb}}$  depends more strongly on temperature for *trapping* process ( $\sim T^2$ ) than for *tunneling* process ( $\sim T$ ).

### ***Hooge mobility fluctuation (HMF) model:***

Hooge attributes the conductance fluctuations to fluctuations in mobility. He stated that the  $1/f$  noise of the drain current is a volume phenomenon due to carrier mobility fluctuations resulting from the phonon scattering [11].

In this case, the flicker noise amplitude is inversely proportional to the total carrier number in the device. The normalized PSD of  $I_D$  in linear regime (*i.e.* in the presence of an uniform channel) is [8]:

$$\frac{S_{I_d}(f)}{I_D^2} = \frac{q\alpha_H}{W L f Q_{inv}} \quad \text{with} \quad S_{V_g} = \frac{S_{I_d}(f)}{I_D^2} \frac{I_D^2}{g_m^2} = \frac{q\alpha_H}{W L f Q_{inv}} \frac{I_D^2}{g_m^2} \quad (\text{III-11})$$

where  $\alpha_H$  is the Hooge parameter, an empirical constant of  $\sim 10^{-5}$  for classical silicon MOSFETs and  $Q_{inv}$  is the inversion charge. If the transistor operates in strong inversion and linear regime,  $Q_{inv} = C_{ox}(V_G - V_{T,FB})$ . Using equation (II-3) of the drain current, equation (III-11) can be written as:

$$\frac{S_{I_d}(f)}{I_D^2} = \frac{q\alpha_H \mu_{eff} V_D}{L^2 f I_D} \quad (\text{III-12})$$

Therefore, Hooge model is identified from equation (III-12) by a dependence  $S_{I_d}/I_D^2 \propto 1/I_D$ .

Once the observed LF noise shows  $1/f$  type spectrum, the diagnostic of LFN sources can be conducted. Because there are two competing theories to explain the LF noise in transistors, it is necessary to distinguish which one is dominant, CNF model or HMF model. First, the normalized  $S_{I_d}/I_D^2$  for a fixed frequency is plotted with respect to  $I_D$  in  $\log$ - $\log$  scale (see Figure III-2). Then, the variation of  $S_{I_d}/I_D^2$  versus  $I_D$  is compared with the shape of the  $(g_m/I_D)^2$  versus  $I_D$  curve (taken from experimental results) by adjusting a constant factor [16]. If the two curves can be superposed, one can conclude that the CNF model dominates and that the adjusting factor yields the trap density according to equation (III-9).

On the other hand, if  $S_{I_d}/I_D^2$  varies inversely with the drain current from weak inversion to strong inversion, it indicates that the Hooge mobility fluctuations are responsible for the observed  $1/f$  noise.

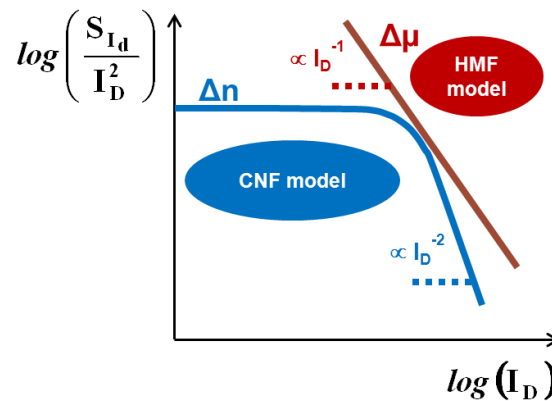


Figure III-2: Schematic representation of the variation of PSD normalized by the square of drain current versus drain current for CNF or HMF  $1/f$  noise models.

### 1.3 LFN on SOI wafers

The  $\Psi$ -MOSFET technique has been successfully used to characterize SOI wafers and to extract  $D_{it}$  from static  $I_D$ - $V_G$  curves using the equation of subthreshold swing:

$$S = 2.3 \frac{kT}{q} \left( 1 + \frac{C_{Si} + qD_{it}}{C_{ox}} \right) \quad (\text{III-13})$$

If we characterize thick SOI films (*i.e.* low  $C_{Si}$ ), the term between brackets ( $C_{Si} + qD_{it}$ ) in equation (III-13) allows extracting  $D_{it}$ , if  $qD_{it}$  is comparable (or higher) with  $C_{Si}$ . However, in ultra-thin films (*i.e.*  $C_{Si} \gg qD_{it}$ ), the  $qD_{it}$  term is negligible and by consequence the resolution is lost.  $1/f$  noise could be useful for  $D_{it}$  extraction in ultra-thin SOI wafers, as it shows, a better sensitivity in qualifying Si-SiO<sub>2</sub> or Si/air interfaces.

Schroder's group already performed LFN measurements on SOI wafers but with evaporated metal contacts ([17], [18]). First, they used permanent-contact  $\Psi$ -MOSFETs with a ground-signal-ground (GSG) geometry and they were able to measure the PSD and to extract the interface trap densities [17]. In [18], they have adopted a circular geometry of concentric rings to study the LFN and to extract  $D_{it}$  which has the advantage, compared to GSG contacts, of perfectly defined the transistor geometry (W/L). But the main inconvenient of this technique comes from the use of Schottky contacts to the Si film.

We performed noise measurements at wafer level using the standard  $\Psi$ -MOSFET configuration ([4], [19]). The interest of our work comes from the use of pressure probes to directly carry out LFN measurements on as-fabricated SOI wafers, which requires no contact processing and ensures ohmic contacts. Therefore, the density of traps can be determined directly at the film-BOX interface, before transistors fabrication or any device processing.

#### 1.3.1 LFN in $\Psi$ -MOSFET: experimental set-up

Before showing results of LFN in  $\Psi$ -MOSFET, let us present the equipment used: a system 3PNMS (Programmable Point Probe Noise Measuring System) from Synergy Concepts (Meylan-France). Figure III-3 shows the manual or automatic

bench of measurement [20]. This system allows to obtain the static (DC) and dynamic (AC) data (*i.e.*, noise) simultaneously. The heart of the system consists of a Programmable Biasing Amplifier (PBA) which has two tri-axial inputs (Input1 and Input2) to bias the gate and the drain and an output for a current-voltage converter to measure the drain current noise.

In MOSFETs LF noise measurements, we need two inputs for source and drain: the Input1 is divided in two outputs with a tri-axial separator. These two outputs are connected to the  $\Psi$ -MOSFET station to form source and drain, while Input2 is directly related to the chuck in order to bias the gate. A voltage power supply is used to ensure static polarization of the system where the maximum gate voltage that can be applied is 5 V. In some specific cases a battery is connected in series with this supply in order to apply higher gate voltage and to make manual measurement for  $V_G > 5$  V.

The outputs ( $V_{ACout}$ ) and ( $V_{DCout}$ ) are connected to a spectrum analyzer which is in fact a National Instrument PC card managed *via* the PC by the software called NOISYS. After connecting the gate, source and drain of the  $\Psi$ -MOSFET to the inputs, the software NOISYS takes care of adjusting automatically the biasing of the drain and the gate, as well as the gain of the current-voltage converter. Finally, the  $\Psi$ -MOSFET station is isolated from the outside in a dark box in order to eliminate the external noise and to obtain better isolation of the system.

From the control windows of the software, we can set the experimental parameters: the voltage range of the gate, the number of measurements, the drain bias and the parameters for the noise measurement: maximum frequency, average (number of chronograms in a train) and number of points.

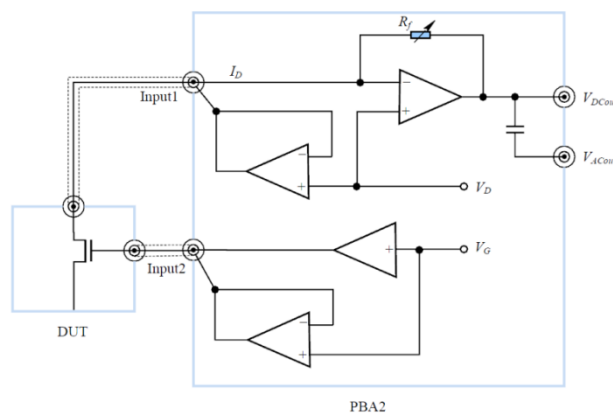


Figure III-3: Schematic representation of the 3PNMS system [20].

An important advantage of this equipment is the wide range of current for which we can measure the noise: from  $10^{-9}$  to  $10^{-2}$  A, that is seven decades of current. The possibility of detecting low current values allows subthreshold noise measurement in MOSFETs. In addition, as shown in Figure III-3, a programmable amplifier can be obtained for variable gain by adjusting the feedback resistance  $R_f$ . The Input1 current of DUT (Device Under Test) is measured; here, it is the drain current of a tested transistor configuration (FET mode is used for  $\Psi$ -MOSFET). After fast Fourier transform, the PSD of the measured signal ( $S_{I_d}$  here) is obtained.

In our study, the PSD is mainly the sum of two noise sources: the excess noise of the drain current and the total noise of the measurement system (including the thermal noise). This total noise of the system is removed by the corrections made before each PSD measurement. In addition, the average values of this noise are subtracted from  $S_{I_d}$  curves. Furthermore, in  $\Psi$ -MOSFET configuration we can neglect the shot noise because no junctions are formed during the penetration of the pressure probes into the silicon film (ohmic contacts).

Note that  $I_D$ - $V_G$  curves can also be measured using this noise system but we prefer for more accuracy to carry out static measurements using a HP-4156 before each noise measurement. Several SOI samples were characterized and the results are presented in the following sub-sections.

### 1.3.2 Experimental results

#### 1.3.2.1 $1/f$ noise behavior

The first step in these measurements is to verify that our new LFN technique using  $\Psi$ -MOSFET with pressure probes leads to exploitable results. Figure III-4a shows the power spectral density,  $S_{I_d}$ , plotted *versus* frequency for a SOI wafer with 88 nm thick Si film and 145 nm BOX for various back-gate voltages. The  $1/f$  (flicker noise) behavior is clearly visible. To verify if this behavior is valid for ultra-thin SOI films, we traced  $S_{I_d}$  *versus* frequency for various  $V_G$  in SOI with 12 nm Si film and 145 nm BOX thicknesses (Figure III-4b). Same type of noise (flicker noise) is found. All the measurements are carried out at low drain voltage ensuring linear mode operation.



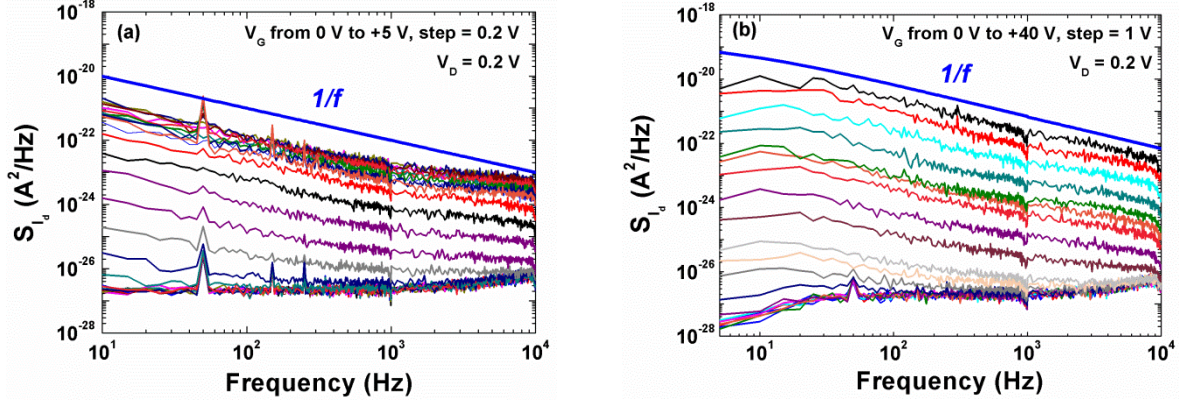


Figure III-4: PSD versus frequency in  $\Psi$ -MOSFET: (a) 88 nm thick Si film and (b) 12 nm ultra-thin Si film with 145 nm BOX.  $1/f$  noise is clearly evidenced in both SOI films.

The results in Figure III-4 prove the possibility to extend the  $\Psi$ -MOSFET capabilities to LFN measurements.  $1/f$  noise type is obtained in either relatively thick or ultra-thin SOI layers. In very thin films (12 nm) the impact of the top free surface on the noise of the remote buried channel (at film-BOX interface) is more significant than in thicker films (88 nm). This is why the noise level is higher in Figure III-4b. Note that the curves in Figure III-4b are obtained by manual measurements using a battery in series with the power supply in order to achieve 40 V as gate bias.

### 1.3.2.2 Noise model: CNF or HMF?

Let us remind that  $1/f$  noise is associated with conductivity fluctuations in the channel and that two phenomena could be responsible for these fluctuations: the carrier number fluctuations (CNF) or the Hooge mobility fluctuations (HMF). In order to determine which of the two models better accounts for the LFN data, it is required to plot a normalized PSD as a function of the drain current in  $\log$ - $\log$  scale as explained in sub-section 1.2.2.2. In the mobility fluctuations model one expects to obtain a linear decrease of  $\log(S_{I_d}/I_D^2)$  with  $\log(I_D)$ . In the CNF, the normalized PSD follows the  $(g_m/I_D)^2$  dependence: a flat part in weak inversion and a  $(I_D)^{-2}$  dependence for the strong inversion regime.

Figure III-5 shows that the normalized PSD follows  $(g_m/I_D)^2$  dependence corroborating the CNF model. In Figure III-5a, the normalized PSD as a function of  $I_D$  shows a plateau in weak inversion and a linear decrease in strong inversion, as it is proportional to a constant  $\times (g_m/I_D)^2$ . For further confirmation of our results, we show

in Figure III-5b the normalized PSD multiplied by frequency plotted *versus*  $I_D$  at different extrapolated frequencies ( $f_{\text{ext}}$ ) equal to 10, 20 and 30 Hz.

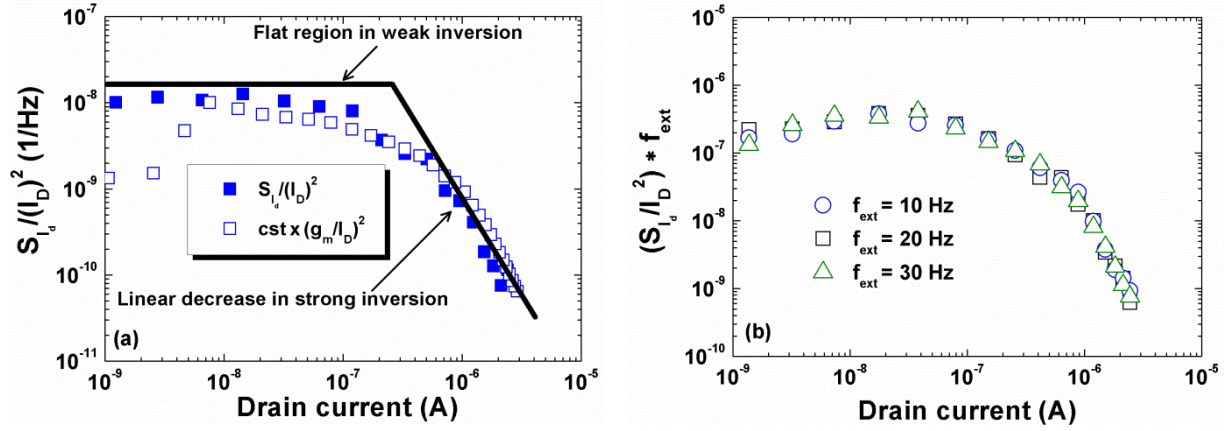


Figure III-5: (a) Normalized PSD and  $\text{cst} \times (g_m/I_D)^2$  versus  $I_D$  (with  $\text{cst} \approx 10^{-9}$  and  $p = 50$  g). (b) Normalized PSD noise multiplied by frequency versus  $I_D$  ( $p = 70$  g) for various frequencies. 88 nm Si film and 145 nm BOX thicknesses.

The curves are superposed. The frequency-independent curve confirms correctness of the CNF model of  $1/f$  noise in thick films. Therefore, the extraction of the  $D_{\text{it}}$  should be possible; we will discuss the method and the values obtained in subsection 1.3.2.4.

### 1.3.2.3 Probe pressure impact on LFN

Before discussing the quantitative results, an important issue is related to the impact of the probe pressure. As already mentioned in chapter II, the transport properties of the  $\Psi$ -MOSFET may depend on the probe pressure. It is well known, that the probe pressure controls the series resistance ( $R_{\text{SD}}$  decrease at higher pressures [21]).

Figure III-6 shows the normalized PSD *versus* drain current on the 88 nm thick film for different pressures applied on the probes. The noise level is almost pressure-independent, even though the series resistance of the device varies. This result proves that the series resistance does not act as an additional noise source or, at least, does not play the dominant role as a noise source in this configuration.

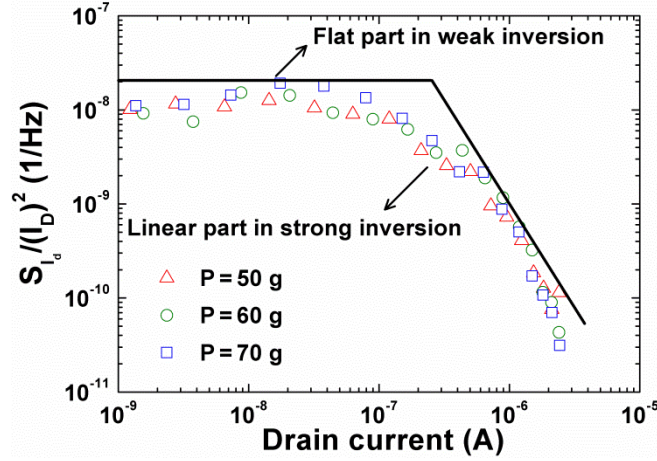


Figure III-6: Normalized power spectral density noise versus drain current in  $\Psi$ -MOSFET with 88 nm film thickness for various probe pressures (50 g, 60 g and 70 g).

#### 1.3.2.4 $D_{it}$ extraction

Our results demonstrate the feasibility of LFN measurements and also that the key mechanism responsible for this noise in 88 nm thick films is the carrier trapping by shallow traps located in the BOX. These results allow us to obtain the  $D_{it}$  value using the equations below:

$$\frac{S_{I_d}(f)}{I_D^2} = \left(1 \pm \alpha \mu_{\text{eff}} C_{\text{ox}} \frac{I_D}{g_m}\right)^2 \frac{g_m^2}{I_D^2} S_{V_{fb}} \quad \text{with} \quad S_{V_{fb}} = \frac{q^2 k T \lambda N_t}{W L C_{\text{ox}}^2 f \gamma} \quad (\text{III-14})$$

We briefly explain the extraction method before we show the obtained values. The variation of the normalized PSD obtained in strong inversion follows  $(I_D)^{-2}$ , this means that there is no mobility correlation with CNF model. Therefore,  $\alpha \approx 0$  and equation (III-14) becomes:

$$\frac{S_{I_d}(f)}{I_D^2} = \frac{g_m^2}{I_D^2} S_{V_{fb}} \quad \text{with} \quad S_{V_{fb}} = \frac{q^2 k T \lambda N_t}{W L C_{\text{ox}}^2 f \gamma} \quad (\text{III-15})$$

First, we extrapolate the  $S_{V_{fb}}$  value by fitting the two curves  $S_{I_d}/I_D^2$  and  $(g_m/I_D)^2$ . Note that the  $(g_m/I_D)^2$  curve is obtained from static measurements and  $S_{I_d}$  represents the values of the PSD for all the  $V_G$  range chosen at the same frequency ( $f$ ). Then, we replace this value and the values of  $q$ ,  $\gamma$ ,  $k$ ,  $T$ ,  $C_{\text{ox}}$  and  $f$  in the second part of equation (III-15). We still have to determine two terms ( $W$  and  $L$ ) in order to extract  $N_t$ . In  $\Psi$ -MOSFET,  $L$  can be interpreted as the space distance between source and drain probes ( $= 1$  mm) but the value of  $W$  (width of the inversion or accumulation

layer in the Si film) is unknown. There is no gate to define the inversion or accumulation area compared to MOSFET transistors.

We tried to solve this problem by using the geometrical factor ( $f_g = W/L \approx 0.75$ ).  $L$  is equal to 1 mm therefore  $W$  is equal to  $f_g$  multiplied by  $L$  (i.e.,  $W = 0.75$  mm). Finally, we extract the Si-SiO<sub>2</sub> interface traps density value from the relation  $D_{it} = \lambda \times N_t$  where  $\lambda$  is equal to 0.1 nm. However, the  $D_{it}$  values ( $\approx 10^{13-14}$  cm<sup>-2</sup>.eV<sup>-1</sup>) obtained from the LFN data are 2-3 orders of magnitude higher than those extracted from the static measurements ( $D_{it} \approx 10^{10-11}$  cm<sup>-2</sup>.eV<sup>-1</sup>). Two arguments can be offered to explain these high  $D_{it}$  values.

First, may be underestimated by  $W \times L$  value. The channel charge controlled by the substrate bias occupies a larger surface, beyond the area defined by the contacts.

The second explanation lies on the idea that the extra-noise might be generated at the free wafer surface (Si/air interface). Since the film is fully depleted, there is a direct electrostatic coupling between the surface and the buried channel. In general and as shown in chapter II, the quality of the free surface influences the transport and thus the LFN of the channel. In the following we will see the impact of this top interface on LFN results in SOI wafers.

#### 1.3.2.5 Impact of the surface preparation on LFN

We investigated the influence of the top free-surface quality on LFN by comparing passivated and non-passivated samples. Let us remind that the non-passivated wafers are covered by native oxide forming a very poor interface with the Si film whereas the passivation step (thermal oxidation) is known to decrease the density of interface states at the free surface.

In static  $I_D$ - $V_G$   $\Psi$ -MOSFET measurements, the surface passivation leads to improvement of mobility, subthreshold swing and threshold voltage, as documented in chapter II. In LFN, the variation of the surface states density is expected to affect the measurements, because these states act as trapping centers also inducing carrier number fluctuations in the device channel *via* electrostatic interface coupling. The noise level should be lower in passivated samples.

That issue was studied on thin Si films where the channel-surface coupling is strong. We plotted in Figure III-7a the PSD *versus* frequency before and after passivation for 12 nm ultra-thin film and 145 nm BOX, measured at the same drain current ( $I_D = 10^{-6}$  A) for the same probe pressure. The passivation does not alter the  $1/f$  noise behavior. However, contrary to our expectations, a higher level of noise is measured in the passivated sample with 12 nm thick film.

The question is whether the film thickness may cause this difference in noise level between passivated and non-passivated samples.

In order to explore further this question, we examined in Figure III-7b the PSD *versus* frequency plots for 88 nm film and 145 nm BOX before and after passivation, measured at the same drain current ( $I_D = 3 \times 10^{-6}$  A). A higher noise level is again observed on passivated wafers. The variation of film thickness for passivated samples does not account for the difference between the levels of noise in samples with and without surface treatments.

The surprising difference in noise level may be explained by change in series resistance.  $R_{SD}$  value in passivated samples (*e.g.*,  $R_{SD} \approx 26$  K $\Omega$  in 12 nm Si film) is one order of magnitude higher than in non-passivated samples (*e.g.*,  $R_{SD} \approx 2.8$  K $\Omega$  in 12 nm Si film). The series resistance values are extracted from  $I_D$ - $V_G$  curves using equation (II-13). In passivated samples, the pressure probes must penetrate first the oxide passivation layer (between 4 and 10 nm thickness) and then the Si film which induces additional access resistance compared to non-passivated samples. Systematic measurements on additional SOI wafers are needed to fully confirm this scenario.

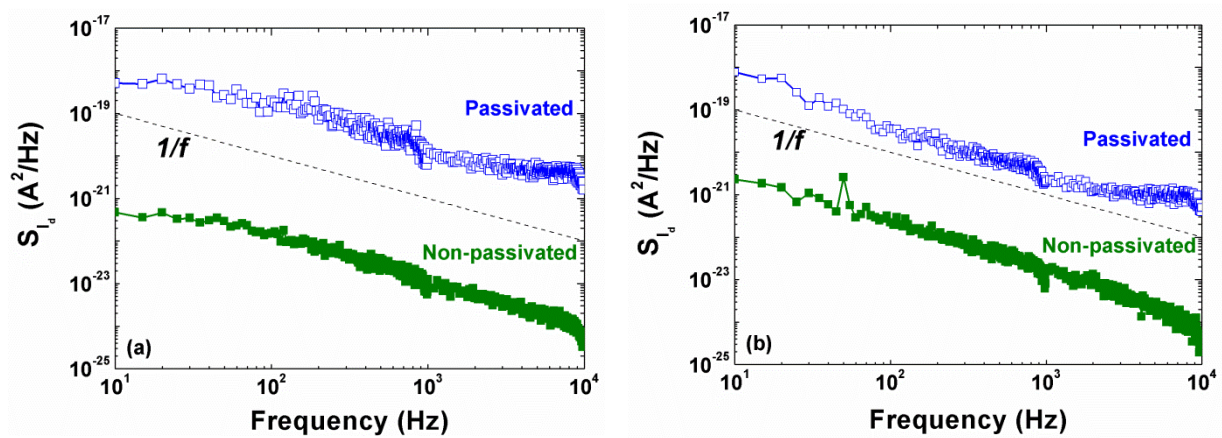


Figure III-7: Power spectral density versus frequency at  $V_D = 0.2$  V in: (a) 12 nm thick film for passivated and non-passivated surface at the same  $I_D = 10^{-6}$  A and probe pressure and (b) in 88 nm thick film for passivated and non-passivated surface at  $I_D = 3 \times 10^{-6}$  A. Box thickness is 145 nm.

### 1.3.2.6 Feasibility of LFN on extra-thin SOI structures

In chapter II, we confirmed the adaptability of  $\Psi$ -MOSFET technique to extra-thin SOI structures (*e.g.*, 20 nm film and 10 nm BOX) for  $I_D$ - $V_G$  measurements. Let us also prove here the feasibility of LFN characterization on these films. The low-frequency noise is of  $1/f$  type (Figure III-8a) for various  $V_G$ , which confirms the same behavior as in the thicker SOI structures shown previously.

We traced in Figure III-8b the normalized PSD *versus* frequency for the SOI wafer with 20 nm film and 10 nm BOX thickness. The clean noise signature ('plateau' in weak inversion and rapid decrease in strong inversion) indicates that CNF model is responsible for the LFN in such SOI structures.

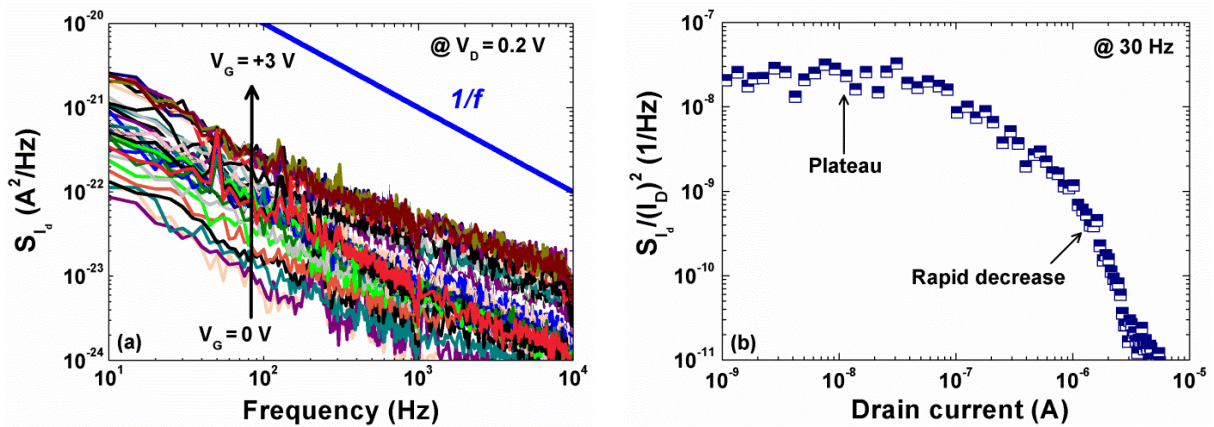


Figure III-8: Power spectral density versus frequency for various gate voltages, (b) normalized power spectral density versus drain current. 20 nm film and 10 nm BOX thicknesses.

While the results in Figure III-8 open the road for noise-based characterization of SOI wafers, the  $D_{it}$  extraction still demands an accurate evaluation of the  $(W \times L)$  term and of the contribution of the free surface traps.

## 1.4 Conclusion of section 1

The results above proved for the first time the feasibility of LFN measurements at wafer level using the  $\Psi$ -MOSFET configuration with pressure probes.  $1/f$  noise behavior in relatively thick and ultra-thin SOI layers is obtained. CNF model accounts best for the  $1/f$  noise. A technique to extract the interface traps density from noise measurements is possible. Unfortunately, the estimation of the actual geometrical factor  $W \times L$  is a real challenge for  $D_{it}$  extraction.

No probe pressure dependence of the noise is observed at least in non-passivated samples. The influence of wafer surface preparation and the sources of noise need further clarification. The quantitative separation of the impact of free surface traps and BOX traps on noise level is a challenging issue. Comparing samples with and without HF treatment could bring additional information for the better understanding of the top surface influence on LFN.

Finally, we demonstrated the capability of exploring very thin as-grown SOI films, down to 20 nm, and BOX layers down to 10 nm, using the  $\Psi$ -MOSFET by combining current, transconductance and noise measurements.

## 2. Split C-V measurement in $\Psi$ -MOSFET configuration

### 2.1 Split C-V technique and principle

The most common method used to measure the effective mobility ( $\mu_{\text{eff}}$ ) is the split C-V technique. The effective mobility is a key parameter that characterizes the electrical transport in MOSFETs. Split C-V method is based on two capacitive measurements and a current-voltage measurement in order to obtain the variation of the effective mobility with the effective electric field ( $E_{\text{eff}}$ ). This technique was first developed for the characterization of the interface trap density and the substrate doping concentration in silicon MOSFETs [22]. Afterwards it was applied to the effective mobility analysis [23]. Nowadays, it is commonly used to compare the impact of the technological parameters on the effective mobility [24].

In a split C-V method, the capacitance between the gate and source-drain (denoted as  $C_{\text{gc}}$ ) and the capacitance between the gate and the substrate (denoted as  $C_{\text{gb}}$ ) are measured, as shown in Figure III-9.

At high frequency, we carry out a measurement of the gate-to-channel capacitance that reflects the variation of the inversion charge with the gate voltage. Figure III-9a illustrates how to measure the  $C_{\text{gc}}$ : the gate is connected to the high potential, the source and the drain are together connected to the low potential and the substrate is grounded. In this configuration, the capacitive response of the inversion channel of carriers is measured. In strong inversion the capacitance tends to saturate to the effective value of the oxide capacitance ( $C_{\text{oxeff}}$ ) [25].

The second step is the measurement of the gate-to-bulk capacitance. This time, the source and the drain are grounded and it is the bulk which is connected to low potential, the gate being always at high potential (see Figure III-9b). In this configuration, the capacitive response is no longer given by the inversion channel but it is related to the charge variation in the depleted area (which is gate controlled).

The inversion and the depletion charges are obtained by the integration of the  $C_{\text{gc}}$  and  $C_{\text{gb}}$  capacitance curves:

$$Q_{\text{inv}}(V_G) = \int_{V_{\text{acc}}}^{V_G} C_{\text{gc}}(u) du \quad \text{and} \quad Q_{\text{dep}}(V_G) = \int_{V_{\text{FB}}}^{V_G} C_{\text{gb}}(u) du \quad (\text{III-16})$$



where  $V_{acc}$  is the gate voltage taken in accumulation.

Let us note that for FD-SOI transistors, the depletion charge ( $Q_{dep}$ ) can be neglected compared to  $Q_{inv}$ , which simplifies the procedure of the  $\mu_{eff}$  extraction.

Finally, the effective mobility is calculated by using the measured values of the drain current in ohmic regime:

$$\mu_{eff} = \frac{LI_D}{WQ_{inv}V_D} \quad (III-17)$$

In the following sub-sections we will extend the split  $C-V$  technique for  $\Psi$ -MOSFET in thick and thin SOI wafers [26].

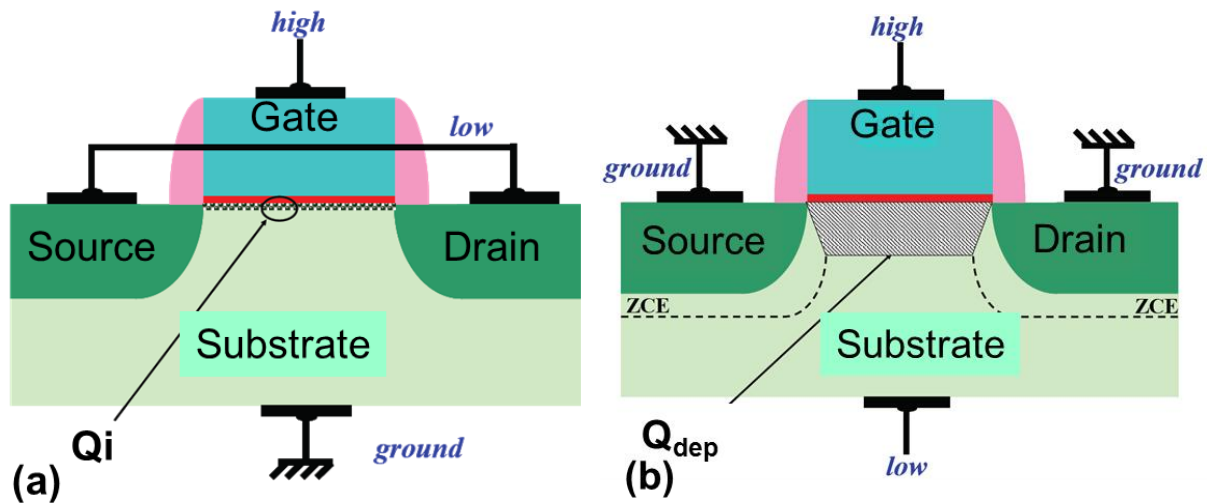


Figure III-9: Schematic representation of (a) gate-to-channel capacitance and (b) gate-to-substrate capacitance measured in bulk Si-MOSFET.

## 2.2 Interest of split $C-V$ for SOI wafer characterization

Split  $C-V$  measurements are usually carried out on fully processed SOI MOSFETs [27]. The interest of our work on split  $C-V$  measurements comes from the use of  $\Psi$ -MOSFET with pressure probes, which requires no contact preparation. For this reason, the rapid extraction of the mobility in SOI wafers before any CMOS processing is a key methodology to monitor and optimize the quality of the starting substrates.

Traditionally, the Y-function [28] has been a preferred technique for such task. However, the information that can be obtained on carrier mobility is limited (low-field mobility), and the plot of mobility *versus* inversion/accumulation charge or effective field is only approximated and reconstructed. A more direct approach is

based on the determination of the inversion or accumulation charge from capacitance measurements combined with static  $I_D$ - $V_G$  curves. Another important aspect of split  $C$ - $V$  is that it is valid from weak to strong inversion.

## 2.3 Extension of $\Psi$ -MOSFET for split $C$ - $V$ measurements

In this sub-section, we will present the method used to characterize SOI wafers with split  $C$ - $V$  using  $\Psi$ -MOSFET and the results obtained.

### 2.3.1 Method and experiment

In MOSFETs, the split  $C$ - $V$  technique is based on the measurements of the  $C_{gc}$  and  $C_{gb}$  capacitances as a function of the gate voltage. However, in  $\Psi$ -MOSFET structure, the Si substrate acts as gate and no top metal gate is available, therefore only the  $C_{gc}$  can be measured.

Two types of  $\Psi$ -MOSFET measurements were performed: static  $I_D$ - $V_G$  curves and split  $C$ - $V$  curves. In our measurements, both  $C_{gc}$ - $V_G$  and  $I_D$ - $V_G$  characterizations were conducted using the JANDEL station with pressure-controlled probes.

In the  $\Psi$ -MOSFET configuration for  $C$ - $V$  measurements, the source and drain probes were connected to low potential, whereas the back gate was biased to  $V_G$  and connected to high potential of the LCR meter (Figure III-10). The schematic of the measurement system and the equivalent circuit are shown in Figure III-10. A  $C_p$ - $G$  model is used for eliminating the dispersive effect of the resistance ( $R = 1/G$ ) in the capacitance curves.

The LCR meter was properly calibrated with two corrections before the measurements, the open procedure and short procedure, in order to eliminate the parasitic capacitance and to guarantee the best accuracy for the absolute capacitance measurement. The mean value of the parasitic capacitance resulting from the two successive corrections is automatically subtracted from the measured capacitance value. The split  $C$ - $V$  measurements were performed using a standard Agilent E 4980A LCR meter for a frequency range from 20 Hz to 5 kHz. Before each split  $C$ - $V$  measurement,  $I_D$ - $V_G$  characteristics were recorded with a HP-4156. The current measurements were performed at low drain voltage to ensure ohmic behavior.

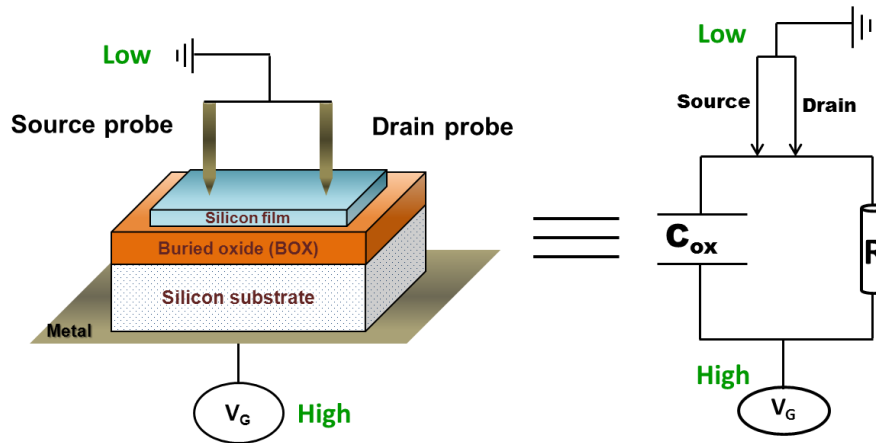


Figure III-10: Schematic configuration for the split  $C$ - $V$  technique with the equivalent circuit representation ( $C_p$ - $G$  model).

### 2.3.2 Experimental $C$ - $V$ curves

The proof of concept was checked on different geometries of SOI structures. We show here only two structures: the first with 200 nm film/400 nm BOX (Figure III-11a & Figure III-11b), the second with 20 nm film/145 nm BOX (Figure III-11c & Figure III-11d). As already known, both electrons ( $V_G > 0$ ) and holes ( $V_G < 0$ ) channels are activated, as illustrated in Figure III-11a and Figure III-11c by the  $I_D$ - $V_G$  curves.

Sweeping the gate voltage, a small AC sinusoidal signal is superposed to the DC bias in order to detect the charge variation with respect to the small AC signal; hence the capacitance of  $C_{gc}$  can be calculated for each bias. The  $C_{gc}$ - $V_G$  curves for different frequencies are reproduced in Figure III-11b & in Figure III-11d. When the film is depleted ( $V_G \approx 0$  V), the capacitance is zero. Then, the capacitance increases reflecting the gradual build-up of the inversion or accumulation channel. When the capacitance of the inversion/accumulation charge well exceeds the oxide capacitance, a maximum value of the capacitance, corresponding to the BOX capacitance ( $C_{BOX}$ ), is obtained at both positive and negative voltages.

The shape of  $C$ - $V$  curves for the two wafers confirms this observation. Therefore, our new technique experimental is successfully validated for thick and for thin SOI structures.

In the following parts we will focus on frequency and probe pressure impact on  $C_{gc}$  curves.

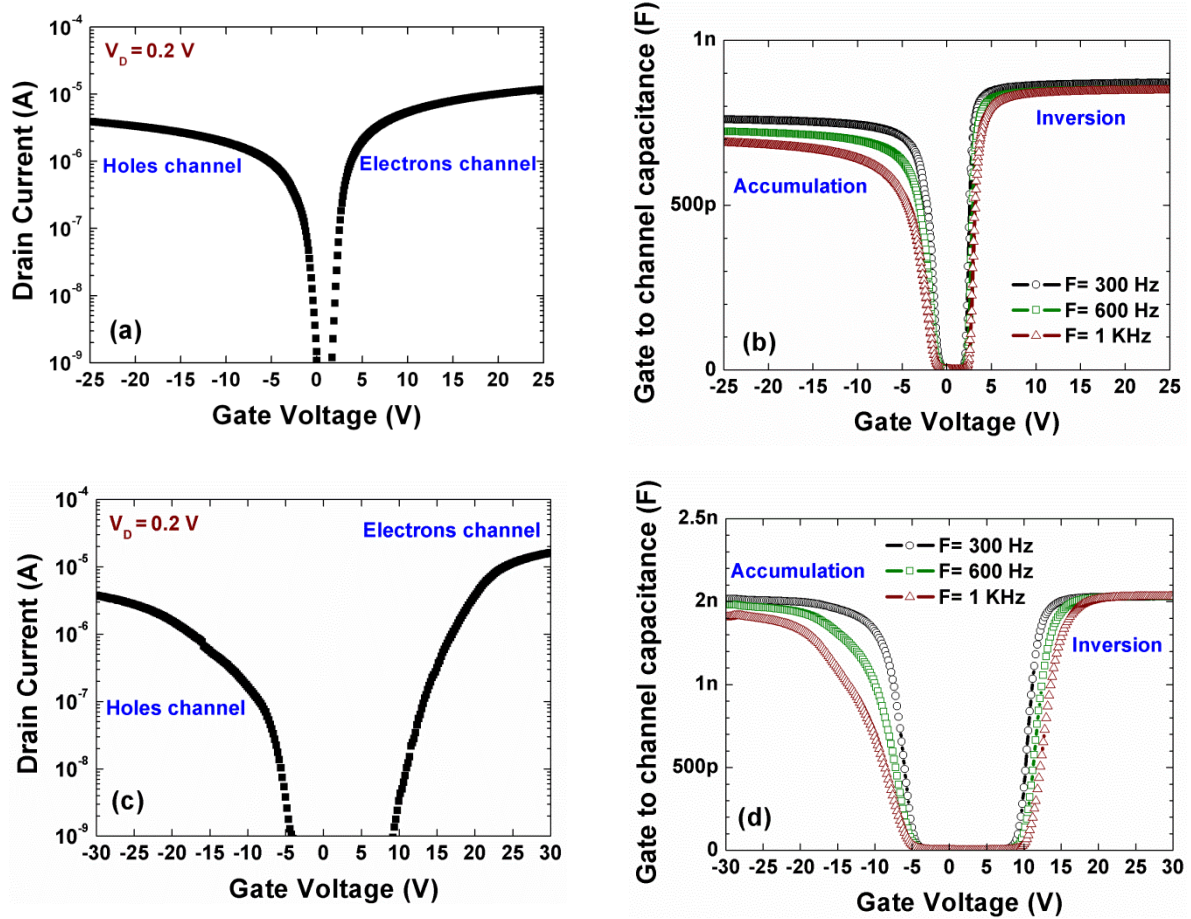


Figure III-11: (a)  $I_D$  vs.  $V_G$  and (b)  $C_{gc}$  vs.  $V_G$  for SOI wafer with 200 nm Si film and 400 nm BOX. (c)  $I_D$  vs.  $V_G$  and (d)  $C_{gc}$  vs.  $V_G$  for SOI wafer with 20 nm thin Si film and 145 nm BOX.

## 2.4 Impact of experimental conditions on C-V measurements

### 2.4.1 Probe pressure impact on C-V curves

From split C-V curves a maximum value of the capacitance is obtained at either positive or negative voltages in  $\Psi$ -MOSFETs. We studied the impact of the pressure of the probes on split C-V measurements. Figure III-12 shows  $C_{gc}$ - $V_G$  curves, where  $C_{max}$  increases for higher probe pressure. This effect is related to the contact improvement (decrease of the drain/source series resistance) as the probe pressure is increased [21]. For lower pressures, the S/D resistance is higher and, therefore, it is more difficult for carriers to be injected and spread. Consequently, the effective surface of the capacitance is reduced. At high pressure values (over 70 g), the capacitance value becomes saturated. The optimum pressure depends on the film and BOX thicknesses and has to be calibrated prior to mobility measurements.

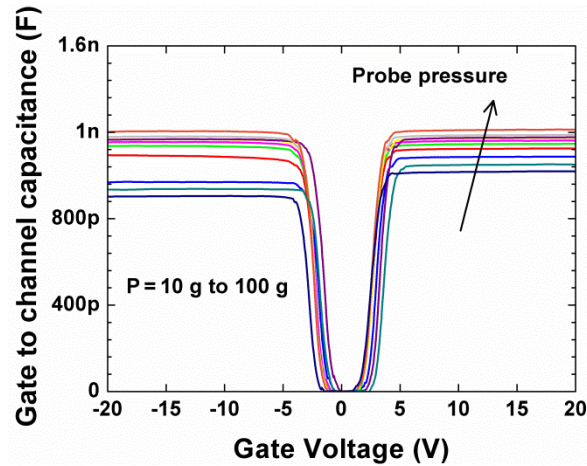


Figure III-12:  $C_{gc}$  vs.  $V_G$  curves for different probe pressures on SOI wafer with 88 nm Si film and 145 nm BOX.

### 2.4.2 Frequency effects

Figure III-13a shows the dependence of the capacitance curves on the frequency from 100 Hz to 5 kHz for SOI wafer with 88 nm thick silicon film and 145 nm thick BOX. As already observed in Figure III-11, the  $C$ - $V$  curve behavior is not similar for electrons and holes. For frequencies below 500 Hz, the maximum capacitance remains saturated and symmetrical for electron and hole channels (see Figure III-13b). Above 500 Hz, the capacitance saturation value decreases due to the limited frequency response of the carriers to the AC signal. For higher frequency, the maximum capacitance value is lowered and the curves become asymmetrical. This reduction of the capacitance can be attributed to several reasons:

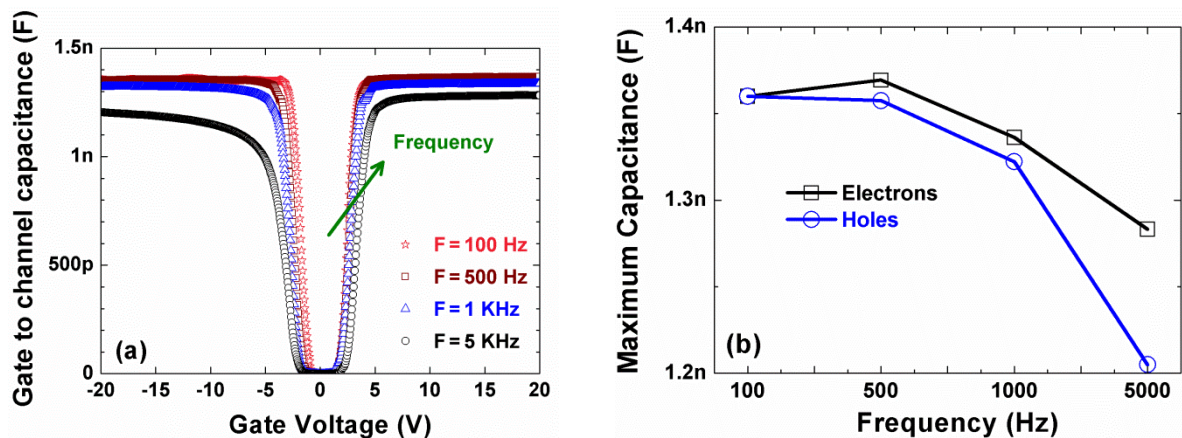


Figure III-13: (a)  $C_{gc}$ - $V_G$  curves for various frequencies. (b)  $C_{max}$  values for various frequencies. 88 nm Si film and 145 nm BOX.

**Time diffusion of carriers.** Since the gate is the substrate, one may imagine that the inversion/accumulation layers cover the whole sample surface. This

is not the case and a  $S_{\text{eff}}$  value must be considered. At higher frequency, the diffusion of the carriers injected from the needles is limited. Carriers located far from the contacts are not able to follow the AC signal. Therefore the effective area covered by the carriers will be lower, leading to a reduction of the total capacitance [29]. As the diffusion coefficient of holes in silicon is about three times lower than that for electrons, the effective area is smaller in accumulation than in inversion and may cause the  $C$ - $V$  asymmetry at higher frequencies.

**Surface carrier spreading.** Another explanation of the area dependence with the AC frequency was proposed by Fernandez *et al* [30] for thick BOX SOI wafers. The model relates the dependence of  $S_{\text{eff}}$  with frequency by a simple model which suggests that the surface carrier spreading is the actual origin of the capacitance reduction. They proposed a simple geometrical method to evaluate the two needle capacitance from single-needle measurements. The area covered by the collected carriers in single-needle configuration is supposed to have a circular shape (Figure III-14a). By consequence, the effective surface in two-needle configuration can be derived as the combination of the areas covered by the carriers injected from each probe (Figure III-14b). Their results show a good agreement between the model and the experimental curves for hole and electron channels (Figure III-15).

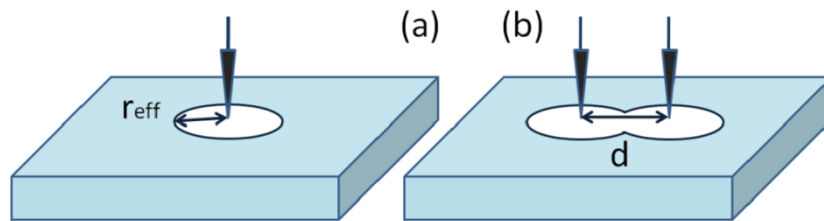


Figure III-14: Schematic representation of the area covered by the carriers in (a) single-needle and (b) two-needle configurations [30].

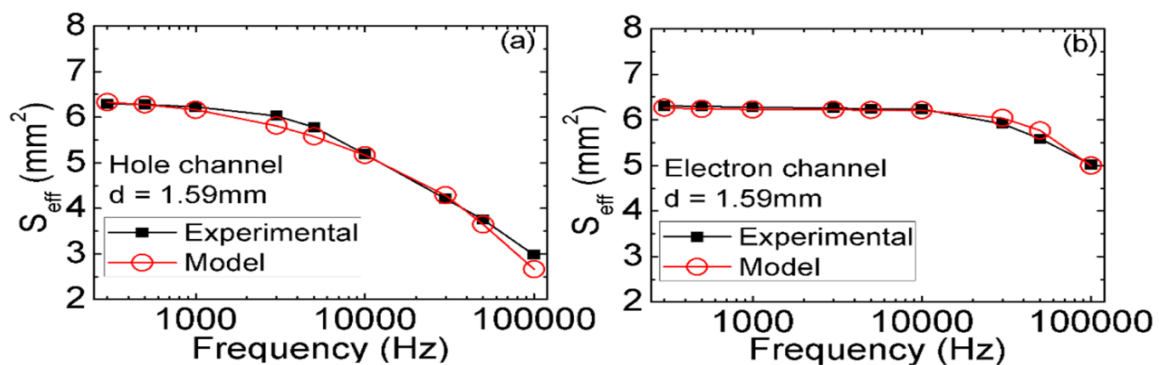


Figure III-15: Comparison between the effective surfaces obtained from experimental and model in two-needle configuration: (a) hole channel and (b) electron channel. 88 nm Si film and 145 nm BOX [30].

**Back-gate depletion.** The gate of the  $\Psi$ -MOSFET is far from being an ideal MOS-like gate. The doping in the substrate of our samples is relatively low ( $N_A \approx 10^{15} \text{ cm}^{-3}$ ) and the total thickness of the substrate exceeds  $500 \mu\text{m}$ . When the gate bias is negative, the wafer substrate tends to be first depleted and then inverted with electrons at the substrate-BOX interface. Due to the  $p$ -type character of the substrates, electrons (minority carriers in the substrate) are more difficult to generate than holes which are available in the substrate. At higher frequencies, the substrate electrons are less prone to follow the AC signal [31]. By contrast, for positive gate bias (inversion channel in the  $\Psi$ -MOSFET film but accumulated substrate-BOX interface), many holes are present in the substrate, so eliminating the substrate effect. The different behavior of carriers transport for positive and negative gate voltage can explain the substrate depletion effect and its impact on  $C$ - $V$  curves.

In order to examine the substrate effect, we characterized SOI with thick silicon film (180 nm) and ultra-thin BOX (10 nm). Figure III-16a shows the  $I_D$ - $V_G$  curve and Figure III-16b illustrates the  $C_{gc}$ - $V_G$  curves for various frequencies. The maximum capacitance values for electrons and holes are different, so the depletion underneath the BOX may be invoked. According to this scenario, the decrease of the measured capacitance for negative  $V_G$  values is the result of the series combination between  $C_{ox}$  and the capacitance associated to the substrate depletion layer (only present for negative  $V_G$  values). Note that this behavior was also obtained for very thick BOX (400 nm) with thick Si film (200 nm) in Figure III-11b. The substrate depletion effect is expected to be more pronounced in thin BOX wafers. The difference between the curves in Figure III-16b and Figure III-11b tends to confirm this hypothesis. A similar effect has been addressed by Schroder *et al* [29] who used metallic contacts deposited on the wafer surface.

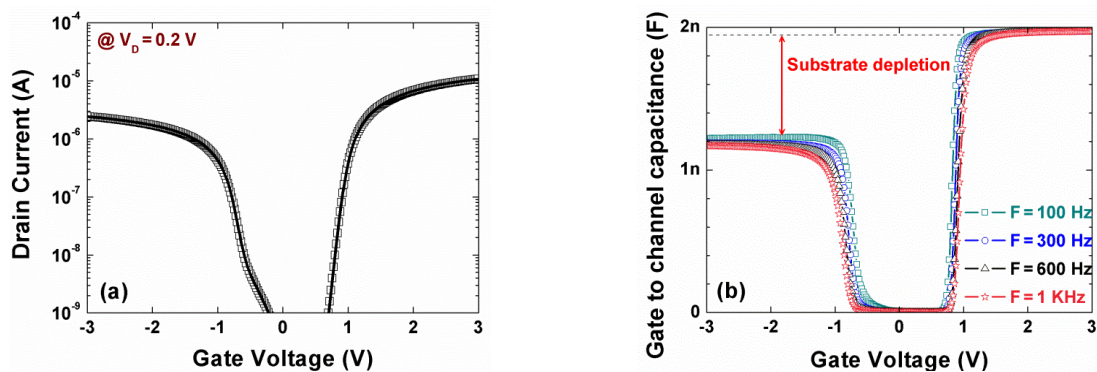


Figure III-16: (a)  $I_D$  vs.  $V_G$  and (b)  $C_{gc}$  vs.  $V_G$  for SOI wafer with 180 nm thick Si film and ultra-thin 10 nm BOX.

In this case, the maximum capacitance value can be corrected by including the depleted substrate capacitance  $C_{\text{sub}}$ :

$$\frac{1}{C_{\text{gc}}} = \frac{1}{C_{\text{ox}}} + \frac{1}{C_{\text{sub}}} \quad (\text{III-18})$$

However, the split  $C$ - $V$  method is frequently and successfully utilized in FD-SOI MOSFETs without corrections for the substrate effects, including the  $C_{\text{sub}}(V_G)$  dependence. Based on this argument and as long we use thick BOX (145 nm for example), we can also neglect the substrate depletion for split  $C$ - $V$  in  $\Psi$ -MOSFET.

From our point of view, the primary reason for frequency effects is the modification of the effective surface. The time constant of the  $RC$  circuit formed by the channel resistance and capacitance depends on carrier mobility, film thickness and BOX thickness. The channel resistance is obviously higher for holes and thinner films, leading to a smaller effective surface, in particular at low frequency. The frequency-dependent effective area corresponding to Figure III-13b,  $S_{\text{eff}}$  is equal to  $C_{\text{max}}$  (F) divided by  $C_{\text{ox}}$  (F/cm<sup>2</sup>), is shown in Figure III-17 and given by:

$$S_{\text{eff}} = \frac{C_{\text{max}}}{C_{\text{ox}}} \quad (\text{III-19})$$

Note that this area is, even at the lower frequencies, smaller than the physical area of the Si island etched on the SOI wafers (25 mm<sup>2</sup>). On the other hand it is much larger than the surface involved in  $\Psi$ -MOSFET operation ( $W/L \approx 0.75$ , hence  $W \times L \approx 0.75$  mm<sup>2</sup>).

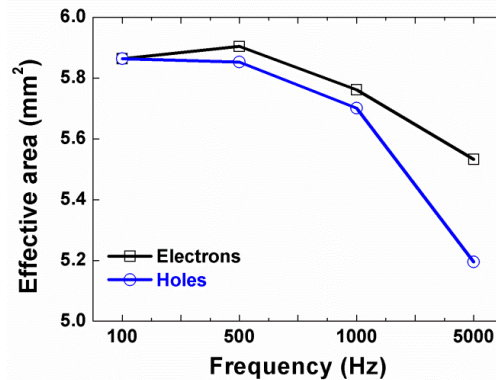


Figure III-17: Frequency dependence of the effective surface,  $S_{\text{eff}}$ , values obtained by neglecting the substrate effects. Same sample as in Figure III-13b with 88 nm Si film and 145 nm BOX.

In order to explain the maximum capacitance variation with the frequency for the split  $C$ - $V$  measurements we propose an analytical model. The physics behind our



model is based on the fact that the creation of the inversion (or accumulation) layer is not instantaneous. Indeed the carriers need to be supplied by the pressure probes. This induces a time constant that can be neglected for low frequency measurements but that can disturb the higher frequency measurements. The equation setting for our model is done using a  $RC$  low-pass filter. The model is under study and here we will only show the preliminary results. The fitting between the model and the experimental curves in (Figure III-18) confirm our expectation for both electron and hole sides.

Note that the effective mobility curves will not be affected by these considerations as long as the measurement is performed at frequency low enough. Although the frequency dependence of  $C$ - $V$  characteristics is theoretically interesting, it does not challenge the practical implementation of the split  $C$ - $V$  method in  $\Psi$ -MOSFET in order to extract the effective mobility.

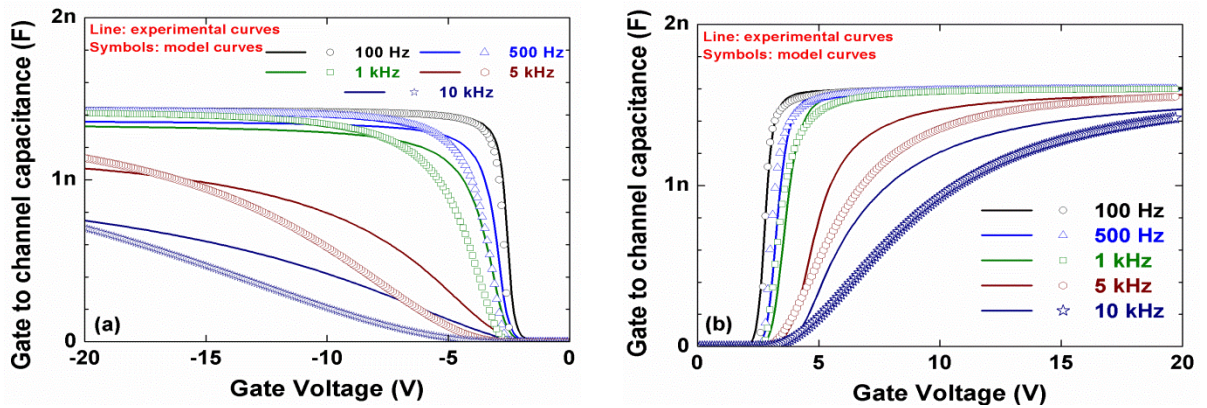


Figure III-18: Experimental and calculated  $C$ - $V$  curves for (a) holes and (b) electrons in 88 nm film thickness and 145 nm BOX thickness.

## 2.5 Extraction of $\mu_{\text{eff}}$ by split $C$ - $V$ technique

In order to obtain more quantitative results, we will discuss, in this subsection, the methodology to extract effective mobility from the experimental curves and the results obtained.

### 2.5.1 Adapted methodology to extract $\mu_{\text{eff}}$

Traditionally, two methods are used to evaluate  $\mu_{\text{eff}}$  versus  $V_G$ , defined as:

$$\mu_{\text{eff}} = \frac{I_D}{f_g Q_{\text{inv,acc}}(V_G) V_D} \quad (\text{III-20})$$

**Y function method.** This technique is indirect, based on the conventional  $I_D$ - $V_G$  measurements [28]. As mentioned earlier that  $V_{T,FB}$  and the low-field mobilities  $\mu_{n,p}$  are extracted from the Y-function.

The inversion charge  $Q_{inv}(V_G)$  and the accumulation charge  $Q_{acc}(V_G)$  are calculated using  $V_T$  and  $V_{FB}$ :

$$Q_{inv}(V_G) = C_{ox}(V_G - V_T) \text{ and } Q_{acc}(V_G) = C_{ox}(V_G - V_{FB}) \quad (\text{III-21})$$

where  $C_{ox}$  is the BOX capacitance per unit area ( $C_{ox} = \epsilon_{ox}/t_{BOX}$ ).

Equation (III-21) is a good approximation in strong inversion and accumulation. It serves to reconstruct the effective mobility  $\mu_{eff}(Q_{inv,acc})$  curves. However, the relations (III-21) fail in weak and moderate inversion.

**Split C-V method.** This direct technique serves to evaluate  $\mu_{eff}(Q_{inv,acc})$  curves from split C-V measurements. For split C-V,  $Q_{inv}(V_G)$  and  $Q_{acc}(V_G)$  are obtained by integrating the measured capacitance over the positive and negative  $V_G$  range, respectively:

$$Q_{inv}(V_G) = \frac{1}{S_{eff}} \int_{V_0}^{V_G} C_{gc}(u) du \text{ and } Q_{acc}(V_G) = \frac{1}{S_{eff}} \int_{V_G}^{V_0} C_{gc}(u) du \quad (\text{III-22})$$

where  $V_0$  is equal to  $(V_T + V_{FB})/2$ , in our case  $V_0 \approx 0V$ . Normalization by the effective surface ( $S_{eff}$ ) is necessary in order to obtain the inversion or accumulation charge density per unit area.

The effective surface represents the maximum area where the electrons (or holes) participating to the strong inversion (or accumulation) are sensed during the measurements. In this area, the carriers are able to follow the AC gate bias signal. The maximum capacitance value  $C_{max}$  represents the gate-oxide capacitance [23]. In regular MOSFETs, where the size of the gate and body is defined by lithography,  $C_{max}$  serves to determine the equivalent oxide thickness.

In bare SOI wafers, the situation is different. The BOX thickness is accurately known from ellipsometry but the  $\Psi$ -MOSFET capacitor dimensions are ill defined and  $S_{eff}$  must be calculated. As showed in equation (III-19), the effective area is found by dividing  $C_{max}$  (F) by  $C_{ox}$  (F/cm<sup>2</sup>), where  $C_{max}$  is the maximum capacitance extracted from split C-V data at positive  $V_G$  for electrons and at negative  $V_G$  for holes.

Two main differences can be concluded from these two methods. First, the  $\mu_{\text{eff}}$  evaluated from static measurements is reconstructed by calculating the  $Q_{\text{inv,acc}}(V_G)$ . For split  $C$ - $V$  technique  $\mu_{\text{eff}}$  is still obtained from equation (III-20) but the charge  $Q_{\text{inv,acc}}(V_G)$  is directly measured by integrating the capacitance ( $C_{\text{gc}}$ ) over the selected  $V_G$  range. The second key difference between these two methods is that split  $C$ - $V$  is valid from weak to strong inversion.

We used these two methods to calculate the electrons and holes mobility  $\mu_{\text{eff}}$ , as shown in Figure III-19. The effective mobility *versus*  $V_G$  in SOI samples with 88 nm film and 145 nm BOX is illustrated in Figure III-19a for electrons and in Figure III-19b for holes. The mobility curves from static and split  $C$ - $V$  match together and superpose in strong inversion for electrons and in strong accumulation for holes. These experimental results confirm the feasibility and efficiency of the split  $C$ - $V$  technique using  $\Psi$ -MOSFETs and also show that our adapted model for the extraction of  $S_{\text{eff}}$  and  $\mu_{\text{eff}}$  is successfully verified.

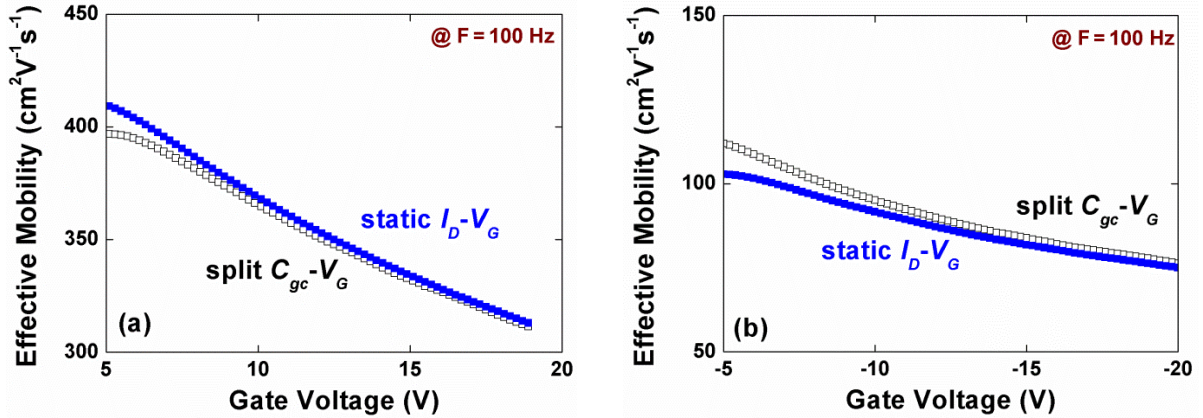


Figure III-19:  $\mu_{\text{eff}}$  as a function of  $V_G$  calculated from static  $I_D$ - $V_G$  and split  $C$ - $V$  curves for electrons (a) and for holes (b). 88 nm Si film and 145 nm BOX.

### 2.5.2 Applications of $\mu_{\text{eff}}$ extraction for advanced SOI structures

The previous sub-section proved that our split  $C$ - $V$  technique of mobility extraction is valid for 145 nm BOX thickness. Very thin BOX (25 nm) is currently needed for short-channel effects reduction in advanced SOI CMOS.

In Figure III-20, the  $C_{\text{gc}}$ - $V_G$  curves in 88 and 12 nm Si film with 25 nm BOX, measured for various frequencies, show same behavior as the one obtained previously for 145 nm BOX.

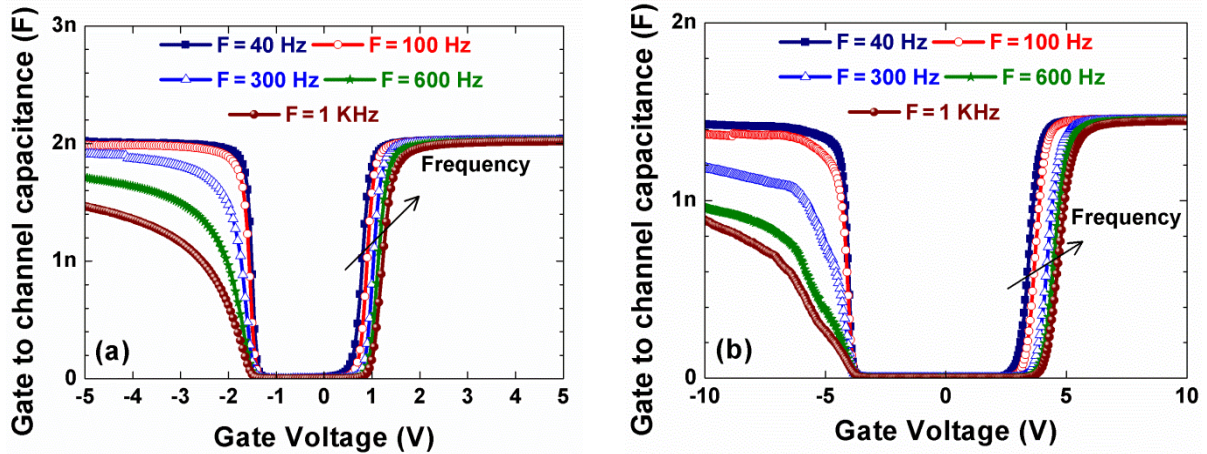


Figure III-20:  $C_{gc}$  vs.  $V_G$  for SOI wafer with: (a) 88 nm thick Si film and thin 25 nm BOX and (b) 12 nm thin Si film and thin 25 nm BOX.

Figure III-21a and Figure III-21b show the corresponding mobility curves for 88 nm Si film thickness. The effective mobility extracted from the two methods (split  $C$ - $V$  and  $Y$ -function) match together for both electrons and holes. Figure III-21c shows the electron effective mobility for ultra-thin 12 nm Si film where the two methods again give the same results. Note that the hole mobility for 12 nm film was not studied due to the high impact of  $R_{SD}$  which is visible in the  $C$ - $V$  curves for negative  $V_G$ .

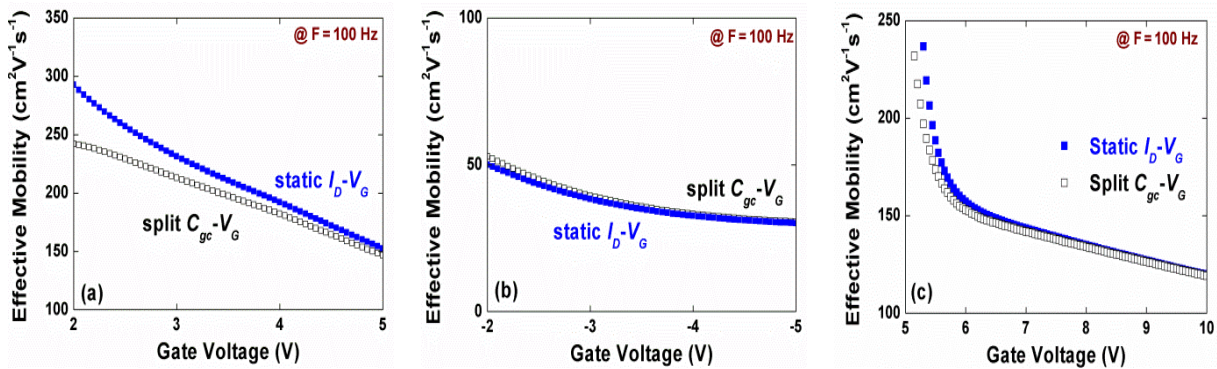


Figure III-21:  $\mu_{eff}$  as a function of  $V_G$  calculated from static  $I_D$ - $V_G$  and split  $C$ - $V$  curves for electrons (a) and for holes (b) in 88 nm Si film and 25 nm BOX and for electrons (c) in 12 nm Si film and 25 nm BOX.

Further investigations were done to validate the method. We compared the mobility, determined by split  $C$ - $V$  in passivated and non-passivated SOI wafers for electrons channel. Figure III-22a shows the effective mobility plotted *versus* back gate voltage for 145 nm thick BOX samples with passivated (empty squares) and non-passivated (solid squares) surfaces, measured for same experimental condition.

The split  $C$ - $V$  method clearly confirms that passivated sample offers better mobility compared to the non-passivated one, in agreement with [32] and [33]. The beneficial effect of surface passivation on electron mobility is also observed for thin BOX (25 nm) with 88 nm Si film in Figure III-22b.

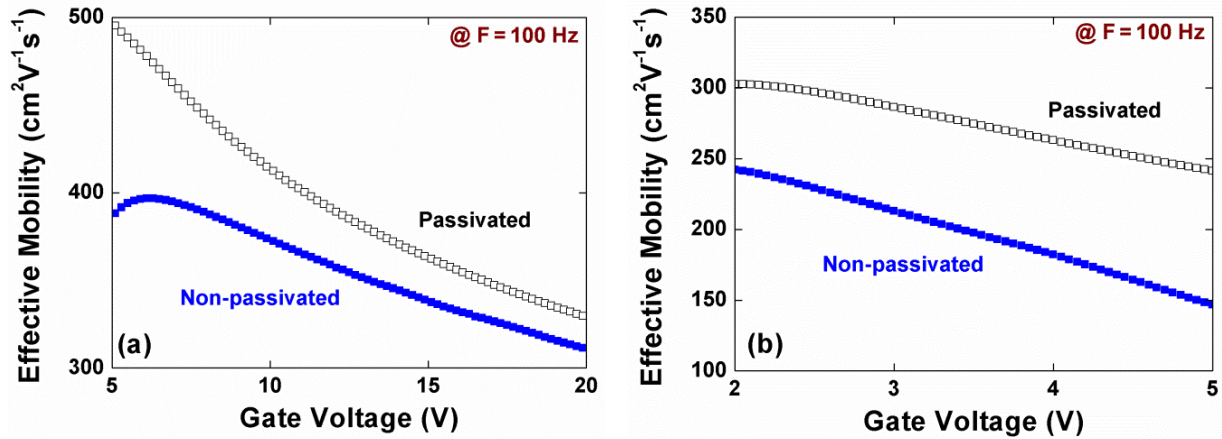


Figure III-22:  $\mu_{eff}$  from split  $C$ - $V$  for passivated and non-passivated wafers for electrons: (a) in 88 nm Si film and 145 nm BOX and (b) in 88 nm Si film and 25 nm BOX.

The passivation reduces the surface charge and the related vertical field. Its effect is therefore expected to be more pronounced in thinner films ( $\sim 10$  nm). To confirm this hypothesis, we compared passivated and non-passivated SOI samples with ultra-thin 12 nm Si film and 25 nm BOX in Figure III-23.

The effective mobility is visibly higher (up to 30 %) in passivated sample than in the non-passivated one. These results confirm the previously reported ones ([32], [33]), but their merit is to be obtained for the first time on such thin film/BOX couple (25 nm BOX) with our new split  $C$ - $V$  technique.

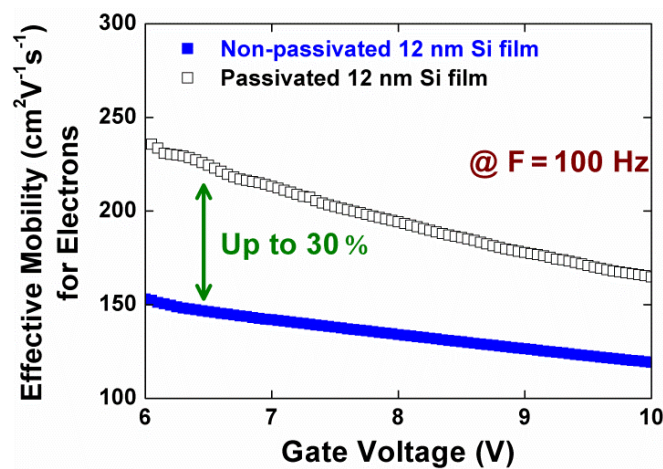


Figure III-23:  $\mu_{eff}$  as a function of  $V_G$  calculated from split  $C$ - $V$  curves for passivated and non-passivated 12 nm Si film with 25 nm BOX.

## 2.6 Conclusion of section 2

We demonstrated the feasibility of split  $C$ - $V$  measurements on as-fabricated SOI wafers using  $\Psi$ -MOSFET configuration. An adapted methodology to determine the effective mobility of electrons and holes by split  $C$ - $V$  technique was proposed and validated through comparison with the effective mobility extracted from static measurements. The method has been applied to different SOI materials (thin and thick film/BOX, passivated and non-passivated surface). The electron mobility can exceed  $500 \text{ cm}^2\text{V}^{-1}\text{s}^{-1}$  in thin SOI films with passivated surface. The frequency and substrate depletion effects as well as the role of probe pressure have been documented.

## Conclusion

In this chapter III, we presented two novel applications of the  $\Psi$ -MOSFET. First, the  $\Psi$ -MOSFET configuration has been extended to the low-frequency noise characterization of as-fabricated SOI wafers. Second, we introduced a new efficient characterization technique for bare SOI, based on split  $C$ - $V$  measurement using  $\Psi$ -MOSFET.

In section 1, low-frequency noise measurements were carried out, for the first time, on SOI substrates in the  $\Psi$ -MOSFET set-up with pressure probes. The low-frequency noise is shown to be of  $1/f$  type and is clearly associated with the carrier number fluctuation in the channel, due to the trapping/de-trapping of carriers. For static measurements the pressure plays a key-role in order to obtain small series resistance; the noise does not seem to depend on the pressure for the thicker films (88 nm).  $D_{it}$  values can be extracted using this new method, but higher values compared to extraction made from static curves were obtained. Passivated samples show an unexpectedly high level of noise compared to non-passivated samples for both 12 and 88 nm film thickness. The impact of series resistance and free surface preparation on the channel properties is suspected to be significant.

In section 2, we showed that the  $\Psi$ -MOSFET can also be used for split  $C$ - $V$  measurements in bare SOI wafers. Several variants of SOI wafers have successfully been tested. The probe pressure needs to be high enough for accurate capacitance curves while avoiding probe penetration through the ultra-thin Si film and BOX. A variation of the maximum capacitance in the high frequency regime was observed and explained. An adapted model for  $\Psi$ -MOSFET was proposed for extracting the effective mobility from the split  $C$ - $V$  curves. The mobility curves were systematically compared with those obtained from static measurements using the Y-function method. Excellent agreement was obtained validating our approach. Samples with passivated surface show higher mobility values than non-passivated ones. The impact of film/BOX thickness and interface quality on the effective carrier mobility can be accurately investigated using this new  $\Psi$ -MOSFET capability to assimilate the split  $C$ - $V$  technique.

## References chapter III

- [1] Y. Nemirovsky, I. Brouk and C. G. Jakobson, "1/f noise in CMOS transistors for analog applications," *Electron Devices, IEEE Transactions on*, vol. 48, pp. 921-927, 2001.
- [2] R. Brederlow, W. Weber, D. Schmitt-Landsiedel and R. Thewes, "Fluctuations of the low frequency noise of MOS transistors and their modeling in analog and RF-circuits," in *Electron Devices Meeting, 1999. IEDM '99. Technical Digest. International*, pp. 159-162, 1999.
- [3] E. Simoen, A. Mercha, C. Claeys and N. Lukyanchikova, "Low-frequency noise in silicon-on-insulator devices and technologies," *Solid-State Electronics*, vol. 51, pp. 16-37, 2007.
- [4] A. Diab, I. Ionica, S. Cristoloveanu, F. Allibert, Y. H. Bae, J. A. Chroboczek and G. Ghibaudo, "Low-frequency noise in SOI pseudo-MOSFET with pressure probes," *Microelectronic Engineering*, vol. 88, pp. 1283-1285, 2011.
- [5] L. K. J. Vandamme, Li Xiaosong and D. Rigaud, "1/f noise in MOS devices, mobility or number fluctuations?," *Electron Devices, IEEE Transactions on*, vol. 41, pp. 1936-1945, 1994.
- [6] F. N. Hooge, "1/f noise sources," *Electron Devices, IEEE Transactions on*, vol. 41, pp. 1926-1935, 1994.
- [7] M. J. Kirton and M. J. Uren, "Noise in solid-state microstructures: A new perspective on individual defects, interface states and low-frequency (1/f) noise," *Advances In Physics*, vol. 38, pp. 367-468, 1989.
- [8] G. Ghibaudo, O. Roux, Ch Nguyen-Duc, F. Balestra and J. Brini, "Improved Analysis of Low Frequency Noise in Field-Effect MOS Transistors," *physica status solidi (a)*, vol. 124, pp. 571-581, 1991.
- [9] Dieter K. Schroder, *Semiconductor material and device characterization (Third Edition)*, Wiley-Interscience, USA, 2006.
- [10] A. L. Mcwhorter and R. H. Kingston, *Semiconductor Surface Physics*,. University of Pennsylvania, USA, pp. 207-228, 1957.
- [11] F. N. Hooge, T. G. M. Kleinpenning and L. K. J. Vandamme, "Experimental studies on 1/f noise," *Rep. Prog. Phys.*, vol. 44, pp. 479-532, 1981.
- [12] Gerard Ghibaudo, "On the theory of carrier number fluctuations in MOS devices," *Solid-State Electronics*, vol. 32, pp. 563-565, 1989.
- [13] S. C. Sun and J. D. Plummer, "Electron Mobility in Inversion and Accumulation Layers on Thermally Oxidized Silicon Surfaces," *Solid-State Circuits, IEEE Journal of*, vol. 15, pp. 562-573, 1980.
- [14] S. Christensson, I. Lundström and C. Svensson, "Low frequency noise in MOS transistors," *Solid-State Electronics*, vol. 11, pp. 797-812, 1968.
- [15] Charles Surya and Thomas Y. Hsiang, "A thermal activation model for  $1/f^{\nu}$  noise in Si-MOSFETs," *Solid-State Electronics*, vol. 31, pp. 959-964, 1988.
- [16] G. Ghibaudo, "Critical MOSFETs operation for low voltage/low power IC's: Ideal characteristics, parameter extraction, electrical noise and RTS fluctuations," *Microelectronic Engineering*, vol. 39, pp. 31-57, 1997.
- [17] Vadim Kushner, Jinman Yang, Joon Choi, Trevor Thornton and Dieter Schroder, "SOI Low Frequency Noise and Interface Trap Density Measurements with the Pseudo MOSFET," *ECS Transactions*, vol. 2, pp. pp. 491-502, 2006.
- [18] V.A. Kushner, K. Park, D.K. Schroder and T.J. Thornton, "Low-Frequency-Noise Spectroscopy of SIMOX and Bonded SOI Wafers," *Electron Devices, IEEE Transactions on*, vol. 54, pp. 3378-3382, 2007.
- [19] A. Diab, I. Ionica, S. Cristoloveanu, F. Allibert, Y. H. Bae, J. A. Chroboczek and G. Ghibaudo, "Static and low-frequency noise characterization of ultrathin SOI with very thin BOX in



- pseudo-MOSFET configuration," in *Semiconductor Device Research Symposium (ISDRS), 2011 International*, pp. 1-2, 2011.
- [20] J. A. Chroboczek, "Automatic, wafer-level, low frequency noise measurements for the interface slow trap density evaluation," in *Microelectronic Test Structures, 2003. International Conference on*, pp. 95-98, 2003.
- [21] I. Ionica, I. Savin, W. Van Den Daele, T. Nguyen, X. Mescot and S. Cristoloveanu, "Characterization of silicon-on-insulator films with pseudo-metal-oxide-semiconductor field-effect transistor: Correlation between contact pressure, crater morphology, and series resistance," *Applied Physics Letters*, vol. 94, pp. 012111-012113, 2009.
- [22] Koomen Jan, "Investigation of the MOST channel conductance in weak inversion," *Solid-State Electronics*, vol. 16, pp. 801-810, 1973.
- [23] C. G. Sodini, T. W. Ekstedt and J. L. Moll, "Charge accumulation and mobility in thin dielectric MOS transistors," *Solid-State Electronics*, vol. 25, pp. 833-841, 1982.
- [24] S. Takagi and M. Takayanagi, "Experimental evidence of inversion-layer mobility lowering in ultrathin gate oxide metal-oxide-semiconductor field-effect-transistors with direct tunneling current," *Japanese Journal of Applied Physics*, vol. 41, pp. 2348-2352, 2002.
- [25] F. Lime, R. Clerc, G. Ghibaudo, G. Pananakakis and G. Guégan, "Impact of gate tunneling leakage on the operation of NMOS transistors with ultra-thin gate oxides," *Microelectronic Engineering*, vol. 59, pp. 119-125, 2001.
- [26] A. Diab, C. Fernández, A. Ohata, N. Rodriguez, I. Ionica, Y. H. Bae, F. Allibert, F. Gámiz, G. Ghibaudo and S. Cristoloveanu, "A New Characterization Technique for SOI Wafers: Split  $C(V)$  in Pseudo-MOSFET Configuration," in *Proceeding of the EUROSOI conference*, pp. 103-104, 2012.
- [27] J. Wang, N. Kistler, J. Woo and C. R. Viswanathan, "Mobility-field behavior of fully depleted SOI MOSFET's," *Electron Device Letters, IEEE*, vol. 15, pp. 117-119, 1994.
- [28] G. Ghibaudo, "New method for the extraction of MOSFET parameters," *Electronics Letters*, vol. 24, pp. 543-545, 1988.
- [29] P. Nayak, M. Seacrist and D. K. Schroder, "Unusual  $C-V$  Characteristics of High-Resistivity SOI Wafers," *Electron Device Letters, IEEE*, vol. 32, pp. 1659-1661, 2011.
- [30] C. Fernández, A. Diab, N. Rodriguez, A. Ohata, F. Allibert, I. Ionica, F. Gámiz and S. Cristoloveanu, "Impact of Effective Capacitance Area on the Characterization of SOI Wafers by Split- $C(V)$  in Pseudo-MOSFET Configuration," in *2012 International Semiconductor Conference Dresden-Grenoble (IEEE-ISCDG)*, pp. 1-2, 2012.
- [31] B. Rong, L. K. Nanver, J. N. Burghartz, A. B. M. Jansman, A. G. R. Evans and B. S. Rejaei, "C-V characterization of MOS capacitors on high resistivity silicon substrate," in *European Solid-State Device Research, 2003. ESSDERC '03. 33rd Conference on*, pp. 489-492, 2003.
- [32] G. Hamaide, F. Allibert, H. Hovel and S. Cristoloveanu, "Impact of free-surface passivation on silicon on insulator buried interface properties by pseudotransistor characterization," *Journal of Applied Physics*, vol. 101, pp. 114513-114516, 2007.
- [33] N. Rodriguez, S. Cristoloveanu and F. Gamiz, "Revisited Pseudo-MOSFET Models for the Characterization of Ultrathin SOI Wafers," *Electron Devices, IEEE Transactions on*, vol. 56, pp. 1507-1515, 2009.

## **Chapter IV:**

### ***Innovative applications of pseudo-MOSFET***

## **Introduction**

In chapters II and III we described the standard operation and application of the  $\Psi$ -MOSFET as well as several advanced variants. In this chapter IV, we will present innovative applications of the  $\Psi$ -MOSFET.

In section 1, we investigate the  $\Psi$ -MOSFET extension for the characterization of heavily doped (HD) SOI wafers (up to  $10^{20}$  cm<sup>-3</sup>). Experimental results and an appropriate model for parameter extraction will be showed. In addition to  $\Psi$ -MOSFET measurements, Hall effect and four-point probe experiments are presented for validation.

In section 2, we present the proof of concept of a new simple SOI sensor for gold nanoparticle detection. The shifts observed in the electrical measurements are explained by the nanoparticle charging and modeled with the pseudo-MOSFET theory. Our experimental results open a wide panel of bio/chemical sensing and memory applications directly achievable on the SOI substrates.

In section 3, we study the electrical transport properties of 3D vertically-stacked Silicon-Germanium (SiGe) and Silicon-Germanium-Carbon (SiGeC) nanowires fabricated on SOI wafers. We demonstrate that the suspended gateless nanowires behave as MOS transistors controlled by the back gate, similar to the  $\Psi$ -MOSFET principle. This technique proves efficient for the preliminary characterization of as-grown nanowires before the processing of MOS gate and source/drain terminals. Measurements carried out at low temperature yield more detailed information on the conduction mechanisms.

## 1. Characterization of heavily doped SOI wafers

### 1.1 From undoped to doped SOI

Standard SOI wafers have a low  $p$ -type doping of silicon film ( $N_A \approx 10^{15} \text{ cm}^{-3}$ ), suitable to fabricate the body of SOI devices [1]. However, heavily-doped film (HD) SOI wafers can be useful for several aspects: source/drain engineering [2], junctionless transistor [3], multiple threshold voltage tuning [4], *etc.* So far, most of the characterizations were performed on undoped or relatively low doped SOI wafers [5], [6] and there is no report to date on the application of  $\Psi$ -MOSFET in heavily-doped ( $10^{19}$ - $10^{20} \text{ cm}^{-3}$ ) SOI wafers.

The aim of  $\Psi$ -MOSFET measurements of heavily-doped SOI wafers is to determine the degree of doping activation, carrier mobility and implantation-induced defects.

Wafers under test were fabricated in SEMATECH [7]. They feature 40 nm thick Si film and 145 nm BOX with various doping types and with target doping concentration of  $10^{19} \text{ cm}^{-3}$ . All wafers were implanted with a dose of  $8 \times 10^{13} \text{ cm}^{-2}$  and annealed at  $1070^\circ\text{C}$ . Three different dopants were used: arsenic (As), phosphorus (P) and boron (B). Besides, undoped SOI wafers were also fabricated as a reference. Silicon  $\Psi$ -MOSFET islands with square size of  $5 \times 5 \text{ mm}^2$  were etched. All measurements were performed at room temperature.

Another set of wafers had thinner film (10 nm) and even higher doping ( $\sim 10^{20} \text{ cm}^{-3}$ ).

### 1.2 $\Psi$ -MOSFET characterizations

For low  $V_D$  values, the characterization of wafers with undoped Si film results in typical curves for  $I_D$ - $V_G$  (Figure IV-1a) and  $g_m$ - $V_G$  (Figure IV-2a). The  $\Psi$ -MOSFET characteristics for 40 nm HD SOI wafers, illustrated in Figure IV-1b (for  $I_D$ - $V_G$ ) and in Figure IV-2b (for  $g_m$ - $V_G$ ), are totally different from those in undoped SOI wafer. The pressure applied on the probes (p) was equal to 60 g in both cases and is not a factor. Heavily doped SOI wafers do not exhibit an off-current region. However, they

still show a small field-effect modulation of the drain current by the back-gate voltage, which is also reflected by the changes in  $g_m$ - $V_G$  curves (Figure IV-2b).

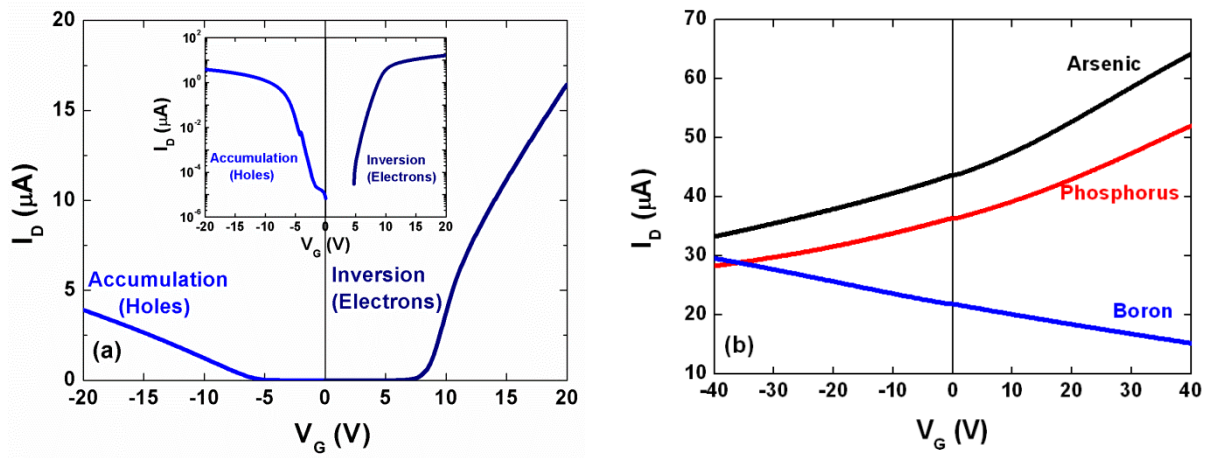


Figure IV-1: Drain current versus gate voltage in (a) undoped (inset: log scale of  $I_D$ - $V_G$ ) and (b) doped SOI.  $t_{Si} = 40$  nm,  $t_{BOX} = 145$  nm,  $V_D = 0.2$  V.

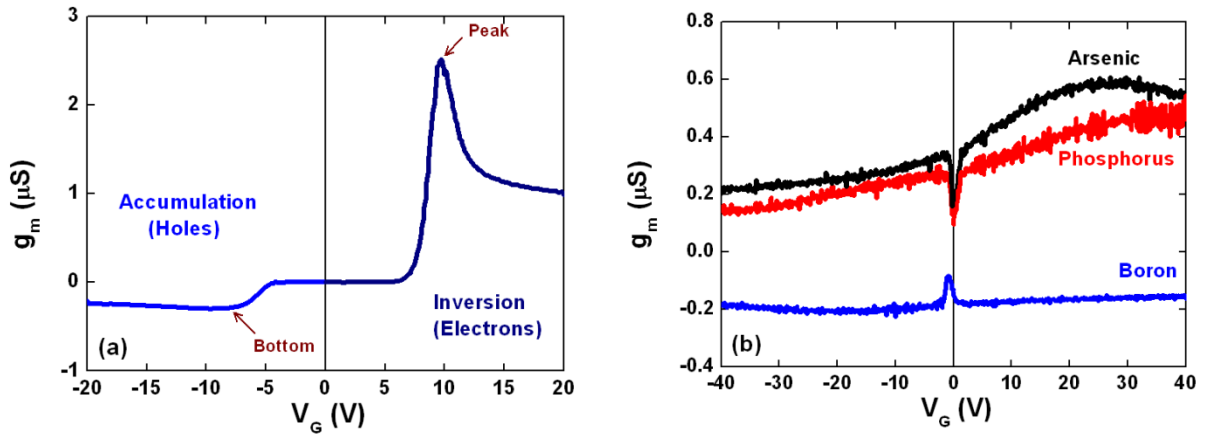


Figure IV-2: Transconductance versus gate voltage in (a) undoped and (b) doped SOI. Same samples as in Figure IV-1.

The drain current and transconductance curves in HD SOI have distinct variations between 0 to + 40 V and 0 to - 40 V, revealing two types of conduction mechanisms. The super-linear curves in Figure IV-1b indicate that an accumulation channel is activated (0 to + 40 V for As-implanted and P-implanted samples and 0 to - 40 V for B-implanted sample). For opposite gate biasing, the films tend to be depleted. However, the heavily doped films cannot be fully depleted: there is no zero-current region at  $V_G \approx 0$  V as in undoped SOI (Figure IV-1a @  $V_G = 0$  V).

We calculated the maximum depletion width ( $W_{Dmax}$ ) and obtained a value close to 12 nm for  $10^{19}$  doping concentration [8]. In other words, only 12 nm from the total 40 nm silicon film thicknesses can be depleted, which means that these films can never be fully depleted.

The expansion of the depletion region is reflected by a linear decrease in volume current ( $I_{vol}$ ). A neutral region with ‘volume’ conduction (as opposed to an ‘interface’ channel) subsists for the entire  $V_G$  range. The current is exclusively due to majority carriers. No inversion channel is created from minority carries because the threshold voltage (e.g. for boron  $V_T \approx 80$  V) is too high and cannot be experimentally reached.

### 1.2.1 Y-function

In Figure IV-3a, the linear shape of Y-function *versus*  $V_G$  [9] for the undoped SOI wafers allows us to extract the main parameters:  $V_{FB}$  and  $\mu_p$  for holes;  $V_T$  and  $\mu_n$  for electrons. The conventional Y-function fails in HD SOI wafers (Figure IV-3b). No straight line of Y *versus*  $V_G$  can be plotted, which makes the parameter extraction impossible. This problem was predictable, being attributed to the strong volume current, about  $10 \mu A$  at  $V_G = 0$  V for HD SOI (for undoped SOI wafers  $I_{vol} \approx 1$  pA at  $V_G = 0$  V), which tends to mask the accumulation channel [10]. A revised model for parameters extraction based on earlier work [6] was detailed in [7]. The main equations and results are exposed in the following section.

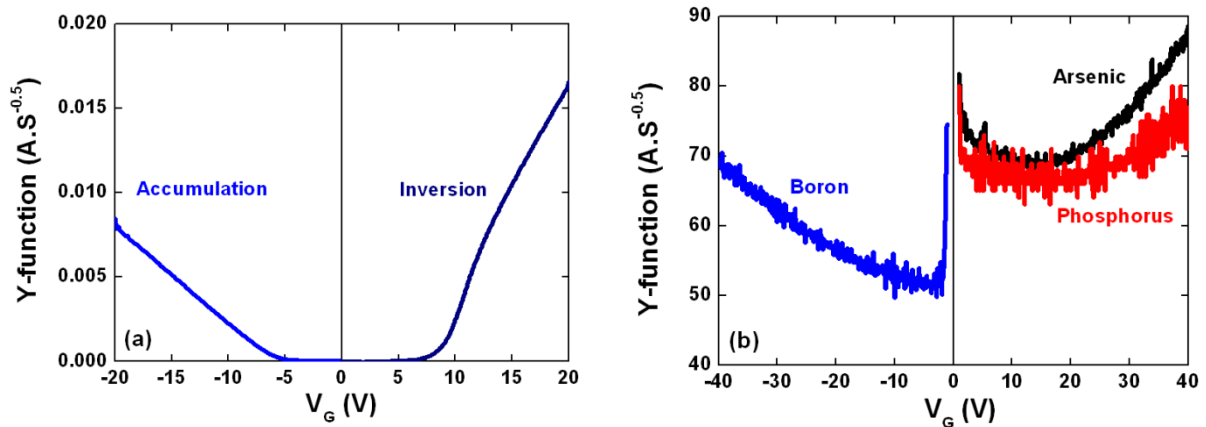


Figure IV-3: Y-function versus  $V_G$  @  $V_D = 0.2$  V for (a) undoped SOI and (b) high-doped 40 nm SOI wafers using the total drain current. The Y-function is meaningless in (b).

## 1.3 Revised model for parameter extraction in HD SOI

We consider boron-implanted SOI wafer in Figure IV-4 as an example but a similar derivation is straight-forward for donor-type doping (arsenic and phosphorus). When  $V_G$  is negative enough for p-type SOI, an accumulation channel is formed at the Si-SiO<sub>2</sub> interface (Figure IV-4a). For positive  $V_G$  a depletion layer is

formed at the Si-SiO<sub>2</sub> interface (Figure IV-4b). The two conduction regimes involved in I<sub>D</sub>-V<sub>G</sub> characteristics of heavily doped substrates (Figure IV-1b) are variable volume contribution assisted by:

- i. the interface accumulation in Figure IV-4a;
- ii. the extension of the depletion region in Figure IV-4b.

We now propose analytical expressions for each region, which can be used to extract the corresponding material parameters [7].

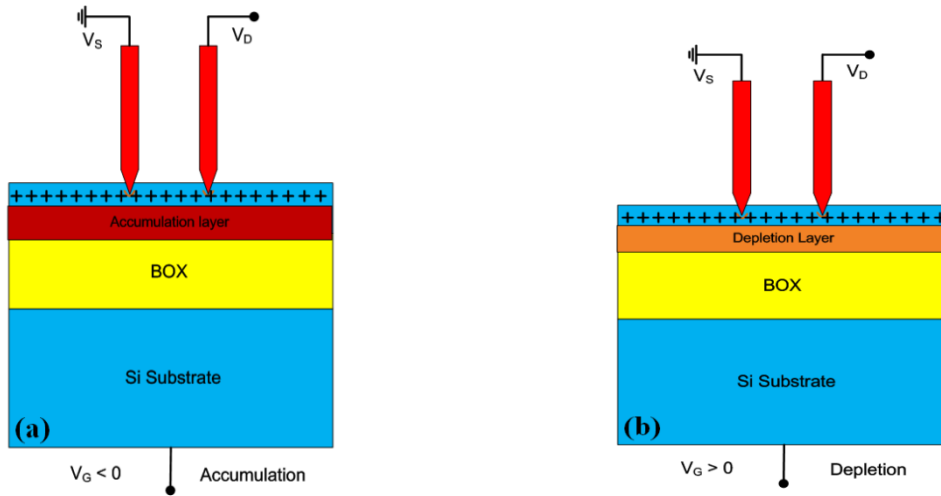


Figure IV-4:  $\psi$ -MOSFET cross-section in boron-implanted SOI wafers for (a)  $V_G < 0$  and (b)  $V_G > 0$ .

### 1.3.1 Volume conduction

The drain current varies as a linear function of  $V_G$ , arising from the non-negligible conduction ( $I_D = I_{vol}$ ) in the undepleted volume of the silicon film (see Figure IV-4b) and from the modulation of the space charge region with  $W_D$  ([6], [7]):

$$I_{vol} = qf_g N_{A,D} \mu_{vol} (t_{Si} - W_D) V_D = f_g C_{ox} \mu_{vol} (V_0 - V_G) V_D \quad (IV-1)$$

where  $\mu_{vol}$  is the volume mobility,  $W_D$  is the depth of the depletion layer, and:

$$V_0 = V_{T,FB} + \frac{q N_{A,D}}{C_{ox}} t_{Si} \quad (IV-2)$$

$V_0$  represents a fictive voltage which would lead to full depletion of the film and it is measured by extrapolating to zero current the linear region of I<sub>D</sub>-V<sub>G</sub> curves of Figure IV-1b. Note that  $V_0$  is very large (> 150 V) because the full depletion cannot be actually achieved due to the very high doping. Two parameters can be extracted from this model in the volume conduction region. From equation (IV-2),  $V_0$  yields the

effective doping concentration  $N_{A,D}$ , whereas the slope of equation (IV-1) allows extracting the volume mobility ( $\mu_{p,vol}$  for holes and  $\mu_{n,vol}$  for electrons). Figure IV-5a shows the application of our model on the measured currents for the variable depletion region. The model fits the measured curves.

### 1.3.2 Surface accumulation

In this regime (Figure IV-4a), there is no depletion layer so the drain current contains the volume current and the accumulation current ( $I_D = I_{vol} + I_{acc}$ ).  $I_{vol}$  represents the maximum volume current flowing through the entire undepleted Si film ( $I_D = I_{vol}$  at  $V_G = V_{FB}$ ):

$$I_{vol} = qf_g N_{A,D} \mu_{vol} t_{Si} V_D \quad (IV-3)$$

In order to access the interface current only, we subtract the maximum volume current from the total measured current ( $I_{acc} = I_D - I_{vol}$ ). The transconductance accounts exclusively for the accumulation channel. Thus, a new Y-function can be defined:

$$Y_{acc} = \frac{I_D - I_{vol}}{\sqrt{g_m}} = \sqrt{f_g C_{ox} V_D \mu_s (V_G - V_{FB})} \quad (IV-4)$$

The low-field mobility  $\mu_s$  is the majority carrier mobility at the Si-SiO<sub>2</sub> interface, different from the volume mobility  $\mu_{vol}$  calculated from equation (IV-1). A linear variation of the new Y-function ( $Y_{acc}$ ) versus  $V_G$  curve is obtained, as shown in Figure IV-5b. By consequence, the intercept of  $Y_{acc}$  with  $V_G$  yields  $V_{FB}$  and  $\mu_s$  is extracted from the slope of the new Y-function ( $\mu_{p,s}$  for holes and  $\mu_{n,s}$  for electrons).

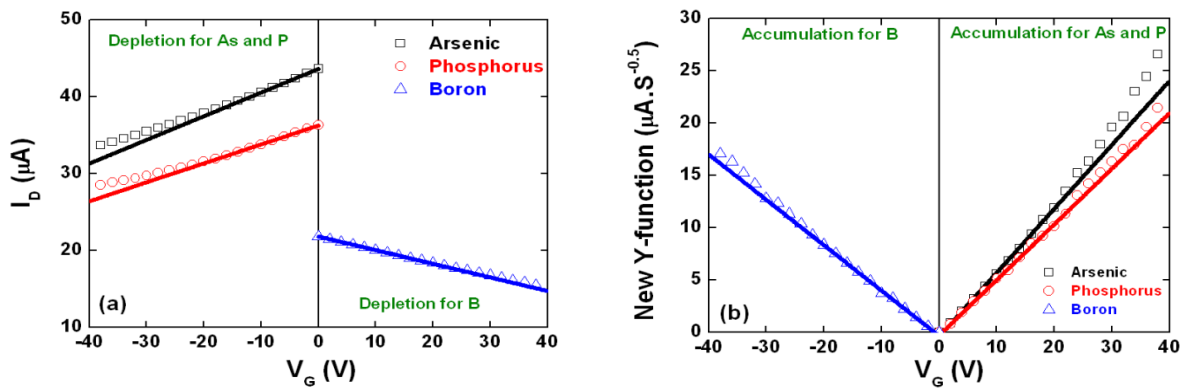


Figure IV-5: (a) Experimental (symbols) and modeled (solid lines from equation (IV-1)) drain currents in volume conduction regime of  $\Psi$ -MOSFET. (b) Revised Y-function vs.  $V_G$  for surface accumulation current. Symbols: experimental data. Solid lines: linear approximation by equation (IV-4). ( $V_D = 0.2$  V).



### 1.3.3 Extracted parameters

The extracted parameters from  $\Psi$ -MOSFET measurements ( $V_{F,B}$ ,  $\mu_{p,s}$ ,  $\mu_{n,s}$ ,  $N_{A,D}$ ,  $\mu_{p,vol}$  and  $\mu_{n,vol}$ ) based on equations (IV-1) & (IV-4) are summarized in Table IV-1. The doping levels are close to the target values ( $10^{19} \text{ cm}^{-3}$ ). This implies that despite the very high implant doses, the impurities are essentially confined within the Si film and exhibit a reasonable electrical activation ( $> 50 \%$ ).

Table IV-1: Extracted activated doping concentration, volume mobility, flat-band voltage and low-field surface mobility from  $\Psi$ -MOSFET measurements for 40 nm film thickness.

Dopants	$N_{A,D}$ ( $10^{19} \text{ cm}^{-3}$ )	$\mu_{vol}$ ( $\text{cm}^2/\text{V.s}$ )	$V_{FB}$ (V)	$\mu_s$ ( $\text{cm}^2/\text{V.s}$ )
Undoped	—	—	- 6.1 ( $V_{FB}$ ) 6.9 ( $V_T$ )	94 ( $h^+$ ) 457 ( $e^-$ )
Arsenic	0.53	86	0.68	104 ( $e^-$ )
Phosphorus	0.52	73	0.57	79 ( $e^-$ )
Boron	0.47	50	- 0.77	53 ( $h^+$ )

The mobility values in Table IV-1 are much lower than those extracted for undoped wafer ( $\mu_p = 94 \text{ cm}^2/\text{V.s}$  and  $\mu_n = 457 \text{ cm}^2/\text{V.s}$ ), which documents the strong reduction of the mobility (5 times for electrons and 2 times for holes) with  $10^{19} \text{ cm}^{-3}$  doping concentration level. The mobility in the accumulation channel ( $\mu_s$ ) is systematically larger than in the volume ( $\mu_{vol}$ ). This can be possibly explained by the accumulation channel screening the effect of Coulomb scattering on interface mobility [11].

The flat-band voltages are small, close to the theoretical values of the work-function difference ( $\approx |0.24 \text{ V}|$ ) between the HD film ( $10^{19} \text{ cm}^{-3}$ ) and the undoped substrate ( $10^{15} \text{ cm}^{-3}$ ). This result indicates a negligible concentration of interface and oxide defects, demonstrating that the implantation process did not degrade the interface quality [12].

Two independent characterizations techniques were used to validate the  $\Psi$ -MOSFET measurements, Hall effect and four-point probe techniques. Below, we will briefly remind Van der Pauw and Hall effect concepts (see Figure IV-6) which are detailed elsewhere ([7], [13]) and apply them to HD SOI wafers utilized in this work.

A comparison of the results between  $\Psi$ -MOSFET with Hall effect and four-point probe follows in the next section.

### 1.3.3.1 Van der Pauw and Hall effect

Before Hall effect measurements, contact resistance experiments are performed in order to verify whether all the contacts are ohmic. Van der Pauw experiments at  $B = 0$  T yield the average resistivity  $\rho_{VDP}$  [13]:

$$\rho_{VDP} = \frac{\pi t_{Si}}{\ln(2)} \frac{R_{12,34} + R_{23,41}}{2} f \quad (IV-5)$$

where  $R_{12,34}$  and  $R_{23,41}$  are pseudoresistances, defined as  $R_{12,34} = V_{34}/I_{12}$  and  $R_{23,41} = V_{41}/I_{23}$ , respectively.  $V_{34}$  corresponds to the voltage applied between probe 3 and probe 4 when the current  $I_{12}$  is injected through probes 1 and 2 (See Figure IV-6). Similar definitions apply to  $V_{41}$  and  $I_{23}$ .  $t_{Si}$  is the Si film thickness and  $f$  is a configuration coefficient given by [13]. For additional accuracy, the Van der Pauw measurements are repeated by injecting the current from probe 3 to probe 4 and from probe 4 to probe 1. The final resistivity is the average value.

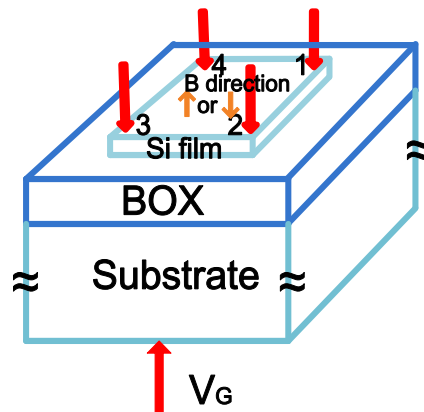


Figure IV-6: Schematic configuration of Van der Pauw and Hall effect measurements. The direction of the magnetic field ( $B$ ) can be reversed. 4 metallic probes were placed in the corners of the die and a back-gate bias can be applied to the substrate.

The Hall effect was discovered in 1879. We consider a schematic representation for a  $p$ -type semiconductor in Figure IV-7. Hall found that a current flowing along a conductor, where a magnetic field ( $B$ ) is perpendicularly applied, induces a deviation of the carriers by the Lorentz force ( $F$ ). The Lorentz force tends to deviate the holes from their originally horizontal path downwards to the bottom. Since no current is allowed in the transversal direction, a Hall electric field ( $E_H$ )

develops to oppose the Lorentz force. Hence, a potential drop ( $V_H$ ) can be measured between the upside and the bottom side of this semiconductor.

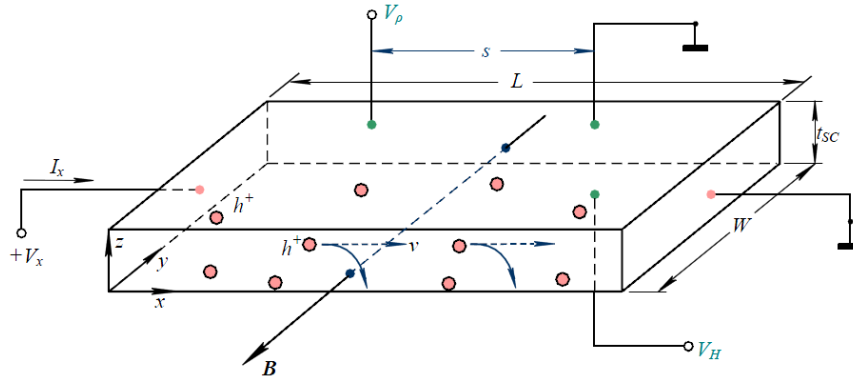


Figure IV-7: Schematic illustration of Hall effect measurements in a p-type semiconductor.

Hall Effect measurement is a very important tool to determine the carrier mobility and the free carrier density independently. The trapped carriers cannot contribute to the Hall voltage as the Lorentz force, relying on the carrier velocity ( $v$ ), becomes zero for them. Hall effect technique is largely used in the characterization of semiconductors materials because it gives the carrier density (which can be smaller than the doping concentration  $N_{A,D}$ ) and the Hall mobility ( $\mu_H$ ). The Hall effect works similarly in Van der Pauw configuration.

In our study, a magnetic field ( $B = 0.5$  T) vertical to the dies is applied. The current ( $I_x$ ) is then injected through diagonally opposite probes (for example, 1 and 3, Figure IV-6) and the corresponding voltage between the two other probes (2 and 4) is measured. The measurement is repeated by (i) injecting the current from the other probe and (ii) reversing the magnetic field ( $+B$ ,  $-B$ ). The same procedure is applied with changing the diagonal opposite probes (for example, 2 and 4) in order to verify the consistency of the measurements.

Finally, the average values represent the Hall voltage  $V_H$ . Hall factor  $R_H$  and  $N_{A,D}$  (by adjusting  $p = N_A$  and  $n = N_D$ ) can be calculated from  $V_H$  using the equation below [13]:

$$R_H = \frac{V_H t_{si}}{BI_x} = \frac{r_H}{q\rho} \quad (\text{IV-6})$$

where  $r_H = \mu_H/\mu_{vol}$  is the Hall scattering factor which depends on the scattering mechanisms and accounts for collision with acoustic phonons ( $\approx 1.18$ ) and for collisions with ionized impurities ( $\approx 1.93$ ) [13].

Finally Hall mobility ( $\mu_H$ ) is computed:

$$\mu_H = \frac{R_H}{\rho_{VDP}} \quad (IV-7)$$

Where the resistivity was measured by Van der Pauw method at  $B = 0$ .

Hall effect measurements on Si with substrate biasing were done 10 years ago [10] and again in 2006 on undoped thin SOI wafers [14].

### 1.3.3.2 Comparison of $\Psi$ -MOSFET, Van der Pauw and Hall effect results

The resistivities extracted from  $\Psi$ -MOSFET using  $\rho = 1/qN_{A,D}\mu_{vol}$  where  $N_{A,D}$  and  $\mu_{vol}$  are known (Table IV-1), Van der Pauw method and four-point probe (showed in chapter II) are compared in Table IV-2 below. The results show good agreement between the values extracted from the three techniques.

Table IV-2: Resistivities in 40 nm HD SOI measured with different methods.

Dopants	$\Psi$ -MOSFET $\rho$ (cm. $\Omega$ )	VDP $\rho$ (cm. $\Omega$ )	Four-point probe $\rho$ (cm. $\Omega$ )
Arsenic	0.014	0.01	0.013
Phosphorus	0.016	0.012	0.016
Boron	0.027	0.018	0.025

In thin 40 nm HD SOI, the four-point technique gives the value of  $\mu_{vol}$  ( $\rho = 1/qN_{A,D}\mu_{vol}$ ) only if the activated doping concentration is known. Up to date, the volume mobility  $\mu_{vol}$  in thick films can be obtained from tables available in the literatures which give the resistivity *versus* doping level [8]. However, such tables have not been computed for ultrathin highly doped Si films.

Table IV-3: Extracted volume and Hall mobility and activated doping concentration for 40 nm thick SOI film from  $\Psi$ -MOSFET and Hall effect measurements.

Dopants	$\Psi$ -MOSFET		Hall effect @ $V_G = 0$ V	
	$N_{A,D}$ ( $10^{19}$ cm $^{-3}$ )	$\mu_{vol}$ (cm $^2$ /V.s)	$N_{A,D}$ ( $10^{19}$ cm $^{-3}$ )	$\mu_H$ (cm $^2$ /V.s)
Arsenic	0.53	86	0.58	108 (e)
Phosphorus	0.52	73	0.46	107 (e)
Boron	0.47	50	0.62	55 (h)

The comparison between the extracted parameters (mobility and doping concentration) from  $\Psi$ -MOSFET and Hall effect experiments is illustrated in Table IV-3. Note that Hall mobility ( $\mu_H$ ) was extracted for  $V_G = 0$  V where the maximum volume conduction ( $I_D = I_{vol}$ ) is obtained. The overall agreement between Hall effect and  $\Psi$ -MOSFET results is excellent for  $N_{A,D}$ . This indicates that the  $\Psi$ -MOSFET delivers reliable results for HD SOI wafers.

However, the comparison of  $\Psi$ -MOSFET and Hall effect offers additional information on the scattering mechanisms. The Hall mobility is consistently larger than the volume drift mobility calculated in depletion (from equation (IV-1)) and larger than the surface mobility calculated in accumulation (from equation (IV-4)). The difference between Hall and drift mobilities results from the combination of Coulomb and phonon scattering. Despite the very high doping of our samples,  $r_H \approx 1.1-1.3$  shows the prevailing role of phonon scattering compared to Coulomb scattering which indirectly indicates a good quality of Si-SiO<sub>2</sub> interface after implantation.

#### **1.4 Conclusion of section 1**

We showed for the first time that the  $\Psi$ -MOSFET configuration can be adapted for heavily doped SOI wafers. The field-effect induced by back-gate biasing is small, due to very high doping level (up to  $10^{19}$  cm<sup>-3</sup>), but still exploitable for detailed characterization. The volume conductance is modulated by the increase of the depletion region and dominates the total current. An accumulation channel is formed and gives insight on the carrier mobility at the film/BOX interface.

$\Psi$ -MOSFET is the only method able to provide independently the carrier concentration and mobility without the need of a magnetic field (B). We also showed that parameters extraction from  $\Psi$ -MOSFET measurements is possible using an updated model which takes the volume current into account. The results for doping concentration and mobility extraction show convincing agreement between  $\Psi$ -MOSFET and Hall effect.

It follows that the  $\Psi$ -MOSFET can be substituted to the more tedious, time-consuming Hall effect measurements. This conclusion has been validated by

comparing  $\Psi$ -MOSFET, Hall and four-point probe experiments for resistivity measurements.

The above experiments procedure has been reported on thinner films (10 nm) with high doping ( $\sim 10^{20} \text{ cm}^{-3}$ ). The results and conclusions are similar.

## **2. SOI-based sensor for gold nanoparticles detection**

### **2.1 SOI as a detection platform**

In the last few years, several detection techniques using SOI wafers were proposed. One of these techniques is based on the conductance variation due to the presence on the SOI surface of chemical or biological species that are aimed to be detected.

In this context, the detection capability of silicon nanowires (Si-NWs), fabricated from SOI substrates, has already been demonstrated. Several groups showed the possibility to detect pH, proteins [15], DNA [16], *etc.* deposited on the nanowire surface. The operating principle of the devices is based on the functionalization of the surface in order to catch the molecules to be detected. If the presence of these molecules is accompanied by a change of the charging state of the surface, a shift in the conductance of the functionalized wire appears. One of the nanowire issues is the fabrication technology that can be complex.

The use of thin SOI films for detection could be an answer to the complicated fabrication techniques of nanowires. Charges deposited on the top of thin film SOI, the film-to-air interface in particular, are sensed by carriers flowing at the film-BOX interface. Therefore, thinner films are more subject to the influence of surface charges due to stronger electrostatic coupling. We believe that SOI substrates with ultra-thin silicon film are successful candidates for chemical and biological detection purposes.

As detailed in chapter II, in pseudo-MOSFETs with thin films (< 88 nm), the threshold/flat-band voltages ( $V_{T,FB}$ ) depend on the surface condition and by extension, on any charge intentionally deposited on the free surface. Our results together with those in ([17], [18]), showed that a surface passivation of SOI films, which changes the charge density at the free surface, has a strong impact on the electrical response. A revised model [18] was presented which takes into account the shift of the threshold voltage and subthreshold swing (S) of the  $\Psi$ -MOSFET, induced by the surface state.

Recent research showed that as-fabricated SOI wafers can be utilized as radiation detectors to monitor the buildup of positive charges in the buried oxide

(BOX) [19]. The proton irradiation induces positively charged oxide traps and defect interface traps (Figure IV-8a). Another application was explored by grafting a monolayer of molecules (Figure IV-8b) with electron-donating abilities on SOI surface [20]. The results show a shift of the threshold voltage that allows opening a channel in the silicon film. The drain current can be modulated according to the electron-donating ability.

Both studies presented above suggest that  $\Psi$ -MOSFET can be easily used for detection functions, which is indeed an exotic application. Moreover, Ionica *et al* showed that  $\Psi$ -MOSFET configuration can be easily used for bio and chemical detection purposes (*i.e.*, for bio-sensing applications as ‘conjugate-holders’) [21].

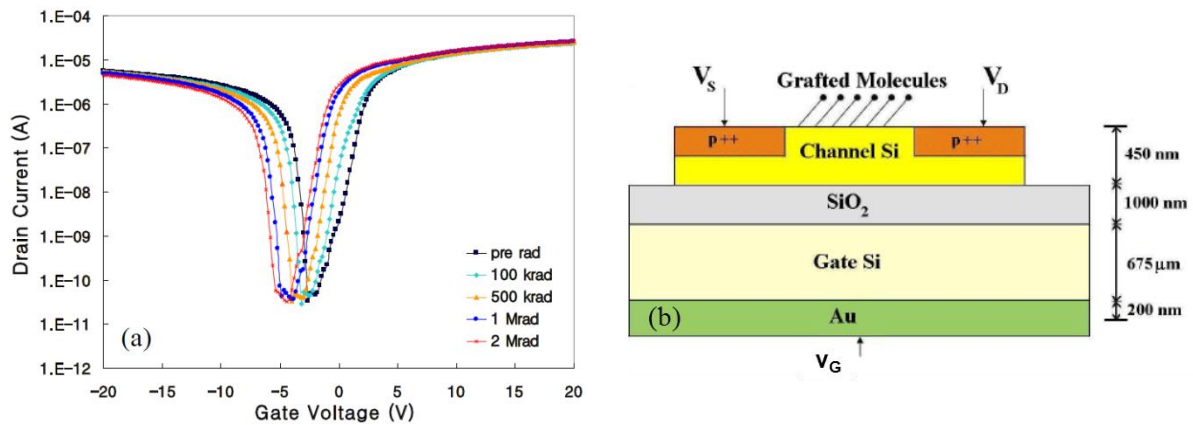


Figure IV-8: (a) Drain current versus gate voltage characteristics of  $\Psi$ -MOSFET for increased total dose radiation after subsequent annealing [19]. (b) Schematic side-view representation of the device used for the molecule detection [20].

Additionally to detection aspects, other authors proposed another application of functionalized SOI substrates for fabrication of hybrid memories. They showed the possibility to obtain hybrid memory devices by grafting porphyrins on SOI [22].

Based on these observations, we will explore in the following section an SOI based sensor with controlled deposition of gold nanoparticles (NP) on the top silicon film.

## 2.2 Gold nanoparticles detection by $\Psi$ -MOSFET

We propose the direct use of ultra-thin SOI films for electrical detection of gold nanoparticles [23]. The choice of SOI substrates comes from the technology-light solution, which makes the sensor very simple to implement and from the



surface-to-channel coupling in thin films. Furthermore, this detection technique with gold nanoparticles is motivated by the wide applications of the nanoparticles (NP) in biochemical sensing and nano-medicine (*e.g.* cancer diagnosis, DNA detection [24]). Indeed, different molecules can be easily attached to gold NP. The nanoparticles also have interest in memory devices as it is possible to store charges inside them [25]. The fabrication steps and the electrical response are discussed below.

### 2.2.1 Fabrication steps of SOI sensors

Dies for the  $\Psi$ -MOSFET were isolated from full SOI wafers. As usually, the pseudo-MOSFET fabrication needs a single lithography step, in order to define SOI islands of 5 mm  $\times$  5 mm area. Afterwards, a two-step procedure for particle attachment has been used:

- i. First, the SOI surface with native oxide was treated with Amino-Propyl-Tri-Ethoxy-Silane (APTES) diluted with ethanol solution for better electrostatic bounding to silicon film. Wafers were baked on a hotplate at 120°C for 30 minutes after the APTES treatment in order to complete the covalent binding between APTES and the surface [26]. An amine terminated surface has been obtained.
- ii. Secondly, colloidal gold particles, stabilized with citric acid, were dispersed on the surface [27]. After a deposition time between 5 and 15 minutes, the samples were rinsed with de-ionized water and dried with nitrogen.

Samples with 5 nm and 50 nm diameter gold nanoparticles on SOI wafers have been fabricated and tested. Figure IV-9 shows atomic force microscopy (AFM) images of the distribution of gold nanoparticles (50 nm diameter) on the SOI surface. In order to test the reproducibility of the technological process, two samples have been processed with the same technological parameters (APTES concentration and time, gold deposition time). Two AFM images corresponding to these samples are presented. Similar densities of particles were obtained:  $3.7 \times 10^8 \text{ cm}^{-2}$  and  $4.1 \times 10^8 \text{ cm}^{-2}$ . The density was calculated by counting the number of gold nanoparticles and dividing by the total area. The variability of the nanoparticle density is of about 5 % - 10 %.

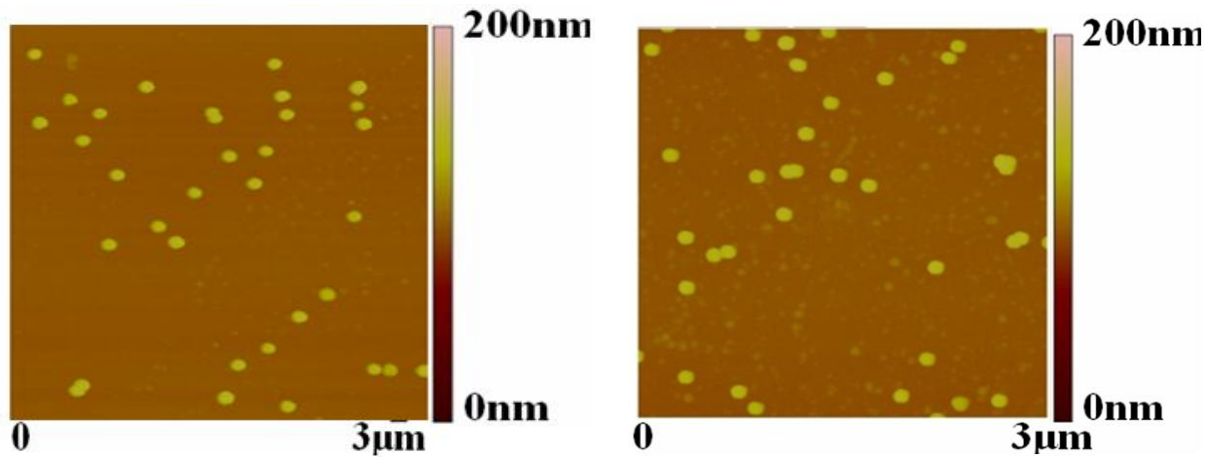


Figure IV-9: AFM images for two samples obtained after attachment of gold nanoparticles (50 nm diameter). The scan area of both images is of  $3\ \mu\text{m}$  per  $3\ \mu\text{m}$ .

### 2.2.2 Sensor response

The key electrical parameters for this study are  $V_T$  and  $V_{FB}$ . In order to extract these two parameters from the measurements, the Y-function [9] is used in order to simplify the dependence *versus*  $V_G$ . Pseudo-MOSFET measurements have been performed after each functionalization step (APTES and gold deposition). The SOI samples under test had 30 nm film thickness and 145 nm BOX thickness. The APTES treatment leaves behind amino-terminated free surface that is positively charged [26]. The results presented in Figure IV-10a indicate indeed a threshold voltage lowering, *i.e.* a shift to the left of the  $I_D$ - $V_G$  curves.

Gold nanoparticles of 50 nm diameter were deposited on the same sample. The gold nanoparticles are surrounded by a chemical coating in order to stabilize them, which leads to a net negative charge [27]. According to MOSFET theory [8], a shift of the curves to the right is expected. Figure IV-10b shows two electrical characteristics measured for the same SOI structure as in Figure IV-10a, one before the gold nanoparticle deposition (empty symbols) and other after deposition (full symbols). The shift to the right of the curve after gold deposition is in agreement with the theoretical expectations for negative surface charge.

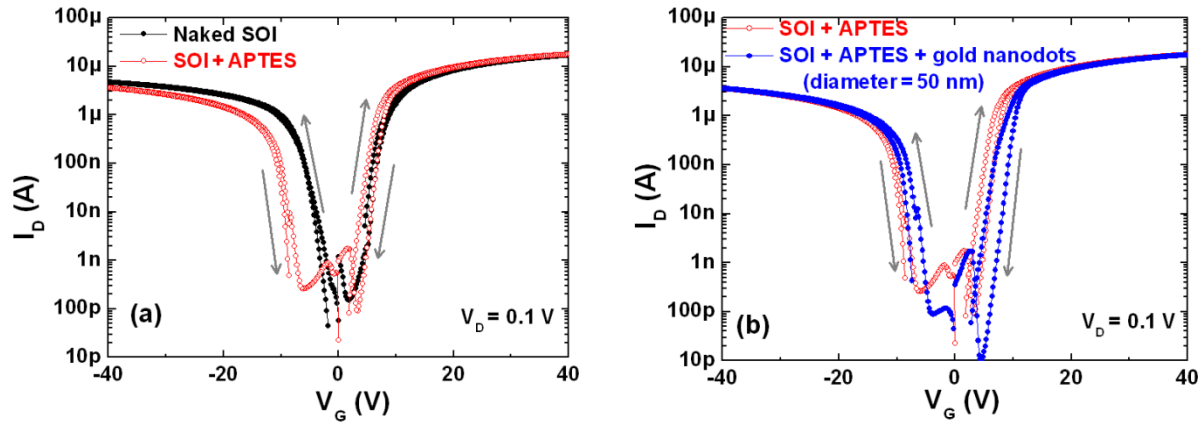


Figure IV-10: (a)  $I_D$ - $V_G$  curves obtained before any chemical treatment (full symbols) and after APTES treatment (empty symbols). (b)  $I_D$ - $V_G$  curves after APTES treatment (empty symbols) and after gold particles deposition (full symbols).  $V_G$  is scanned forwards and backwards from 0 to -40 V and from 0 to +40 V. Film thickness of 30 nm and 145 nm BOX.

It is worth pointing out that a hysteresis appeared in the curves after the nanoparticle deposition (see Figure IV-10b). The hysteresis effect comes from the fact that gold nanoparticles act as charge holders where the electrons can be trapped and de-trapped depending on the gate voltage sweep. This phenomenon opens a road towards nano-memory applications for these hybrid devices. These results were validated with other geometries of SOI (20 nm film thickness) and of gold nanoparticles (5 nm and 100 nm diameter). After the qualitative proof of concept of our device, the following sub-sections are dedicated to more quantitative analysis of the sensor (reproducibility, sensitivity and particle size/density improvements).

### 2.2.2.1 Reproducibility

In order to validate that the  $V_T$  shifts obtained above result from the chemical treatments applied and that the data is reproducible, we fabricated and tested two samples (A & B) of 30 nm film thickness with the same density of particles ( $\sim 4 \times 10^8$   $\text{cm}^{-2}$  with 50 nm diameter). Table IV-4 and Table IV-5 show the extracted parameters before any process (naked SOI) and after completing gold deposition.

Table IV-4: Comparison of  $V_{FB}$  for two quasi identical samples A & B. Gold nanoparticles with 50 nm diameter and  $4 \times 10^8$  density.

	Naked SOI	SOI + gold	$\Delta V_{FB}$
Sample A	-4.2 V	-7.2 V	3 V
Sample B	-4 V	-7.7 V	3.7 V

Table IV-5: Comparison of  $V_T$  for two quasi identical samples A & B. Gold nanoparticles with 50 nm diameter and  $4 \times 10^8$  density.

	Naked SOI	SOI + gold	$\Delta V_T$
Sample A	7.5 V	6.4 V	1.1 V
Sample B	8 V	6.4 V	1.6 V

The flat-band voltage shows a variation of  $\sim 18\%$  from sample A to sample B after completing gold deposition. For the threshold voltage shift, the absolute values are within 5% but the relative shift  $\Delta V_T$  varies by 30%. As the measurement is based on pressure probes and is done on large-area samples (5 mm  $\times$  5 mm), typical variations in  $\Psi$ -MOSFETs extracted parameters, from one sample to another, are of maximum 5%. We also saw previously that the process itself can produce variations of particles densities of about 5%. It is concluded that  $V_T/V_{FB}$  values and their shifts due to the presence of particles present a reasonable reproducibility. Note that the sensitivity (shift magnitude:  $\Delta V_{FB}$ ) on the holes side (negative back gate voltages) is higher than on the electrons side ( $\Delta V_T$ ) and the variability is lower. This result was repeatedly confirmed on all other 30 nm film thickness samples we fabricated.

### 2.2.2.2 Impact of particle size and density

As previously stated, the charge for gold nanoparticles is actually given by the chemical coating that allows them to remain independent and not to agglomerate. Therefore, one expects to have a higher quantity of charges associated to a higher diameter [28]. In a very rough approximation, the shifts of the curves after adding gold nanoparticles are given by:

$$\Delta V \approx \frac{Q_T}{C_{ox}} \quad (IV-8)$$

with  $C_{ox}$  being the buried oxide capacitance and  $Q_T$  the total charge associated to all the particles on the surface. The charge associated to one single gold nanoparticle,  $Q_{particle}$ , can be estimated by using the density of particles measured with AFM (density<sub>AFM</sub>):

$$Q_{particle} = \frac{Q_T}{\text{density}_{AFM}} \quad (IV-9)$$

Table IV-6 shows the extracted charge/particle for two samples with 20 nm film thickness, one with 5 nm particle diameter and the other with 50 nm particle diameter. The charge per particle is higher for the higher diameter which is consistent with the fact that the charged coating has larger surface.

Table IV-6: Particle size impact on electrical response.

Particle diameter (nm)	Particle density (cm <sup>-2</sup> )	Shift ( $\Delta V$ ) (V)	Q <sub>/particle</sub> (C)
5	$4.7 \times 10^9$	5.1	$0.3 \times 10^{16}$
50	$5.5 \times 10^8$	3.5	$1.5 \times 10^{16}$

The sensitivity of our simple detector with respect to particles density was demonstrated. The proportionality of the response was tested on SOI with 20 nm film and 145 nm BOX thicknesses. All samples had 5 nm diameter particles. Figure IV-11 shows the shifts of the curves, for negative and for positive gate voltages, with respect to the density of particles. A clear proportionality between the  $V_T$  and  $V_{FB}$  shifts and the density of particles is evidenced.

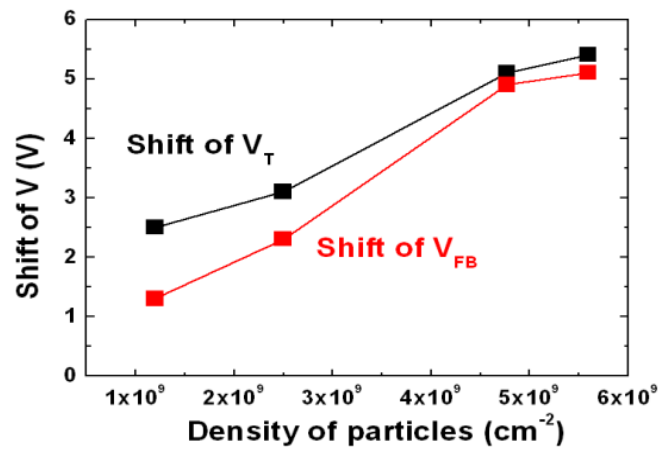


Figure IV-11: Shifts of  $V_T$  and  $V_{FB}$  versus density of gold nano-particles (5 nm diameter) on the surface of SOI wafer.

### 2.2.2.3 Sensitivity improvement

The sensitivity of the detection is expected to depend on the thickness of the SOI film, because coupling between the free surface and the channel located at the film-BOX interface is stronger for thinner films [18]. This means that the shifts of the curves should be larger with thinner films. In order to test this effect, we fabricated two samples with 50 nm diameter gold nanoparticles and with two different film thicknesses (20 nm and 30 nm) for the same BOX thickness (145 nm).

Figure IV-12a and Figure IV-12b show drain current curves for positive  $V_G$ . For negative  $V_G$ ,  $I_D$ - $V_G$  curves were traced in Figure IV-12c and in Figure IV-12d. The filled symbols represent the curves just before adding gold particles and empty symbols represent the curves after gold particle deposition. The shifts after gold deposition are clearly higher for the 20 nm film than for the 30 nm film, and this conclusion applies to both electron and hole conduction. The larger shift of the curves for thinner films implies an improvement of the sensitivity.

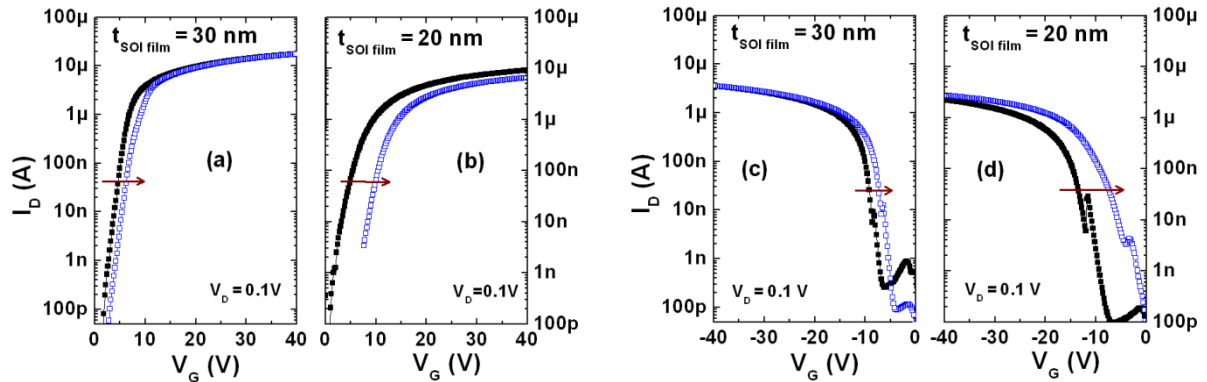


Figure IV-12:  $I_D$ - $V_G$  curves for 30 nm film thickness (a and c) and 20 nm film thickness (b and d). On each curve, the full symbols represent the curves before adding the particles and the empty symbols after adding gold particles (50 nm diameter). The back-gate voltage has been scanned for positive (a and b) and negative values (c and d).

Table IV-7 shows the extracted shift values for  $V_T$  and  $V_{FB}$ . The shift in  $V_{FB}$  is about 94 % higher and the shift in  $V_T$  is about 444 % higher for the thinner film (20 nm). This result should be multiplied by the density of the particles (40 % higher for the thinner film), the electrical response being proportional to the density of particles, as it was shown in the previous sub-section. However, the parameter variation is too large to be explained just by the higher particle density. Therefore, with thinner SOI films, larger curve shifts are obtained, hence higher sensitivity can be achieved with thinner silicon films.

Table IV-7: Shifts of the  $\Psi$ -MOSFET curves after gold nanoparticle deposition with two film thicknesses (145 nm BOX).

Film thickness (nm)	Particle density ( $\text{cm}^{-2}$ )	$V_T$ shift (V)	$V_{FB}$ shift (V)
20	$5.5 \times 10^8$	4	3.5
30	$4 \times 10^8$	0.9	1.8

## 2.3 Conclusion of section 2

We presented the proof of concept of a new, SOI sensor, the simplest that can be imagined based on the coupling between the channel at the film-BOX interface and the charge placed intentionally on the top free surface. The interest of SOI substrates comes from the technology-light solution, easy to implement. The shifts observed in the measured  $I_D$ - $V_G$  characteristics are explained with the pseudo-MOSFET theory.

The selectivity of the detection was addressed by a proper surface functionalization (APTES) which enhances the adhesion of gold nanoparticles on the surface. The reproducibility of the technological process as well as of the electrical response has been proven. The shifts in the drain current curves are proportional to the density of the charge on the surface, *i.e.* to the density of the gold nanoparticles. A gain in the sensitivity was found for thinner films SOI where the surface-to-channel coupling is more intense.

The  $\Psi$ -MOSFET configuration can be easily used for detection purposes, as long as the phenomena to be sensed are accompanied by a change in the charge distribution on the SOI structure. Our experimental results open a wide panel of bio and chemical sensing applications based on SOI wafers. Moreover, the road to memory applications is suggested by the appearance of a hysteresis effect.

### **3. $\Psi$ -MOSFET characterization of 3D vertically stacked SiGe and SiGeC nanowires**

#### **3.1 Overview**

Nowadays challenges in CMOS device performance can be approached by alternatives to silicon planar integration which is reaching fundamental limits in terms of miniaturization, power and performance ([1], [29]). The short-channel effects (SCEs), shallow junctions and gate current leakage are some examples of possible disturbances affecting the good operation of microelectronic devices. To better illustrate the implications of miniaturization on the transistor operation, we will focus on short-channel effects [30].

In a long channel transistor, the profile of the surface potential is practically flat along the entire gate length. Reducing the size of transistors, the lateral component of the electrical field (due to  $V_D$  for example) is no longer negligible. The potential distribution changes from one dimensional (1D) distribution (governed by the vertical gate-induced field  $E_y$ ) to a two-dimensional (2D) distribution ( $E_x$  and  $E_y$ ). Scaling down the length implies that electrostatic control of the channel by the gate is disturbed by space charge areas dominated by junctions (source/substrate and drain/substrate). In short-channel MOS transistors, these areas became closer to each-other, until they are partially overlapped. The depletion charge in the channel is then largely controlled by the junctions and not by the gate. This effect is even more important when the drain voltage increases. The mechanism is called Drain-Induced Barrier Lowering (DIBL) [31] and it results in a decrease of threshold voltage.

Furthermore, the effective mobility ( $\mu_{\text{eff}}$ ) depends on the bias applied between drain and source and on the gate. Shrinking the devices, the impact of the longitudinal field component on the mobility increases leading to velocity saturation. The channel resistance decreases in shorter channels and we can no longer neglect the effect of series resistance of the source and drain.

Faced with so many challenges, it is necessary to find innovative solutions adapted to each of these issues in order to perpetuate the miniaturization of devices while ensuring the amelioration of their performance. In order to do so, recent trends in microelectronics are to explore nanowire gate-all-around (GAA) structures and



alternative channel materials with superior properties. For example, the best possible electrostatic control and immunity against short-channel effects can be achieved by using GAA nanowire-based transistors [32]. Nevertheless, the small diameters of nanowire devices drastically limit the drive current. To overcome this issue, nanowires can be integrated in parallel tri-dimensional (3D) networks [33].

Furthermore, the transport properties can be improved by changing the channel materials. For instance, replacing silicon with Germanium (Ge) or SiGe allows obtaining higher mobility for holes [34]. Germanium nanowires for multi-channel technology appear as promising candidates for transistor performance enhancement. One of the critical issues in Ge nanostructures is again the low level of drain current that can be supported. Bundling more NWs per device and vertically stacking them (see Figure IV-13) improves the on-state current [35]. Figure IV-13a shows a schematic view of vertically stacked SiGe NWs and Figure IV-13b and Figure IV-13c show SEM images of three-stacked and four-stacked NWs respectively. Figure IV-13d illustrates four-stacked levels of SiGe NWs with 5 rows.

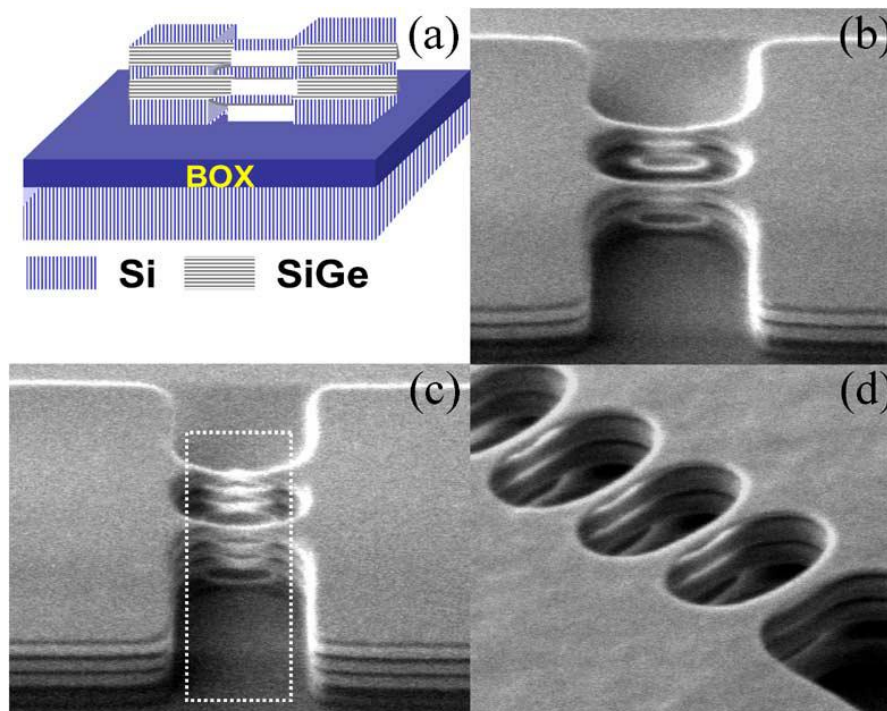


Figure IV-13: (a) Schematic representation of SiGe NW stacks. Tilted view SEM images after release of stacked NW for (b) 2X laterally arrayed three-stacked NWs, (c) 2X laterally arrayed four-stacked NWs and (d) 5X laterally arrayed four-stacked NWs [35].

The electrical study of NWs *before* CMOS process offers relevant information and feed-back on optimization solution before starting the long technological sequence [36]. One of our research partners (CEA-Leti, France) fabricated 3D

vertically stacked Ge-enriched SiGe or SiGeC NWs by a top-down technique. The fabrication process is described in section 3.2. We proposed a characterization technique of nanowires before gate processing in order to qualify the quality of these structures (in section 3.3).

### 3.2 Fabrication process

The Ge enrichment method has been proposed in 2001 for the fabrication of strained SiGe and Ge short-channel MOSFETs [37]. It is based on the dry oxidation, at high temperature, of a SiGe layer with a low initial concentration of Ge. The fabrication process has been proposed in CEA-Leti using the germanium condensation technique in silicon on insulator layers ([38], [39]). The fabrication method is based on the epitaxial growth of Si/SiGe super lattice, selective etching of Si compared to SiGe and on the Ge enrichment technique (Figure IV-14).

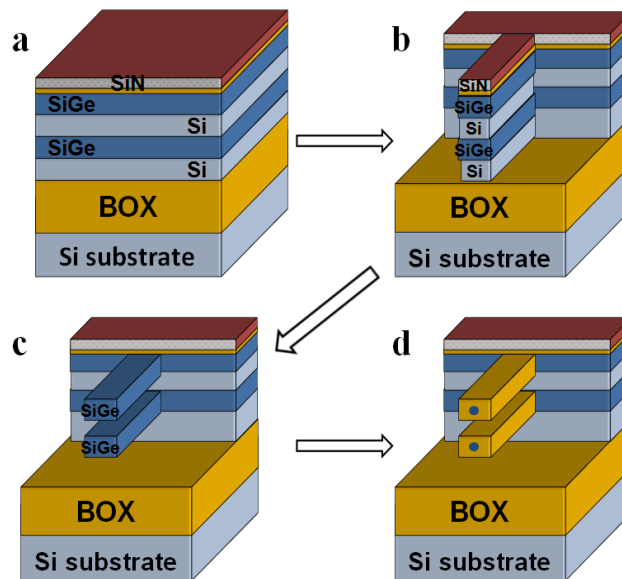


Figure IV-14: Fabrication process of suspended 3D SiGe nanowires. (a) Epitaxy of Si and SiGe layers. (b) Photolithography and anisotropic etching to define the geometry (width and length) of the wires. (c) Selective isotropic etching of intermediate Si layers. (d) Ge condensation under dry oxidation.

Figure IV-14 shows the fabrication process of two suspended Ge nanowires starting from an SOI wafer:

- a. The epitaxy step (Figure IV-14a) is performed at 650°C by Reduced Pressure Chemical Vapor Deposition (RPCVD) on SOI wafer. A super-lattice of Si layers alternating with SiGe layers is obtained. A 5 nm thick

silicon dioxide layer followed by a 100 nm thick silicon nitride (SiN) layer are then deposited on the surface and used as a hard mask.

- b. Mesa structures are isolated by photolithography and anisotropic etching (Figure IV-14b).
- c. Selective isotropic etching of Si layers *versus* SiGe layers allows SiGe beams releasing (Figure IV-14c).
- d. The SiGe beams are then enriched by Ge condensation under 900°C in dry oxygen (Figure IV-14d) in order to increase the Ge content and achieve almost pure Ge, in the middle of the structures by consuming the Si during the oxidation process.

The above processing sequence was used here to fabricate two-level stacked SiGe (Figure IV-15a) and three-levels stacked SiGeC (Figure IV-15b) wires. Fabricated nanowire channels are suspended and surrounded by silicon dioxide.

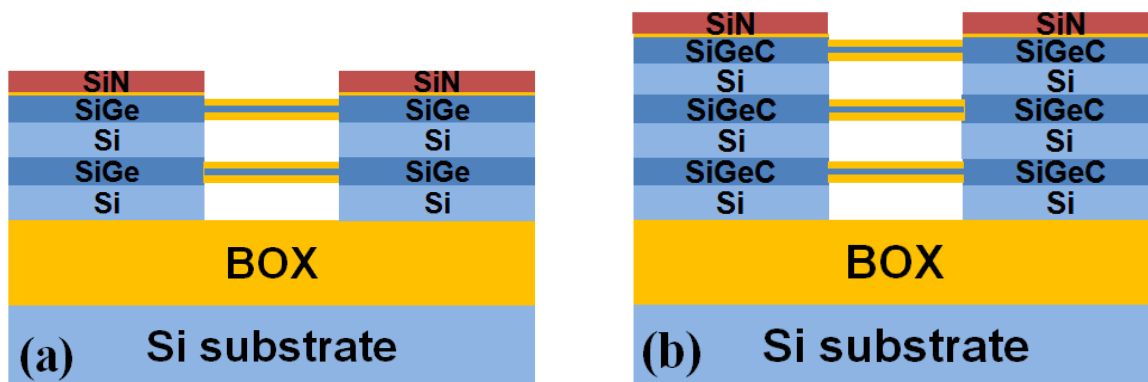


Figure IV-15: Schematic view of two suspended germanium-enriched nanowires fabricated from SiGe layers. (b) Three suspended germanium-enriched nanowires fabricated from SiGeC layers. Each suspended nanowire is surrounded by silicon dioxide.

From the fabrication point of view, the interest in adding carbon (C) in the super-lattice structure is to reduce the mismatch between the lattice parameters of SiGeC and Si. In this case, the selective etching used to free the nanowires is more stable and avoids the bowing of the structures.

Figure IV-16 shows a scanning electron microscope (SEM) image of the cross-section of Ge-enriched NWs obtained from SiGeC and surrounded by SiO<sub>2</sub>. In order to be able to view this image by SEM, polycrystalline silicon was used to fill-in the suspended structures before cutting them. Nanowires of crystalline quality have been obtained (dark dots in Figure IV-16a). Figure IV-16b shows a SEM image of the top

view of multiple parallel nanowires after the selective etching of Si *versus* SiGeC. The material sandwich seen from above is composed of silicon dioxide surrounding the SiGeC NWs. Only the upper wire is visible. At the top of the source and drain mesas, a silicon nitride layer is visible.

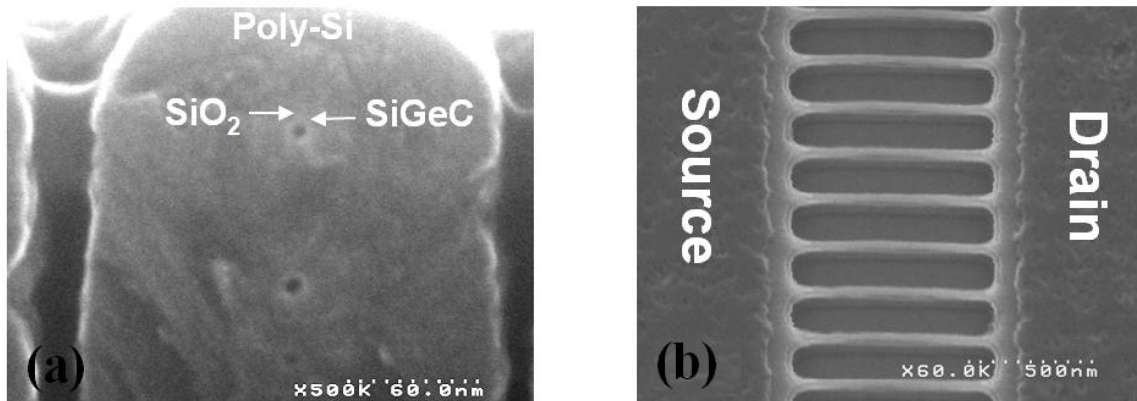


Figure IV-16: (a) SEM image of cross-section nanowires after germanium condensation. Ge-enriched wires (dark dots) are surrounded by silicon dioxide. (b) Top view SEM picture of multiple parallel nanowires [39].

Before moving to electrical characterization let us give one important detail about the geometry of the structures. When referring to the geometry of the structure, we define two kinds of widths. The ‘designed’ width corresponds to the designed pattern on the mask used for the lithography and anisotropic etching (Figure IV-14b). During the condensation process, the Si is oxidized selectively with respect to Ge, so a germanium enriched channel surrounded by silicon oxide is obtained, as seen in Figure IV-16a. The effective width ( $w_{eff}$ ) of the Ge enriched channel is smaller than the designed width ( $w_{des}$ ) as shown in Figure IV-17. A relevant consequence is observed when starting from the same material but with two different designed widths. After the same oxidation time (meaning the same silicon consumption), it is possible to obtain wires with different germanium concentrations. The designed geometry of the wires under test is 100 or 500 nm long and 50 or 100 nm wide.

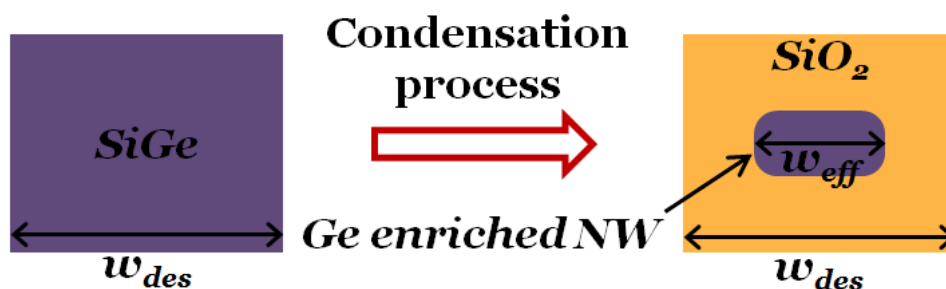


Figure IV-17: Schematic representation of the nanowire width before and after condensation process.

The use of both selective etching of Si *versus* Ge and condensation technique allows the 3D integration of SiGe and Ge 3D nanowires. This new architecture will increase the current per unit area by multiplying the number of stacked conduction channels.

### 3.3 Electrical transport properties of SiGe NWs

Once the NWs have been liberated and isolated, it is important to probe their electrical properties before completing the time-consuming CMOS process (gate stack, source/drain implants, back end). Knowing the properties of as-grown nanowires enables the optimization of the material content, device configuration and fabrication steps.

#### 3.3.1 Basic characteristics

The characterization task is challenging because undoped NWs are fully depleted, preventing current flow. The only subsisting solution for inducing a mobile charge is to bias the substrate and therefore to use it as a back-gate. The capacitive coupling between the substrate and the nanowires is done *via* the buried oxide of 145 nm thickness. This is exactly the principle of the pseudo-MOSFET, which is adapted here to investigate the electrical transport properties of NWs. The electrical set-up is shown in Figure IV-18a for SiGe NWs and in Figure IV-18b for SiGeC NWs. Two metallic probes placed on the top surface of the NW stack are used as source and drain.

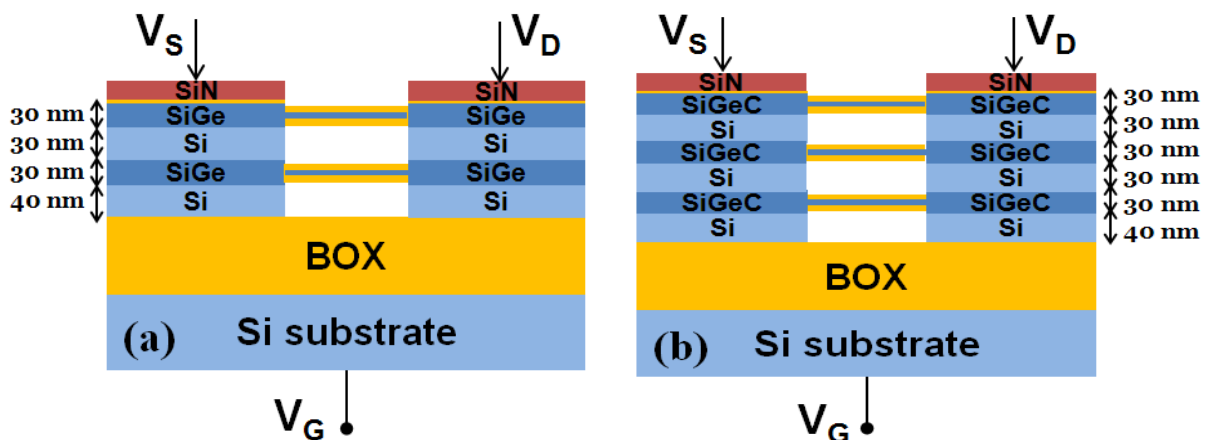


Figure IV-18: Electrical set-up of (a) two suspended and (b) three suspended nanowires.

The first step before we go into detailed characterization is to test the ohmic behavior of connected NWs. Figure IV-19 shows linear drain current *versus* drain voltage curves for various back-gate voltages. The nanowires exhibit clear ohmic conduction. Moreover, the drain current is modulated by the voltage applied on the substrate, which opens the way to MOSFET-like characterization. Without substrate biasing ( $V_G = 0$  V), the current is zero which proves that the NWs are fully depleted.

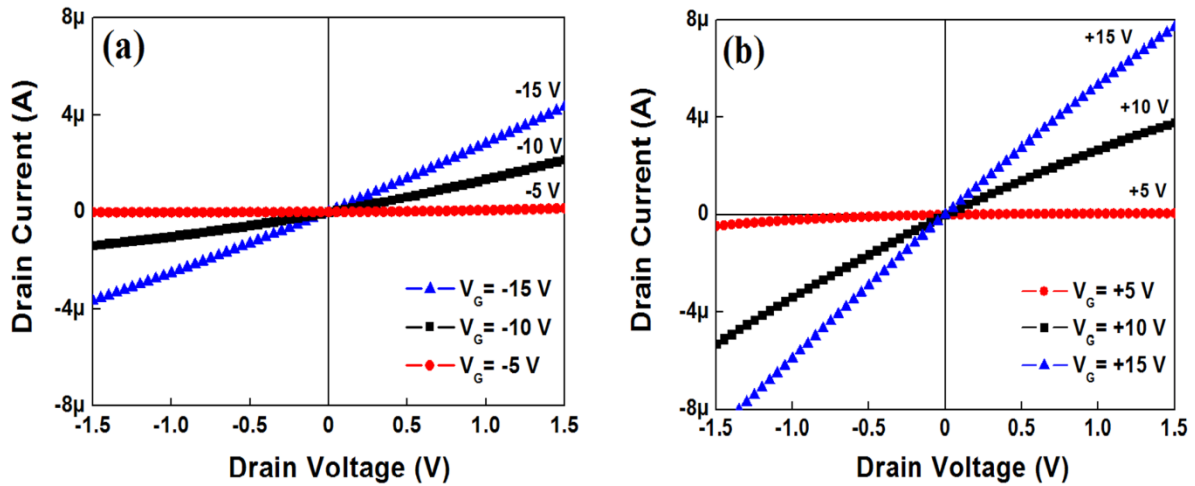


Figure IV-19: Drain current versus drain voltage for various back-gate voltages: negative in (a) and positive in (b). The designed geometry of the wire under test is 100 nm long and 100 nm wide.

The peculiarity of the two graphics (Figure IV-19a & Figure IV-19b) is the possibility to activate a drain current with both positive and negative back-gate voltages. As the chemical content of the nanowires is mainly germanium, in which the mobility of holes is much higher than the mobility of electrons [34], one would expect to primarily observe a channel of holes. This means that only a negative back-gate voltage should give rise to a drain current, which is not the case.

In order to document this puzzling ambipolar conduction, we show in Figure IV-20 drain current *versus* back-gate voltage ( $I_D$ - $V_G$ ) curves obtained for two structures of 100 nm length, one with a designed width of 100 nm (Figure IV-20a) and the other of 50 nm (Figure IV-20b). The curve obtained for a width of 100 nm confirms the results in Figure IV-19: transport shows both electron and hole channels. Surprisingly, when the same characteristic is traced for a narrower nanowire ( $w_{des} = 50$  nm), only a channel of holes is created (Figure IV-20b). Moreover, the study of a 100 nm wide and 500 nm long structure also shows a loss of the electron channel (inset of Figure IV-20b). So, electrons and holes channels are

created in the structure with  $W/L$  of 1 while only the hole side is visible for  $W/L$  of  $1/2$  and  $1/5$ .

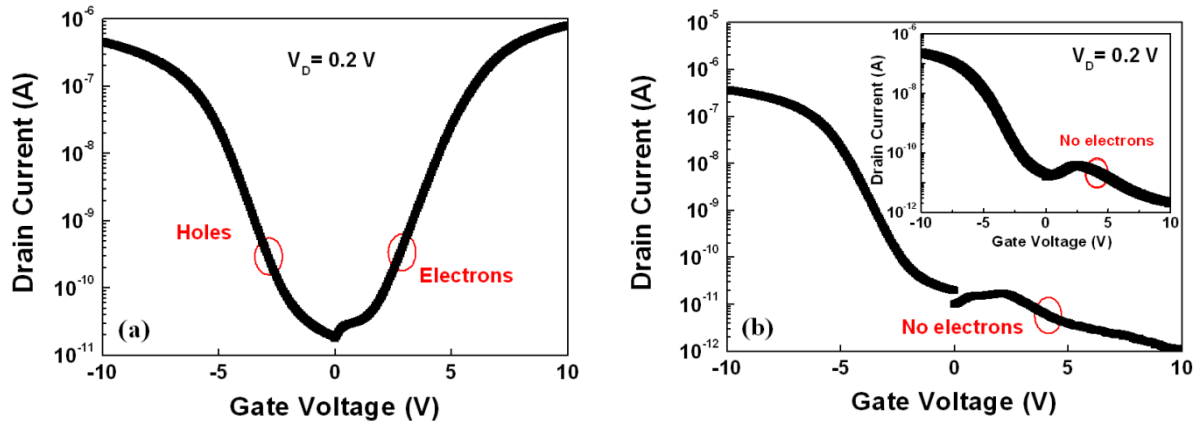


Figure IV-20: Drain current versus back-gate voltage for a SiGeC-based NW of 100 nm length with  $w_{des} = 100$  nm (a) and  $w_{des} = 50$  nm (b). Inset:  $I_D$  versus gate voltage  $V_G$  for a nanowire with  $w_{des} = 100$  nm and  $L = 500$  nm.

We therefore conclude that the aspect-ratio ( $W/L$ ) plays an important role controlling the appearance of the electron channel. Two possible phenomena, both geometry-dependent, need to be taken into consideration, as they might be responsible for the onset of the electron channel:

- i. during the condensation process, a parasitic wire of silicon subsists under the short and wide SiGeC wires and enables the conduction of electrons and holes;
- ii. bowing and sticking of the nanowires can occur during the selective etching process.

We also considered the possibility of enhanced enrichment (higher Ge concentration) in the narrow NW ( $w_{des} = 50$  nm), which can suppress electron conduction. However, the two NW with  $w_{des} = 100$  nm exhibit contrasting behavior according to their length.

### 3.3.2 Carrier transport and impact of series resistance

The impacts of device geometry and germanium concentration on the current flowing through the NWs will be discussed. We will also show that a correction of the measured drain current is necessary in order to mitigate the strong influence of series resistance ( $R_{SD}$ ).

### 3.3.2.1 Hole carrier transport and mobility

For parameter extraction, the geometrical factor ( $f_g$ ) is normally equal to  $W/L$  where  $W$  and  $L$  represent the width and length of the transistor. In order to take into account the real value of the drain current in our parameter extractions, we considered that  $f_g$  is equal to number of nanowires that are vertically stacked multiplied by  $w_{eff}/L$  (here  $3 \times (w_{eff}/L)$ ). The extractions of  $\mu_o$ ,  $V_T$  are done using the Y-function method [9]. Other parameters such as subthreshold swing  $S$  and series resistance  $R_{SD}$  can also be extracted as documented in chapter II.

Table IV-8 shows the geometry, the Ge concentration (Ge %) and the extracted low-field mobility of holes ( $\mu_p$ ). Superior hole mobility values were obtained in the nanowire with a higher Ge (100 %) concentration, *i.e.* narrow width ( $w_{des} = 50$  nm). This result is in agreement with previous data obtained for SiGe thin films on insulator [34]. It suggests that hole transport is primarily dominated by the material nature (Ge) rather than by the interface traps, the density of which can increase in nanowires with smaller diameter [40]. In principle, the interface between Ge enriched NW and the surrounding silicon oxide has high quality because  $SiO_2$  was grown during the Ge condensation, with a dry oxidation process and high temperature. Therefore, the density of states at the interface is presumably low and does not affect the channel conduction.

Table IV-8: Geometry and electrical properties of SiGeC vertically stacked 3-level nanowires in a single row.

L (nm)	Per NW		3-level NWs		@ $V_G = -10$ V
	$w_{des}$ (nm)	$w_{eff}$ (nm)	Ge (%)	$\mu_p$ ( $cm^2/V.s$ )	$I_D$ (nA)
100	50	9	100	80	390
100	100	60	40	14	450
500	100	60	40	34	230

The values of the  $w_{eff}$  and the Ge concentration were taken from [41] after investigation by SEM and EDX studies, respectively. The relatively low values of extracted mobility are explained by the difficulty to determine the precise effective width and also by the fact that the series resistance in these samples is very high (due to undoped source and drain). Using the experimental  $\theta_1$  values, we can estimate the series resistance to about 60 k $\Omega$  for  $w_{des} = 100$  nm and  $L = 100$  nm.



Another way to validate our experimental results is suggested by the drain current formula. The drain current should be proportional to the aspect-ratio multiplied by the mobility. We know that the mobility is Ge-concentration dependent, so the drain current should be roughly proportional to Ge concentration multiplied by  $3 \times (w_{eff}/L)$ . Figure IV-21 shows that this proportionality is qualitatively verified. We used here experimental values of drain current measured for -10 V on the back-gate (strong accumulation).

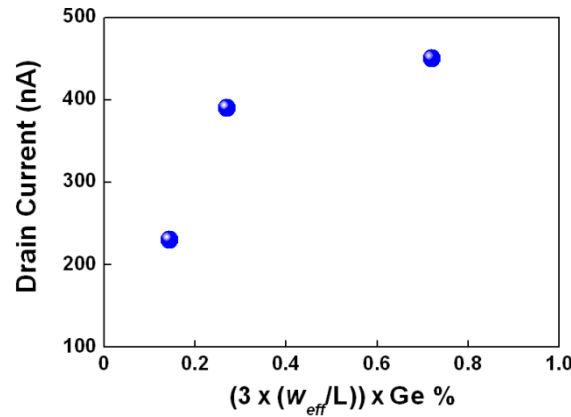


Figure IV-21:  $I_D$  measured at  $V_G = -10$  V as a function of  $(3 \times w_{eff}/L)$  multiplied by Ge-concentration.

All extracted parameters suffer from an unknown information: where is the dominant current flowing through? Normally, we have parallel conduction through multiple stacked nanowires with different gate dielectric thicknesses. As a consequence, a variable oxide capacitance should be seen by each NW: the stacked parallel channels should exhibit different threshold voltages. However, multiple threshold voltages could not be evidenced from the experimental curves: when plotting the second derivative of current with respect to gate voltage (Figure IV-22), we obtained one peak, not multiple peaks (which would be the signature of multiple  $V_T$ ). We explain this result by the thickness of the buried oxide which is much larger than the inter-wire separation. In our experimental conditions, the threshold voltage measurement cannot confirm whether the drain current flows mainly through the lowest nanowire or through several stacked nanowires, which are simultaneously unblocked by the field effect.

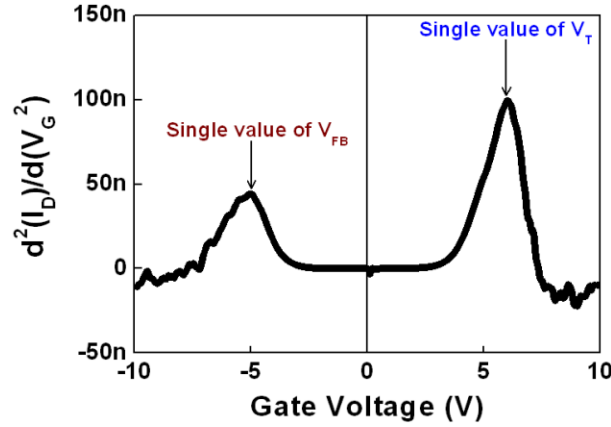


Figure IV-22: Second derivative of drain current with respect to gate voltage versus gate voltage for a nanowire with  $w_{des} = 100$  nm and  $L = 100$  nm. The peak positions indicate the threshold voltage and the flat-band voltage. These values confirm the ones obtained by the Y-function method.

### 3.3.2.2 Impact of series resistance

The series resistance is significant in this nanowire configuration because the source/drain stacks are not doped. Furthermore, the undoped nature of source/drain suggests that a field effect might also be present in source and drain stacks. This phenomenon was explored by conducting  $\Psi$ -MOSFET experiments on the source stack only (Figure IV-23a). Figure IV-23b confirms that the current through the source stack is depending on the gate voltage. The contribution of the gate-dependent series resistance has not been taken into account in the extracted values of mobility presented above. The series resistance effect is complicated due to the contributions of the *vertical* current flow in the source/drain terminals (through the Si/SiGe superlattice) and *horizontal* flow (along the SiGe layers contacting the NWs).

The average value of the nanowire series resistance is found to be higher for SiGe ( $\approx 2 \times 10^6 \Omega$ ) than for SiGeC ( $\approx 4 \times 10^4 \Omega$ ): series resistance in SiGe exceeds by about two orders of magnitude that in SiGeC NWs. The  $R_{SD}$  values were extracted using equation (II-13) illustrated in chapter II.

To clarify the effect of series resistance, we corrected the drain current by the voltage drop on  $R_{SD} = R_S + R_D$  for SiGe NWs using the equation below detailed in [42]:

$$I_{D,corr} = \frac{I_D}{1 - \frac{I_D}{V_D} (R_S + R_D)} \quad (IV-10)$$

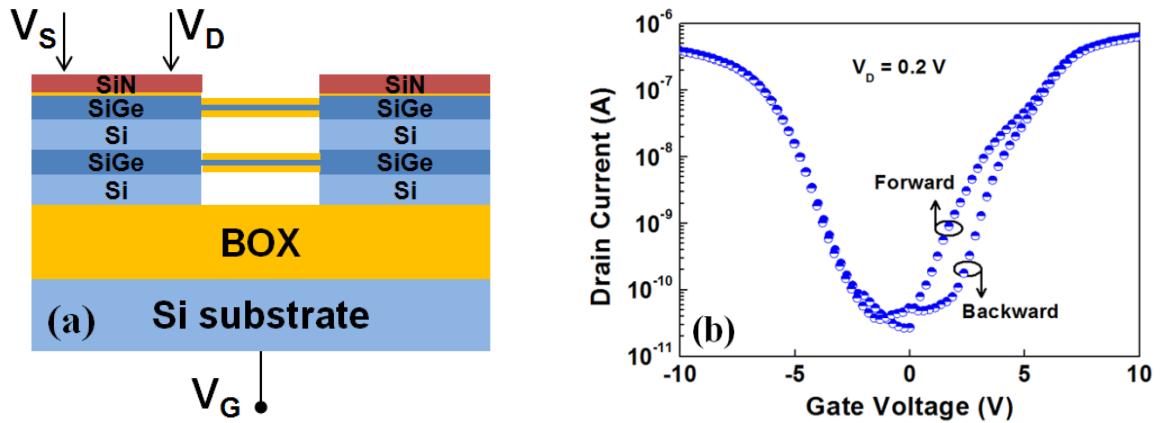


Figure IV-23: (a) Schematic view of the pseudo-MOSFET measurement on the contact stack: probes are placed on the same contact pad. (b) Drain current versus back-gate voltage in double sweep mode (forward and backward) for the SiGeC-Si super-lattice.

Figure IV-24a shows a comparison between  $I_D$  before and after correction for SiGe NWs. The corrected current is much higher than the measured one for both positive and negative back-gate voltage. This confirms our expectations about the strong  $R_{SD}$  consequence on SiGe NWs. The mobility extracted after correction is almost six times larger. For SiGeC NWs no variation was obtained between corrected and non-corrected drain current (Figure IV-24b); this result points out low value of  $R_{SD}$ .

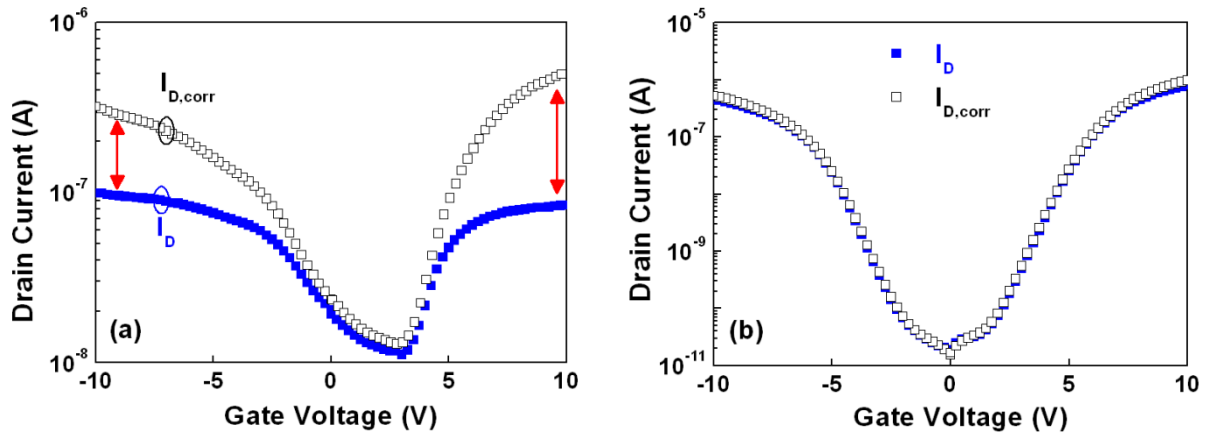


Figure IV-24: Drain current versus back-gate voltage (a) for a SiGe-based NW and (b) for a SiGeC-based NW before and after correction of series resistance.  $V_D = 0.2$  V,  $L = 100$  nm and  $w_{des} = 100$  nm.

### 3.3.3 Low-temperature measurements

We present SiGeC NWs properties measured at low-temperature (low-T). The aim of this characterization is to investigate the variation of electrical parameters with temperature.

Before decreasing the temperature, vacuum is created at 300 K in the chamber where the NWs are (pressure inside the chamber is then around  $10^{-6}$  mbar). It is worth noting that the simple fact of pumping the chamber might induce changes in the electrical response of SiGeC nanowires, because the nanowires are not encapsulated and therefore may suffer from surface contamination.

Figure IV-25a shows the drain current as a function of back-gate voltage for  $w_{des} = 100$  nm and  $L = 100$  nm in air and vacuum conditions in the cryogenic station. The drain current level decreases in vacuum compared to air condition for both negative and positive  $V_G$ . In Figure IV-25, the lateral shifts of the  $I_D$ - $V_G$  curves are related to the change in threshold voltage and flat-band voltage. Higher  $V_T$  and  $V_{FB}$  were obtained for vacuum condition, probably due to the contribution of the surface contamination when the experiments are conducted in air.

Liquid nitrogen was injected into the chamber in order to reach low temperature (77 K). We compared the electrical characteristics at different conditions: air, 300 K (in vacuum) and 77 K (in vacuum). Figure IV-25b shows the variation of the drain current curves for these three different conditions of measurement. As usually with crystalline semiconductors, the drain current level at low temperature is higher than at room temperature (in vacuum conditions).

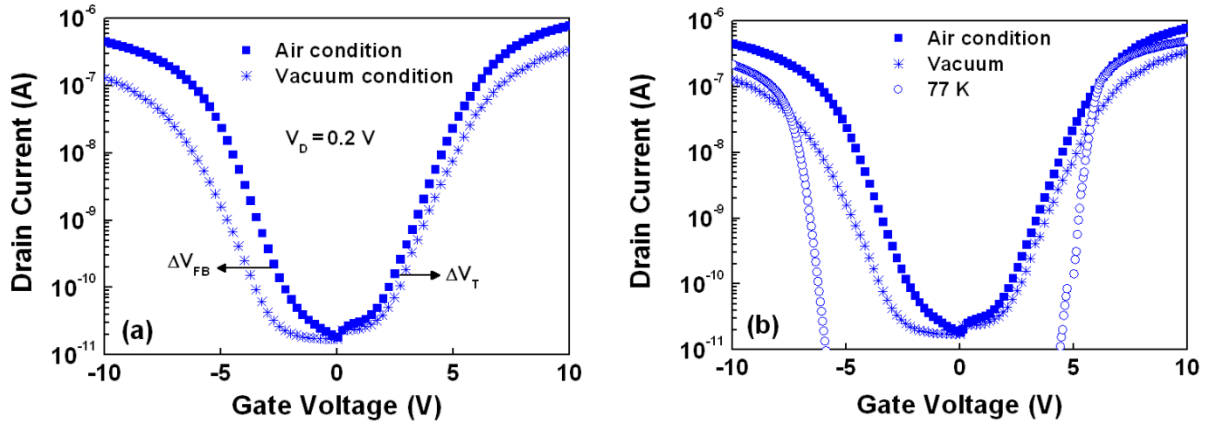


Figure IV-25: Drain current versus back-gate voltage for a SiGeC-based NW of 100 nm length with  $w_{des} = 100$  nm. (a) air and vacuum condition: the shifts of  $V_T$  and  $V_{FB}$  are clearly visible. (b)  $I_D$ - $V_G$  curves at room temperature (in air and vacuum) and at 77 K (vacuum).  $V_D = 0.2$  V.

For more quantitative analysis, we show in Table IV-9 the extracted low-field mobility for holes and electrons ( $\mu_p$ ,  $\mu_n$ ), and the subthreshold swing (S) for two different temperatures (77 and 300 K). The electron and hole mobility increases by a factor of two with the decrease of temperature from 300 K to 77 K. The mobility enhancement is dominated by the reduction in phonon scattering rate as the

temperature decreases [43]. Another scattering mechanism is suspected because pure phonon interactions would lead to  $\mu \sim T^{-1}$ . The swing decreases almost four times between 300 K and 77 K which is consistent with  $S \sim kT$ . This result indicates that the density of interface traps does not increase significantly at low temperature.

Table IV-9: Variation of electrical parameters for a SiGeC-based NW of 100 nm length with  $w_{des} = 100$  nm for different temperatures.

T (K)	$\mu_n$ (cm <sup>2</sup> /V.s)	$\mu_p$ (cm <sup>2</sup> /V.s)	S (V/dec)
300	12	5	1.1
77	24	10	0.3

### 3.3.4 Multiple parallel NWs at 300 K

Another aspect studied here concerns the transport through multiple parallel channels. The comparison of structures composed of a single row or 50 parallel rows in 3D vertically stacked NWs is intriguing. Figure IV-26 shows the current measured in vacuum at room temperature through a single row and through multi-row structures (50 in parallel). Two different geometries were under test ( $w_{des} = 50$  nm,  $L = 100$  nm in Figure IV-26a and  $w_{des} = 100$  nm,  $L = 500$  nm in Figure IV-26b). The drain current values hardly correspond to the aspect ratio or to the number of nanowires. This implies that the current in the multi-parallel structures is defined either by the contact (source/drain) resistance or by the most conductive nanowires of the stack.

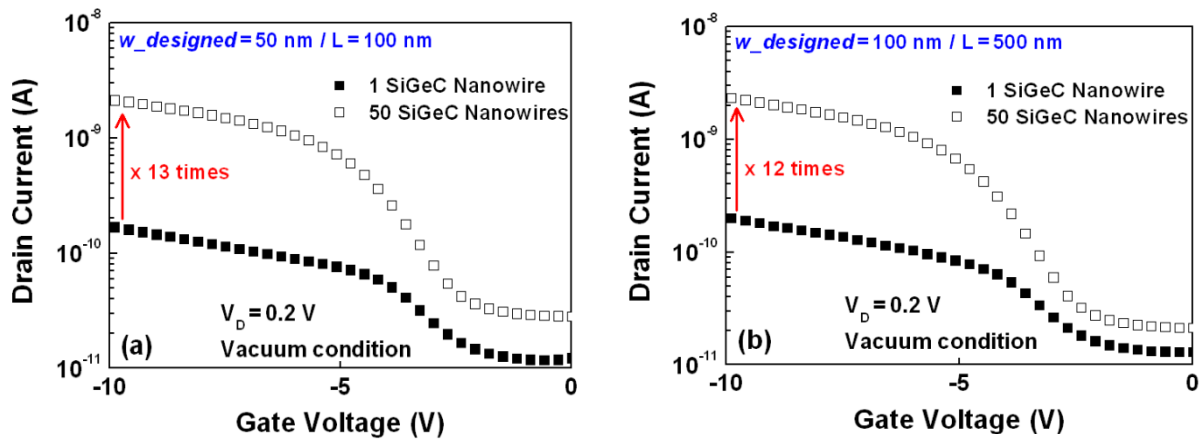


Figure IV-26: Drain current versus negative back-gate voltage for SiGeC based NWs of 100 nm length with  $w_{des} = 50$  nm (a) and 500 nm length with  $w_{des} = 100$  nm (b).

### 3.4 Conclusion of section 3

We have studied 3D vertically-stacked SiGe and SiGeC nanowires fabricated at CEA-Leti with a new method based on the Ge condensation technique on silicon-on-insulator wafers. We have demonstrated that the 3D vertically stacked suspended gateless nanowires behave as MOS transistors controlled by the back gate. An original characterization method, inspired by the pseudo-MOSFET, has been implemented. This technique proves efficient for the preliminary characterization of as-grown nanowires before the processing of MOS gate and source/drain terminals.

Transport measurements show that the hole mobility is improved by increasing the Ge concentration. Typical issue of these structures is the high series resistance. Our data demonstrates that the contact resistance is field-effect sensitive. The undoped nature of the contacts explains this problem, which can easily be solved by implanting the contacts of the NWs stacks when fabricating a complete device.

At low temperature, the carrier mobility and subthreshold slope are clearly improved. The benefit of integrating multiple parallel nanowires for increasing on-current is obvious even though the current gain was not as high as expected for GAA architecture. Source and drain doping should improve the electrical properties of NWs.

The comparison of NWs with different widths, lengths and parallel combinations is informative but opens questions that will probably be answered after full CMOS completion of GAA NWs.

## Conclusion

This chapter IV was dedicated to innovative applications of the  $\Psi$ -MOSFET. First, the  $\Psi$ -MOSFET configuration has been extended for the characterization of heavily doped SOI wafers. Second, we introduced a new SOI sensor for gold nanoparticles detection. Finally, we studied the electrical transport properties of 3D vertically-stacked SiGe and SiGeC NWs fabricated on SOI wafers.

The  $\Psi$ -MOSFET configuration was used for the first time to characterize heavily doped SOI wafers with doping concentration of  $10^{19}$ - $10^{20}$  cm<sup>-3</sup>. Unusual  $\Psi$ -MOSFET characteristics were obtained and a revised model was proposed to extract independently the carrier conduction, volume mobility and surface mobility. Two characterizations techniques (Hall effect and four-point probes) were also used for comparison. The results show good agreement between these three different techniques and prove that  $\Psi$ -MOSFET delivers reliable results.

We proposed and verified that the  $\Psi$ -MOSFET stands as a simple sensor of gold nanoparticles deposited on the top Si film. The shifts of  $V_T$  and  $V_{FB}$  obtained after adding charged gold nanoparticles on the top surface are large enough for detection. The shifts in the  $I_D$ - $V_G$  curves are proportional to the amount of surface charge, *i.e.* to the density of the gold nanoparticles. The sensitivity was found to be higher for thinner Si films due to the stronger coupling between the channel at the film-BOX interface and the surface charge.

3D vertically-stacked SiGe and SiGeC nanowires were tentatively characterized by  $\Psi$ -MOSFET, which delivers useful I-V characteristics. The 3D vertically stacked suspended gateless nanowires behave as MOS transistors controlled by the back gate. The contacts were ohmic albeit their resistance shows strong gate bias dependence. Hole mobility is improved by increasing the Ge concentration. The carrier mobility and the subthreshold slope are improved at low temperature. Finally, integrating multiple parallel nanowires raise the on-current without confirming that all NWs are active.

## References chapter IV

- [1] Sorin Cristoloveanu, "A Review of the Electrical Properties of SIMOX Substrates and Their Impact on Device Performance," *Journal of the Electrochemical Society*, vol. 138, pp. 3131-3139, 1991.
- [2] Dae-Hyun Moon, Jae-Joon Song and Ohyun Kim, "Effect of Source/Drain Doping Gradient on Threshold Voltage Variation in Double-Gate Fin Field Effect Transistors as Determined by Discrete Random Doping," *Japanese Journal of Applied Physics*, vol. 49, pp. 104301-104305, 2010.
- [3] Jean-Pierre Colinge, Chi-Woo Lee, Aryan Afzalian, Nima Dehdashti Akhavan, Ran Yan, Isabelle Ferain, Pedram Razavi, Brendan O'Neill, Alan Blake, Mary White, Anne-Marie Kelleher, Brendan McCarthy and Richard Murphy, "Nanowire transistors without junctions," *Nat Nano*, vol. 5, pp. 225-229, 2010.
- [4] J. Hartwich, L. Dreeskornfeld, F. Hofmann, J. Kretz, E. Landgraf, R. J. Luyken, M. Specht, M. Stadel, T. Schulz, W. Rosner and L. Risch, "Off current adjustment in ultra-thin SOI MOSFETs," in *Solid-State Device Research conference, 2004. ESSDERC 2004. Proceeding of the 34th European*, pp. 305-308, 2004.
- [5] S. Cristoloveanu and S. Williams, "Point-contact pseudo-MOSFET for in-situ characterization of as-grown silicon-on-insulator wafers," *Electron Device Letters, IEEE*, vol. 13, pp. 102-104, 1992.
- [6] T. Ouisse, P. Morfouli, O. Faynot, H. Seghir, J. Margail and S. Cristoloveanu, "A Detailed Investigation of the Pseudo-Mos Transistor for in Situ Characterization of Soi Wafers," in *SOI Conference, 1992. IEEE International*, pp. 30-31, 1992.
- [7] F. Y. Liu, A. Diab, I. Ionica, K. Akarvardar, C. Hobbs, T. Ouisse, X. Mescot and S. Cristoloveanu, "Characterization of Heavily Doped SOI wafers under Pseudo-MOSFETs Configuration," *Solid-State Electronics*, vol. Submitted, 2012.
- [8] S. M. Sze, *Physics of Semiconductor Devices (Second Edition)*, Wiley press, New York, 1981.
- [9] G. Ghibaudo, "New method for the extraction of MOSFET parameters," *Electronics Letters*, vol. 24, pp. 543-545, 1988.
- [10] S. Cristoloveanu, D. Munteanu and M. S. T. Liu, "A review of the pseudo-MOS transistor in SOI wafers: operation, parameter extraction, and applications," *Electron Devices, IEEE Transactions on*, vol. 47, pp. 1018-1027, 2000.
- [11] Naotoshi Kadotani, Teruyuki Ohashi, Tsunaki Takahashi, Shunri Oda and Ken Uchida, "Experimental Study on Electron Mobility in Accumulation-Mode Silicon-on-Insulator Metal-Oxide-Semiconductor Field-Effect Transistors," *Japanese Journal of Applied Physics*, vol. 50, pp. 094101-094105, 2011.
- [12] T. Ouisse, S. Cristoloveanu and G. Borel, "Electron trapping in irradiated SIMOX buried oxides," *Electron Device Letters, IEEE*, vol. 12, pp. 312-314, 1991.
- [13] S. Cristoloveanu and S. S. Li, *Electrical Characterization of Silicon-On-Insulator Materials and Devices*, Kluwer, Boston, 1995.
- [14] Q. T. Nguyen, J. Antoszewski, L. Faraone, N. Bresson, P. Gentil and S. Cristoloveanu, "Correlation of Pseudo-MOS transistor and Hall effect measurements in thin SOI wafers," in *Optoelectronic and Microelectronic Materials and Devices, 2006 Conference on*, pp. 39-40, 2006.
- [15] Cui Yi, Wei Qingqiao, Park Hongkun and C. M. Lieber, "Nanowire nanosensors for highly sensitive and selective detection of biological and chemical species," *Science*, vol. 293, pp. 1289-1292, 2001.
- [16] J. Hahm and C. M. Lieber, "Direct ultrasensitive electrical detection of DNA and DNA sequence variations using nanowire nanosensors," *Nano Letters. Jan.*, vol. 4, pp. 51-54, 2004.



- [17] G. Hamaide, F. Allibert, H. Hovel and S. Cristoloveanu, "Impact of free-surface passivation on silicon on insulator buried interface properties by pseudotransistor characterization," *Journal of Applied Physics*, vol. 101, pp. 114513-114516, 2007.
- [18] N. Rodriguez, S. Cristoloveanu and F. Gamiz, "Revisited Pseudo-MOSFET Models for the Characterization of Ultrathin SOI Wafers," *Electron Devices, IEEE Transactions on*, vol. 56, pp. 1507-1515, 2009.
- [19] Sung-Hoon Jung, Jae-Min Kim, Lak-Myung Jung, Yong-Hyun Lee, S. Cristoloveanu and Young Ho Bae, "Pseudo-Mosfet Analysis of Proton Irradiated and Annealed SOI Wafer," *ECS Transactions*, vol. 19, pp. 329-334, 2009.
- [20] Tao He, Jianli He, Meng Lu, Bo Chen, Harry Pang, William F. Reus, Whitney M. Nolte, David P. Nackashi, Paul D. Franzon and James M. Tour, "Controlled Modulation of Conductance in Silicon Devices by Molecular Monolayers," *Journal of the American Chemical Society*, vol. 128, pp. 14537-14541, 2006.
- [21] I. Ionica, J. Champlaud, Y.H. Bae and S. Cristoloveanu, "SOI Pseudo-MOSFET: platform for high sensitivity charge detection," in *Advanced Workshop on Frontiers in Electronics (WOFE)*, Porto Rico, p. 18, 2009.
- [22] Duclairoir Florence, Dubois Lionel, Calborean Adrian, Fateeva Alexandra, Fleury Benoit, Kalaiselvan Anbarasan, Marchon Jean-Claude, Maldivi Pascale, Billon Martial, Bidan Gerard, De Salvo Barbara, Delapierre Guillaume, Buckley Julien, Huang Kai, Barattin Régis, P. R. O. Tiziana and Levy Laurent P, "Bistable molecules development and Si surface grafting: two chemical tools used for the fabrication of hybrid molecule/Si CMOS component," *International journal of nanotechnology*, vol. 7, pp. 719-737, 2010.
- [23] I. Ionica, A. El Hajj Diab and S. Cristoloveanu, "Gold nanoparticles detection using intrinsic SOI-based sensor," in *Nanotechnology (IEEE-NANO), 2011 11th IEEE Conference on*, pp. 38-43, 2011.
- [24] Elodie Boisselier and Didier Astruc, "Gold nanoparticles in nanomedicine: preparations, imaging, diagnostics, therapies and toxicity," *Chemical Society Reviews*, vol. 38, pp. 1759-1782, 2009.
- [25] Jang-Sik Lee, "Recent progress in gold nanoparticle-based non-volatile memory devices," *Gold Bulletin*, vol. 43, pp. 189-199, 2010.
- [26] Elaine T. Vandenberg, Lars Bertilsson, Bo Liedberg, Kajsa Uvdal, Ragnar Erlandsson, Hans Elwing and Ingemar Lundström, "Structure of 3-aminopropyl triethoxy silane on silicon oxide," *Journal of Colloid and Interface Science*, vol. 147, pp. 103-118, 1991.
- [27] Jiwen Zheng, Zihua Zhu, Haifeng Chen and Zhongfan Liu, "Nanopatterned Assembling of Colloidal Gold Nanoparticles on Silicon," *Langmuir*, vol. 16, pp. 4409-4412, 2000.
- [28] Wissanu Patungwasa and José H. Hodak, "pH tunable morphology of the gold nanoparticles produced by citrate reduction," *Materials Chemistry and Physics*, vol. 108, pp. 45-54, 2008.
- [29] T. Skotnicki, J. A. Hutchby, King Tsu-Jae, H. S. P. Wong and F. Boeuf, "The end of CMOS scaling: toward the introduction of new materials and structural changes to improve MOSFET performance," *Circuits and Devices Magazine, IEEE*, vol. 21, pp. 16-26, 2005.
- [30] T. N. Nguyen and J. D. Plummer, "Physical mechanisms responsible for short channel effects in MOS devices," in *Electron Devices Meeting, 1981 International*, pp. 596-599, 1981.
- [31] T. Grotjohn and B. Hoefflinger, "A parametric short-channel MOS transistor model for subthreshold and strong inversion current," *Solid-State Circuits, IEEE Journal of*, vol. 19, pp. 100-112, 1984.
- [32] N. Singh, A. Agarwal, L. K. Bera, T. Y. Liow, R. Yang, S. C. Rustagi, C. H. Tung, R. Kumar, G. Q. Lo, N. Balasubramanian and D. L. Kwong, "High-performance fully depleted silicon nanowire (diameter  $\leq$  5 nm) gate-all-around CMOS devices," *Electron Device Letters, IEEE*, vol. 27, pp. 383-386, 2006.
- [33] C. Dupre, T. Ernst, V. Maffim-Alvaro, V. Delaye, J. M. Hartmann, S. Borel, C. Vizoz, O. Faynot, G. Ghibaudo and S. Deleonibus, "3D nanowire gate-all-around transistors: Specific integration and electrical features," *Solid-State Electronics*, vol. 52, pp. 519-525, 2008.

- [34] Q. T. Nguyen, J. F. Damlencourt, B. Vincent, L. Clavelier, Y. Morand, P. Gentil and S. Cristoloveanu, "High quality Germanium-On-Insulator wafers with excellent hole mobility," *Solid-State Electronics*, vol. 51, pp. 1172-1179, 2007.
- [35] W. W. Fang, N. Singh, L. K. Bera, H. S. Nguyen, S. C. Rustagi, G. Q. Lo, N. Balasubramanian and D. L. Kwong, "Vertically Stacked SiGe Nanowire Array Channel CMOS Transistors," *Electron Device Letters, IEEE*, vol. 28, pp. 211-213, 2007.
- [36] A. Diab, E. Saracco, I. Ionica, C. Bonafos, J. F. Damlencourt, J. H. Lee and S. Cristoloveanu, "Electrical Transport at Room and Low Temperature in 3D Vertically Stacked SiGe and SiGeC Nanowires," *Journal of the Electrochemical Society*, vol. 159, pp. H467-H472, 2012.
- [37] T. Tezuka, N. Sugiyama, T. Mizuno and S. Takagi, "Novel fully-depleted SiGe-on-insulator pMOSFETs with high-mobility SiGe surface channels," in *Electron Devices Meeting, 2001. IEDM Technical Digest. International*, pp. 33.36.31-33.36.33, 2001.
- [38] Jean-François Damlencourt, "Method for manufacturing a device having a structure with one or a plurality of SI and GE-based micro or nanowires, using germanium condensation," U.S. Patent n°FR2905197, 2008.
- [39] Emeline D. Saracco, Jean-Francois Damlencourt, Dominique Lafond, Sophie Bernasconi, Veronique Benevent, Pierette Rivallin, Yves Morand, Jean-Michel Hartmann, Pauline Gautier, Christian Vizioz, Thomas Ernst, Caroline Bonafos and Pier Francesco Fazzini, "Fabrication of Suspended Ge-rich Nanowires by Ge Enrichment Technique for Multi-channel Devices," *ECS Transactions*, vol. 19, pp. 207-212, 2009.
- [40] K. Tachi, M. Casse, D. Jang, C. Dupre, A. Hubert, N. Vulliet, V. Maffini-Alvaro, C. Vizioz, C. Carabasse, V. Delaye, J. M. Hartmann, G. Ghibaudo, H. Iwai, S. Cristoloveanu, O. Faynot and T. Ernst, "Relationship between mobility and high-k interface properties in advanced Si and SiGe nanowires," in *Electron Devices Meeting (IEDM), 2009 IEEE International*, pp. 1-4, 2009.
- [41] Emeline Saracco, "FABRICATION ET COINTEGRATION DE TRANSISTORS N-MOS A BASE DE NANOFILS DE SILICIUM ET DE TRANSISTORS P-MOS A BASE DE NANOFILS DE GERMANIUM", Ph.D. dissertation, Grenoble-INP, France, 2011.
- [42] Krunoslav Romanjek, "CARACTÉRISATION ET MODÉLISATION DES TRANSISTORS CMOS DES TECHNOLOGIES 50nm ET EN DEÇÀ", Ph.D. dissertation, Grenoble-INP, France, 2004.
- [43] Shinji Kawaji, "The Two-Dimensional Lattice Scattering Mobility in a Semiconductor Inversion Layer," *Journal of the Physical Society of Japan (J. Phys. Soc. Jpn.)*, vol. 27, pp. 906-908, 1969.

# ***General conclusion***

During these three years of Ph.D., I focused on the study of SOI and pseudo-MOSFET, in a very broad definition. The SOI used was not only the Silicon-On-Insulator standard material, but also ultra-thin film (down to 12 nm), ultra-thin BOX (down to 10 nm), highly doped films (up to  $10^{20}$  cm<sup>-3</sup>), SiGe nanowires stacked in 3D architectures or silicon films decorated with gold nanoparticles.

In a general definition, the  $\Psi$ -MOSFET is a configuration in which the electrical regime of the top film is electrostatically controlled by a back-gate, that is capacitively coupled through a buried oxide. The physical parameters measured in  $\Psi$ -MOSFET will not only be limited to current, but they can go to capacitance or low frequency noise spectra.

With this extended definitions, we studied the electrical characterization of SOI in  $\Psi$ -MOSFET configuration. A sum of technical conclusions will be presented. Our study allowed also discovering new roads to explore which will be presented in the perspectives section.

## ***Main conclusions***

1. We demonstrated for the first time the capability of exploring ultra and extra thin SOI wafers down to 12 nm silicon film and 10 nm BOX using the  $\Psi$ -MOSFET with pressure probes. The impact of the top surface silicon film state and its passivation on the  $I_D$ - $V_G$  and  $g_m$ - $V_G$  curves for advanced SOI structures were showed and clarified.
2. We extended the characterization of SOI wafers to low-temperature measurements using  $\Psi$ -MOSFET concept. The feasibility of the measurements using cryogenic station was verified and ohmic contacts were ensured. The measured temperature dependence of holes and electrons mobility fits with the theoretical curves. For  $T > 100$  K, phonon scattering mechanism dominates and indicates a good quality of Si-BOX interface in SOI wafers. The impact of the top interface defects on the swing and the threshold voltage is more prominent in thinner films and at lower temperature.

3. We initiated low-frequency noise characterization of as-fabricated SOI wafers using the  $\Psi$ -MOSFET. The LFN is shown to be of  $1/f$  type and is clearly associated with the carrier number fluctuation in the channel, due to the trapping/detrapping of carriers. The interface trap values can be extracted using this novel method. The noise does not seem to depend on the probe pressure for the thicker films (88 nm). The impact of the free surface preparation on the channel properties is significant. The LFN technique using  $\Psi$ -MOSFET can be used to characterize thin SOI films, down to 20 nm, and BOX layers down to 10 nm.
4. We implemented a novel characterization technique for bare SOI, based on split  $C$ - $V$  measurement using  $\Psi$ -MOSFET. Different SOI structures have successfully been tested from thick to thin film/BOX couples. The effective mobility of electrons and holes can be obtained by this split  $C$ - $V$  technique using an appropriate model. The adapted methodology to determine  $\mu_{\text{eff}}$  was showed and validated through comparison with  $\mu_{\text{eff}}$  extracted from  $I_D$ - $V_G$  measurements. Excellent agreement was obtained between effective mobility curves from  $Y$ -function method and from our new method, validating our approach. The impact of surface passivation on the effective mobility was confirmed by our technique and the values show that electron mobility can exceed  $500 \text{ cm}^2\text{V}^{-1}\text{s}^{-1}$  in thin SOI films with passivated surface. The variation of the maximum capacitance in the high frequency regime was observed and explained by a  $RC$  analytical model.
5. We characterized for the first time heavily doped SOI wafers with doping concentration of  $10^{19}$ - $10^{20} \text{ cm}^{-3}$  by  $\Psi$ -MOSFET method and validated the results by Hall effect and 4-point probe. Unusual  $\Psi$ -MOSFET characteristics ( $I_D$ - $V_G$  and  $g_m$ - $V_G$  curves) were obtained. We showed that  $\Psi$ -MOSFET is the only method able to provide independently the carrier concentration and mobility without the need of a magnetic field. We demonstrated that parameters extraction is possible using a revised model which takes the volume current into account. As the  $\Psi$ -MOSFET yields independently the carrier mobility (in volume and at the interface) and carrier concentration, it can successfully replace more complex Hall effect measurements.
6. We proposed and verified an innovative  $\Psi$ -MOSFET based sensor of gold nanoparticles deposited on the top Si film. The shifts of  $V_T$  and  $V_{\text{FB}}$  after adding

gold nanoparticles on the top surface, observed in the measured  $I_D$ - $V_G$  characteristics, are explained with the  $\Psi$ -MOSFET theory. The shifts are related to the change of the surface potential (density of the charge) on the surface, *i.e.* to the density of the gold nanoparticles. The sensitivity proved to be higher for thinner SOI films. The reproducibility of the technological process as well as of the electrical response has been proven.

7. We have demonstrated that the 3D vertically-stacked SiGe and SiGeC suspended gateless nanowires behave as MOS transistors controlled by the back gate. An original characterization method before the processing of the gate stack and source/drain contacts, inspired by the  $\Psi$ -MOSFET, has been implemented which delivers useful I-V characteristics. Ohmic contacts were obtained albeit their resistance shows strong gate bias dependence. Hole mobility is improved by increasing the Ge concentration. At low-temperature measurements, the carrier mobility and the subthreshold slope are improved. Integrating multiple parallel nanowires raises the on-current.

### ***Future perspectives***

Our work opened the road to new questions about further improvements and developments in these research fields.

1. A still opened question remains about the ultra-thin film/BOX structure. What is the thinnest film/BOX for which the  $\Psi$ -MOSFET can still give reliable results?
2. In the noise sections, we saw the critical importance of the geometrical factor in order to correctly determine the density of states. Due to time constraints, a simple calculation method for the effective geometry has not been developed. A more sophisticated model should be explained where numerical simulations would presumably bring interesting information.
3. The impact of the surface preparation on the noise measurements was not clear for some of our experiments (*e.g.* before/after HF treatment). A complementary study would be necessary to clarify the impact of each interface to the global noise.
4. The influence of experimental parameters (*e.g.* probe spacing and sample size) on split  $C$ - $V$  measurements has to be clarified. We started numerical simulations (i) to verify that substrate effects are indeed negligible and (ii) to determine the

impact of film thickness, BOX thickness and substrate/BOX interface quality on the effective surface and frequency. My younger colleagues will complete this work. I thank them in advance.

# List of scientific publications

## Journal publications:

1. **A. Diab**, C. Fernández, A. Ohata, N. Rodriguez, I. Ionica, Y. Bae, W. Van Den Daele, F. Allibert, F. Gámiz, G. Ghibaudo, C. Mazure and S. Cristoloveanu, “A New Characterization Technique for SOI Wafers: Split  $C(V)$  in Pseudo-MOSFET Configuration”, *to be published in Solid-State Electronics*.
2. F. Y. Liu, **A. Diab**, I. Ionica, K. Akarvardar, C. Hobbs, T. Ouisse, X. Mescot and S. Cristoloveanu, “Characterization of Heavily Doped SOI Wafers under Pseudo-MOSFETs Configuration”, *to be published in Solid-State Electronics*.
3. **A. Diab**, L. Pirro, I. Ionica, X. Mescot, G. Ghibaudo and S. Cristoloveanu, “Low-temperature pseudo-metal-oxide-semiconductor field-effect transistor measurements on bare silicon-on-insulator wafers”, *Applied Physics Letters*, vol. 101, p. 092110, 2012.
4. **A. Diab**, E. Saracco, I. Ionica, C. Bonafos, J. F. Damlencourt, J. H. Lee and S. Cristoloveanu, “Electrical Transport at Room and Low Temperature in 3D Vertically Stacked SiGe and SiGeC Nanowires”, *Journal of the Electrochemical Society*, vol. 159, p. H467, 2012.
5. **A. Diab**, I. Ionica, S. Cristoloveanu, F. Allibert, Y. H. Bae, J. A. Chroboczek and G. Ghibaudo, “Low-frequency noise in SOI pseudo-MOSFET with pressure probes”, *Microelectronic Engineering*, vol. 88, p. 1283, 2011.

## International conference papers:

1. **A. Diab**, C. Fernández, L. Pirro, N. Rodriguez, I. Ionica, A. Ohata, Y. H. Bae, W. Van Den Daele, F. Allibert, F. Gámiz, G. Ghibaudo, D. Delprat, C. Mazuré and S. Cristoloveanu, “Effective Mobility in Extra-Thin Film and Ultra-Thin BOX SOI Wafers”, Proc. of the EUROSIOI conference, Paris, France, pp. 1-2, 2013. (Oral presentation)
2. M. Daanoune, S. Sirajeddine, **A. Diab**, A. Kaminski-Cachopo, I. Ionica, and S. Cristoloveanu, “Pseudo-MOSFET under illumination: a novel method for extraction of carrier lifetime”, Proc. of the EUROSIOI conference, Paris, pp. 1-2, France, 2013. (Poster presentation)
3. S. Cristoloveanu, I. Ionica, **A. Diab** and F. Liu, “The Pseudo-MOSFET: Principles and Recent Trends”, *Proc. of the ECS 222<sup>th</sup> International Symposium on Advanced Substrates and Characterization, Honolulu PRIME 2012*, Hawaii, USA, pp. 249–258, 2012. (**Invited paper**)
4. C. Fernández, **A. Diab**, N. Rodriguez, A. Ohata, F. Allibert, I. Ionica, F. Gámiz and S. Cristoloveanu, “Impact of Effective Capacitance Area on the Characterization of SOI Wafers by Split- $C(V)$  in Pseudo-MOSFET Configuration”, *2012 International Semiconductor Conference Dresden-Grenoble (IEEE-ISCDG)*, Grenoble, pp. 123-126, France, 2012. (Oral presentation)
5. **A. Diab**, C. Fernández, A. Ohata, N. Rodriguez, I. Ionica, Y. H. Bae, F. Allibert, F. Gámiz, G. Ghibaudo and S. Cristoloveanu, “A New Characterization Technique for SOI Wafers: Split  $C(V)$  in Pseudo-MOSFET Configuration”, *Proc. of the EUROSIOI conference*, Montpellier, France, pp. 103-104, 2012. (Oral presentation)
6. F. Y. Liu, **A. Diab**, I. Ionica, K. Akarvardar, C. Hobbs and S. Cristoloveanu, “Transport Properties in Heavily Doped SOI Wafers”, *Proc. of the EUROSIOI conference*, Montpellier, France, pp. 57-58, 2012. (Poster presentation)
7. **A. Diab**, I. Ionica, S. Cristoloveanu, F. Allibert, Y. H. Bae, J. A. Chroboczek and G. Ghibaudo, “Static and Low-Frequency Noise Characterization of Ultrathin SOI with Very Thin BOX in

- Pseudo-MOSFET Configuration”, *Semiconductor Device Research Symposium (IEEE)*, Maryland, USA, pp. 1-2, 2011. (Oral presentation)
8. I. Ionica, **A. Diab** and S. Cristoloveanu, “Gold nanoparticles detection using an intrinsic SOI-based sensor”, *Nanotechnology (IEEE-NANO)*, Portland, USA, pp. 38-43, 2011. (Oral presentation)
  9. **A. Diab**, E. Saracco, I. Ionica, C. Bonafos, J. F. Damlencourt and S. Cristoloveanu, “Transport Properties of 3D Vertically Stacked SiGe and SiGeC Nanowires”, *Proc. of the ECS 219<sup>th</sup> International Symposium on Silicon-on-Insulator Technology and Devices*, Montreal, Canada, pp. 157-162, 2011. (Oral presentation)
  10. **A. Diab**, I. Ionica, S. Cristoloveanu, F. Allibert, Young Ho Bae, J. A. Chroboczek and G. Ghibaudo, “Low-Frequency Noise in SOI Pseudo-MOSFET with Pressure Probes”, *17<sup>th</sup> Conference on “Insulating Films on semiconductors” (INFOS 2011)*, Grenoble, France, pp. 1-2, 2011. (Poster presentation)
  11. **A. Diab**, I. Ionica, S. Cristoloveanu, F. Allibert, N. Rodriguez, F. Gamiz, M. Bawedin, Y. H. Bae, J. Chroboczek and G. Ghibaudo, “Low-Frequency Noise in Ultrathin SOI Pseudo-MOSFET: Where is the Noise Coming From?”, *Proc. of the EUROSOI conference*, Granada, Spain, pp. 23-24, 2011. (Oral presentation)
  12. I. Ionica, **A. Diab**, Y. H. Bae, X. Mescot, A. Ohata, F. Allibert and S. Cristoloveanu, “Advances in the Pseudo-MOSFET Characterization Method”, *IEEE Semiconductor Conference (CAS)*, Sinaia, Romania, pp. 45-51, 2010. (**Invited paper**)

### **Published book chapter:**

1. S. Cristoloveanu, M. Bawedin, K. I. Na, W. Den Daele, K. H. Park, L. Pham-Nguyen, J. Wan, K. Tachi, S. J. Chang, I. Ionica, **A. Diab**, Y. H. Bae, J. A. Chroboczek, A. Ohata, C. Fenouillet-Beranger, T. Ernst, E. Augendre, C. Royer, A. Zaslavsky and H. Iwai, “A Selection of SOI Puzzles and Tentative Answers”, in *Semiconductor-On-Insulator Materials for Nanoelectronics Applications*, Springer Berlin Heidelberg, pp. 425-441, 2011. (Invited chapter)

### **National conference papers:**

1. **A. Diab**, I. Ionica and S. Cristoloveanu, “Bruit basse fréquence sur Silicium sur Isolant dans la configuration Pseudo-MOSFET”, *Proc. of the JNRDM*, Paris, France, pp. 1-4, 2011. (Oral presentation)



# Abstract/Résumé

---

**Title:** Novel pseudo-MOSFET methods for the characterization of advanced SOI substrates

---

**Abstract:**

Silicon-On-Insulator (SOI) device architectures represent attractive alternatives to bulk ones thanks to the improvement of transistors and circuits performances. In this context, the SOI starting material should be of prime quality.

In this thesis, we develop novel electrical characterization tools and models for advanced SOI substrates. The classical pseudo-MOSFET ( $\Psi$ -MOSFET) characterization for SOI was revisited and extended to low temperatures. Enriched variants of  $\Psi$ -MOSFET, proposed and demonstrated on numerous geometries, concern split  $C$ - $V$  and low-frequency noise measurements. Based on split  $C$ - $V$ , an extraction method for the effective mobility was validated. A model explaining the capacitance variations with the frequency shows good agreement with the experimental results. The  $\Psi$ -MOSFET was also extended to highly doped SOI films and a model for parameter extraction was derived. Furthermore, we proved the possibility to characterize SiGe nanowire 3D stacks using the  $\Psi$ -MOSFET concept. Finally thin film  $\Psi$ -MOSFET proved to be an interesting, technology-light detector for gold nanoparticles.

**Keywords:** Silicon-On-Insulator,  $\Psi$ -MOSFET (Pseudo-MOSFET), Smart-Cut™, Split  $C$ - $V$ , Low-frequency noise, Low-temperature, Heavily doped SOI, SiGe NWs, Gold nanoparticles.

---

**Titre:** Nouvelles méthodes pseudo-MOSFET pour la caractérisation des substrats SOI avancés

---

**Résumé:**

Les architectures des dispositifs Silicium-Sur-Isolant (SOI) représentent des alternatives attractives par rapport à celles en Si massif grâce à l'amélioration des performances des transistors et des circuits. Dans ce contexte, les plaquettes SOI doivent être d'excellente qualité.

Dans cette thèse nous développons des nouveaux outils de caractérisation électrique et des modèles pour des substrats SOI avancés. La caractérisation classique pseudo-MOSFET ( $\Psi$ -MOSFET) pour le SOI a été revisitée et étendue pour des mesures à basses températures. Les variantes enrichies de  $\Psi$ -MOSFET, proposées et validées sur des nombreuses géométries, concernent des mesures split  $C$ - $V$  et des mesures bruit basse fréquence. A partir des courbes split  $C$ - $V$ , une méthode d'extraction de la mobilité effective a été validée. Un modèle expliquant les variations de la capacité avec la fréquence s'accorde bien avec les résultats expérimentaux. Le  $\Psi$ -MOSFET a été aussi étendu pour les films SOI fortement dopés et un modèle pour l'extraction des paramètres a été élaboré. En outre, nous avons prouvé la possibilité de caractériser des nanofils de SiGe empilés dans des architectures 3D, en utilisant le concept  $\Psi$ -MOSFET. Finalement, le SOI ultra-mince dans la configuration  $\Psi$ -MOSFET s'est avéré intéressant pour la détection des nanoparticules d'or.

**Mots-clefs:** Silicium-Sur-Isolant,  $\Psi$ -MOSFET (Pseudo-MOSFET), Split  $C$ - $V$ , Bruit basse fréquence, Basse température, SOI fortement dopé, Nanofils SiGe, Nanoparticules d'or.

# **French thesis summary**

***Nouvelles méthodes pseudo-MOSFET pour la  
caractérisation des substrats SOI avancés***

***Amer EL HAJJ DIAB***

## **Introduction générale**

Depuis l'ère du multimédia portable, des Smartphones et d'autres applications, la demande des processeurs plus petits, plus intelligents et moins voraces en énergie a été accélérée, tirant derrière toute l'industrie de la microélectronique et intensifiant le rythme de la recherche technologique. Dans ce contexte de l'évolution de la microélectronique, l'utilisation des substrats Silicium-Sur-Isolant (SOI) en remplacement des substrats de silicium massif ouvre des nouvelles voies pour l'innovation, offrant des meilleures performances, de la puissance et de la miniaturisation.

En effet, la technologie SOI peut surmonter certains des problèmes majeurs de la technologie du silicium massif (par exemple l'isolation des dispositifs est moins complexe grâce à la présence de l'oxyde enterré). En outre, les dispositifs SOI offrent un meilleur contrôle électrostatique du canal grâce à des architectures avancées (par exemple des transistors à multi-grilles).

Afin de profiter de tous les avantages du SOI, ces plaques SOI doivent être d'une excellente qualité électrique. Dans ce domaine fortement concurrentiel, l'objectif de cette thèse est de contribuer à l'analyse et à l'optimisation des substrats SOI avancés par le développement des méthodes innovantes de caractérisation électrique et de nouveaux modèles physiques, à partir de la configuration classique la plus connue du pseudo-MOSFET ( $\Psi$ -MOSFET).

Ce résumé est composé de deux grandes parties qui donnent une vue générale de mon travail de thèse. La première partie, portant sur la technologie de la fabrication du SOI (Smart-Cut™) et la technique de caractérisation  $\Psi$ -MOSFET, montre le contexte de notre travail avec l'extension de cette technique pour la caractérisation des structures SOI avancées. La seconde partie présente les méthodes innovantes que nous avons proposées pour la caractérisation électrique des plaques SOI (mesures basse température, mesures bruit basse fréquence et mesures split  $C-V$ ). Des modèles ont été conçus, adaptés et appliqués à chaque technique de mesure.

## Partie I: Le matériau SOI fabrication et caractérisation

Le SOI est une nouvelle génération des matériaux pour une technologie alternative aux substrats traditionnels “silicium massif” utilisés dans l'industrie de la microélectronique. Les substrats SOI sont composés d'un oxyde enterré (BOX) inséré entre la couche active de silicium (film de silicium) et un substrat de silicium qui sert de support mécanique (Figure 1) [1].

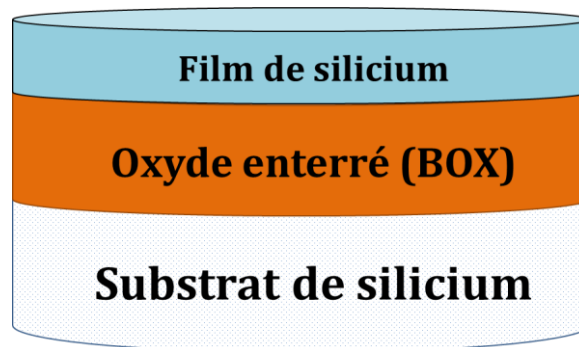


Figure 1: Représentation schématique de la structure SOI.

Grâce à l'avancement dans la technologie et particulièrement le brevet du procédé Smart-Cut™ [2], le matériau SOI a pu entrer dans le monde industriel de la microélectronique. L'évolution du SOI et son emploi de plus en plus fréquent dans la fabrication des circuits intégrés s'accompagne d'un besoin de contrôle de qualité efficace et rapide. La caractérisation électrique du SOI vise à révéler les paramètres des plaques qui auront un impact direct sur les composants réalisés par la suite sur ce substrat.

La caractérisation des matériaux et des dispositifs SOI nécessite des techniques capables de s'adapter aux difficultés induites par les couches du film de silicium très mince, la présence d'oxyde enterré mince, le couplage fort entre les interfaces (Si/BOX, BOX/substrat et Si/air) et les défauts typiques (les effets du stress, les homogénéités dans les profondeurs, les dislocations, les précipités, *etc.*). Certaines méthodes classiques montrent leurs limites pour les films et BOX minces, alors que de nouvelles techniques ont été mises en œuvre et seront discutées dans la section II.

Dans cette partie, nous montrons le procédé principal de fabrication des plaques SOI: le Smart Cut™ (section A), la technique de caractérisation classique  $\Psi$ -MOSFET (section B) avec la fonction Y pour l'extraction des paramètres électriques

(section C) et finalement les résultats obtenues pour des substrats SOI avancés (section D).

## A. Le procédé Unibond (Smart-Cut™)

La technologie Smart-Cut™ a été mise au point dans les années 1990 au CEA-Léti par Michel Bruel [3] et constitue maintenant l'exclusivité technologique de l'entreprise Soitec (France-Bernin). Ce procédé repose sur l'implantation d'hydrogène (H) dans un substrat dont on souhaite reporter une couche sur un substrat isolant (Figure 2). On peut le diviser en cinq étapes majeures (voir Figure 2).

Le matériau SOI Unibond est fabriqué par collage de plaques, mais tout en évitant les aléas du processus d'amincissement mécano-chimique. Pour cela, on implante, dans la plaquette oxydée A, de l'hydrogène qui engendre la formation de microcavités (zone en pointillés de la Figure 2). Lors du collage des plaques A et B et du recuit qui suit, les microcavités coalescent, provoquant ainsi une fracture horizontale qui permet la séparation naturelle des plaques. Cette séparation a lieu, non pas à l'interface de collage, mais à une profondeur définie par la localisation des microcavités produites lors de l'implantation d'hydrogène. Une étape finale de polissage a pour but de gommer la rugosité de surface de la nouvelle plaque SOI [4].

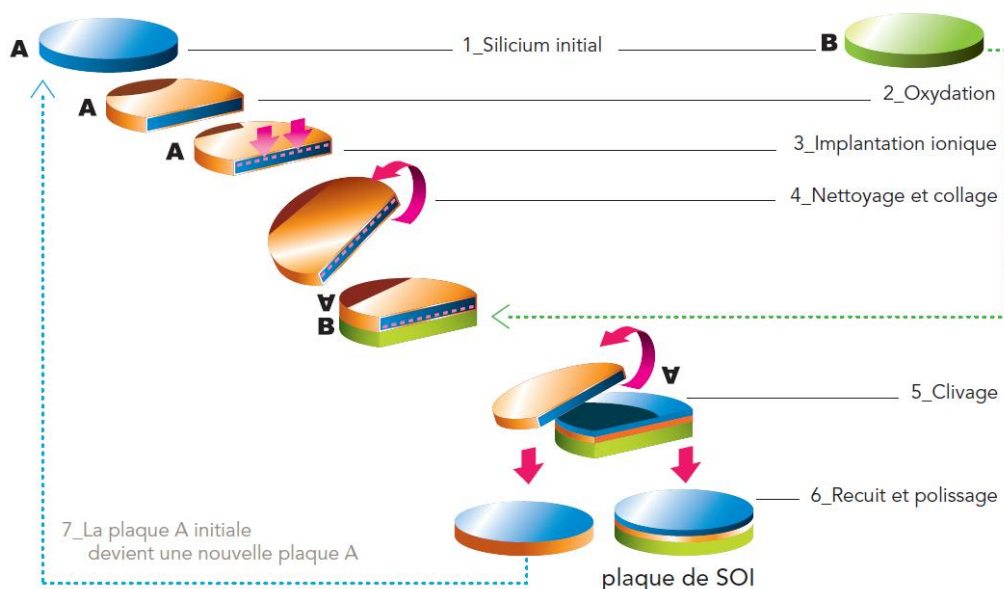


Figure 2: Représentation schématique des étapes de fabrication d'une plaque Unibond SOI avec le procédé Smart Cut™ décrit par Soitec [5].

Ce procédé propose donc des avantages très importants, pour la réalisation des plaques SOI [6]:

- Un procédé viable qui offre peu de pertes de matériau. Le procédé Smart-Cut™ est quasiment monoplaquette (le substrat donneur est utilisé pour créer plusieurs films);
- Un large panel d'épaisseurs du film de silicium et du BOX sont ajustables dans une gamme étendue ( $t_{Si} = 0.01$  à  $1.5$  microns et  $t_{BOX} = 0.01$  à  $5$  microns) en jouant sur la dose et l'énergie d'implantation d'hydrogène ( $H^+$ );
- Une excellente qualité cristalline et une grande uniformité;
- Une très bonne qualité d'interface Si/BOX (obtenu par oxydation);

## **B. La technique pseudo-MOSFET**

La technique  $\Psi$ -MOSFET a été mise au point au début des années 1990 par Cristoloveanu *et al* dans le laboratoire IMEP [7] et a depuis conquis le monde de la caractérisation des substrats SOI par sa simplicité et sa rapidité de mise en œuvre. Le  $\Psi$ -MOSFET se présente comme une structure MOSFET simple, inversée. Les contacts (source et drain) sont assurés par deux pointes métalliques (Figure 3a), le plus souvent en carbure de tungstène (WC). On applique sur la face arrière du substrat, une tension  $V_G$  par l'intermédiaire d'un support métallique appelé "chuck". La polarisation en face arrière a pour effet de créer un canal de conduction à l'interface film/BOX (Figure 3a). Le canal de conduction permet notamment d'extraire un grand nombre des paramètres électriques du SOI comme la mobilité des porteurs, les défauts à l'interface, *etc.*

La particularité du  $\Psi$ -MOSFET est que les pointes sont métalliques et donc il est possible d'étudier le comportement des deux types de porteurs (trous  $h^+$  et électrons  $e^-$ ) en une seule mesure standard du courant de drain ( $I_D$ ) et de la transconductance ( $g_m = \partial I_D / \partial V_G$ ) en fonction de  $V_G$  (Figure 3b). Les films reportés sont généralement non dopés (type  $p$ ,  $N_A \approx 10^{15} \text{ cm}^{-3}$ ); le contact entre les pointes et le film est donc supposé Schottky. La pression appliquée sur les pointes est réglable de 0 à 100 grammes et elle permet de transformer le contact Schottky en contact ohmique. Suivant la pression appliquée, un nombre plus ou moins important de

défauts sont créés autour des pointes, générant ainsi des pièges (Figure 3a). Ces derniers facilitent le passage des porteurs en abaissant la barrière énergétique entre le métal et le film semiconducteur faiblement dopé. Il est donc possible d'obtenir un comportement ohmique pour les contacts S/D avec le film de silicium [8].

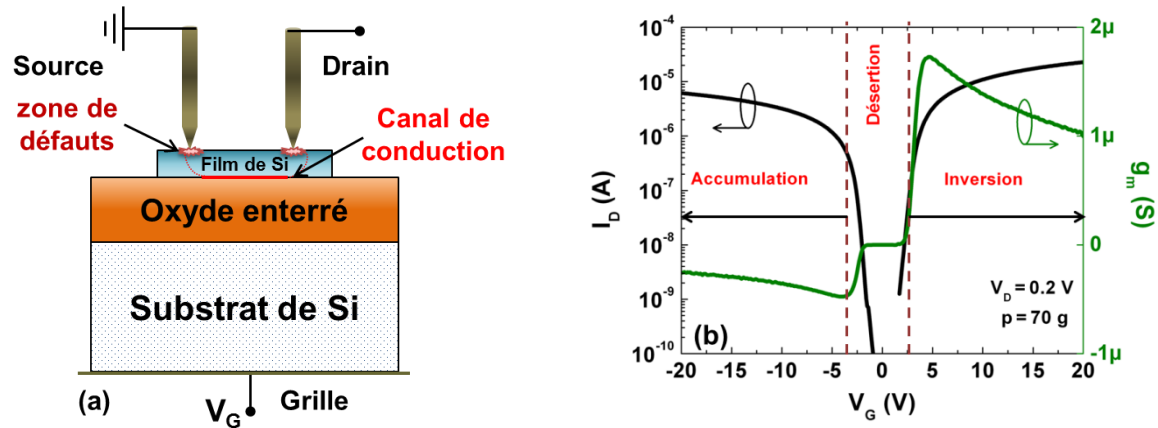


Figure 3: (a) Schéma expérimental d'une mesure  $\Psi$ -MOSFET avec deux pointes métalliques qui sont utilisées comme Source et Drain. Un canal de conduction est créé à l'interface film/BOX par l'intermédiaire de la polarisation du substrat  $V_G$  et les zones de défauts sont générées par la pénétration des pointes dans le film de silicium. (b) Illustration de la conduction ambipolaire (canal d'électrons et canal de trous):  $I_D$ - $V_G$  (échelle logarithmique) et  $g_m$ - $V_G$  sur un film SOI type p avec  $t_{Si} = 88$  nm et  $t_{BOX} = 145$  nm.

Comme mentionné précédemment, la technique  $\Psi$ -MOSFET nécessite très peu d'étapes technologiques pour être mise en place. En effet, les seules étapes utiles sont la gravure des tranchées de largeur de 2 mm du film semiconducteur pour séparer des "plots" de SOI de  $5 \times 5$  mm<sup>2</sup>. Cette isolation est souhaitable pour éviter toute fuite dans le film et des problèmes aux bords de plaque, qui dégraderaient les caractéristiques électriques mesurées. L'appareillage de mesure est constitué d'une station sous pointes JANDEL et d'un analyseur de paramètres Agilent HP-4156B (ou HP-4155A).

### C. Extraction des paramètres électriques

Comme dans le cas d'un MOSFET ordinaire, il existe pour le  $\Psi$ -MOSFET deux types de régimes de conduction: ohmique et saturé. Pour toutes les extractions de paramètres, nous serons dans le régime linéaire (ou ohmique), soit à tension de drain  $V_D$  faible. Dans une telle configuration, les formules théoriques du MOS peuvent être appliquées.

Nous retrouvons donc les expressions pour le courant de drain ( $I_D$ ) et la transconductance ( $g_m$ ):

$$I_D(V_G) = f_g C_{ox} \frac{\mu_0}{[1 + \theta_1(V_G - V_{T,FB})]} (V_G - V_{T,FB}) V_D \quad (1)$$

$$g_m = \frac{\partial I_D}{\partial V_G} = f_g C_{ox} V_D \frac{\mu_0}{[1 + \theta_1(V_G - V_{T,FB})]^2} \quad (2)$$

avec:

- $f_g$  le facteur géométrique (similaire au ratio  $f_g = W/L$  dans un MOSFET classique;  $f_g = 0,75$  dans un  $\Psi$ -MOSFET [9], [10]);
- $C_{ox}$ , la capacité surfacique du BOX
- $\mu_0$ , la mobilité à faible champ ( $\mu_n$  pour les électrons et  $\mu_p$  pour les trous)
- $V_{T,FB}$ , les tensions de seuil pour les canaux des électrons ( $V_T$ ) et des trous ( $V_{FB}$ )
- $\theta_1$ , le facteur de réduction de mobilité relié aux résistances séries ( $R_{SD}$ )

Il existe diverses méthodes pour faire les extractions en utilisant les équations (1) et (2), mais pour une raison de précision seulement la méthode de la fonction Y développée par Ghibaudo [11] sera utilisée dans notre étude (Figure 4a). L'avantage principal de cette méthode vient de son indépendance du facteur de réduction  $\theta_1$  permettant d'éviter l'impact de la  $R_{SD}$  qui est critique dans nos mesures. Si l'on considère que le courant de drain est donné par l'équation (1), dans ce cas la fonction Y, linéaire pour  $|V_G| \geq |V_{T,FB}|$ , est donnée par [11]:

$$Y(V_G) = \frac{I_D}{\sqrt{g_m}} = \sqrt{f_g C_{ox} \mu_0 V_D} (V_G - V_{T,FB}) \quad (3)$$

Du fait de l'ambipolarité des mesures  $\Psi$ -MOSFET, la fonction Y peut être tracée à la fois en accumulation et en inversion. L'intersection de la partie linéaire de Y avec l'axe des abscisses ( $V_G$ ) donne les valeurs  $V_T$  et  $V_{FB}$  (Figure 4a). Afin de déterminer la mobilité à faible champ pour les électrons et les trous, on utilise la pente d'une partie linéaire de la fonction Y (Figure 4a).



Un autre paramètre à extraire est la pente sous le seuil ( $S$ ) de la courbe du courant de drain (Figure 4b), en calculant l'inverse de la dérivée du logarithme du courant par rapport à la tension de grille:

$$S = \left( \frac{\partial \log(I_D)}{\partial V_G} \right)^{-1}_{V_D=\text{cte}} \quad (4)$$

Il est possible d'extraire la pente sous seuil  $S$  pour chacun des modes de conduction du  $\Psi$ -MOSFET, l'accumulation  $S_p$  et l'inversion  $S_n$ . Les pentes  $S_n$  et  $S_p$  peuvent être différentes pour l'accumulation ou l'inversion car elles sont directement impactées par les défauts d'interface qui peuvent agir différemment selon le type de porteurs.

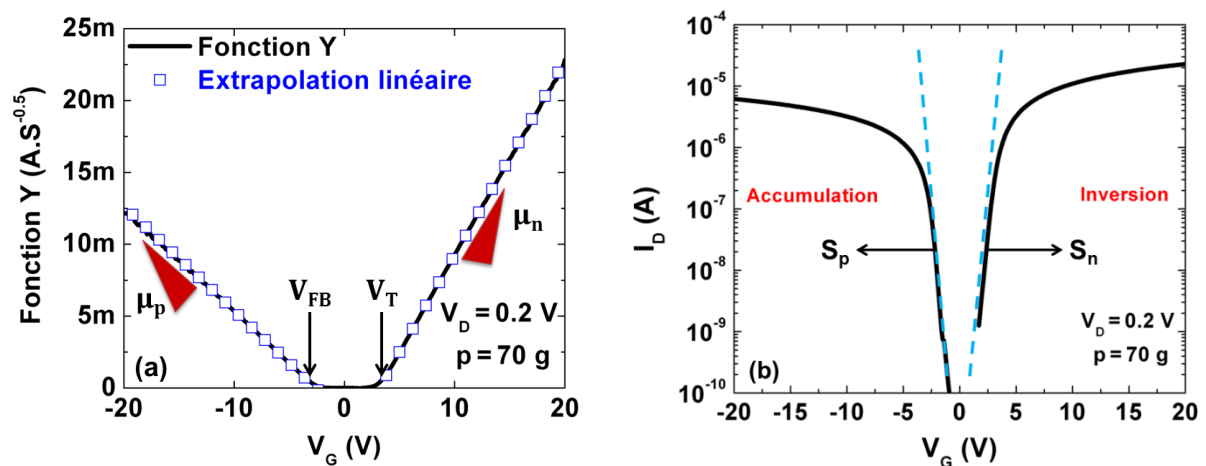


Figure 4: (a) Extraction de  $V_{T,FB}$  et  $\mu_{n,p}$  par la fonction  $Y$  dans le cas d'un substrat SOI. (b) Extraction des pentes sous seuil  $S_n$  et  $S_p$  pour les deux canaux de conduction d'un  $\Psi$ -MOSFET.  $t_{Si} = 88$  nm et  $t_{BOX} = 145$  nm.

## D. Caractérisation des plaques SOI très minces

Dans notre travail, différents couples des couches du film de Si et de BOX ont été caractérisés: entre 12 et 200 nm pour l'épaisseur du film et entre 10 et 400 nm pour l'épaisseur du BOX. Certaines des plaques ont subi une oxydation thermique et sèche à 900°C afin de passiver la surface du film de Si avec 4-10 nm d'oxyde ( $\text{SiO}_2$ ).

Dans ce paragraphe, nous allons prouver que le  $\Psi$ -MOSFET est encore une technique de caractérisation très réussie pour les plaques SOI nues même lorsque les épaisseurs du film et du BOX sont considérablement réduites [12]. En outre, l'impact de la passivation de surface sur quelques échantillons est également montré et discuté.

En ajustant les paramètres de configuration de mesure tels que la pression des pointes, les temps d'attente entre les points de mesure et la polarisation de la grille, nous avons réussi à caractériser avec succès ces structures très minces. Tout d'abord, nous avons mesuré le courant de drain (Figure 5a) et la transconductance (Figure 5b) en fonction de la tension du grille pour des plaques SOI passivées et non passivées avec 12 nm d'épaisseur de film et 25 nm d'épaisseur de BOX. Le premier résultat remarquable est qu'aucun endommagement du BOX par les pointes (et par conséquent aucun courant de fuite) n'est visible.

Dans les films très minces ( $< 100$  nm), le couplage entre le canal et les défauts présents sur la surface libre du film de Si est très grand [13]. Nous avons étudié l'impact de ce couplage en mesurant deux échantillons, passivé (avec 4 nm de couche d'oxyde sur la surface du film) et non passivé dans la Figure 5.

La courbe du courant de drain pour les échantillons passivés (Figure 5a) présente une diminution de la tension de seuil/bande plate ( $V_{T,FB}$ ) et une diminution des pentes sous le seuil ( $S_{n,p}$ ) comparées au film non-passivé. Ceci est une conséquence directe de la réduction de la densité d'états de surface par l'effet de passivation ([13], [14]). La courbe  $g_m$ - $V_G$  (Figure 5b) pour l'échantillon passivé montre une forte augmentation de la mobilité apparente par rapport à l'échantillon non-passivé (si on extrait la mobilité par la méthode du pic de  $g_m$  [15], un pic plus élevé de  $g_m$  implique une plus grande mobilité).

Les résultats de la Figure 5 sur la passivation de surface pour un oxyde enterré mince (25 nm) confirment ceux obtenus pour un oxyde épais (145 nm) [13]. Leur mérite est d'avoir été obtenus sur un tel couple film/BOX mince.

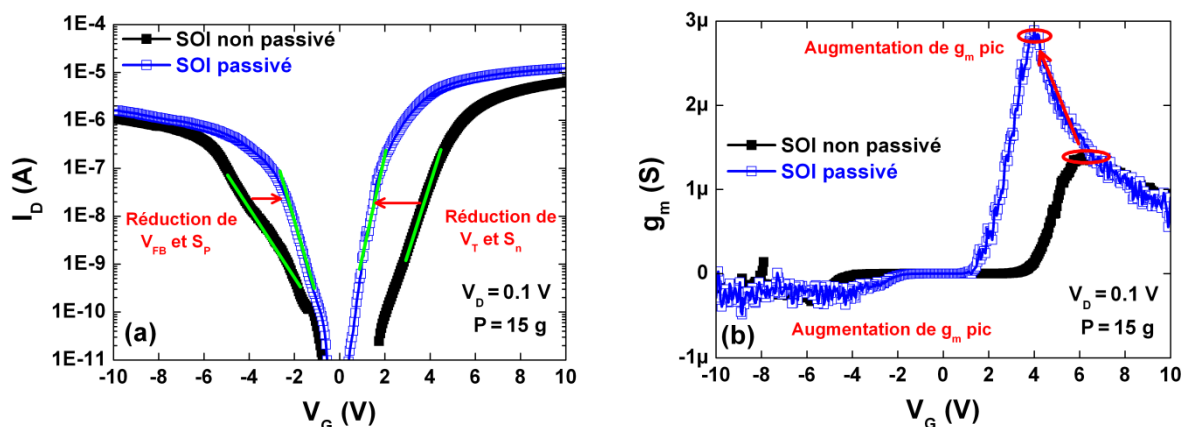


Figure 5: (a) Le courant de drain et (b) la transconductance en fonction de la tension de grille pour un film de Si d'épaisseur 12 nm (passivé et non passivé) et 25 nm d'épaisseur de BOX.

## **Partie II: Nouvelles techniques de caractérisation des plaques SOI**

Dans cette partie, qui constitue le cœur de cette thèse, nous allons étendre tout d'abord la méthode  $\Psi$ -MOSFET pour réaliser des mesures à basse température, puis nous présenterons deux développements inédits du  $\Psi$ -MOSFET: le bruit à basse fréquence et le split  $C$ - $V$ .

### **A. Mesures $\Psi$ -MOSFET à basse température**

Les mesures à basse température donnent des informations détaillées sur les paramètres de transport (mécanismes dominants de collisions, qualité des interfaces), qui ne sont pas disponibles à partir des mesures à température ambiante. Identifier le mécanisme de collision principal révèle la qualité du film et de l'interface Si-SiO<sub>2</sub> qui est très importante pour le procédé de fabrication du SOI. Ici, nous avons démontré l'extension de la technique  $\Psi$ -MOSFET à basse température afin d'étudier les propriétés du transport des plaques SOI [16].

En utilisant la station cryogénique sous pointe 200 mm (Suss Microtec), nous avons effectué des mesures dans une gamme de température de l'azote liquide ( $T = 77$  K) à la température ambiante ( $T = 300$  K) avec un contrôle de la température meilleur que  $\pm 0,1$  K. Deux pointes métalliques ont été utilisées pour former les contacts de source et de drain sur la surface de la plaque SOI. Une tension ( $V_G$ ) est appliquée au support métallique "chuck" pour assurer une polarisation face arrière du substrat de silicium, comme dans une configuration  $\Psi$ -MOSFET normale. La distance entre la source et le drain a été maintenue fixe ( $\sim 1$  mm).

La principale différence entre les mesures à température ambiante et à basse température provient des pointes utilisées. Dans une configuration standard  $\Psi$ -MOSFET à température ambiante, avec la station JANDEL, les pointes sont à pression réglable (les contacts obtenus sont ohmiques). Dans la station cryogénique, la pression sur les pointes n'est pas contrôlable, ce qui peut causer des problèmes de contact dans les mesures.

Afin de vérifier la possibilité d'obtenir des contacts ohmiques dans la station cryogénique, des courbes  $I_D$ - $V_D$  à différentes températures ont été mesurées pour des

tensions  $V_G$  positives et négatives (Figure 6a) sur un film de Si d'épaisseur 40 nm et un BOX d'épaisseur 145 nm. L'allure linéaire des courbes confirme pour les deux types de porteurs (électrons et trous) que les contacts pointes-film de Si sont ohmiques, bien qu'il n'y ait pas de contrôle de pression sur les pointes.

Les courbes  $I_D$ - $V_G$  à plusieurs températures pour le film de Si de 40 nm d'épaisseur sont présentées dans la Figure 6b, où les canaux des électrons et des trous sont progressivement activés, ce qui confirme que le  $\Psi$ -MOSFET fonctionne toujours à basse température. Dans la région de  $V_G$  positive, le courant de drain diminue avec l'augmentation de la température, étant dominé par l'évolution de la mobilité avec la température. Pour la région  $V_G$  négative, ce qui correspond au canal des trous, les courbes  $I_D$  ont un comportement plus complexe résultant des variations concurrentes de la mobilité,  $V_{FB}$  et la résistance série  $R_{SD}$  (environ un ordre de grandeur plus élevé que pour le canal d'électrons) [8].

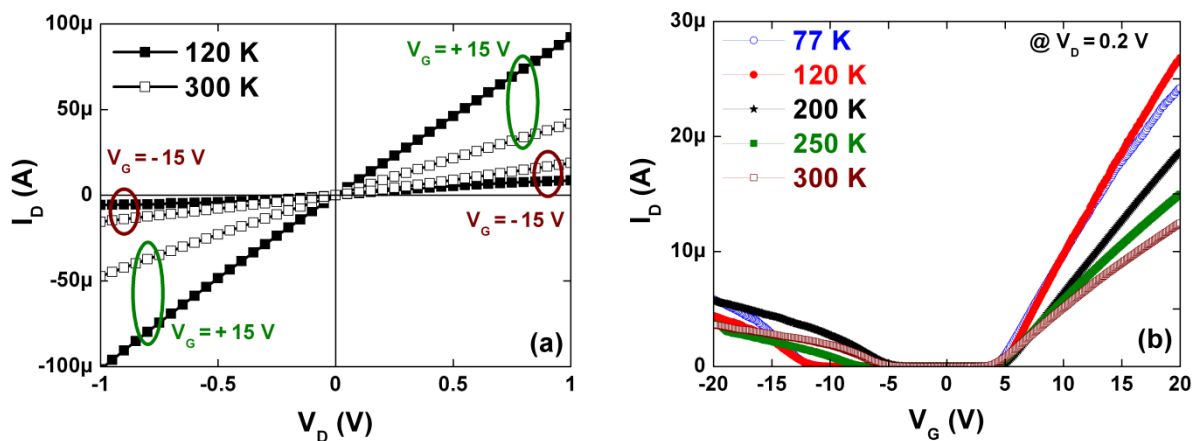


Figure 6: (a) Courant de drain vs. tension de drain avec  $V_G = \pm 15$  V pour deux différentes températures (120 K et 300 K) et (b) courant de drain vs. tension de grille pour différentes températures (77 K, 120 K, 200 K, 250 K et 300 K). L'épaisseur de BOX est de 145 nm et  $t_{Si} = 40$  nm.

Le comportement des courbes  $I_D$ - $V_G$  a été reproduit sur des échantillons avec 88 nm d'épaisseur du film de Si (Figure 7) pour plusieurs températures. L'échelle semi-logarithmique des courbes du courant de drain (Figure 7a) montre une augmentation de la pente en régime de faible inversion en diminuant la température. Ce résultat est théoriquement prévisible. Les courbes de la transconductance  $g_m$  vs.  $V_G$  (Figure 7b) montrent qu'en diminuant la température, le pic du  $g_m$  augmente (pour  $V_G > 0$ ) grâce à l'amélioration de la mobilité à basse température. Les courbes illustrées dans la Figure 6 et dans la Figure 7 valident qualitativement la faisabilité de nos mesures.

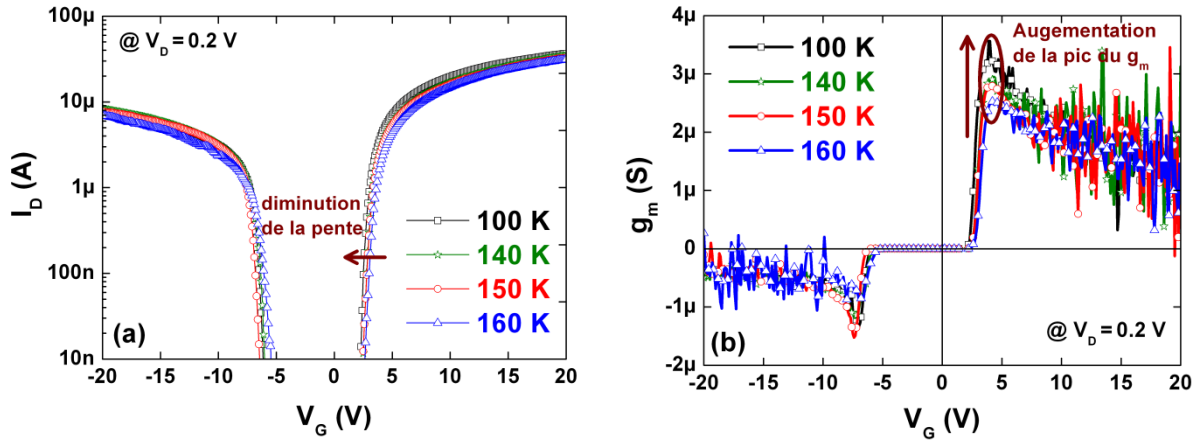


Figure 7: (a) Courant de drain vs. tension de grille dans l'échelle semi-logarithmique pour différentes températures (100 K, 140 K, 150 K et 160 K) et (b) transconductance vs. tension de grille pour les mêmes températures. Épaisseur de BOX est de 145 nm et  $t_{Si} = 88$  nm.

Afin d'éviter l'impact de la  $R_{SD}$ , ce qui est essentiel dans nos mesures, l'extraction des paramètres électriques a été réalisée avec la méthode de la fonction Y précédemment décrite. En outre, nous avons calculé la variabilité entre les valeurs des paramètres extraites et nous avons obtenu moins de 20 % d'erreur pour les valeurs de  $\mu_p$  et  $\mu_n$  (barres d'erreur dans la Figure 8).

Dans ce résumé, nous allons montrer et discuter seulement la mobilité des porteurs. Le travail complémentaire mené sur la tension de seuil et la pente sous le seuil est décrit dans le manuscrit complet [16].

Ici, nous allons extraire les valeurs de mobilité dans le but d'identifier le mécanisme de collision dominant qui apporte des informations importantes sur la qualité du film et de l'interface Si-SiO<sub>2</sub>. Il existe plusieurs types d'interactions, dont les trois mécanismes principaux sont:

- (i) Collisions avec les Phonons:  $\mu_{Ph} \propto T^{-n}$ , où n varie entre 1 et 2.
- (ii) Collisions Coulombiennes:  $\mu_C \propto T^n$ , où n varie entre 1 et 2.
- (iii) Rugosité de surface avec  $\mu_{Sr} \propto E_{eff}^{-2}$ .

Le total de l'inverse de la mobilité suit la loi de Matthiessen [17]:

$$\frac{1}{\mu} = \sum_n \frac{1}{\mu_n} \quad (5)$$

où n est le nombre de mécanismes des collisions.

Les résultats de la Figure 8a et la Figure 8b montrent la dépendance de la mobilité à faible champ avec la température pour les électrons et les trous, respectivement. Comme théoriquement prévu, la mobilité des porteurs augmente en diminuant la température jusqu'au 100 K puis elle diminue pour  $T < 100$  K.

Pour mettre en évidence la contribution des effets de collisions sur la mobilité à faible champ, nous avons superposé les courbes expérimentales (en trait continu) et les courbes théoriques (en pointillés) de la mobilité  $\mu_0(T)$  déduites de la loi du Matthiessen pour les électrons et les trous:

$$\frac{1}{\mu_0(T)} = \frac{1}{\mu_{Ph}(T)} + \frac{1}{\mu_C(T)} \quad (6)$$

avec:

$$\mu_{Ph}(T) = \mu_{0@300} \left(\frac{300}{T}\right)^{1.5} \quad \text{et} \quad \mu_C(T) = \alpha \mu_{0@77} \left(\frac{T}{77}\right)^{1.5} \quad (7)$$

où  $\mu_{0@300}$  et  $\mu_{0@77}$  représentent les valeurs mesurées de la mobilité à faible champ aux températures 300 K et 77 K, respectivement. Pour la mobilité Coulombienne, nous avons ajouté 20 % pour les électrons ( $\alpha = 1,2$ ) et 50 % pour les trous ( $\alpha = 1,5$ ) aux valeurs de  $\mu_0$  extraites à 77 K, afin de prendre en compte des résidus des collisions avec les phonons et pour améliorer le fit. Aucun autre paramètre d'ajustement n'a été utilisé pour les superpositions des courbes.

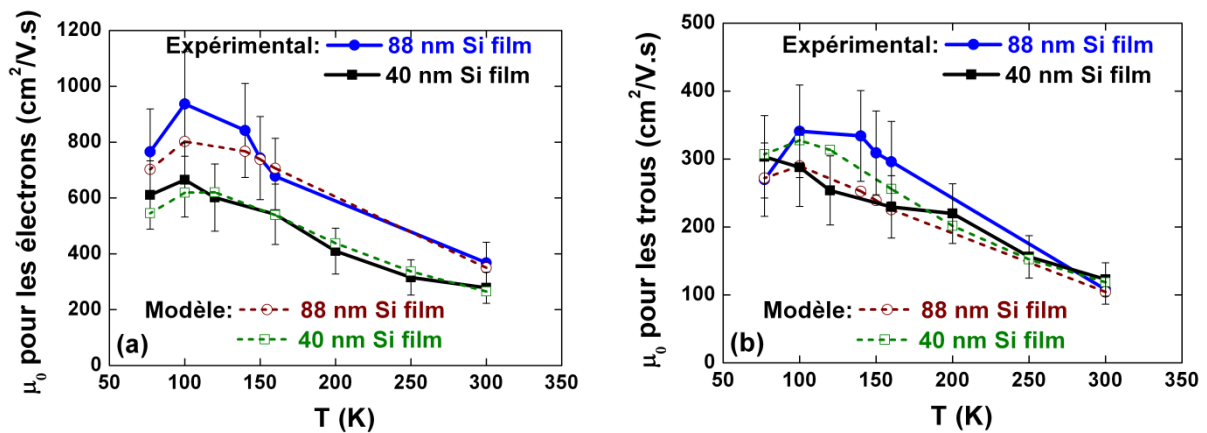


Figure 8: Mobilité à faible champ expérimentale (trait continu) et modèle (pointillés) des électrons (a) et des trous (b) en fonction de la température pour 88 nm et 40 nm d'épaisseur de film de Si.

Les courbes modélisées déduites des équations (6) et (7) et les courbes expérimentales de la Figure 8a se superposent, en particulier pour des températures élevés. La petite différence qui subsiste à très basse température, se trouve dans les limites des barres d'erreur pour plusieurs échantillons testés. Un comportement

similaire est obtenu pour la mobilité des trous (Figure 8b). Afin de confirmer encore plus nos résultats, on note que les courbes des mobilités varient comme  $T^{-n}$  pour  $T > 100$  K (où  $n$  est la valeur extraite des courbes de  $\mu(T)$  en échelle *log-log* et varie entre 1 et 2 pour les deux films de Si d'épaisseurs 88 et 40 nm). Cela implique que le mécanisme de collision avec les phonons domine à haute T.

Rappelons que les collisions coulombiennes résultent des pièges ( $D_{it}$ ) à l'interface Si-BOX ou à la surface supérieure du film. Par conséquent, la diminution de la mobilité avec l'augmentation de la température montre que les collisions des phonons (et non les collisions coulombienne) sont responsables de la réduction de la mobilité dans les plaques SOI. Cela reflète indirectement la bonne qualité du film de Si et de l'interface Si-SiO<sub>2</sub>.

## **B. Mesures de bruit à basse fréquence**

Dans le monde des dispositifs électroniques, le bruit indique des fluctuations aléatoires de courant ou de tension autour d'une valeur moyenne. Le bruit basse fréquence (LFN) constitue un outil de caractérisation puissant. Les mesures LFN révèlent les fluctuations de la concentration et de la mobilité des porteurs dans le canal d'un MOSFET, de même que la qualité de l'oxyde en termes de densité des pièges.

Dans notre travail, nous avons étudié pour la première fois le bruit LFN sur des plaques SOI nues avant tout procès CMOS afin de déterminer la source de bruit dominante et de qualifier les interfaces Si/BOX et Si/air [18]. Avant de passer aux mesures LFN sur les plaques SOI, rappelons brièvement la théorie de base du bruit électronique, les différentes sources de bruits et leurs méthodes d'analyse.

Différentes types de bruit existent mais nous nous concentrerons ici sur le bruit  $1/f$  (Figure 9a) qui domine généralement le spectre du bruit global pour le courant de drain dans le domaine des basses fréquences. Ce type de bruit est associé à des fluctuations de la conductivité dans le canal [19].

La définition de la conductance électrique d'un matériau est donnée par [20]:

$$G = \frac{qn\mu S}{L} \quad (8)$$

où  $\mu$ ,  $n$ ,  $S$  et  $L$  sont respectivement la mobilité, la densité de porteurs libres, la surface et la longueur du matériau considéré.

Selon l'équation (8), la fluctuation de  $G$  peut être due soit à la fluctuation de nombres des porteurs  $\Delta n$  (modèle proposé par McWhorter [21]) soit à la fluctuation de la mobilité  $\Delta\mu$  (modèle proposé par Hooge [22]). Donnons quelques détails sur les deux modèles.

*Modèle de fluctuation du nombre des porteurs (CNF):*

McWhorter a proposé que la fluctuation du courant de drain est due à la fluctuation du nombre des charges mobiles dans le canal, près de l'interface semiconducteur/oxyde [21].  $\Delta n$  résulte de la capture/libération de charge dynamique par les pièges lents distribués dans l'oxyde. Dans ce cas, la densité spectrale normalisée ( $S_{I_d}/I_D^2$ ) peut être écrite comme ([19], [11] et [23]):

$$\frac{S_{I_d}(f)}{I_D^2} = \frac{g_m^2}{I_D^2} S_{V_{fb}} = \frac{g_m^2}{I_D^2} \frac{q^2 k T \lambda N_t}{W L C_{ox}^2 f^\gamma} \quad (9)$$

où  $S_{V_{fb}}$  est la densité spectrale de puissance de la tension de bandes plates,  $f$  est la fréquence,  $\gamma$  est l'exposant caractéristique proche de l'unité,  $\lambda$  est la constante caractéristique de l'effet de tunnel ( $\approx 0,1$  nm pour une interface Si/SiO<sub>2</sub>) et  $N_t$  est la densité volumique des pièges lents dans l'oxyde au voisinage du niveau de Fermi.

*Modèle de fluctuation de la mobilité Hooge (HMF):*

Hooge attribue les fluctuations de la conductance aux fluctuations de la mobilité. Dans son modèle, le bruit  $1/f$  du courant de drain est un phénomène de volume dû aux fluctuations de la mobilité des porteurs résultant des collisions avec les phonons [22]. Dans ce cas,  $S_{I_d}/I_D^2$  en régime linéaire et forte inversion est [19]:

$$\frac{S_{I_d}(f)}{I_D^2} = \frac{q \alpha_H \mu_{eff} V_D}{L^2 f I_D} \quad (10)$$

Dès que le bruit basse fréquence (LF) montre un spectre du type  $1/f$ , il est nécessaire de distinguer le modèle qui domine, le bruit CNF ou HMF. Tout d'abord, nous traçons  $S_{I_d}/I_D^2$  pour une fréquence fixe en fonction de  $I_D$  en échelle logarithmique (voir la Figure 9b). D'après les équations (9) et (10) les allures des courbes obtenues sont différentes, ce qui permet de distinguer les modèles.



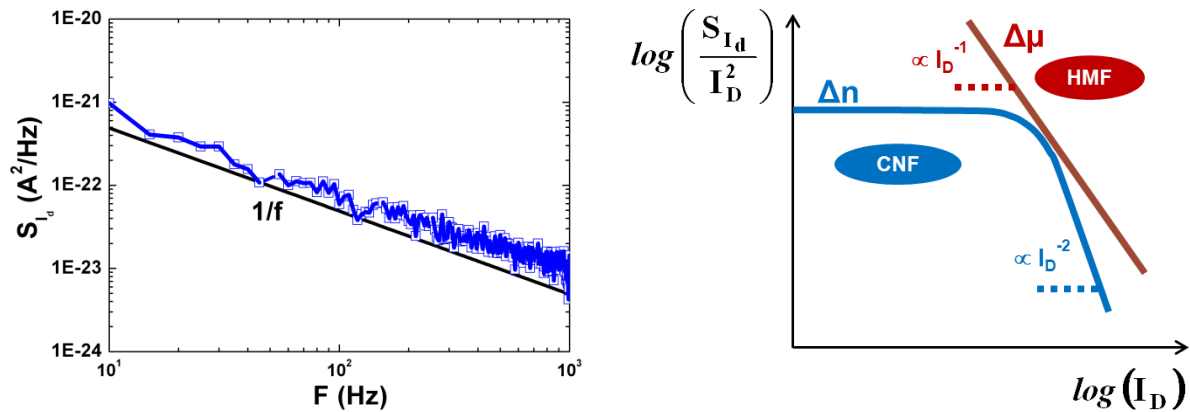


Figure 9: (a) Densité spectrale de puissance ( $S_{I_d}$ ) du spectre  $1/f$  dans le domaine fréquentiel pour un substrat SOI. (b) Représentation schématique de la variation de la densité spectrale normalisée par le courant de drain au carré en fonction du courant de drain pour les modèles CNF ou HMF du bruit  $1/f$ .

Nous avons effectué des mesures de bruit au niveau des plaques en utilisant la configuration standard  $\Psi$ -MOSFET ([18], [12]). Par conséquent, la densité de pièges peut être déterminée directement à l'interface film-BOX, avant la fabrication des transistors.

La Figure 10a montre la densité spectrale de puissance,  $S_{I_d}$ , tracée en fonction de la fréquence pour une plaque SOI avec 88 nm de film de Si et 145 nm de BOX pour différentes tensions appliqués sur la grille-arrière. Le comportement en  $1/f$  (flicker noise) est clairement visible. Pour vérifier si ce comportement est valable pour les films SOI très minces, nous avons tracé  $S_{I_d}$  également en fonction de la fréquence pour différentes  $V_G$  pour un SOI avec 12 nm d'épaisseur de film et 145 nm de BOX (Figure 10b). Même type de bruit (flicker noise) est trouvé.

Dans les films très minces (12 nm) l'impact de la surface supérieure sur le bruit du canal enterré (à l'interface film-BOX) est plus important que celui dans des films plus épais (88 nm). C'est pourquoi le niveau de bruit est supérieur dans la Figure 10b.

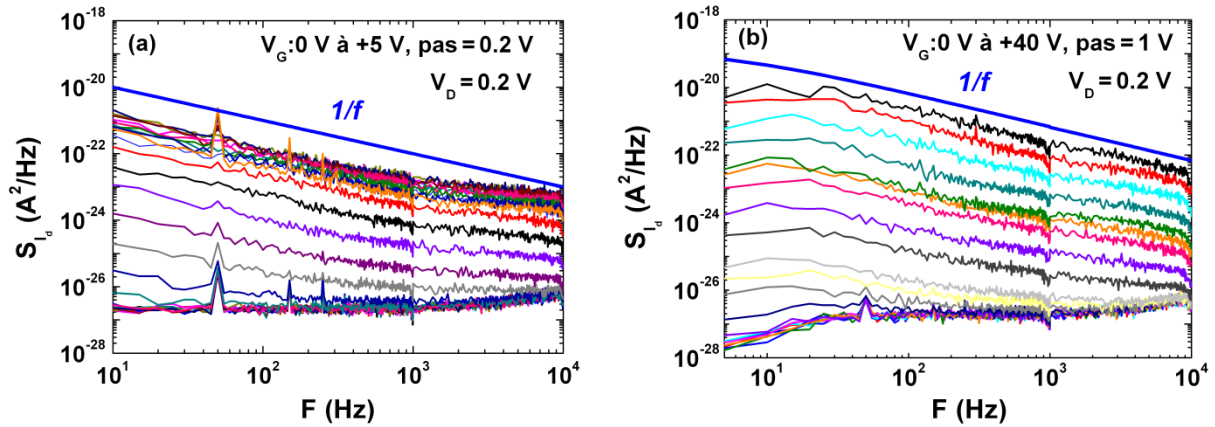


Figure 10: Bruit basse fréquence en fonction de la fréquence dans un  $\Psi$ -MOSFET: (a) 88 nm d'épaisseur de film de Si et (b) 12 nm d'épaisseur de film de Si avec 145 nm de BOX. Le bruit  $1/f$  est clairement visible dans les deux films SOI.

Afin de déterminer lequel des deux modèles CNF ou HMF compte mieux pour les données du bruit basse fréquence, il est nécessaire de tracer  $S_{I_D}/I_D^2$  en fonction du courant de drain en échelle logarithmique comme expliqué précédemment. La Figure 11 montre que  $S_{I_D}/I_D^2$  suit la dépendance en  $(g_m/I_D)^2$  confirmant le modèle CNF. Dans la Figure 11, la courbe de  $S_{I_D}/I_D^2$  en fonction de  $I_D$  montre un plateau en faible inversion et une décroissance linéaire en forte inversion, étant proportionnel à  $(g_m/I_D)^2$ . La faisabilité de ces mesures de bruit basse fréquence sur les structures SOI très minces a donc été démontrée dans cette thèse.

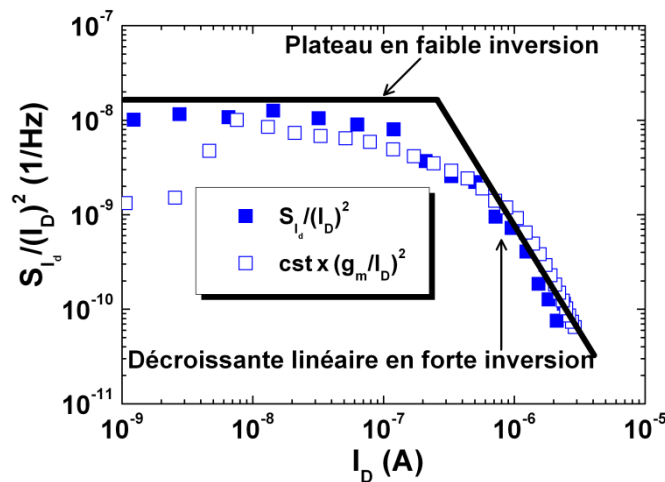


Figure 11: Bruit basse fréquence normalisé et  $k \times (g_m/I_D)^2$  en fonction du courant de drain (avec  $k \approx 10^{-9}$  et  $p = 50$  g). 88 nm d'épaisseur du film de Si et 145 nm de BOX.

Par conséquent, l'extraction du  $D_{it}$  est envisageable. Cependant, les valeurs  $D_{it}$  ( $\approx 10^{13-14} \text{ cm}^{-2} \cdot \text{eV}^{-1}$ ) obtenues à partir des mesures de bruit basse fréquence sont 2 à 3 ordres de grandeur plus élevées que celles obtenues à partir des mesures statiques  $I_D$ -

$V_G$  ( $D_{it} \approx 10^{11} \text{ cm}^{-2} \cdot \text{eV}^{-1}$ ). Deux arguments peuvent être donnés pour expliquer ces valeurs élevées des  $D_{it}$ :

- La difficulté d'estimer la surface effective qui engendre le bruit.
- Le bruit en excès peut être généré à la surface libre de la plaque SOI (Si/interface air).

En plus de la mise en place de cette méthode de mesure, nous avons également montré que le bruit n'est pas affecté par la pression des pointes. Nous avons également étudié l'effet de la passivation de la surface des plaques sur les résultats du bruit. Même s'il y a quelques points à approfondir dans cette étude, elle a le mérite de montrer la faisabilité expérimentale des mesures de bruit basse fréquence sur des plaques SOI vierges en configuration  $\Psi$ -MOSFET.

### C. Mesures split C-V

La méthode la plus couramment utilisée pour mesurer la mobilité effective ( $\mu_{\text{eff}}$ ) est la technique split C-V. Les mesures split C-V sont généralement effectuées sur des transistors SOI MOSFET entièrement procédés [24]. L'intérêt de notre travail sur les mesures split C-V vient de l'utilisation de la technique  $\Psi$ -MOSFET avec des pointes en pression, qui ne nécessite aucune préparation des contacts. Pour cette raison, l'extraction rapide de la mobilité dans les plaques SOI avant tout procès CMOS est de grand intérêt pour contrôler et optimiser la qualité des substrats de départ.

Traditionnellement, la fonction Y [11] a été la technique préférée. Toutefois, les informations qui peuvent être obtenues sur la mobilité des porteurs sont limitées (mobilité à faible champ); le graphe de la mobilité en fonction de l'inversion/l'accumulation des charges ou du champ effectif n'est pas mesuré mais reconstruit. Une approche plus directe est basée sur la détermination de la charge d'inversion ou d'accumulation à partir des mesures de capacité combinées avec des courbes statiques  $I_D$ - $V_G$ . Un autre aspect important de la split C-V est que la mobilité est valable de faible à forte inversion, contrairement à celles extraites en mode statique qui est correcte juste en forte inversion.

Dans les MOSFETs, la technique de split C-V est basée sur les mesures des capacités  $C_{gc}$  (capacité grille-canal) et  $C_{gb}$  (capacité grille-substrat) en fonction de la

tension de grille. Toutefois, dans la structure  $\Psi$ -MOSFET, le substrat de Si agit en tant qu'une grille (il n'y a pas de grille métallique supérieure), donc seulement la  $C_{gc}$  peut être mesurée. Deux types de mesures  $\Psi$ -MOSFET ont été effectuées: courbes statique  $I_D-V_G$  et courbes split  $C-V$ . Pour les mesures de  $C-V$  dans la configuration  $\Psi$ -MOSFET, les pointes de source et de drain sont reliées à un potentiel bas, tandis que la grille arrière a été polarisée par  $V_G$  et reliée au potentiel haut du LCR-mètre (Figure 12). Le schéma du système de mesure et le circuit équivalent sont présentés dans la Figure 12 ci-dessous.

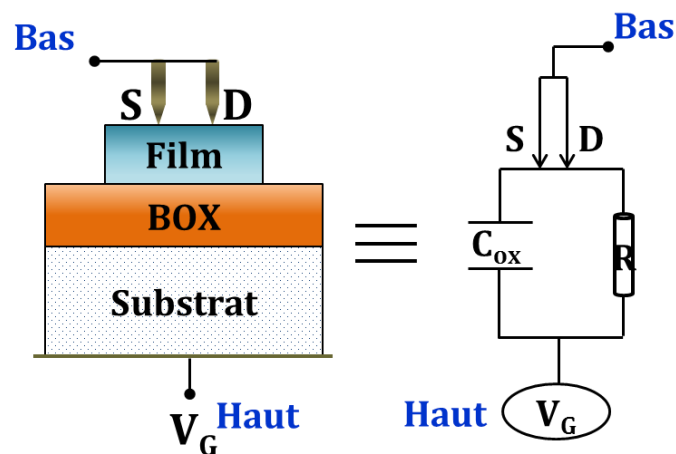


Figure 12: Configuration schématique de la technique split  $C-V$  avec la représentation du circuit équivalent (modèle  $C_p-G$ ).

Le concept a été vérifié pour différentes géométries de structures SOI. Nous montrons ici une seule structure de 20 nm de film de Si et 145 nm de BOX (Figure 13). Comme habituellement pour le  $\Psi$ -MOSFET, les deux canaux des électrons ( $V_G > 0$ ) et des trous ( $V_G < 0$ ) sont activés (Figure 13a). Les courbes  $C_{gc}-V_G$  pour différentes fréquences sont reproduites dans la Figure 13b. Lorsque le film est déserté ( $V_G \approx 0$  V), la capacité est égale à zéro. Ensuite, la capacité augmente en raison de l'accumulation progressive de la couche d'inversion ou d'accumulation. Une fois l'inversion (ou l'accumulation) atteinte la capacité sature à une valeur fixée par  $C_{BOX}$ .

La forme des courbes  $C-V$  dans la Figure 13b confirme cette observation. Par conséquent, notre nouvelle technique est expérimentalement validée avec succès pour les structures SOI. La dépendance en fréquence de ces courbes a été également abordée dans le manuscrit.

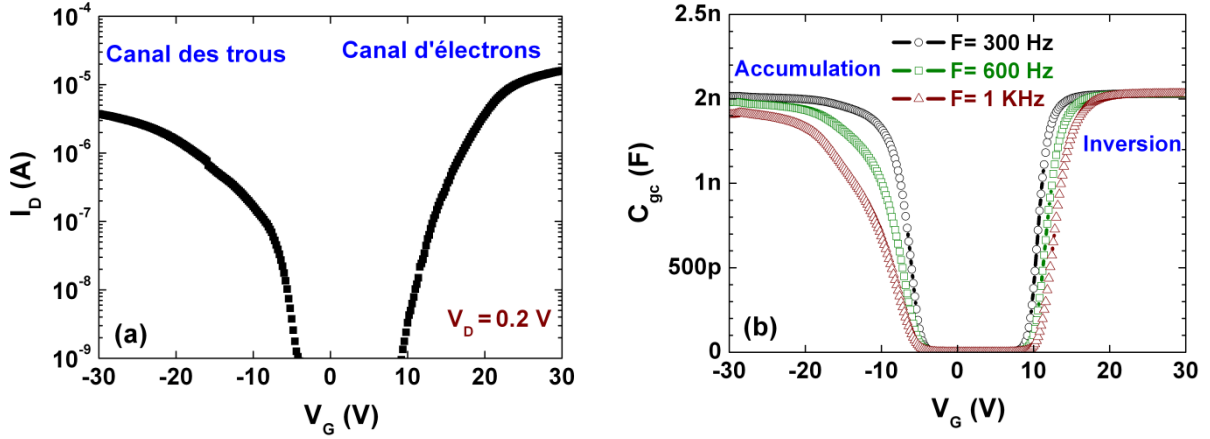


Figure 13: (a)  $I_D$  vs.  $V_G$  and (b)  $C_{gc}$  vs.  $V_G$  pour un substrat SOI avec 20 nm d'épaisseur du film de Si et 145 nm de BOX.

Nous montrons ici la méthodologie pour extraire la mobilité effective à partir des courbes expérimentales et les résultats obtenus. Traditionnellement, deux méthodes sont utilisées pour évaluer  $\mu_{\text{eff}}$  en fonction de  $V_G$ :

$$\mu_{\text{eff}} = \frac{I_D}{f_g Q_{\text{inv,acc}}(V_G) V_D} \quad (11)$$

**Méthode de la fonction Y.** Cette technique est indirecte, elle se base sur des mesures conventionnelles  $I_D$ - $V_G$  [11]. La charge d'inversion  $Q_{\text{inv}}(V_G)$  et la charge d'accumulation  $Q_{\text{acc}}(V_G)$  sont calculées en utilisant  $V_T$  et  $V_{\text{FB}}$  extraits par la fonction Y:

$$Q_{\text{inv}}(V_G) = C_{\text{ox}}(V_G - V_T) \text{ et } Q_{\text{acc}}(V_G) = C_{\text{ox}}(V_G - V_{\text{FB}}) \quad (12)$$

où  $C_{\text{ox}}$  est la capacité du BOX par unité de surface ( $C_{\text{ox}} = \epsilon_{\text{ox}}/t_{\text{BOX}}$ ).

**Méthode split C-V.** Cette technique directe sert à évaluer les courbes de la  $\mu_{\text{eff}}$  ( $Q_{\text{inv, acc}}$ ) à partir des mesures split C-V. Pour le split C-V,  $Q_{\text{inv}}(V_G)$  et  $Q_{\text{acc}}(V_G)$  sont obtenues par intégration de la capacité mesurée sur toute la gamme de  $V_G$  positive et négative, respectivement:

$$Q_{\text{inv}}(V_G) = \frac{1}{S_{\text{eff}}} \int_{V_0}^{V_G} C_{\text{gc}}(u) du \text{ et } Q_{\text{acc}}(V_G) = \frac{1}{S_{\text{eff}}} \int_{V_G}^{V_0} C_{\text{gc}}(u) du \quad (13)$$

où  $V_0$  dans notre cas est  $\approx 0$  V. La normalisation par la surface effective ( $S_{\text{eff}}$ ) est nécessaire pour obtenir la densité des charges d'inversion ou d'accumulation par unité de surface. La surface effective est obtenue en divisant  $C_{\text{max}}$  (F) par  $C_{\text{ox}}$  (F/cm<sup>2</sup>), où  $C_{\text{max}}$  est la capacité maximale extraite des mesures split C-V à  $V_G$  positif pour les électrons et à  $V_G$  négatif pour les trous.

Nous avons utilisé ces deux méthodes pour calculer la mobilité effective des électrons et des trous, comme le montre la Figure 14. La mobilité effective en fonction de  $V_G$  pour l'échantillon SOI avec 88 nm d'épaisseur de film et 145 nm de BOX est illustrée dans la Figure 14a pour les électrons et dans la Figure 14b pour les trous. Les courbes de mobilité obtenues en statique et par split  $C-V$  se superposent en forte inversion pour les électrons et en forte accumulation pour les trous.

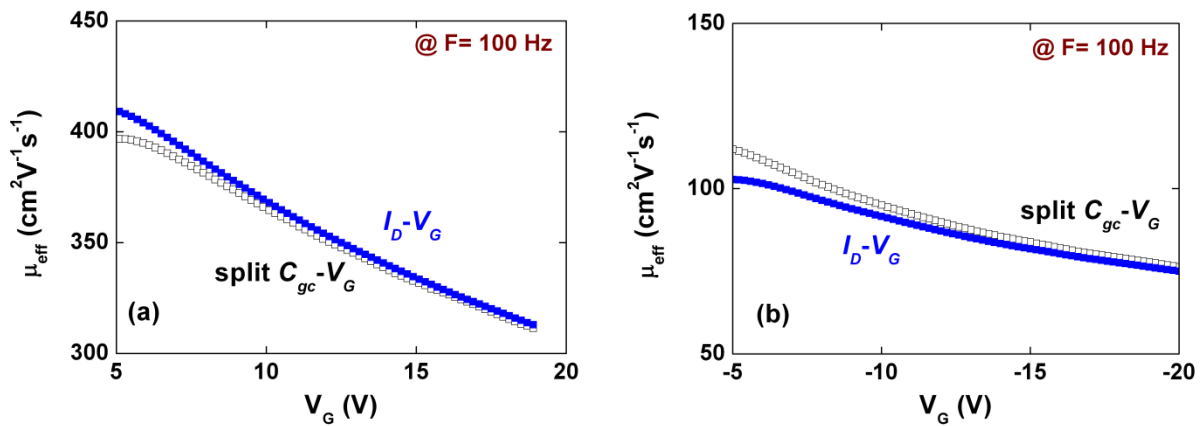


Figure 14:  $\mu_{eff}$  en fonction du  $V_G$  calculée à partir des mesures statique  $I_D-V_G$  et des courbes split  $C-V$  pour les électrons (a) et pour les trous (b). 88 nm du film de Si et 145 nm de BOX.

Après avoir démontré la faisabilité de la mesure et validé la technique d'extraction de la mobilité sur plusieurs géométries d'échantillons, nous nous sommes intéressés à des études plus subtiles, comme le développement et la validation d'un modèle physique pour expliquer la variation de la valeur maximale de la capacité avec la fréquence ou l'étude de la passivation des surfaces des échantillons.

## Conclusion générale

Au cours de ces trois années de doctorat, je me suis concentré sur l'étude de matériaux SOI et du pseudo-MOSFET dans une définition large. Le SOI utilisé n'est pas seulement le matériau standard Silicium-Sur-Isolant. Nous avons aussi étudié des films très minces (moins de 12 nm d'épaisseur), des BOX très minces (jusqu'à 10 nm d'épaisseur), des films fortement dopés (jusqu'à  $10^{20}$  cm<sup>-3</sup>), des nanofils SiGe empilés dans des architectures 3D ou des films de silicium décorés avec des nanoparticules d'or.

Les paramètres physiques mesurés dans un  $\Psi$ -MOSFET ne sont pas seulement limités au courant, mais ils peuvent s'étendre à la capacité ou à des spectres de bruit de basse fréquence. Avec ces extensions, nous avons enrichi la caractérisation électrique des plaques SOI dans la configuration  $\Psi$ -MOSFET. Des conclusions regroupant la totalité de notre travail sont présentées ici:

- La possibilité d'explorer des plaques SOI très minces jusqu'à 12 nm d'épaisseur du film de silicium et 10 nm de BOX en utilisant le  $\Psi$ -MOSFET avec les pointes de pression réglable a été prouvée.
- La caractérisation des substrats SOI par  $\Psi$ -MOSFET a été mise en place pour les mesures à basse température et les modèles adaptés ont permis d'expliquer la variation des paramètres avec la température.
- Nous avons initié la caractérisation du bruit basse fréquence pour les plaques SOI nues en utilisant le  $\Psi$ -MOSFET.
- Nous avons implémenté une nouvelle technique de caractérisation des substrats SOI nu, basée sur des mesures split  $C-V$  à l'aide du  $\Psi$ -MOSFET.
- Nous avons caractérisé pour la première fois des films SOI fortement dopés de  $10^{19-20}$  cm<sup>-3</sup> par la méthode  $\Psi$ -MOSFET et nous avons validé ces résultats par des mesures d'effet Hall et 4-pointes.
- Nous avons proposé et vérifié un capteur innovant basé sur le  $\Psi$ -MOSFET pour la détection des nanoparticules d'or déposées sur la surface supérieure du film de Si.

- Une méthode de caractérisation originale pour les nanofils 3D SiGe/SiGeC suspendus et verticalement empilés avant la fabrication de la grille et des contacts source/drain, inspiré du principe  $\Psi$ -MOSFET, a été mise en œuvre.



## Références

- [1] S. Cristoloveanu and S. S. Li, *Electrical Characterization of Silicon-On-Insulator Materials and Devices*, Kluwer, Boston, 1995.
- [2] Michel Bruel, "Process for the production of thin semiconductor materials films," U.S. Patent n°5,374,564, 1994.
- [3] M. Bruel, "Silicon on insulator material technology," *Electronics Letters*, vol. 31, pp. 1201-1202, 1995.
- [4] Balestra Francis and Cristoloveanu Sorin, "Technologie silicium sur isolant (SOI)," *Techniques de l'ingénieur Technologies des dispositifs actifs*, vol. base documentaire : TIB286DUO, 2002.
- [5] Soitec (Smart Cut): [http://www.soitec.com/pdf/Soitec\\_SmartCut\\_FR.pdf](http://www.soitec.com/pdf/Soitec_SmartCut_FR.pdf)
- [6] G. K. Celler and Sorin Cristoloveanu, "Frontiers of silicon-on-insulator," *Journal of Applied Physics*, vol. 93, pp. 4955-4978, 2003.
- [7] S. Cristoloveanu and S. Williams, "Point-contact pseudo-MOSFET for in-situ characterization of as-grown silicon-on-insulator wafers," *Electron Device Letters, IEEE*, vol. 13, pp. 102-104, 1992.
- [8] I. Ionica, I. Savin, W. Van Den Daele, T. Nguyen, X. Mescot and S. Cristoloveanu, "Characterization of silicon-on-insulator films with pseudo-metal-oxide-semiconductor field-effect transistor: Correlation between contact pressure, crater morphology, and series resistance," *Applied Physics Letters*, vol. 94, pp. 012111-012113, 2009.
- [9] D. Munteanu, S. Cristoloveanu and E. Guichard, "Numerical simulation of the pseudo-MOSFET characterization technique," *Solid-State Electronics*, vol. 43, pp. 547-554, 1999.
- [10] K. Komiya, N. Bresson, Sato Shingo, S. Cristoloveanu and Y. Omura, "Detailed investigation of geometrical factor for pseudo-MOS transistor technique," *Electron Devices, IEEE Transactions on*, vol. 52, pp. 406-412, 2005.
- [11] G. Ghibaudo, "New method for the extraction of MOSFET parameters," *Electronics Letters*, vol. 24, pp. 543-545, 1988.
- [12] A. Diab, I. Ionica, S. Cristoloveanu, F. Allibert, Y. H. Bae, J. A. Chroboczek and G. Ghibaudo, "Static and low-frequency noise characterization of ultrathin SOI with very thin BOX in pseudo-MOSFET configuration," in *Semiconductor Device Research Symposium (ISDRS), 2011 International*, pp. 1-2, 2011.
- [13] G. Hamaide, F. Allibert, H. Hovel and S. Cristoloveanu, "Impact of free-surface passivation on silicon on insulator buried interface properties by pseudotransistor characterization," *Journal of Applied Physics*, vol. 101, pp. 114513-114516, 2007.
- [14] N. Rodriguez, S. Cristoloveanu and F. Gamiz, "Revisited Pseudo-MOSFET Models for the Characterization of Ultrathin SOI Wafers," *Electron Devices, IEEE Transactions on*, vol. 56, pp. 1507-1515, 2009.
- [15] Hao Chu, B. Cabon-Till, S. Cristoloveanu and G. Ghibaudo, "Experimental determination of short-channel MOSFET parameters," *Solid-State Electronics*, vol. 28, pp. 1025-1030, 1985.
- [16] A. Diab, L. Pirro, I. Ionica, X. Mescot, G. Ghibaudo and S. Cristoloveanu, "Low-temperature pseudo-metal-oxide-semiconductor field-effect transistor measurements on bare silicon-on-insulator wafers," *Applied Physics Letters*, vol. 101, pp. 092110-092114, 2012.
- [17] S. M. Sze, *Physics of Semiconductor Devices (Second Edition)*, Wiley press, New York, 1981.
- [18] A. Diab, I. Ionica, S. Cristoloveanu, F. Allibert, Y. H. Bae, J. A. Chroboczek and G. Ghibaudo, "Low-frequency noise in SOI pseudo-MOSFET with pressure probes," *Microelectronic Engineering*, vol. 88, pp. 1283-1285, 2011.
- [19] G. Ghibaudo, O. Roux, Ch Nguyen-Duc, F. Balestra and J. Brini, "Improved Analysis of Low Frequency Noise in Field-Effect MOS Transistors," *physica status solidi (a)*, vol. 124, pp. 571-581, 1991.

- [20] Dieter K. Schroder, *Semiconductor material and device characterization (Third Edition)*, Wiley-Interscience, USA, 2006.
- [21] A. L. Mcwhorter and R. H. Kingston, *Semiconductor Surface Physics*,. University of Pennsylvania, USA, pp. 207-228, 1957.
- [22] F. N. Hooge, T. G. M. Kleinpenning and L. K. J. Vandamme, "Experimental studies on  $1/f$  noise," *Rep. Prog. Phys.*, vol. 44, pp. 479-532, 1981.
- [23] S. Christensson, I. Lundström and C. Svensson, "Low frequency noise in MOS transistors," *Solid-State Electronics*, vol. 11, pp. 797-812, 1968.
- [24] J. Wang, N. Kistler, J. Woo and C. R. Viswanathan, "Mobility-field behavior of fully depleted SOI MOSFET's," *Electron Device Letters, IEEE*, vol. 15, pp. 117-119, 1994.